

# ELECTRO-OPTICAL SYSTEMS, INC.

A Subsidiary of Xerox Corporation

300 N. Halstead Street, Pasadena, California

FACILITY FORM 602

N65 25271

(ACCESSION NUMBER)

282

(PAGES)

CR 62976

(NASA CR OR TMX OR AD NUMBER)

(THRU)

1

(CODE)

30

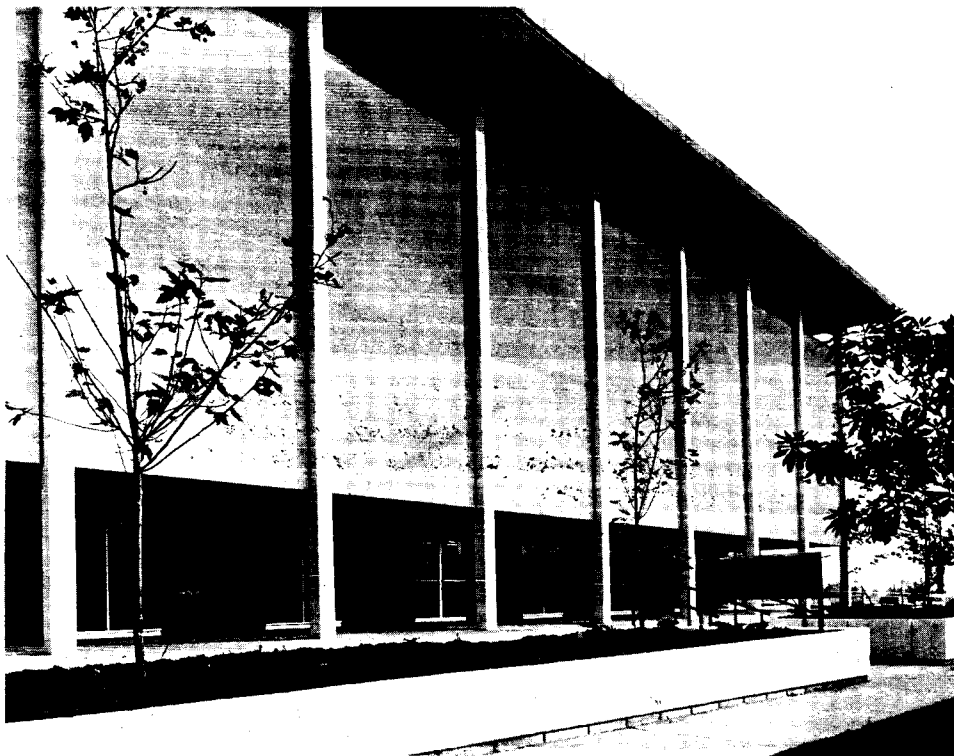
(CATEGORY)

GPO PRICE \$ \_\_\_\_\_

OTS PRICE(S) \$ \_\_\_\_\_

Hard copy (HC) 6.00

Microfiche (MF) 1.50



CASE FILE COPY

RE-ORDER NO. 65-287

VOL. II  
SEC. 1-6

Final Report

ANALYSIS OF ANCILLARY EQUIPMENT FOR  
SOLAR-THERMIONIC SYSTEM

Prepared for  
Jet Propulsion Laboratory  
4800 Oak Grove Drive  
Pasadena, California  
Attention: R. Boring

Contract 950699 - Task III

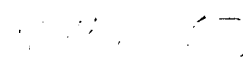
EOS Report 4326-Final

10 March 1965

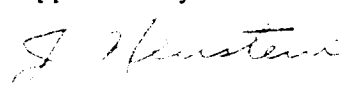
Volume II: Technical Background  
Section 1 through 6

Prepared by Staff  
Space Power Systems

Approved by

  
W. R. Menetrey, Manager  
Space Power Systems

Approved by

  
J. Neustein, Associate Manager  
Program Management and Systems Engineering

This work was performed for the Jet Propulsion Laboratory,  
California Institute of Technology, sponsored by the  
National Aeronautics and Space Administration under  
Contract NAS7-100.

ELECTRO-OPTICAL SYSTEMS, INC. - PASADENA, CALIFORNIA

## CONTENTS

|       |  |      |
|-------|--|------|
| 1.    | INTRODUCTION: VOLUME II                              | 1-1  |
| 1.1   | Study Scope  | 1-1  |
| 1.2   | Vehicle Integration and Packaging Problems           | 1-5  |
| 2.    | SYSTEM CONSIDERATIONS                                | 2-1  |
| 2.1   | Aspects of System Reliability                        | 2-1  |
| 2.2   | System Weight Estimates                              | 2-9  |
|       | REFERENCES - Section 2                               | 2-15 |
| 3.    | SOLAR CONCENTRATORS                                  | 3-1  |
| 3.1   | Physical Description                                 | 3-1  |
| 3.2   | Design Rationale                                     | 3-3  |
| 3.3   | State of the Art                                     | 3-3  |
| 3.4   | Optical Performance Characteristics of Concentrators | 3-11 |
| 3.4.1 | Optimum Collector Rim Angle                          | 3-13 |
| 3.4.2 | Mirror Efficiency                                    | 3-23 |
| 3.4.3 | The Nature of Surface Errors                         | 3-29 |
| 3.4.4 | Misorientation                                       | 3-35 |
| 3.5   | Thermal Effects                                      | 3-35 |
| 3.6   | Structural Aspects                                   | 3-56 |
| 3.6.1 | Concentrator Weight                                  | 3-56 |
| 3.6.2 | Membrane Stresses                                    | 3-58 |
| 3.6.3 | Compressive Buckling Stress                          | 3-60 |
| 3.6.4 | Lateral Acceleration Effects                         | 3-66 |
| 3.6.5 | Vibration  | 3-68 |
| 3.6.6 | Vibration Effects                                    | 3-76 |
| 3.6.7 | Shock  | 3-79 |
| 3.6.8 | Acoustical Noise                                     | 3-80 |
| 3.6.9 | Thermal Effects                                      | 3-82 |

## CONTENTS (contd)

|       |  |       |
|-------|--|-------|
| 3.7   | Concentrator Coatings  | 3-83  |
| 3.7.1 | Solar Intensity  | 3-87  |
| 3.7.2 | Reflective Surface Degradation   | 3-87  |
| 3.8   | Collector-Absorber Efficiency  | 3-91  |
|       | REFERENCES - Section 3   | 3-107 |
| 4.    | SYSTEM STRUCTURE AND MECHANISMS  | 4-1   |
| 4.1   | Rationale for Generator Support Design   | 4-5   |
| 4.2   | Design for Nonmagnetic Characteristics   | 4-5   |
| 4.3   | Generator Support Length   | 4-10  |
| 4.4   | Typical Unfolding Schemes  | 4-10  |
| 4.5   | Material Considerations  | 4-17  |
| 4.6   | Thermal Expansion Effects  | 4-21  |
| 4.7   | Thermal Conductivity Effects   | 4-22  |
| 4.8   | Vibration Considerations   | 4-29  |
| 4.8.1 | Launch Vibration Mode  | 4-29  |
| 4.8.2 | Vibration of the Solar-Thermionic Generator<br>and Generator Support in the Deployed Position<br>and Gener | 4-31  |
| 4.9   | Weight   | 4-45  |
| 4.10  | Other Thermal Effects  | 4-51  |
| 5.    | THERMIONIC CONVERTER   | 5-1   |
| 5.1   | Converter Description  | 5-2   |
| 5.2   | Performance Characteristics  | 5-9   |
| 5.3   | Life and Reliability   | 5-25  |
| 5.4   | Future Performance   | 5-29  |
| 6.    | THERMIONIC GENERATOR   | 6-1   |
| 6.1   | Description  | 6-1   |
| 6.2   | Performance Characteristics  | 6-7   |
| 6.3   | Thermal Response   | 6-12  |
| 6.4   | Misorientation Losses  | 6-15  |
| 6.5   | Generator Losses   | 6-17  |
| 6.5.1 | Heat Loss Through Insulation Gap   | 6-17  |

## CONTENTS (contd)

|        |   |      |
|--------|---|------|
| 6.5.2  | Conduction Loss   | 6-23 |
| 6.5.3  | Heat Loss Through Radiation Shielding of<br>the Generator Structure | 6-27 |
| 7.     | INSTRUMENTATION   | 7-1  |
| 7.1    | Instrumentation for Various Components                              | 7-3  |
| 7.1.1  | Generator Instrumentation   | 7-3  |
| 7.1.2  | Concentrator Instrumentation  | 7-5  |
| 7.2    | Temperature Sensors   | 7-11 |
| 7.3    | Current Measurements  | 7-15 |
| 7.4    | Voltage Measurements  | 7-17 |
| 8.     | SOLAR FLUX CONTROL  | 8-1  |
| 8.1    | Passive Control   | 8-3  |
| 8.2    | Control and Misorientation  | 8-8  |
| 8.3    | Solar Thermionic Generator Cavity Shutters and<br>Controls          | 8-9  |
| 8.3.1  | Basic Requirements  | 8-9  |
| 8.3.2  | Types of Shutters   | 8-11 |
| 8.3.3  | Shutter Operators   | 8-18 |
| 8.3.4  | Shutter Systems   | 8-38 |
|        | REFERENCES - Section 8  | 8-59 |
| 9.     | CESIUM RESERVOIR CONTROL  | 9-1  |
| 9.1    | Need for Control - Effect on Performance                            | 9-1  |
| 9.2    | Startup and Passive Cesium Control                                  | 9-3  |
| 9.3    | Heater Characteristics  | 9-7  |
| 9.4    | Active Temperature Control  | 9-8  |
| 9.4.1  | Temperature Sensors   | 9-8  |
| 9.4.2  | Block Diagram and Principles of Operation                           | 9-12 |
| 9.4.3  | Weight and Power Requirements                                       | 9-17 |
| 9.4.4  | Heater Design   | 9-17 |
| 10.    | POWER CONDITIONING AND CONTROL                                      | 10-1 |
| 10.1   | Series Versus Parallel Connection of Diodes/Generators              | 10-3 |
| 10.1.1 | Electrical Matching   | 10-3 |

## CONTENTS (contd)

|        |   |       |
|--------|---|-------|
| 10.1.2 | Reliability/Redundancy Considerations   | 10-9  |
| 10.2   | Subsystem Operation   | 10-14 |
| 10.2.1 | Voltage Controlled Subsystems   | 10-15 |
| 10.2.2 | Systems Which Utilize a PSL Unit  | 10-27 |
| 10.2.3 | Recommended System Description  | 10-35 |
| 10.2.4 | Low Input Voltage DC/DC Converter   | 10-40 |
| 10.2.5 | Shunt Load Control  | 10-45 |
| 10.2.6 | High Voltage DC/DC Converter/Regulator  | 10-47 |
| 10.2.7 | Battery Charger   | 10-49 |
| 10.2.8 | Battery Converter   | 10-51 |
| 10.3   | Configuration and Performance   | 10-64 |
| 11.    | RECOMMENDATIONS FOR DEVELOPMENT PROGRAMS  | 11-1  |
| 11.1   | Concentrator Programs   | 11-4  |
| 11.1.1 | Program 1: Evaluation of Mirror Coatings  | 11-4  |
| 11.1.2 | Program 2: Establishment of Concentrator Coating Techniques                         | 11-7  |
| 11.1.3 | Program 3: Dynamic Analysis and Test of 5-Foot Concentrator Structures              | 11-9  |
| 11.1.4 | Program 4: Dynamic Analysis and Test of 9-1/2-Foot Concentrator Structure           | 11-10 |
| 11.1.5 | Program 5: Development of 9-1/2-Foot 50 to 60° Rim Angle Master                     | 11-10 |
| 11.1.6 | Program 6: An Investigation and Environmental Test of Al, Be and other Minors       | 11-11 |
| 11.1.7 | Program 7: Rear Surface Coatings for Concentrators                                  | 11-12 |
| 11.1.8 | Program 8: Investigation of Techniques for Stiffening Thin Mirror Skin              | 11-13 |
| 11.1.9 | Program 9: Investigation of Torus Attachment Techniques                             | 11-14 |
| 11.2   | Generator Support   | 11-15 |
| 11.2.1 | Program 10: Design and Development of Unfolding Generator Support for 5-Foot System | 11-15 |

## CONTENTS (contd)

|        |   |       |
|--------|---|-------|
| 11.2.2 | Program 11: Design and Development of a Rigid Generator Support for 5-Foot System           | 11-16 |
| 11.2.3 | Program 12: Optimization of Generator Support Design  | 11-17 |
| 11.3   | Generator   | 11-18 |
| 11.3.1 | Program 14: High Power Density Diode Advanced Heat Transfer Program                         | 11-18 |
| 11.3.2 | Program 15: High Power Density Diode Material Development Program                           | 11-19 |
| 11.3.3 | Program 15: Thermionic Converter and Generator Life Testing Program                         | 11-22 |
| 11.3.4 | Program 16: Acquisition of Diode Application Data   | 11-29 |
| 11.3.5 | Program 17: Prototype Converter and Generator Manufacturing and Development Program         | 11-29 |
| 11.3.6 | Program 18: Design Study of 1kw Thermionic Generator  | 11-31 |
| 11.3.7 | Program 19: Cavity Design and Development   | 11-33 |
| 11.3.8 | Program 20: Investigation of Effect of Lower Temperatures on Converter Life and Performance | 11-34 |
| 11.4   | Converters  | 11-35 |
| 11.4.1 | Program 21: Power Distribution and Control Breadboard Assembly and Test                     | 11-35 |
| 11.4.2 | Program 22: Investigation of High Temperature Low Voltage dc to dc Converters               | 11-40 |
| 11.5   | Solar Flux Control  | 11-41 |
| 11.5.1 | Program 23: Development of Solar Flux Control Mechanisms                                    | 11-41 |
| 11.5.2 | Program 24: Development of Solar Flux Control Electronics                                   | 11-44 |
| 11.6   | Cesium Reservoir Control System   | 11-44 |
| 11.6.1 | Program 25: Development of Prototype Cesium Reservoir Control System                        | 11-44 |



CONTENTS (contd)

|             |  |       |
|-------------|--|-------|
| 11.7        | Systems Analysis and Test  | 11-45 |
| 11.7.1      | Program 26: Development of Test Plan and<br>Test Techniques for Solar-Thermionic Systems | 11-45 |
| 11.7.2      | Program 27: Development of System<br>Optimization Program                                | 11-46 |
| APPENDIX I  | - SPACE ENVIRONMENTAL EFFECTS ON REFLECTIVE<br>SURFACES                                  |       |
| APPENDIX II | - REFLECTANCE MEASUREMENTS AND SIMULATED MICRO-<br>METEORITE TESTS                       |       |

## 1. INTRODUCTION: VOLUME II

### 1.1 Study Scope

Table 1-I is a list of component parameters which were considered during the study program in the summarization of component status and analysis. Emphasis on specific parameters varied according to their importance. Table 1-I is not all-inclusive but does illustrate the scope of the study.

Table 1-II contains a list of missions which were used as guidelines during the study which further define the scope of the planned study.

The missions were selected to provide practical application of varying distances from the sun and dark times. Missions were selected to provide the following variables:

1. Operation at Earth, Mars, or Venus
2. Operation during travel from Earth to Mars or Earth to Venus
3. Operation with constant or variable dark times

The study assumed that near future flights would utilize single skin concentrators similar to those now under development. A maximum diameter of 9.5 feet was selected as being the largest concentrator available in the near future and was based upon the projected use of a 120-inch shroud. It is possible that other types of mirrors might prove desirable in the future.

Voltage outputs were selected as being typical of spacecraft load requirements. Thermionic converter parameters are based on projected ability to achieve high power densities with hardware diodes at reasonable weight. The choice of 0.5-lb constant weight for a converter was done to limit the study to reasonable proportions. It is recognized that converter weight will vary with power density and current; however, this variation is almost a second order effect in weight calculation.

TABLE 1-I  
COMPONENT PARAMETERS

I. CONCENTRATOR

- Material
- Weight - skin and support
- Diameter
- Reflective Surface Characteristics
- Temperature - transient and steady-state
- Surface Error- due to manufacture, mission environment, support
- Mirror Efficiency - aligned and misoriented
- Rim Angle
- Vibration Characteristics
- Life and Deterioration Modes

II. THERMIONIC CONVERTER

- Efficiency (at different conditions)
- Heat Losses
- Current - temperature relationships
- Weight
- Vibration Characteristics
- I-V Characteristics at Different Temperatures
- Life and Deterioration Modes
  - a) evaporation
  - b) seal temperature
  - c) vibration
  - d) material degradation
- P-V Characteristics at Different Temperatures
- Variations in Characteristics due to Manufacturing
- Startup, Shutdown Characteristics

III. THERMIONIC GENERATOR

- Efficiency
- Heat Losses
- I-V Characteristics
- P-V Characteristics
- Effects of Converter Matching
- Cavity Temperature - power, efficiency relationships
- Power vs Number of Converters
- Failure Modes and Effects
- Startup Problems
- Weight
- Effect of Variable Load
- Cavity Effects - reradiation losses
  - reflective losses
  - temperature distribution
  - surface absorptivity
- Cavity - mirror effects
  - a) misorientation
  - b) misalignment

TABLE 1-II  
MISSIONS

A. SOLAR INTENSITY

1. 1000 n. miles modified sun synchronous earth orbiter
2. 325 n. miles circular earth orbiter - 55 minutes light time, 35 minutes dark time
3. Highly elliptical earth orbiter - shadow time ranging from zero to 2 hrs for 10 hr period, zero to 3 hrs for 50 hr period
4. Earth to Venus probe - vehicle always in sun from 1 AU to 0.728 AU
5. Earth to Mars probe - vehicle always in sun from 1 AU to 1.67 AU
6. Venus orbiter - distance from sun is 0.728 AU, dark time constant at 2 hrs for a 10 hr orbit
7. Mars orbiter - distance from sun varies from 1.42 AU to 1.67 AU, dark time constant at 2 hrs for a 10 hr orbit

B. MIRROR SIZE - range up to 9-1/2 ft with system power of 0.3 to 4 KW

## 1.2 Vehicle Integration and Packaging Problems

The practical use of the solar-thermionic system depends upon a large number of factors, many of which are listed in Table 1-III. The design of the solar-thermionic system cannot be accomplished independently of the requirements of the mission and of the vehicle. Figure 1-1 is a block diagram of the solar thermionic system.

Table 1-III is included here as being of some use in consideration of the practical application of future solar-thermionic systems. Table 1-III was not used except in a cursory sense during the analysis.

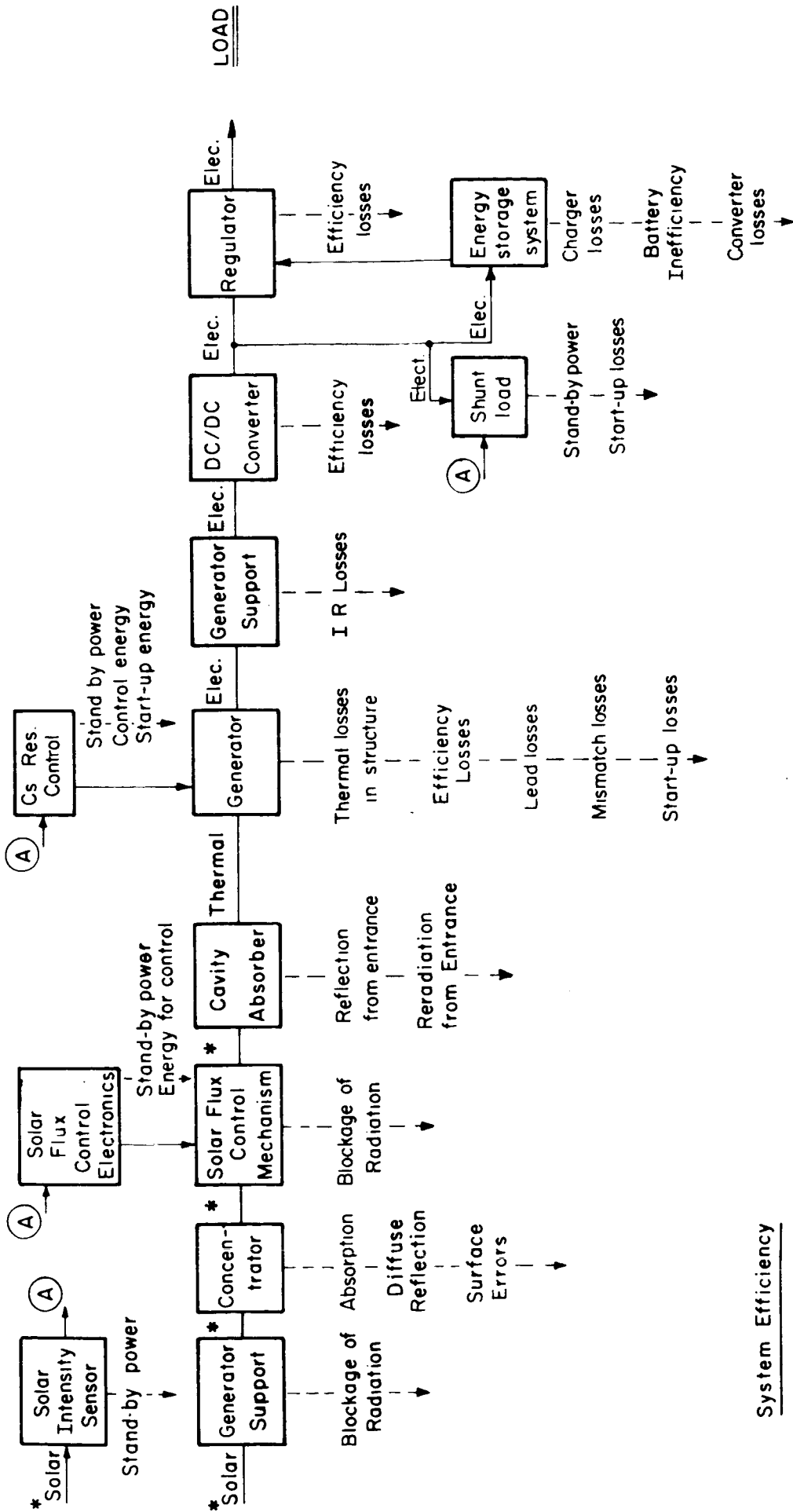
An examination was made of possible configurations of solar-thermionic systems as packaged within shrouds. Three shrouds which were considered were the Mariner C shroud, Surveyor shroud, and Saturn IB nose fairing illustrated in Figs. 1-2, 1-3 and 1-4.

Figures 1-5 through 1-12 illustrate configuration studies showing concentrator arrangements within given shrouds. Spacecraft dimensions of reasonable size comparable to Surveyor, Voyager, and Mariner were assumed. The concentrators were fitted between the spacecraft and the shroud.

It is very difficult to determine limits on the number of concentrators that can be fitted within the shroud without knowing details of the adapter and spacecraft design. In particular, the stacking of concentrators in the adapter section of the spacecraft involves considerable difficulty in adapter design.

Figure 1-13 illustrates an approximate maximum for the number of concentrators vs mirror diameter that can be fitted within a given shroud. As shown by the shaded band, estimates can only be approximate at this time.

One piece of interesting information is the number of concentrators required as a function of power level, distance from the sun, and system efficiency. The nomograph of Fig. 1-14 summarizes this information. An example of how the nomograph can be used is given in the figure. Figure 1-15 is an expansion of one part of the nomograph.



$$\eta_{sys} = \eta_{absr} \times \eta_{c-a} \times \eta_{gen} \times \eta_{lead} \times \eta_{conv} \times \eta_{reg} \times \eta_{cont}$$

Obscuration      Concentrator - Absorber Efficiency      Generator Efficiency      Lead eff.      DC/DC Converter Efficiency      Regulator Efficiency      Control Efficiency

System Efficiency

(K = Factor depending on time in dark, peak power, start-up time, etc.  
 $\tau_L$  = Light time     $\eta_{stor}$  = Storage efficiency)

$$\times \frac{1}{1 + K/\tau_L \eta_{stor}}$$

FIG. 1-1 SOLAR-THERMIONIC SYSTEM - POWER PLANT AND ENERGY LOSSES

TABLE 1-III

SOME CONSIDERATIONS IN VEHICLE INTEGRATION OF  
A SOLAR-THERMIONIC SYSTEM

I. STRUCTURAL ASPECTS

1. Packaging

- a. Ability to fit within shroud (with adequate clearance) static and dynamic shroud envelope, jettison envelope, thermal growth
- b. Number of attachments, linkages, dampers, etc., required and their placement on vehicle frame to provide support during launch
- c. Adapter characteristics
- d. Support position requirements and interference with antenna and other vehicle equipment - open truss and/or monocoque bus and superstructure
- e. Ability to have access to vehicle for ground checkout, etc., after packaging
- f. C.G. location from launch to deployment
- g. Ability to provide entire power system on common mounting assembly
- h. Interstage connections - telemetry, ground power, switching

2. Deployment Mechanics

- a. Effect on vehicle inertial characteristics - nature of mass movement
- b. Interference with other vehicle equipment
- c. Number of commands and complexity of unfolding sequence
- d. Pyrotechnic design
- e. Need for jettison of modules

3. Dynamics of Deployed Structure

- a. Undamped natural frequencies and the matching between sources - interaction with attitude control - undamped first natural cantilever (or other) frequency (between 0.5 and 5.0 cps typical)
- b. Damping ratio of the solar-thermionic structure and matching between sources - ratio of damping to critical damping in the first mode of 0.2 to 0.7
- c. C.G. location envelope and C.G. variation envelope
- d. Moment of inertia and their ratios
- e. Products of inertia and their ratios
- f. Variation in moments about centerline (vary less than 5 percent)
- g. Center of radiation pressure envelope
- h. The effects of vernier control on system movement
- i. Separation dynamics and acceleration forces and direction
- j. Mid-course maneuver acceleration forces and direction
- k. Terminal maneuver acceleration forces and direction

TABLE 1-III  
SOME CONSIDERATIONS IN VEHICLE INTEGRATION OF  
A SOLAR-THERMIONIC SYSTEM (contd)

4. Support for Other Equipment (not considered in study)
  - a. Celestial, sun or other sensors
  - b. Gas jets, solar vanes for attitude control
  - c. Antennas
5. Obstruction
  - a. Exhaust plume of attitude control, maneuver motors
  - b. Fields of view of sensors or scientific instruments
  - c. Antenna

II. THERMAL ASPECTS

1. Effect of thermal radiation field on vehicle temperature budget;
  - a. Transients during non-Sun-oriented mode
  - b. Conduction of heat into vehicle through leads
  - c. Power dissipation
  - d. Need for active (or passive) temperature control to handle above

III. ELECTRICAL ASPECTS

1. Power requirements and profile
2. Harness and connector requirements - framework required, resistance criteria, thermal criteria, etc.
3. Nature of output from power system - regulation, spikes, ripple, etc.
4. Nature of transient and switching, power factor, other load characteristics
5. Possibility of electrical disconnection without mechanical disturbance for test, etc.
6. Output power level with time - allowable performance margin

IV. ATTITUDE CONTROL

1. Structural characteristics (see above).
2. Limit on misorientation during cruise mode for power.
3. Effect on ability to maneuver - time for acquisition, gas and power requirement, etc.

V. TELEMETRY AND COMMAND

1. Number and frequency of commands needed to operate system  
Example: Battery charging instructions  
Startup commands  
Solar flux control commands
2. Telemetry needed for operation, command, monitoring



TABLE 1-III  
SOME CONSIDERATIONS IN VEHICLE INTEGRATION OF  
A SOLAR-THERMIONIC SYSTEM (contd)

- VI. TEST AND CHECKOUT
  - 1. Ability to interchange modules (such as panels) without damaging mechanical integrity of spacecraft or performance
  - 2. Ability to test after integration with spacecraft
- VII. MAGNETIC DESIGN CRITERIA
  - 1. Magnetic - static and dynamic flux limits, stability characteristics
  - 2. Location of critical components
- VIII. RF INTERFERENCE DESIGN CRITERIA
  - 1. Location of critical components
  - 2. Shielding limits
- IX. CONTAMINATION
  - 1. Evaporation
  - 2. Contamination from attitude control, terminal propulsion
- X. COMMUNICATION SYSTEM
  - 1. Antenna pattern interference
- XI. MISSION AND ENVIRONMENT
  - 1. Acceleration
  - 2. Vibration spectra
  - 3. Acoustic spectra
  - 4. S/C roll and pitch profile
  - 5. Firing window and period, launch azimuth range

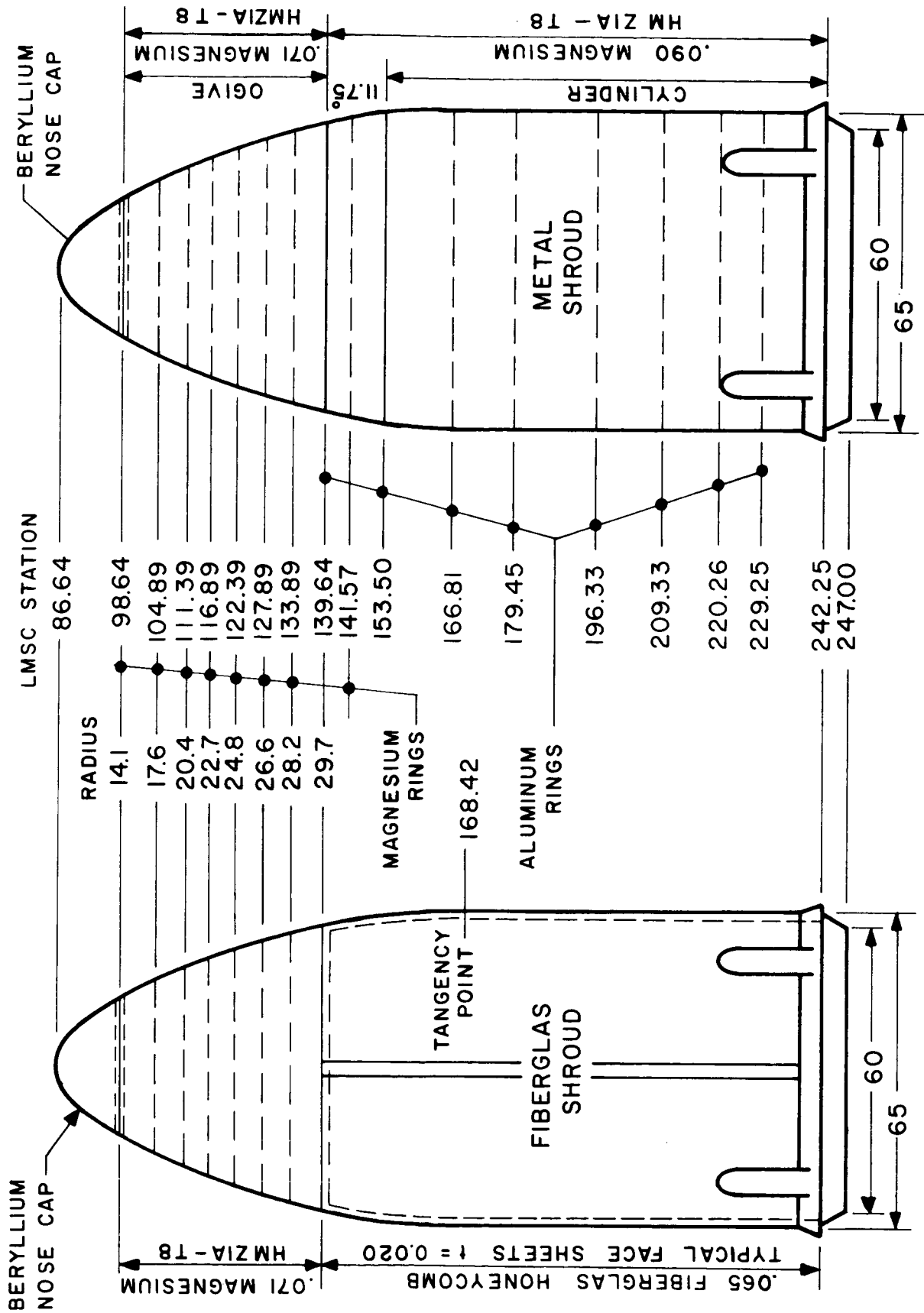


FIG. 1-2. MARKER C-8-40-TDS STRUTTER CASE (RADIUS)

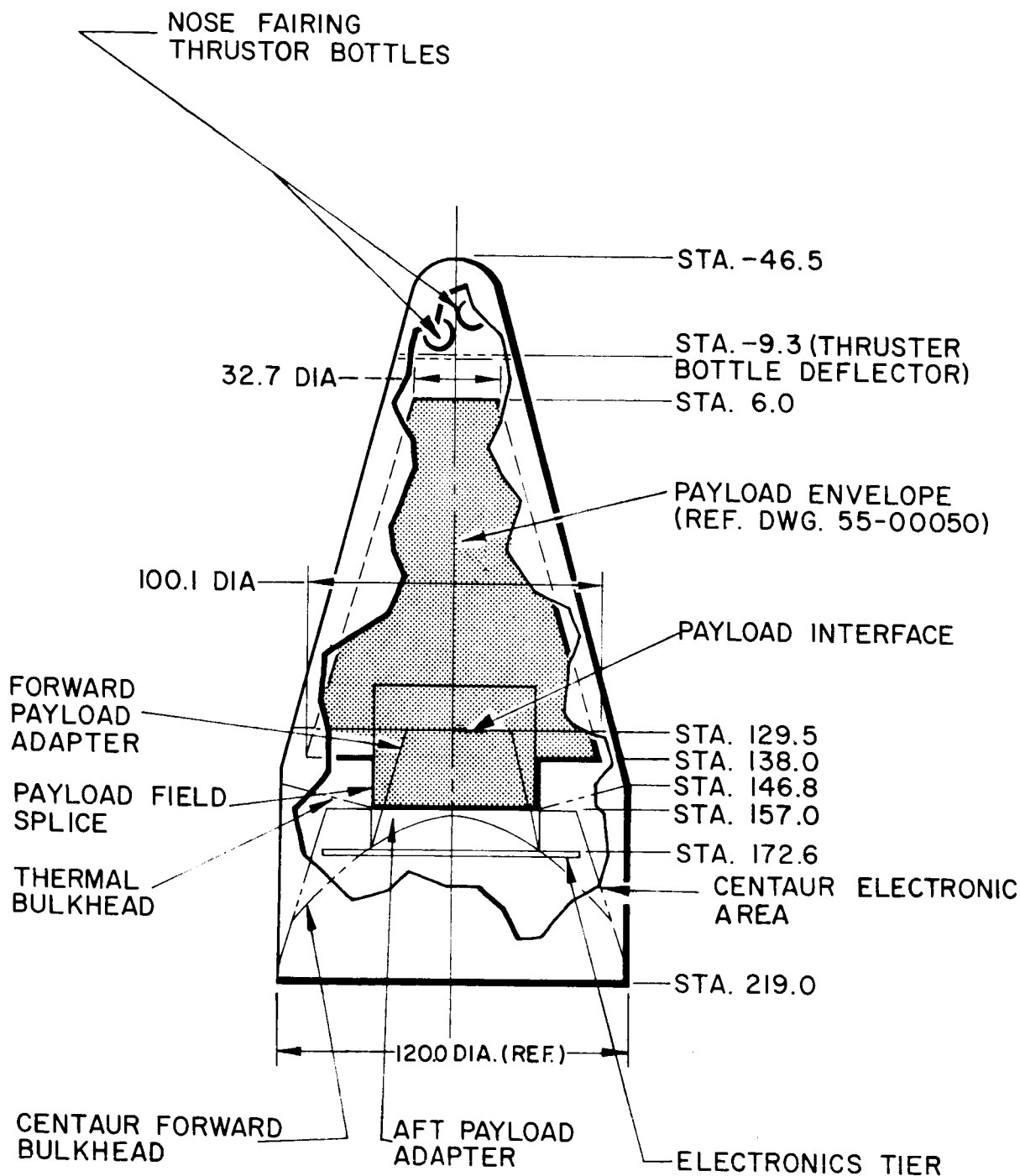


FIG. 1-3 SURVEYOR NOSE FAIRING PAYLOAD ENVELOPE FOR CENTAUR

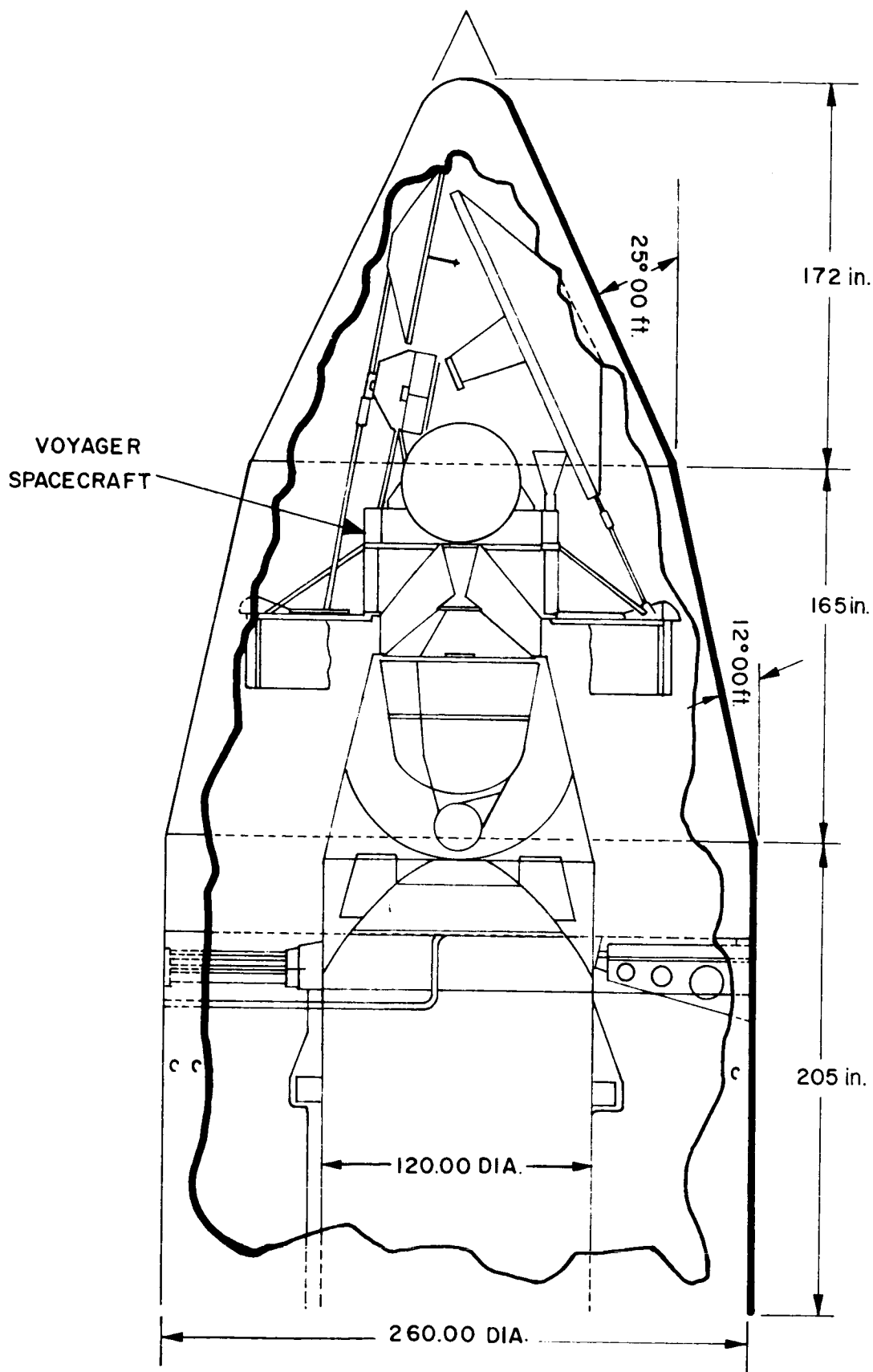
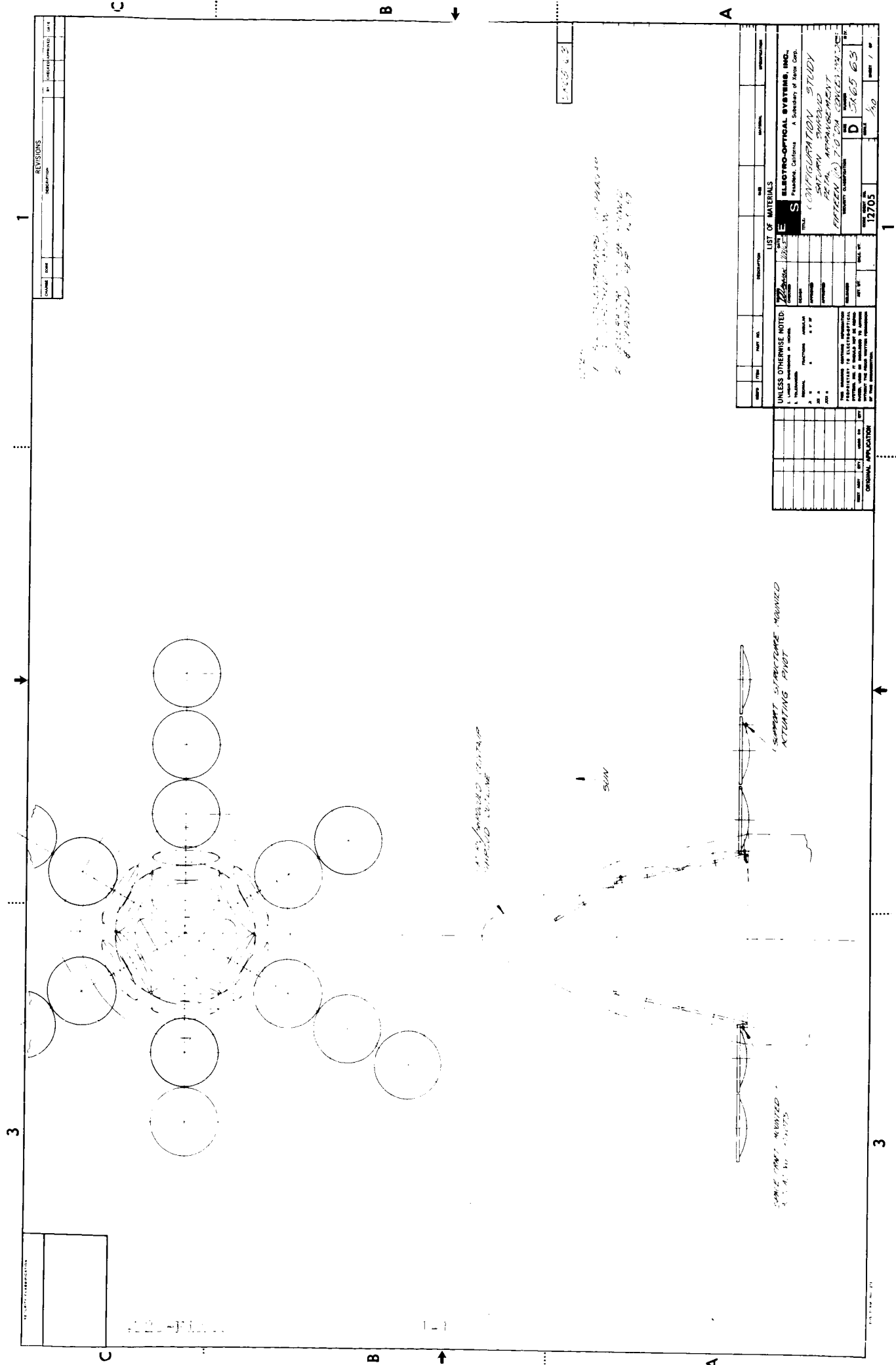


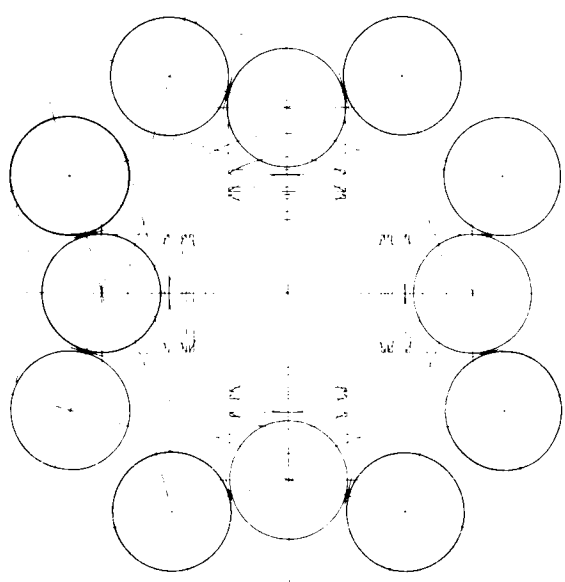
FIG. 1-4 SATURN V ROCKET FAIRING (2 OR 3 STAGE)



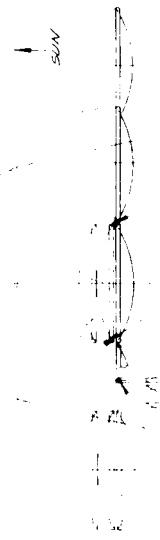


SECRET CLASSIFICATION

4426-11-101



SATURN/SURROUND CENTAUR  
SHARED OUTLINE



CENTAUR OUTLINE

SUPPORT STRUCTURE MOUNTED  
ACTUATING PIVOTS

SOME DRAFT MOUNTED  
ACTUATING PIVOT

NOTES  
1 ALL CONCENTRATIONS TO BE MADE  
2 ALL CONCENTRATIONS TO BE FILLED  
3 ALL CONCENTRATIONS TO BE FILLED  
4 ALL CONCENTRATIONS TO BE FILLED

3165-64

| REVISED | DATE | DESCRIPTION | BY | APPROVED |
|---------|------|-------------|----|----------|
|         |      |             |    |          |

|                             |                             |                             |                              |
|-----------------------------|-----------------------------|-----------------------------|------------------------------|
| UNLESS OTHERWISE NOTED:     |                             | LIST OF MATERIALS           |                              |
| 1. UNLESS OTHERWISE NOTED:  | 2. UNLESS OTHERWISE NOTED:  | 3. UNLESS OTHERWISE NOTED:  | 4. UNLESS OTHERWISE NOTED:   |
| 5. UNLESS OTHERWISE NOTED:  | 6. UNLESS OTHERWISE NOTED:  | 7. UNLESS OTHERWISE NOTED:  | 8. UNLESS OTHERWISE NOTED:   |
| 9. UNLESS OTHERWISE NOTED:  | 10. UNLESS OTHERWISE NOTED: | 11. UNLESS OTHERWISE NOTED: | 12. UNLESS OTHERWISE NOTED:  |
| 13. UNLESS OTHERWISE NOTED: | 14. UNLESS OTHERWISE NOTED: | 15. UNLESS OTHERWISE NOTED: | 16. UNLESS OTHERWISE NOTED:  |
| 17. UNLESS OTHERWISE NOTED: | 18. UNLESS OTHERWISE NOTED: | 19. UNLESS OTHERWISE NOTED: | 20. UNLESS OTHERWISE NOTED:  |
| 21. UNLESS OTHERWISE NOTED: | 22. UNLESS OTHERWISE NOTED: | 23. UNLESS OTHERWISE NOTED: | 24. UNLESS OTHERWISE NOTED:  |
| 25. UNLESS OTHERWISE NOTED: | 26. UNLESS OTHERWISE NOTED: | 27. UNLESS OTHERWISE NOTED: | 28. UNLESS OTHERWISE NOTED:  |
| 29. UNLESS OTHERWISE NOTED: | 30. UNLESS OTHERWISE NOTED: | 31. UNLESS OTHERWISE NOTED: | 32. UNLESS OTHERWISE NOTED:  |
| 33. UNLESS OTHERWISE NOTED: | 34. UNLESS OTHERWISE NOTED: | 35. UNLESS OTHERWISE NOTED: | 36. UNLESS OTHERWISE NOTED:  |
| 37. UNLESS OTHERWISE NOTED: | 38. UNLESS OTHERWISE NOTED: | 39. UNLESS OTHERWISE NOTED: | 40. UNLESS OTHERWISE NOTED:  |
| 41. UNLESS OTHERWISE NOTED: | 42. UNLESS OTHERWISE NOTED: | 43. UNLESS OTHERWISE NOTED: | 44. UNLESS OTHERWISE NOTED:  |
| 45. UNLESS OTHERWISE NOTED: | 46. UNLESS OTHERWISE NOTED: | 47. UNLESS OTHERWISE NOTED: | 48. UNLESS OTHERWISE NOTED:  |
| 49. UNLESS OTHERWISE NOTED: | 50. UNLESS OTHERWISE NOTED: | 51. UNLESS OTHERWISE NOTED: | 52. UNLESS OTHERWISE NOTED:  |
| 53. UNLESS OTHERWISE NOTED: | 54. UNLESS OTHERWISE NOTED: | 55. UNLESS OTHERWISE NOTED: | 56. UNLESS OTHERWISE NOTED:  |
| 57. UNLESS OTHERWISE NOTED: | 58. UNLESS OTHERWISE NOTED: | 59. UNLESS OTHERWISE NOTED: | 60. UNLESS OTHERWISE NOTED:  |
| 61. UNLESS OTHERWISE NOTED: | 62. UNLESS OTHERWISE NOTED: | 63. UNLESS OTHERWISE NOTED: | 64. UNLESS OTHERWISE NOTED:  |
| 65. UNLESS OTHERWISE NOTED: | 66. UNLESS OTHERWISE NOTED: | 67. UNLESS OTHERWISE NOTED: | 68. UNLESS OTHERWISE NOTED:  |
| 69. UNLESS OTHERWISE NOTED: | 70. UNLESS OTHERWISE NOTED: | 71. UNLESS OTHERWISE NOTED: | 72. UNLESS OTHERWISE NOTED:  |
| 73. UNLESS OTHERWISE NOTED: | 74. UNLESS OTHERWISE NOTED: | 75. UNLESS OTHERWISE NOTED: | 76. UNLESS OTHERWISE NOTED:  |
| 77. UNLESS OTHERWISE NOTED: | 78. UNLESS OTHERWISE NOTED: | 79. UNLESS OTHERWISE NOTED: | 80. UNLESS OTHERWISE NOTED:  |
| 81. UNLESS OTHERWISE NOTED: | 82. UNLESS OTHERWISE NOTED: | 83. UNLESS OTHERWISE NOTED: | 84. UNLESS OTHERWISE NOTED:  |
| 85. UNLESS OTHERWISE NOTED: | 86. UNLESS OTHERWISE NOTED: | 87. UNLESS OTHERWISE NOTED: | 88. UNLESS OTHERWISE NOTED:  |
| 89. UNLESS OTHERWISE NOTED: | 90. UNLESS OTHERWISE NOTED: | 91. UNLESS OTHERWISE NOTED: | 92. UNLESS OTHERWISE NOTED:  |
| 93. UNLESS OTHERWISE NOTED: | 94. UNLESS OTHERWISE NOTED: | 95. UNLESS OTHERWISE NOTED: | 96. UNLESS OTHERWISE NOTED:  |
| 97. UNLESS OTHERWISE NOTED: | 98. UNLESS OTHERWISE NOTED: | 99. UNLESS OTHERWISE NOTED: | 100. UNLESS OTHERWISE NOTED: |

REVISIONS

| CHANGE | DESCRIPTION | BY | CHECKED | DATE |
|--------|-------------|----|---------|------|
|        |             |    |         |      |

SECURITY CLASSIFICATION

402-773.1

ENVELOPE

CONCENTRATOR  
LOCATION CURVE

SUN

SPACE CRAFT MOUNTED  
ACTUATING PILOT

NOTES

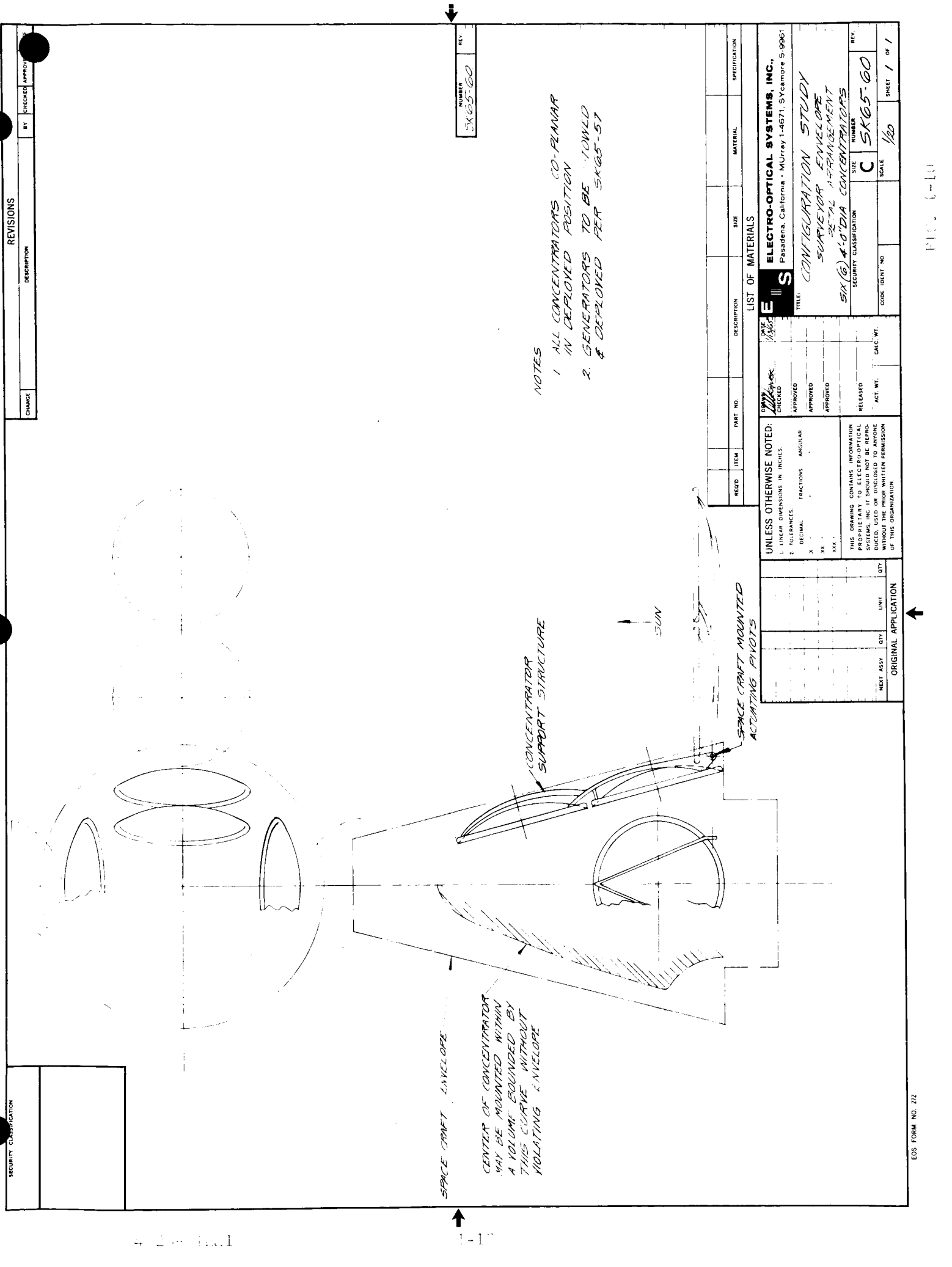
1. ALL CONCENTRATORS CO-PLANAR
2. IN DEPLOYED POSITION
3. GENERATORS TO BE STOWED
4. DEPLOYED PER SK65-57

NUMBER  
SK65-62  
REV

|  |      |          |             |      |          |               |
|--|------|----------|-------------|------|----------|---------------|
| REGD.  | ITEM | PART NO. | DESCRIPTION | SIZE | MATERIAL | SPECIFICATION |
| LIST OF MATERIALS  |      |          |             |      |          |               |
| ELECTRO-OPTICAL SYSTEMS, INC.,<br>Pasadena, California • MURRAY 1-4671, SYCAMORE 5-9961  |      |          |             |      |          |               |
| TITLE: CONFIGURATION STUDY<br>SURVEYOR ENVELOPE<br>GENERAL ACTUATING PILOT<br>THREE (3) 6-1/2 DIA CONCENTRATOR   |      |          |             |      |          |               |
| SECURITY CLASSIFICATION: C   |      |          |             |      |          |               |
| SIZE: C  |      |          |             |      |          |               |
| SCALE: 1/20  |      |          |             |      |          |               |
| SHEET 1 OF 1   |      |          |             |      |          |               |
| UNLESS OTHERWISE NOTED:<br>1. LINEAR DIMENSIONS IN INCHES<br>2. TOLERANCES:<br>DECIMAL FRACTIONS ANGULAR<br>X ± ± ±<br>XX ± ± ±<br>XXX ± ± ±   |      |          |             |      |          |               |
| THIS DRAWING CONTAINS INFORMATION PROPRIETARY TO ELECTRO-OPTICAL SYSTEMS, INC. IT SHOULD NOT BE REPRODUCED, USED OR DISCLOSED TO ANYONE WITHOUT THE PRIOR WRITTEN PERMISSION OF THIS ORGANIZATION. |      |          |             |      |          |               |
| ORIGINAL APPLICATION   |      |          |             |      |          |               |
| NEXT ASSY QTY UNIT QTY   |      |          |             |      |          |               |







| SECURITY CLASSIFICATION |             | REVISIONS |                  |
|-------------------------|-------------|-----------|------------------|
| CHANGE                  | DESCRIPTION | BY        | CHECKED APPROVED |

NUMBER  
REV.  
SK65-60

NOTES

1. ALL CONCENTRATORS CO-PLANAR IN DEPLOYED POSITION
2. GENERATORS TO BE TOWED & DEPLOYED PER SK65-57

| REGD.  | ITEM | PART NO. | DESCRIPTION | SIZE                               | MATERIAL                | SPECIFICATION           |
|--|------|----------|-------------|------------------------------------|-------------------------|-------------------------|
| LIST OF MATERIALS  |      |          |             |                                    |                         |                         |
| <b>E</b> ELECTRO-OPTICAL SYSTEMS, INC.,<br>Pasadena, California • Murray 1-4671, SYcamore 5-9961   |      |          |             |                                    |                         |                         |
| TITLE: CONFIGURATION STUDY<br>SUBJECT: ENVELOPE<br>DETAIL ARRANGEMENT<br>SIX (6) 4'-0" DIA CONCENTRATORS   |      |          |             |                                    |                         |                         |
| UNLESS OTHERWISE NOTED:<br>1. LINEAR DIMENSIONS IN INCHES<br>2. TOLERANCES<br>X DECIMAL<br>XX FRACTIONS<br>XXX ANGULAR   |      |          |             | APPROVED<br>CHECKED<br>DATE 1/1/62 | APPROVED<br>DATE 1/1/62 | APPROVED<br>DATE 1/1/62 |
| THIS DRAWING CONTAINS INFORMATION PROPRIETARY TO ELECTRO-OPTICAL SYSTEMS, INC. IT SHOULD NOT BE REPRODUCED, USED OR DISCLOSED TO ANYONE WITHOUT THE WRITTEN PERMISSION OF THIS ORGANIZATION. |      |          |             | RELEASED<br>ACT. WT.               | SCALE<br>1/60           | REV<br>SK65-60          |
| ORIGINAL APPLICATION   |      |          |             | QTY                                | UNIT                    | SHEET 1 OF 1            |



**NOTES:** UNLESS OTHERWISE SPECIFIED:

NOTES:

1. ALL CONVENTION'S AG PLANAR  
IN EMPLOYED POSITION  
GENERATORS TO BE DOWN L &  
FELDERED IN CASE 2.

THIS INFORMATION SHOULD HAVE BEEN  
SPECIFICALLY STATED IN THE PRO-

SPACE, RAFT MOUNTED  
ACTUATING PIVOTS

3. PERMANENTLY IDENTIFY A PART NO. AND REVISION LETTER  
ELECTRONICALLY BY METAL STAMP; TAG 3, 18 HIGH NUMERALS

1. REPLACE FINISH ☒ MAX

TESTES: UNIFORMITY, HERMATIC SEALING

TESTES: UNIFORMITY, HERMATIC SEALING

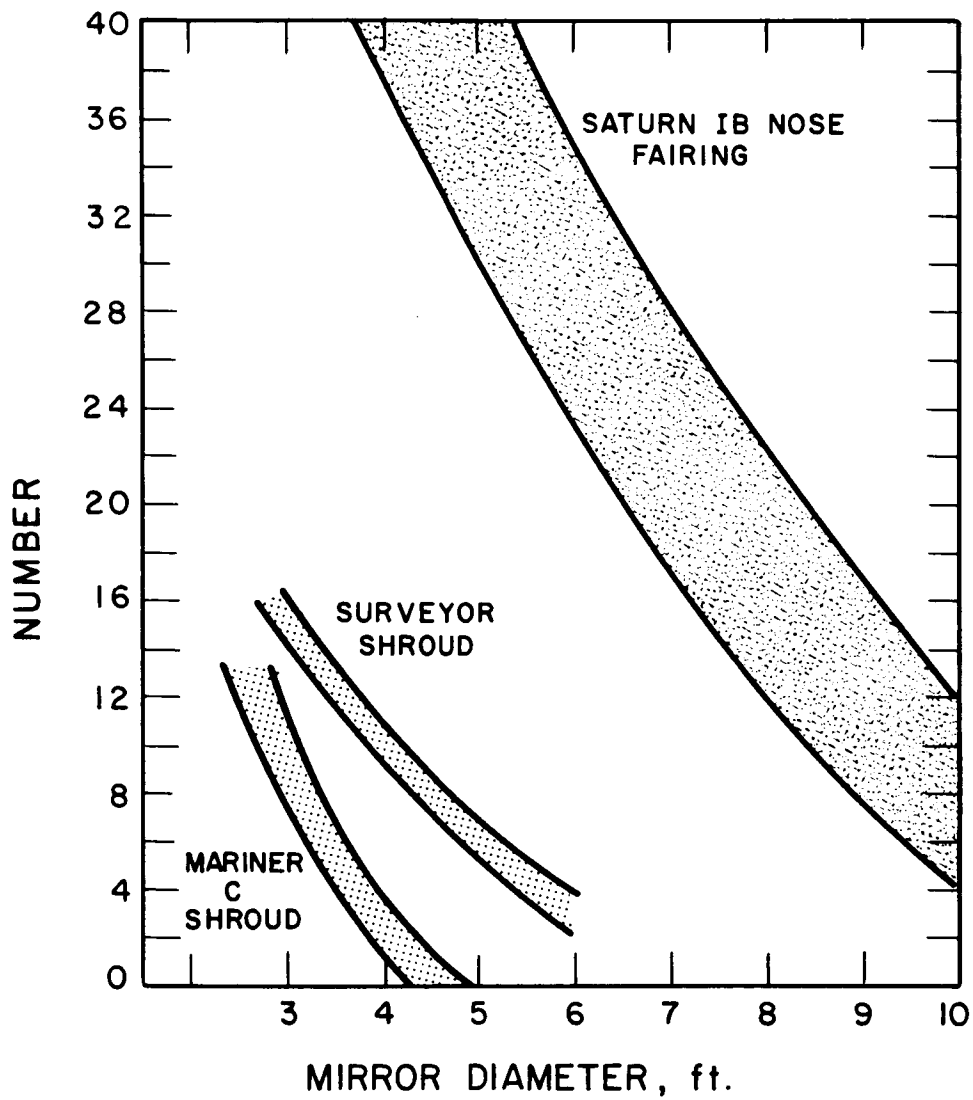


FIG. 1-13 ESTIMATE OF NUMBER OF CONCENTRATORS VS DIAMETER WHICH CAN PRACTICALLY FIT INSIDE A GIVEN SHROUD

Figure 1-16 extracts some numbers from the nomographs of Figures 1-14 and 1-15 as a further illustration of the number of concentrators necessary for given missions.

Figures 1-17, 1-18 and 1-19 illustrate the number of concentrators required at the Earth's, Mars', and Venus' distance from the Sun with system efficiencies of 13.5 percent. All of these graphs illustrate the fact that large power levels would require a large number of small concentrators; this is obvious but is better appreciated by examination of the curve.

NOTE: \* REFERS TO OVERALL STP SYSTEM EFFICIENCY

| MISSION                          | Assumed<br>Spacecraft<br>Power<br>Requirements<br>(Watts) | NUMBER OF CONCENTRATORS REQUIRED |     |     |         |     |     |         |     |     |         |     |     |         |     |     |         |     |     | COMMENTS |           |            |
|----------------------------------|---|----------------------------------|-----|-----|---------|-----|-----|---------|-----|-----|---------|-----|-----|---------|-----|-----|---------|-----|-----|----------|-----------|------------|
|                                  |   | 4' Dia.                          |     |     | 5' Dia. |     |     | 6' Dia. |     |     | 7' Dia. |     |     | 8' Dia. |     |     | 9' Dia. |     |     |          | 9.5' Dia. |            |
|                                  |   | 10%                              | 15% | 10% | 15%     | 10% | 15% | 10%     | 15% | 10% | 15%     | 10% | 15% | 10%     | 15% | 10% | 15%     | 10% | 15% |          |           |            |
|                                  |   |                                  |     |     |         |     |     |         |     |     |         |     |     |         |     |     |         |     |     |          |           |            |
| 1. SUN SYNCHRONOUS EARTH ORBITER | 1000 in ORBIT   | 6                                | 4   | 4   | 2       | 3   | 2   | 2       | 1   | 2   | 1       | 1   | 2   | 1       | 1   | 1   | 1       | 1   | 1   | 1        | 1         | SEE NOTE 1 |
| 2. CIRCULAR EARTH ORBITER        | 1000 in ORBIT   | 6                                | 4   | 4   | 3       | 3   | 2   | 2       | 1   | 2   | 1       | 1   | 2   | 1       | 1   | 1   | 1       | 1   | 1   | 1        | 1         | SEE NOTE 1 |
| 3. ELLIPTICAL EARTH ORBITER      | 200 at 1. A. U.   | 2                                | 1   | 1   | 1       | 1   | 1   | 1       | 1   | 1   | 1       | 1   | 1   | 1       | 1   | 1   | 1       | 1   | 1   | 1        | 1         | SEE NOTE 2 |
| 4. VENUS FLY-BY                  | 1000 at 1. A. U.  | 6                                | 4   | 4   | 2       | 3   | 2   | 2       | 1   | 2   | 1       | 1   | 2   | 1       | 1   | 1   | 1       | 1   | 1   | 1        | 1         | SEE NOTE 1 |
| 5. MARS FLY-BY                   | 200 at 1.67 A. U.   | 4                                | 3   | 3   | 2       | 2   | 1   | 1       | 1   | 1   | 1       | 1   | 1   | 1       | 1   | 1   | 1       | 1   | 1   | 1        | 1         | SEE NOTE 3 |
| 6. VENUS ORBITER                 | 4000 at .728 A. U.  | 13                               | 9   | 8   | 6       | 6   | 4   | 4       | 3   | 3   | 2       | 2   | 3   | 2       | 3   | 2   | 2       | 2   | 2   | 2        | 2         | SEE NOTE 4 |
| 7. MARS ORBITER                  | 4000 at 1.67 A. U.  | 68                               | 45  | 43  | 29      | 30  | 20  | 22      | 15  | 17  | 11      | 15  | 9   | 12      | 8   | 12  | 8       | 12  | 8   | 12       | 8         | SEE NOTE 5 |

NOTE 1: CONCENTRATOR SIZE GREATER THAN 8' DIA. IS UNNECESSARY

NOTE 2: CONCENTRATOR SIZE GREATER THAN 4' DIA. IS UNNECESSARY

NOTE 3: CONCENTRATOR SIZE GREATER THAN 6' DIA. IS UNNECESSARY

NOTE 4: CONCENTRATOR SIZE GREATER THAN 9' DIA. IS UNNECESSARY

NOTE 5: STOWAGE AND DEPLOYMENT OF SMALLER SIZE MIRRORS IS IMPRACTICAL.

FIG. 1-10 NUMBER OF CONCENTRATORS REQUIRED FOR SELECTED MISSIONS

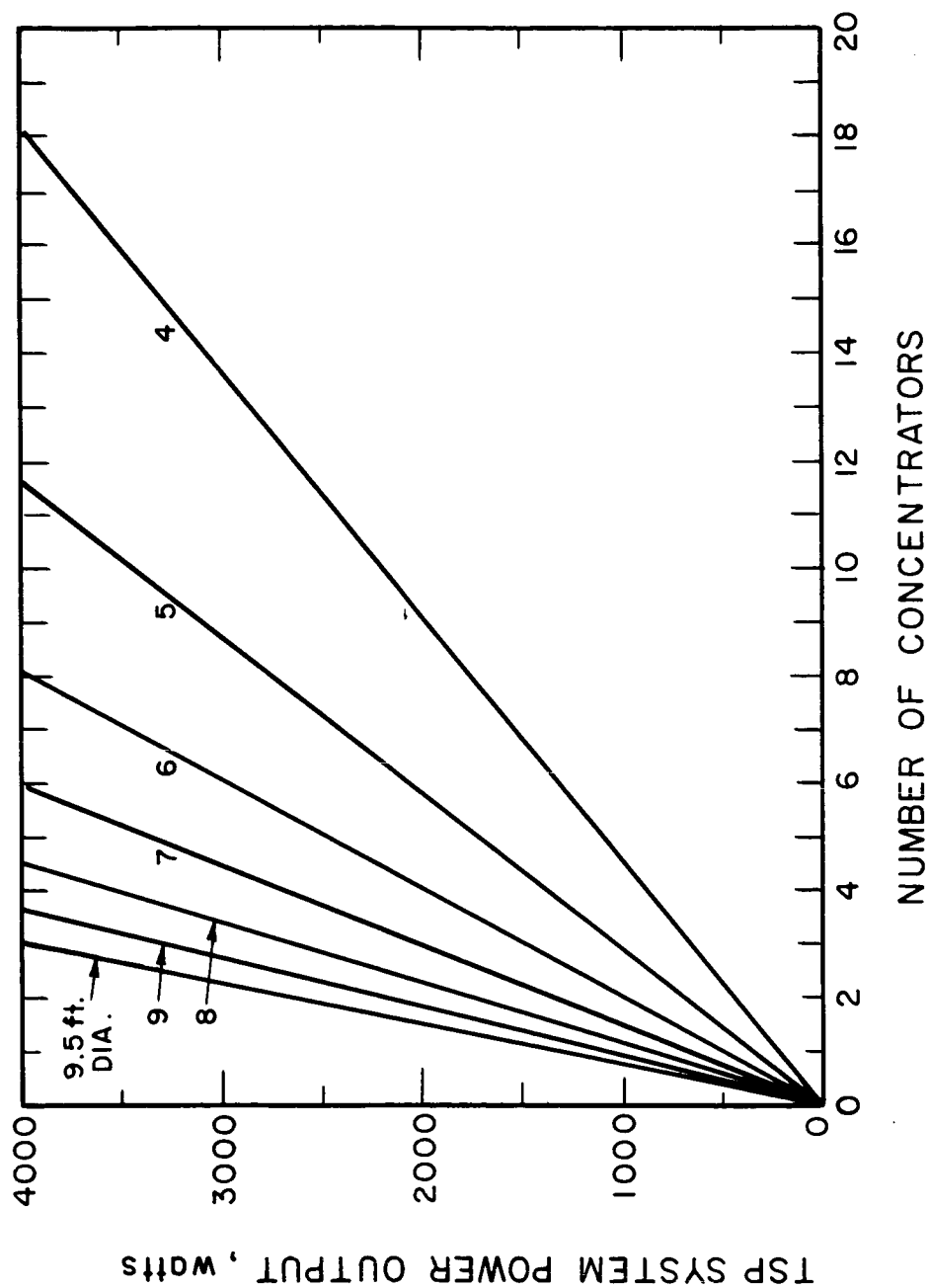


FIG. 1-17 POWER OUTPUT VS NUMBER OF CONCENTRATORS FOR TSP SYSTEM  
EFFICIENCY = 13.5%, DISTANCE FROM SUN = 1 A.U.



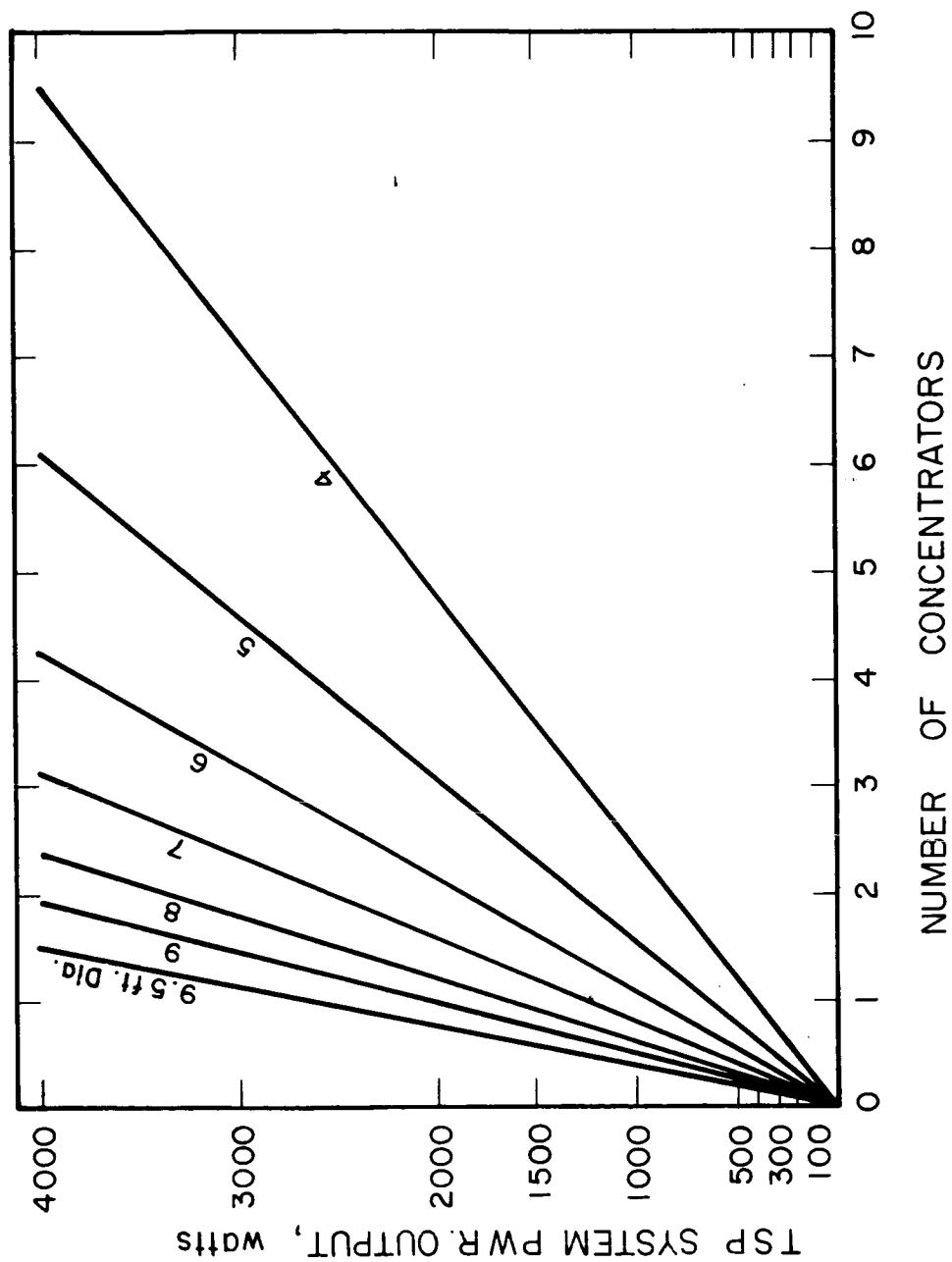


FIG. 1-18 POWER OUTPUT VS NUMBER OF CONCENTRATORS FOR TSP SYSTEM  
EFFICIENCY = 13.5%, DISTANCE FROM SUN = 0.728 A.U.

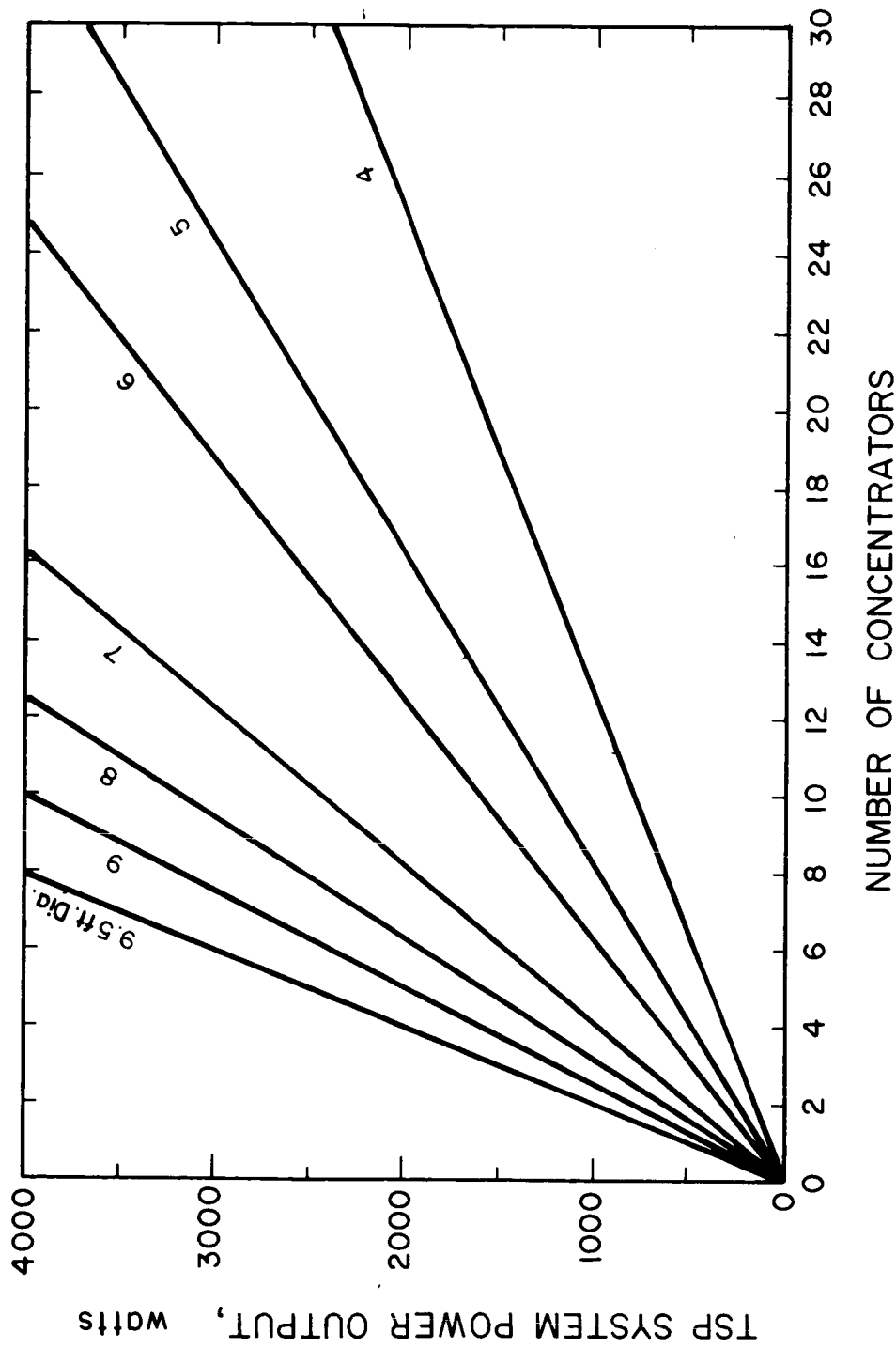


FIG. 1-10 POWER OUTPUT VS. NUMBER OF CONCENTRATORS FOR TSP SYSTEM  
EFFICIENCY = 13.5%, DISTANCE FROM SUN = 1.67 A.U.

## 2. SYSTEM CONSIDERATIONS

This section discusses several aspects of system reliability and summarizes system efficiency and weight in a variety of missions and using different mirror diameters.

### 2.1 Aspects of System Reliability

Operating experience with many of the solar-thermionic system components is limited and only partial estimates of the modes of failure and associated failure probabilities can be made.

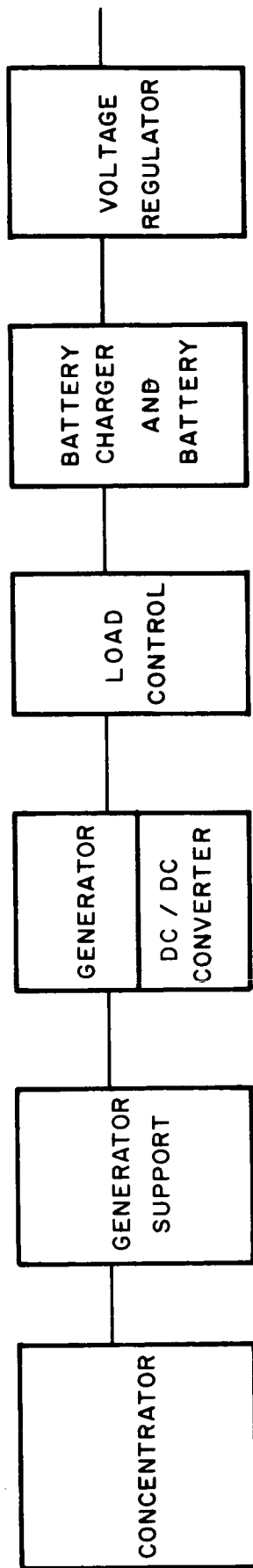
Table 2-I summarizes several significant system modes of failure according to component affected, nature of failure, the effect on system operation, and possible compensation or correction. The mode of failure can be partial (such as one converter out of several failing), gradual (such as degradation of the concentrator surface), or complete (such as total loss of a subsystem).

The items listed in Table 2-I are general in nature. Specific failure rates and reliability estimates must depend on further experimental data beyond that presently available.

Figure 2-1 shows a simplified reliability model of the solar-thermionic system. Six main subsystems are shown, which are concentrator, generator support, generator/DC converter, load control, battery charger and battery, and voltage regulator. Other items in the system such as sensors, current sensing devices, etc. can be related to one or more of the six main subsystems. Additional subsystems might be cesium reservoir and solar flux controls. A typical system reliability calculation is shown which illustrates that, although the reliability of each subsystem might be high, the combined reliability of the entire system can be low due to the large number of components.

TABLE 2-I  
SIGNIFICANT SYSTEM MODES OF FAILURE

| <u>Component</u>               | <u>Nature</u>   | <u>Effect</u>   | <u>Mode</u>         | <u>Compensation or Correction</u>                               |
|--------------------------------|---|---|---------------------|---|
| Concentrator                   | Degradation of surface  | 1) Decrease of cavity temperature, loss of power  | Gradual             | 1) Increased concentrator area combined with solar flux control |
|                                | Skin buckling   | 2) Decrease of cavity temperature, loss of power  | Partial or complete | 1) Extra concentrator area                                      |
| Generator support              | Failure to unfold properly  | 1) No power   | Complete            | 1) Extra systems  |
|                                |   | 2) Misalignment, loss of power, overheating of generator structure  | Partial or complete | 2) Override mechanisms for unfolding                            |
| Generator                      | Converter open  | 1) Loss of series string, no power  | Partial or complete | 1) Extra leads and dc/dc converters                             |
|                                |   | 2) Overheating of other converters in generator   |                     | 2) Parallel connections of converters                           |
| Converter short                |   | 1) Loss of power from converter   |                     | 3) Design of system to produce more power than required         |
|                                |   | 2) Possible cooling of other converters   | Partial             | 1) As many series connections as possible                       |
| Converter decay                |   | 1) Loss of power  | Partial             | 2) Design of system   |
|                                |   |   |                     | 1) Above  |
| Power conditioning and control | Shunt load failure  | 1) Variation of current from generator  | Partial to complete | 1) Redundant loads  |
|                                |   | 2) Overheating of generator   |                     | 2) Ground override  |
| Converter, regulator failure   |   | 3) Extra energy withdrawal from battery during peak loads   |                     |   |
|                                |   | 4) Inability of diodes to open at startup   |                     |   |
| Energy storage system failure  |   | 1) Loss of power from system  | Complete            | 1) Bypass converters to redundant systems                       |
|                                |   | 2) Unregulated power output from system   | Partial             | 1) Redundant components   |
|                                |   | 1) Inability to supply peak loads   | Partial             | 1) Eliminate some loads   |
|                                |   | 2) Variation of current voltage from generator - possible overheating of generator and loss of regulation |                     | 2) Redundant storage systems                                    |
| Cs reservoir control           | Heating system short  | 1) Overheat reservoir   | Partial to complete | 1) Fuse   |
|                                |   | 2) Cause of diode failure   |                     |   |
| Heating system open            |   | 1) Slower startup   | Partial             | 1) Redundant heaters  |
|                                | Sensor degradation  | 1) Nonoptimization of reservoir   | Partial             | 1) Switch to redundant sensor                                   |
|                                |   | 2) Extra energy drain on battery  | Partial             | 1) Current limiter or fuse                                      |
| Solar flux control             | Actuator Failure  | 1) Too little solar energy into cavity - cool converters  | Partial to complete | 1) Override and/or release for actuator                         |
|                                | Electronics Failure   | 2) Too much solar energy into cavity - too hot converters   |                     | 2) Release or ejection mechanism for flux control mechanisms    |
| 4326-Final                     | Flap (or other mechanism) distortion, or other phenomenon leading to impeded movement | 3) Uneven heating of converters   |                     | 3) Redundant electronics, mechanisms 2-2                        |



TYPICAL CALCULATION

|                        |      |   |      |   |      |   |      |   |     |   |     |   |      |                              |
|------------------------|------|---|------|---|------|---|------|---|-----|---|-----|---|------|------------------------------|
| PROB.<br>OF<br>SUCCESS | 0.99 | X | 0.99 | X | 0.99 | X | 0.95 | X | 0.9 | X | 0.9 | = | 0.68 | PROBABILITY<br>OF<br>SUCCESS |
|------------------------|------|---|------|---|------|---|------|---|-----|---|-----|---|------|------------------------------|

FIG. 2-1 SIMPLIFIED RELIABILITY MODEL

During the next few years, it is expected that a great deal of statistical experience will be obtained in the use of storage systems and electronics which are similar or identical to those which would be used on a flight solar-thermionic system. For the concentrator and generator support, the physical mechanisms will acquire high reliability through mechanical tests and experiments on similar devices in space.

The limiting factor in reliability of the solar-thermionic system is likely to be the generator/DC-DC converter combination. As discussed in Section 10, redundancy can be incorporated into the generator/DC-DC converter design by using several DC/DC converters in conjunction with a number of thermionic diodes, initial power output would exceed the minimum requirement.

Figure 2-2 illustrates the increased reliability which can be obtained in the generator-DC/DC converter combination through the use of spares. Three cases are considered: one diode per DC/DC converter, two diodes per converter, and three diodes per converter. Figure 2-2 assumes that 18 diodes are needed to provide the minimum power output to the remainder of the system. For case 1, where one diode per converter is used, the system would include 18 DC/DC converters. This number appears excessive, however, large numbers of DC/DC converters may be needed for reliability purposes.

As shown in Fig. 2-2, the failure rate for the diodes was assumed to be  $2 \times 10^{-6}$  over a 10,000-hr life period. The use of these failure rates assumes that diode failures are random in nature and that the diode is not operating on the "initial failure" or "wearout" part of the life curve.

The failure rate of the device is the inverse of the mean time to failure as shown in Eq. 1

$$(F.R.) = \frac{1}{MTTF} \text{ (mean-time-to-failure)} \quad (1)$$

where F.R. = failure rate.

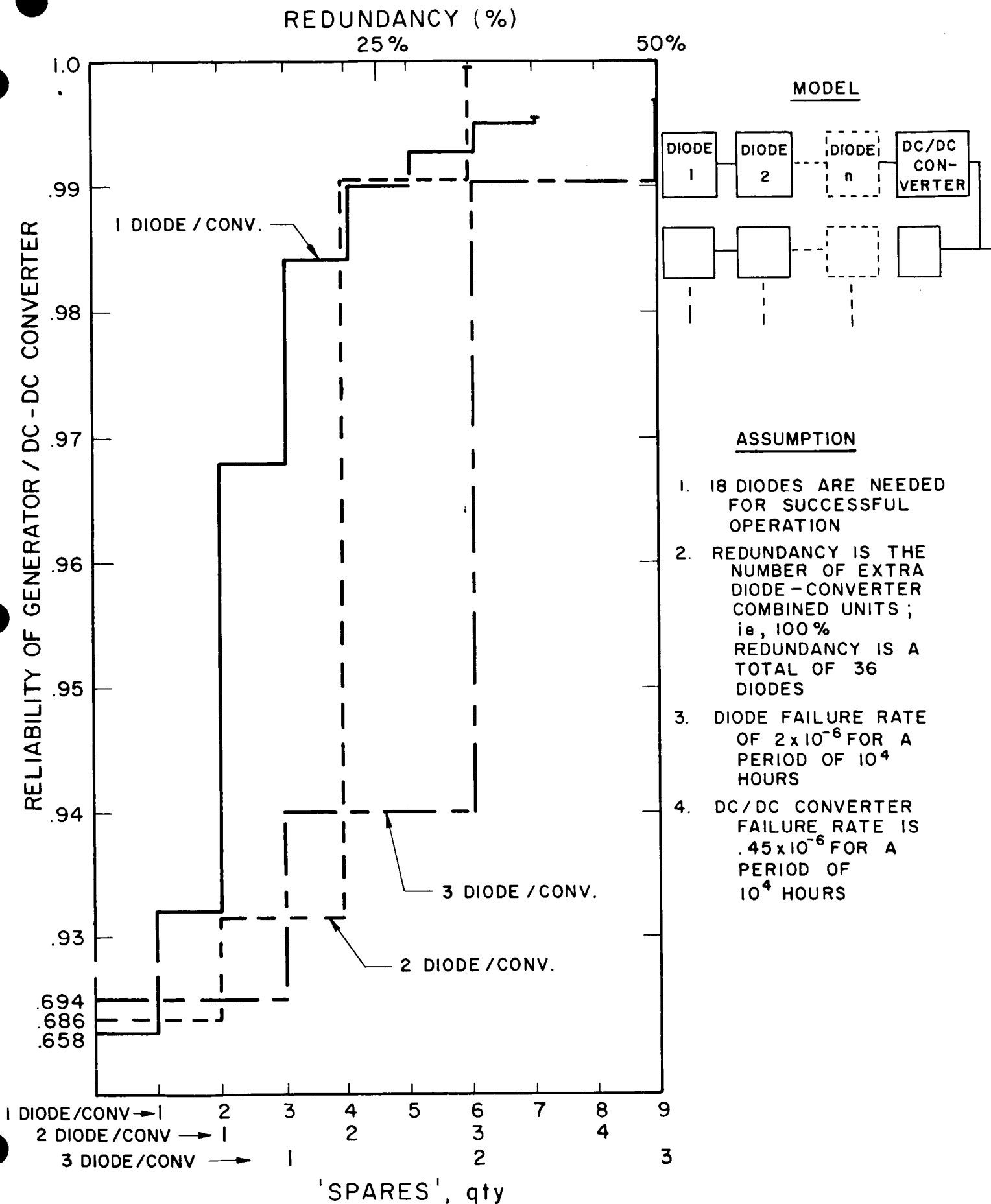


FIG. 2-2 ILLUSTRATION OF INCREASED RELIABILITY THROUGH THE USE OF SPARES

A failure rate of  $2 \times 10^{-6}$  per hour implies a MTTF of 50,000 hours. The reliability of a device can be expressed in terms of its MTTF as shown in Eq. 2.

$$R = e^{-t/T} \quad (2)$$

where R = "reliability", i.e., probability that unit will operate for a period of time, t

t = time

T = MTTF

The probability that a unit will operate for a period of time equivalent to the mean time to failure is 0.37.

The curves of Fig. 2-2 were derived using the addition and binomial laws of probability expressed in Eqs. 3 and 4.

#### Addition Law

$$P(A+B) = P(A) + P(B) \quad (3)$$

where  $P(A+B)$  = probability of either (A) or (B) occurring when (A) and (B) are mutually exclusive.

#### Binomial Law

$$Pr = \binom{n}{x} P_s (1 - P_s)^{n-x} \quad (4)$$

where Pr = probability of x items out of a group of n items being successful

$P_s$  = individual probability of success

$$\binom{n}{x} = \frac{n!}{x! (n-x)!}$$

The addition law is equivalent to stating that the probability of either zero or one failure occurring out of eighteen diodes is equal to the sum of the separate probabilities of zero failures occurring, plus one failure occurring. The binomial law, expressed in Eq. 4, expresses the probability that x number of diodes out of a total group of n diodes will be operating, given an individual probability of success  $P_s$ .

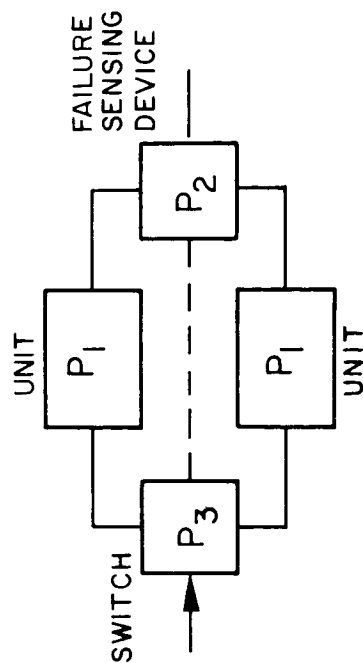


Figure 2-2 indicates that with zero redundancy, i.e., no extra diodes, the probability of an 18 diode generator continuing to function for 10,000 hours using one DC/DC converter per diode is 0.658, while using three diodes per converter the probability is at 0.694'. Thus, under the assumptions stated, the generator/converter combination actually becomes less reliable (with no spare diodes) when too many DC/DC converters are used. A large number of tradeoffs can be derived using as variables the MTTF of diodes, DC/DC converters, and the degree of redundancy. These tradeoffs can be done by using Eqs. 3 and 4.

As shown in Fig. 2-2, when 4 diodes are added to the system, and when two diodes are matched to each DC/DC converter, reliability of the generator can be increased from 0.686 to 0.99. Using three diodes per converter, it would take six extra diodes to achieve the same reliability.

Figure 2-2 is only an example of a large number of tradeoff analyses in reliability and redundancy which can be made. These tradeoff analyses, however, are directly dependent on the failure rates assumed for the thermionic diode and DC/DC converter. At the present time, these failure rates are not known within orders of magnitude and any conclusions derived at this time would have to be questioned.

Figure 2-3 illustrates the effects of redundancy on subsystem reliability. The use of redundancy could be considered for use in the voltage regulator, battery charger, and other modules. In general, the use of redundancy will increase overall reliability when the failure sensing device and switch are also highly reliable. The probability of successful operation is illustrated in Fig. 2-3 as a function of the probability of successful operation of the failure sensing and switch device. As shown, when failure sensing equipment has a reliability of one, a twice redundant system can increase the reliability from 0.9 for one unit to 0.99 for the combination of units. However, if the reliability of the failure sensing devices is only 0.5,



$$P_0 = \text{PROBABILITY OF SUCCESSFUL OPERATION} = 2P_1 P_2 P_3 \left\{ 1 - P_1 + \frac{P_1}{2P_2 P_3} \right\}$$

WHERE  $P_1$  = PROBABILITY OF UNIT OPERATION  
 $P_2$  = PROBABILITY OF FAILURE SENSING DEVICE OPERATING  
 $P_3$  = PROBABILITY OF SWITCHING OPERATING

NOTE: WHEN  $P_2$  &  $P_3 = 1$ , THEN  $P_0 = 2P_1 - P_1^2$

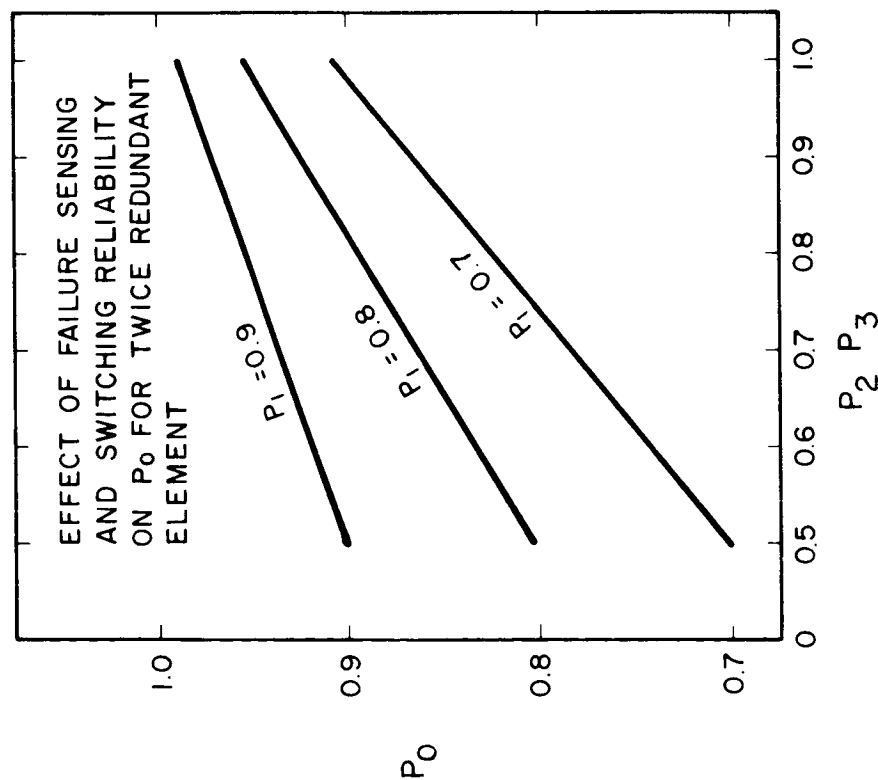


FIGURE 1 - EFFECT OF FAILURE SENSING AND SWITCHING RELIABILITY ON  $P_0$  FOR TWICE REDUNDANT ELEMENT

the overall reliability of the twice redundant system drops back to 0.9, thus negating any advantages of redundancy. No conclusions can be drawn from this exercise toward solar-thermionic systems at this time. However, it should be noted that examination of redundancy is insufficient without examination of the mechanisms and devices used for sensing the failure of a component and/or switching from one unit to the next.

The example of Fig. 2-2 used a failure rate for the thermionic diode which corresponds to a MTTF of 50,000 hours. To demonstrate this MTTF will consume considerable test time. An illustration of this test time is shown in Fig. 2-4 which shows the percent confidence in the MTTF figure (probability that the MTTF is correct) as a function of the total test time obtained on the units and the number of failures seen during the test. The curves correspond to obtaining a MTTF figure of 5,000 hours. As shown, if zero failures occur during test, a 90 percent confidence can be given to a 5,000-hr MTTF if 11,500 hours have been accumulated on devices. This could correspond to ten diodes operating for 1,115 hours each. However, if one failure occurs, the required test time increases to 19,500 hours. The above calculations are based on use of the  $\chi^2$  squared distribution which is a standard statistical tool described in Ref. 2-1.

To obtain MTTF of 50,000 hours, several orders of magnitude more test hours are required; for example, 1,000 diodes instead of 10 diodes should be placed on test.

## 2.2 System Weight Estimates

An examination was made of the potential system weights in a variety of missions with a variety of mirror diameters. The results of the calculations are shown in Table 2-II. The table is self-explanatory.

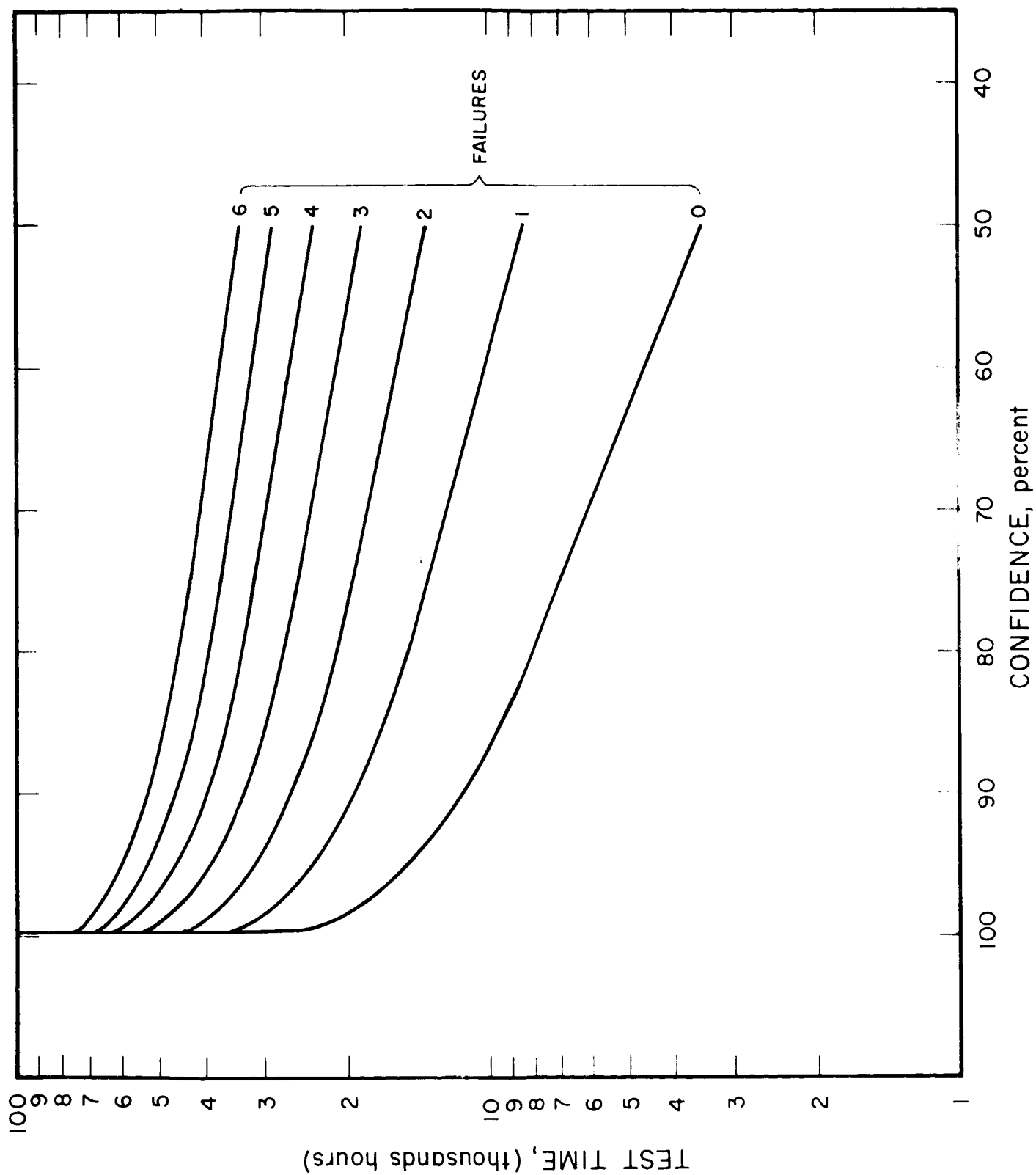


FIG. 2-17 DEVICE HOURS OF TEST TIME FOR VARIOUS NUMBERS OF FAILURES

TABLE 2-II

ESTIMATED SYSTEM PERFORMANCE PARAMETERS (1968)

|   |   |       |      |      |      |       |
|---|---|-------|------|------|------|-------|
| Mission   | 1000 n. mi. Sun Synchronous Earth Orbiter |       |      |      |      |       |
| Percentage of Light   | 100 percent                               |       |      |      |      |       |
| Distance From Sun   | 1 AU                                      |       |      |      |      |       |
| Solar Intensity ( $\text{w}/\text{ft}^2$ )  | 150                                       |       |      |      |      |       |
| Concentrator Diameter (ft)  | 4   | 5     | 6    | 7    | 8    | 9-1/2 |
| <u>Efficiency (Percent)</u>   |   |       |      |      |      |       |
| Collector-Absorber Efficiency   | 54  | 57    | 59   | 61   | 62.5 | 63.5  |
| Generator Observation and IR Efficiency   | 95  | 96    | 96.3 | 96.5 | 96.8 | 97    |
| Generator Efficiency  | 15  | 15    | 15   | 15   | 15   | 15    |
| Power Conditioning Efficiency   | 7   | 77    | 77.5 | 78.5 | 79.2 | 80    |
| Control Efficiency  | -   | -     | -    | -    | -    | -     |
| System Efficiency   | 7.0                                       | 7.6   | 7.9  | 8.0  | 8.0  | 8.8   |
| Power Output (Watts)  | 114                                       | 194   | 291  | 415  | 551  | 611   |
| <u>Weight (lb)</u>  |   |       |      |      |      |       |
| Concentrator  | 5.1                                       | 8     | 11.5 | 15.7 | 20.5 | 29    |
| Generator Support   | 1.2                                       | 1.5   | 2    | 3    | 4    | 5     |
| Generator   | 1.5                                       | 2.8   | 4.0  | 5.2  | 7.1  | 10.4  |
| Power Conditioning  | 6   | 8     | 11   | 14   | 19   | 21    |
| Control Wt.   | -   | -     | -    | -    | -    | -     |
| System Wt. (lb)   | 13.3                                      | 20.3  | 28.5 | 37.9 | 47.6 | 65.4  |
| System Specific Wt. (lb/W)  | 121                                       | 104.5 | 98   | 91.3 | 84.7 | 74.1  |
| System Power Density ( $\text{w}/\text{ft}^2$ )   | 9.9                                       | 10.0  | 10.1 | 10.3 | 10.5 | 10.8  |
| <u>Assumptions:</u>   |   |       |      |      |      |       |
| 1) Cavity temperature of $1700^\circ\text{C}$ .   |   |       |      |      |      |       |
| 2) Concentrator Specific Wt. = $6.4 \text{ lb}/\text{ft}^2$ assuming Al concentrators.  |   |       |      |      |      |       |
| 3) The most simple system is assumed:   |   |       |      |      |      |       |
| a) Steady-state conditions.   |   |       |      |      |      |       |
| b) No energy storage  |   |       |      |      |      |       |
| c) No Cs Res or solar flux controls   |   |       |      |      |      |       |
| 4) Weight for auxiliary attachments to vehicle not included.  |   |       |      |      |      |       |
| 5) Weight for instrumentation not included.   |   |       |      |      |      |       |
| 6) Performance is based on reasonable judgement of performance available in prototypes in 1966-67, system availability in 1968. |   |       |      |      |      |       |

TABLE 2-II (Contd.)

## ESTIMATED SYSTEM PERFORMANCE PARAMETERS (1968)

| Mission                              | Mars Orbiter                                  |      |      |      |      |      |
|--------------------------------------|---|------|------|------|------|------|
| Percentage of Light                  | 80 percent (8 hr light, 2 hr dark) worst case |      |      |      |      |      |
| Distance from Sun                    | 1.57 AU                                       |      |      |      |      |      |
| Solar Intensity ( $w/ft^2$ )         | 46.9  |      |      |      |      |      |
| Concentrator Diameter (ft)           | 4   | 5    | 6    | 7    | 8    | -1/2 |
| <u>Efficiency (percent)</u>          |   |      |      |      |      |      |
| Collector-Absorber                   | 42  | 47   | 51   | 55   | 58   | 60   |
| Generator Obscuration and IR         | 93  | 93.8 | 94.5 | 95   | 95.4 | 95.5 |
| Generator                            | 15  | 15   | 15   | 15   | 15   | 15   |
| Power Conditioning                   | 7   | 74   | 75   | 75   | 76.8 | 77.5 |
| Control                              | 95  | 95   | 95   | 95   | 95   | 95   |
| Storage                              | 54  | 54   | 54   | 54   | 54   | 54   |
| System (excluding storage)           | 4.9   | 5.7  | 6.2  | 6.7  | 7.3  | 7.6  |
| <u>Solar Thermionic Source</u>       | 29  | 52   | 82   | 121  | 171  | 251  |
| <u>Power Output (watts)</u>          |   |      |      |      |      |      |
| <u>System Power Output (watts)</u>   | 20  | 36   | 56   | 83   | 117  | 172  |
| <u>Weight (lb)</u>                   |   |      |      |      |      |      |
| Concentrator                         | 5.1   | 8    | 11.5 | 15.7 | 20.5 | 29   |
| Generator Support                    | 1.5   | 2.5  | 3.7  | 4.2  | 5    | 5.5  |
| Generator                            | 1.8   | 1.6  | 1.2  | 1.5  | 2.4  | 2.6  |
| Power Conditioning                   | 4   | 4.5  | 5    | 6    | 7.5  | 11   |
| Control                              | 1   | 1.2  | 1.5  | 1.7  | 2    | 2.5  |
| Storage                              | 1.5   | 12.1 | 15.5 | 20.5 | 40.2 | 50   |
| System wt. (wo-Storage)              | 12.4  | 17.2 | 22.9 | 26.4 | 37.7 | 41.3 |
| Solar Thermionic Source              | 227   | 350  | 280  | 243  | 220  | 200  |
| Specific wt. (lb/watt)               |   |      |      |      |      |      |
| Solar Thermionic Source <sub>2</sub> |   |      |      |      |      |      |
| Power Density ( $w/ft^2$ )           | 2.3   | 2.7  | 2.9  | 3.2  | 3.4  | 3.6  |

Assumptions:

- 1) Cavity temperature of  $1700^\circ C$ .
- 2) Concentrator Specific wt. = 0.4 lb/ft<sup>2</sup> assuming Al concentrators.
- 3) Weight for auxiliary attachments to vehicle not included.
- 4) Weight for instrumentation not included.
- 5) Performance is based on reasonable judgement of prototype performance in 1966-67, Systems availability in 1968.
- 6) Battery is Ag-Zn; assume 50 percent depth of discharge equivalent to 10 whr/lb.

TABLE 2-II (Cont.)

## ESTIMATED SYSTEM PERFORMANCE PARAMETERS (1968)

|  |  |      |      |      |      |       |
|--|--|------|------|------|------|-------|
| Mission  | 25 n. mi. Circular Earth Orbiter                   |      |      |      |      |       |
| Percentage of Light  | 1 percent (55 min. light, 35 min. dark) worst case |      |      |      |      |       |
| Distance from Sun  | 1 AU   |      |      |      |      |       |
| Solar Intensity (w/ft <sup>2</sup> )   | 130  |      |      |      |      |       |
| Concentrator Diameter (ft)   | 4  | 5    | 6    | 7    | 8    | 8-1/2 |
| <u>Efficiency (Percent)</u>  |  |      |      |      |      |       |
| Collector-Absorber   | 54   | 57   | 59   | 61   | 62.5 | 63.5  |
| Generator Obscuration and IR   | 95   | 96   | 96.3 | 96.5 | 96.8 | 97    |
| Generator  | 15   | 18   | 18   | 18   | 18   | 18    |
| Power Conditioning   | 76   | 77   | 77.6 | 78.5 | 79.2 | 80    |
| Control  | 95   | 95   | 95   | 95   | 95   | 95    |
| Storage  | 54   | 54   | 54   | 54   | 54   | 54    |
| System (excluding storage)   | 6.7  | 7.2  | 7.4  | 7.9  | 8.2  | 8.4   |
| <u>Solar Thermionic Source</u>   |  |      |      |      |      |       |
| Power Output (watts)   | 109  | 185  | 277  | 395  | 525  | 771   |
| <u>System Power Output (watts)</u>   | 50   | 85   | 127  | 181  | 241  | 354   |
| <u>Weight (lb)</u>   |  |      |      |      |      |       |
| Concentrator   | 5.1  | 8    | 11.5 | 15.7 | 20.5 | 29    |
| Generator Support  | 1.2  | 1.5  | 2    | 3    | 4    | 5     |
| Generator  | 1.5  | 2.8  | 4.0  | 5.2  | 7.1  | 11.4  |
| Power Conditioning   | 6  | 8    | 11   | 14   | 18   | 21    |
| Control  | 1.5  | 1.8  | 2.1  | 2.5  | 2.8  | 3     |
| Storage  | 7.5  | 12.7 | 19   | 27   | 36   | 53    |
| System Wt.   | 17.3   | 22.1 | 30.6 | 40.4 | 50.4 | 68.4  |
| Solar Thermionic Source  | 140  | 120  | 111  | 103  | 96   | 89    |
| Specific Wt. (lb/watt)   |  |      |      |      |      |       |
| Solar Thermionic Source  |  |      |      |      |      |       |
| Power Density (w/ft <sup>2</sup> )   | 8.7  | 9.4  | 9.8  | 10.3 | 10.5 | 10.9  |
| <u>Assumptions:</u>  |  |      |      |      |      |       |
| 1) Cavity Temperature of 1700°C.   |  |      |      |      |      |       |
| 2) Concentrator Specific Wt. = 0.4 lb/ft <sup>2</sup> assuming Al concentrators.                                   |  |      |      |      |      |       |
| 3) Weight for auxiliary attachments to vehicle not included.   |  |      |      |      |      |       |
| 4) Weight for instrumentation not included.  |  |      |      |      |      |       |
| 5) Performance is based on reasonable judgement of prototype performance in 1966-67, Systems Availability in 1968. |  |      |      |      |      |       |
| 6) Battery is Ag-Cd; assume 50 percent depth of discharge equivalent to 10 wh/4lb.                                 |  |      |      |      |      |       |

TABLE 2-II (Contd.)

## ESTIMATED SYSTEM PERFORMANCE PARAMETERS (1968)

|                                      |   |      |      |      |      |       |
|--------------------------------------|---|------|------|------|------|-------|
| Mission                              | Venus Orbiter                                 |      |      |      |      |       |
| Percentage of Light                  | 80 percent (8 hr light, 2 hr dark) worst case |      |      |      |      |       |
| Distance from Sun                    | .728 AU                                       |      |      |      |      |       |
| Solar Intensity (w/ft <sup>2</sup> ) | 245   |      |      |      |      |       |
| Concentrator Diameter (ft)           | 4   | 5    | 6    | 7    | 8    | 9-1/2 |
| <u>Efficiency (Percent)</u>          |   |      |      |      |      |       |
| Collector-Absorber                   | 53  | 54   | 55   | 55   | 56   | 56    |
| Generator Obscuration and IR         | 97  | 97.5 | 98   | 98.2 | 98.3 | 98.5  |
| Generator                            | 18  | 18   | 18   | 18   | 18   | 18    |
| Power Conditioning                   | 77  | 78.5 | 79.2 | 80   | 81   | 82    |
| Control                              | 95  | 95   | 95   | 95   | 95   | 95    |
| Storage                              | 54  | 54   | 54   | 54   | 54   | 54    |
| System (excluding storage)           | 7.8   | 7.05 | 7.3  | 7.42 | 7.62 | 7.85  |
| <u>Solar Thermionic Source</u>       | 269   | 440  | 504  | 627  | 946  | 1362  |
| <u>Power Output (watts)</u>          |   |      |      |      |      |       |
| <u>System Power Output (Watts)</u>   | 143   | 252  | 344  | 476  | 645  | 951   |
| <u>Weight (lb)</u>                   |   |      |      |      |      |       |
| Concentrator                         | 5.1   | 8    | 11.5 | 15.7 | 20.5 | 29    |
| Generator Support                    | 1.4   | 2    | 3    | 4    | 5    | 6     |
| Generator                            | 2.4   | 4.2  | 6    | 8.4  | 11.5 | 16.2  |
| Power Conditioning                   | 8   | 12.5 | 15   | 18   | 25   | 32    |
| Control                              | 2   | 2.5  | 3    | 3.2  | 3.7  | 4     |
| System Wt. (w/o storage)             | 18.9  | 29.2 | 38.5 | 48.7 | 65.7 | 97.2  |
| Storage Wt. (lb)                     | 3.1   | 54.5 | 80.9 | 112  | 152  | 214   |
| Solar Thermionic Source              | 90.5  | 85.9 | 76.5 | 70   | 67.4 | 71.5  |
| Specific Wt. (lb/w)                  |   |      |      |      |      |       |
| Solar Thermionic Source              | 16.7  | 17.4 | 17.9 | 18.2 | 18.9 | 19.5  |
| Power Density (w/ft <sup>2</sup> )   |   |      |      |      |      |       |

Assumptions:

- 1) Cavity Temperature of 1700°C.
- 2) Concentrator Specific Wt. = 0.4 lb/ft<sup>2</sup> assuming Al concentrators.
- 3) Weight for auxiliary attachments to vehicle not included.
- 4) Weight for instrumentation not included.
- 5) Performance is based on reasonable judgement of prototype performance in 1967-68; Systems availability in 1968.
- 6) Battery is Ag-Cd; assume 50 percent depth of discharge equivalent to 10 whr/lb.



## REFERENCES

### Section 2

- 2-1 A. Hald, Statistical Theory with Engineering Applications,  
John Wiley and Sons, Inc., N.Y., 1952, Chapter 22

### 3. SOLAR CONCENTRATORS

The solar concentrator is a key element in determining the performance and weight of the solar-thermionic system. This section describes achievements to date in the concentrator area and considerations in future concentrators.

#### 3.1 Physical Description

Figure 3-1 illustrates the components of a solar concentrator and the elements which must be considered in concentrator design. The three main subassemblies are the reflective skin, the skin support, and the attachment from the support to skin.

A reflective skin consists of a thin substrate material, such as electroformed nickel, which supports coatings of various types. Stretchformed concentrators are made in sections which are bonded together typically by epoxy and tape materials.

The skin support is a rigid member used to hold the skin in place. The support includes attachments for various purposes. The most popular form of support to date for "one-piece" concentrators has been a torus which supports the edge of the concentrator. The torus-paraboloid skin combination results in a relatively stiff monocoque-type structure.

The attachment from the support to the skin can have a significant effect on the skin surface qualities. Ideally, the attachment is of such a nature that no distortion is introduced into the thin skin material. Practically, the need for withstanding vibration, acoustic and other environments dictates that a small portion of the skin is likely to be distorted due to the bonding of the inter-connecting web.

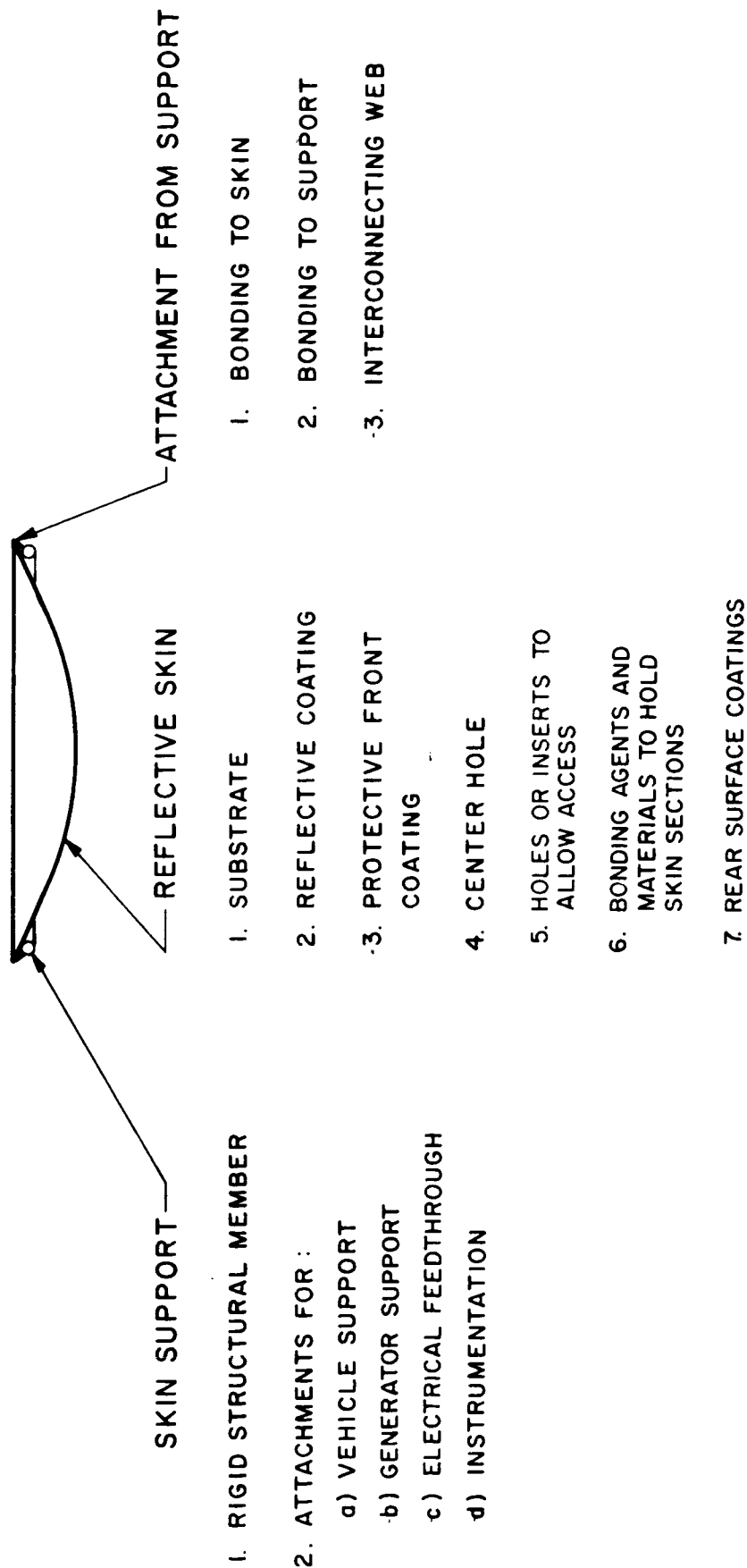


FIG. 1-1 CO-GENERATOR CONFIG. MTS

### 3.2 Design Rationale

The rationale for concentrator design is illustrated in Fig. 3-2. The mirror size and geometry is dictated by:

1. Mission requirements, including power load profile, orbit or trajectory, etc.
2. Vehicle interface requirements
3. Expected environmental effects
4. The generator/cavity design
5. The electronic power system design

Using these factors, the mirror size and geometry can be selected. The selection is usually an iterative process which involves an optimization of the overall solar-thermionic system.

The details of the concentrator structure can be determined after mirror sizing. The structure design must withstand the launch and cruise environment. All of the vehicle interface problems discussed in Section 1 must be considered. The generator support design is an integral part of concentrator design. The design parameters which offer problems vary in importance depending on mirror size. Parameters include:

- I. Optical Performance
- II. Nature and Stability of Reflective Surface
- III. Thermal Profile
- IV. Structural Restraints - acoustic response, compressive buckling, vibration response, transportation, etc.
- V. Dimensions
- VI. Weight
- VII. Support Design

### 3.3 State of the Art

A variety of solar concentrator structures have been assembled over the past several years using many materials and assembly techniques.

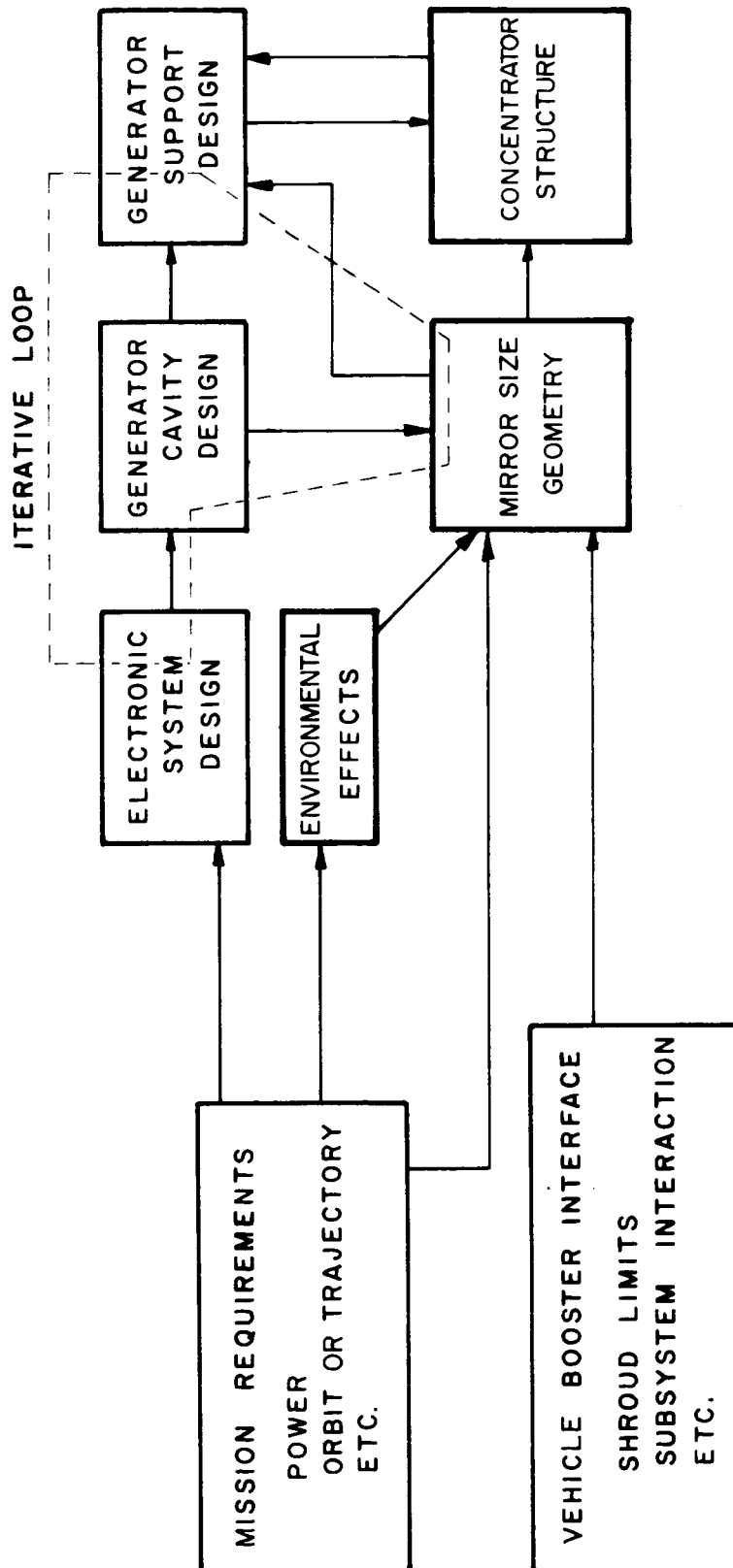


FIG. 1-2 DESIGN RATIONALE FOR CONCENTRATORS

These include foam-backed, inflated, vapor deposited, stretchformed, electroformed, and other varieties.

As a general rule, solar-thermionic systems require highly reflective, highly accurate surfaces which approach a true paraboloid. No other surface has yet been devised for achieving the high temperatures necessary for efficient system performance.

The two techniques showing most promise for paraboloid fabrication have been the electroformed and stretchformed concentrators. Two sizes of nickel electroformed concentrators have been fabricated - 5 ft, 60° rim angle and 9-1/2 ft, 42° rim angle. The 5 ft nickel concentrators fabricated in 1962 exhibited surface accuracies within a few minutes of arc of a true paraboloid. Concentrator weights in the 5-ft size have ranged from 0.7 to 1 lbs/sq ft using nickel electroformed techniques with aluminum and nickel torus support.

The state of the art for 9-1/2 ft nickel concentrators is still young; two concentrators have been fabricated, the first weighing 450 lbs and the second weighing 90 lbs.

Five-ft aluminum stretchformed mirrors to date have shown efficiencies which are less than those of the nickel electroformed concentrators. The lb per watt of energy into a cavity absorber is still less than the nickel concentrators, however, and much work can be accomplished in the stretchformed concentrator area. Aluminum has been used to date; other materials are being investigated.

Aluminum electroforming investigations to date have resulted in concentrators 30 inches in diameter with a promise of larger diameters. The aluminum electroformed material is rather soft and techniques are being investigated to create a harder, more rigid material using fiber materials.

Figure 3-3 is a photograph of a 5 ft nickel electroformed concentrator with a front-mounted torus assembled in 1962. Figure 3-4 is a photograph of a 9-1/2 ft nickel electroformed concentrator using a rear-mounted torus, assembled in late 1964, weighing a total

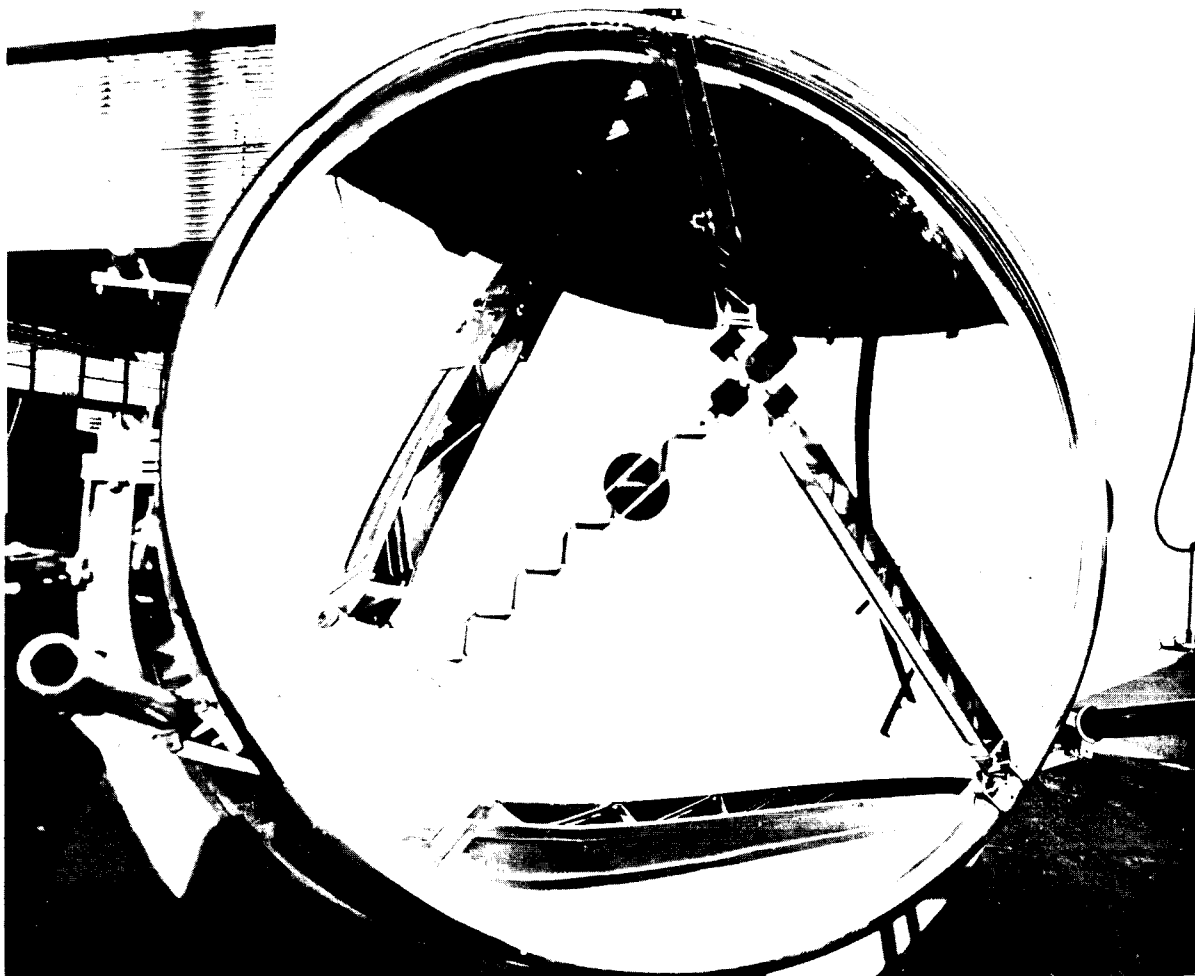


FIG. 3-3 - PROTOTYPE SOLAR-THERMIONIC SYSTEM WITH FIVE-FOOT CONCENTRATOR ,  
SUPPORT ARMS AND GENERATOR MODEL

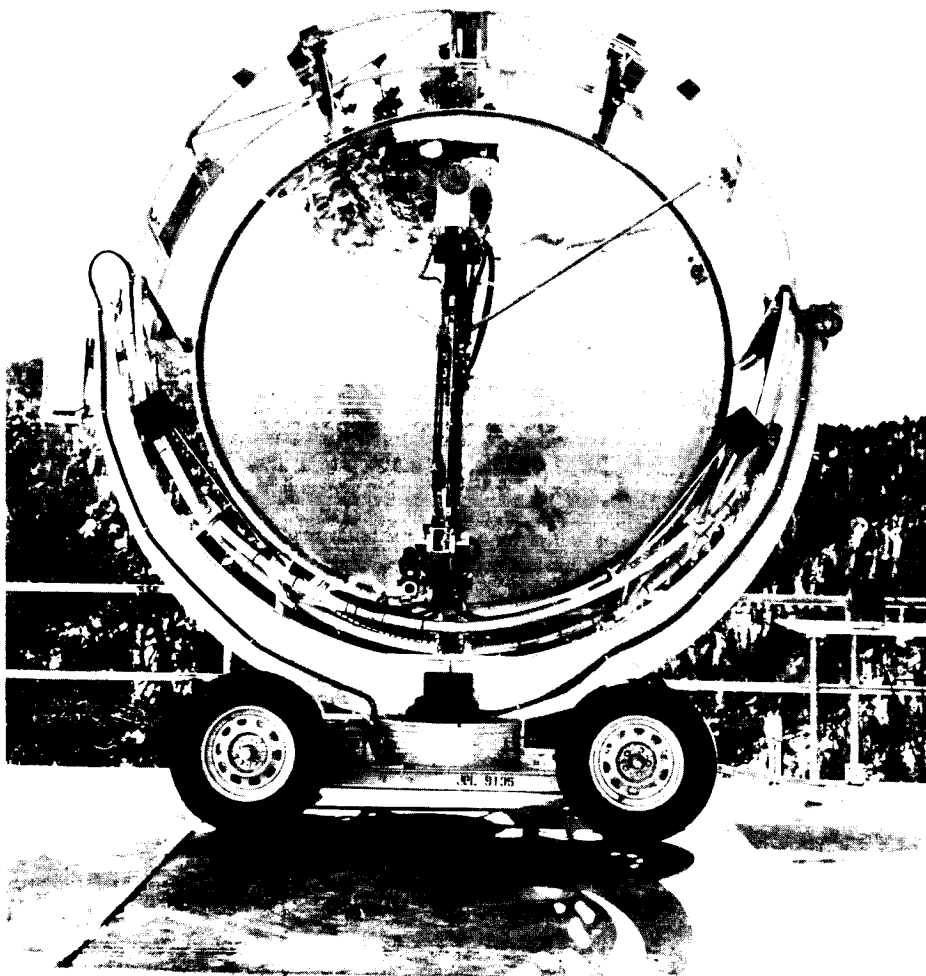


FIG. 1 - NINE AND ONE-HALF-FOOT CONCENTRATOR



of 92 lbs. Figure 3-5 is a pictorial sketch of a 5-ft aluminum stretchformed concentrator showing the torus and eight skin gores.

The results of solar calorimetric tests performed on the electroformed nickel and stretchformed aluminum concentrators are shown in Fig. 3-6. The calorimetric efficiency is defined as the ratio of the energy reflected from a concentrator and collected by a cavity-type cold calorimeter to the energy incident on the concentrator as measured by a pyrheliometer. Concentration ratio is the ratio of the net projected reflective area of the concentrator to the area of the aperture of the cavity calorimeter. To give an indication of the quality of the various concentrators, a theoretical maximum efficiency curve for a perfect concentrator with a specular reflectivity of 0.91 is shown.

The electroformed nickel concentrator with the rear-mounted torus has slightly lower specular reflectivity as well as less accurate geometry. The less accurate geometry appears to be located over sections of the paraboloid near the rim as determined by an optical ray trace method of measurement. It is probable that the greater error in the mirror surface near the rim can be attributed to the torus location.

The stretchformed aluminum concentrator data show less accurate geometry and lower specular reflectivity than the data from the nickel concentrators. The errors in the mirror surface geometry are mainly located where backing strips are used to join sectors together as well as in the region where the torus is bonded to the shell. The lower specular reflectivity can be attributed to the inability of the epoxy surface improvement coat to cover the grainy surface of the stretched aluminum.

The efficiency of the 9-1/2 ft diameter electroformed nickel concentrator is below the data for all the other concentrators. Several reasons for the lower values have been determined. First, the master had a slightly etched surface thus lowering the specular

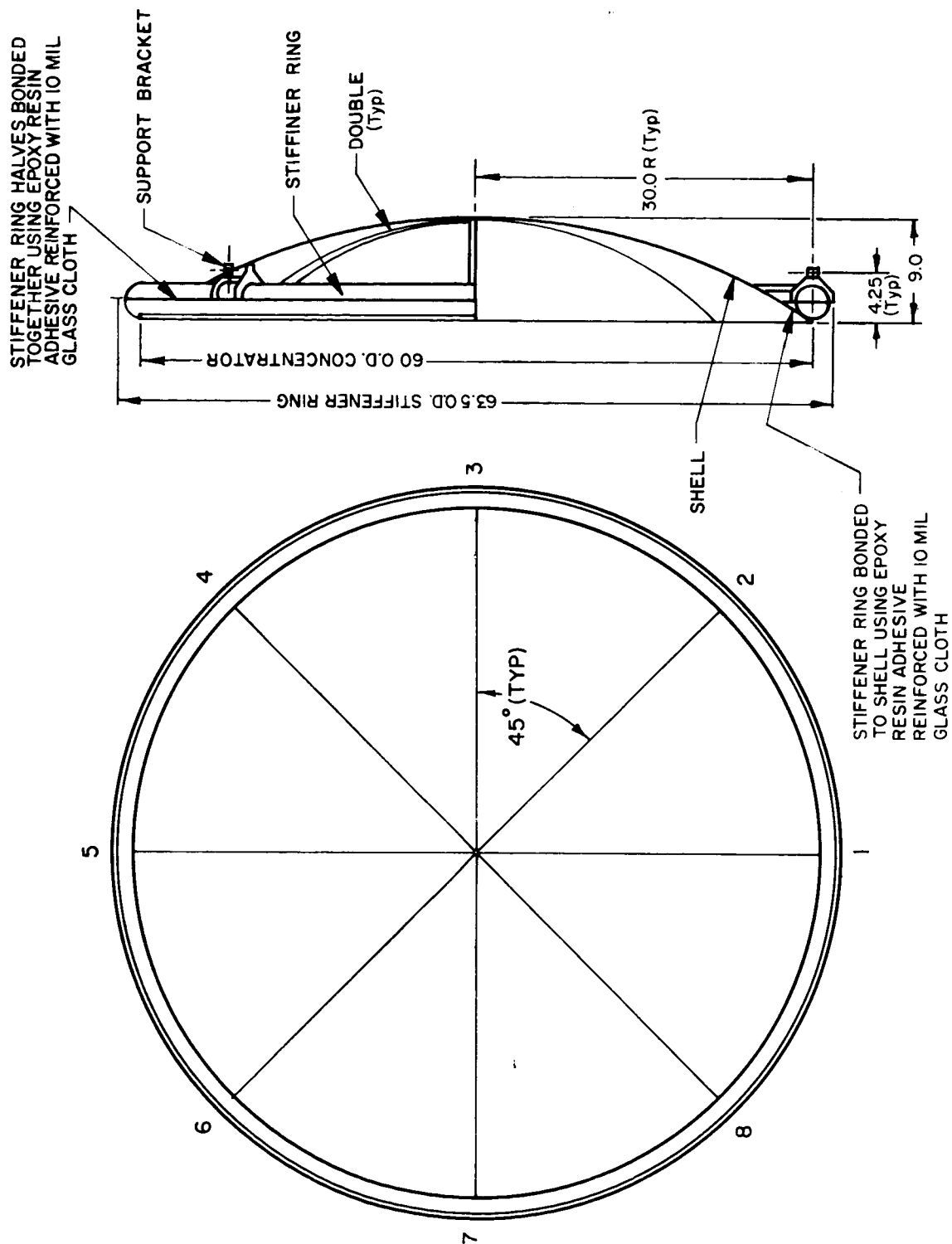


FIG. 1-1 PICTORIAL SKETCH OF ALUMINUM STRETCH-FORMED CONCENTRATOR

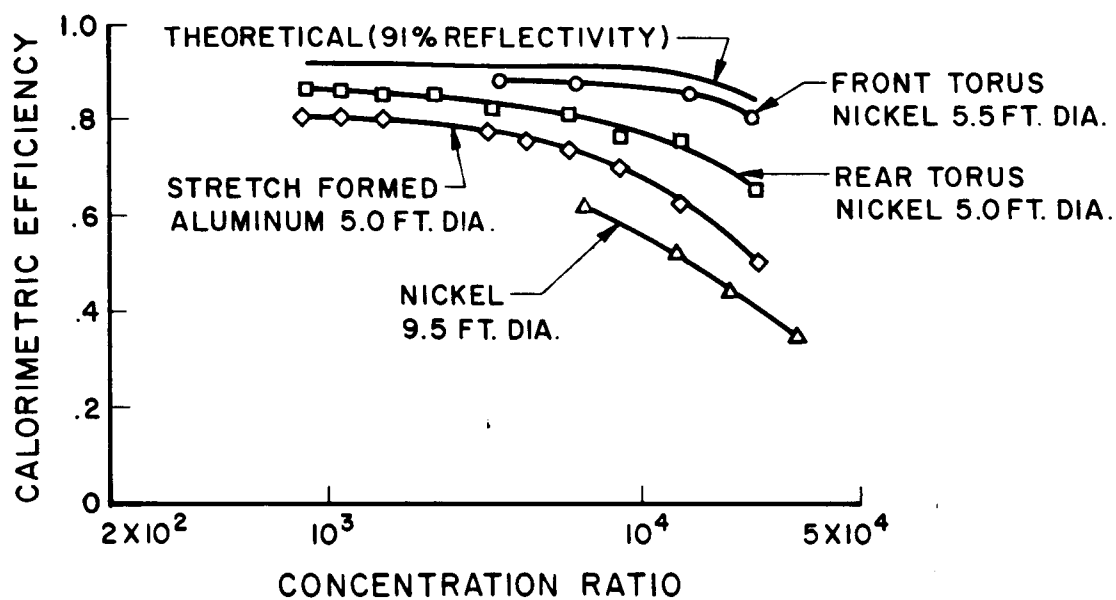


FIG. 1-50 CALORIMETRIC EFFICIENCY OF ON-TELESCOPIC SOLAR CONCENTRATORS\*

\* "NASA SOLAR CONCENTRATOR DEVELOPMENT"  
 P. A. BAATHUR, AND J. L. POTEMAN  
 AIAA PAPER NO. 67-1060

reflectivity of the concentrator. Second, the area near the rim was found to have a shorter focal length than the rest of the mirror thus lowering the overall concentrating ability.

Figure 3-7 shows the power per pound of concentrator weight (specific power) that would be available in an absorber combined with each of the three small concentrators of Fig. 3-6. The cold calorimeter data of Fig. 3-6 have been combined with a hypothetical absorber having an absorptivity and emissivity of 1.00 to obtain these curves. The 9-1/2 ft diameter concentrator is not shown because it was made as a check on the master fabrication process and no attempt was made to minimize the weight of the concentrator.

Figure 3-7 can only be used as an indication of results to date. The concentrators are far from optimized and weight improvements will occur.

Data on the dynamic qualities of the concentrator structure is sketchy. A nickel-electroformed 3-ft concentrator with rear-mounted torus was subjected to the Atlas-Agena vibration spectrum at a flight acceptance level with no damage. This test demonstrated the basic ability of the structure to survive a vibration test. The tests were performed at JPL during March, 1965. Support arms (see Fig. 4-2) and a simulated generator were mounted on the concentrator during the tests.

#### 3.4 Optical Performance Characteristics of Concentrators

This section details with the optical performance characteristics of the mirror surface. Surface characteristics and structural aspects are treated elsewhere. This section includes:

1. The rationale for rim angle selection
2. The performance of an ideal concentrator
3. The effects of surface deviation
4. The effects of misorientation

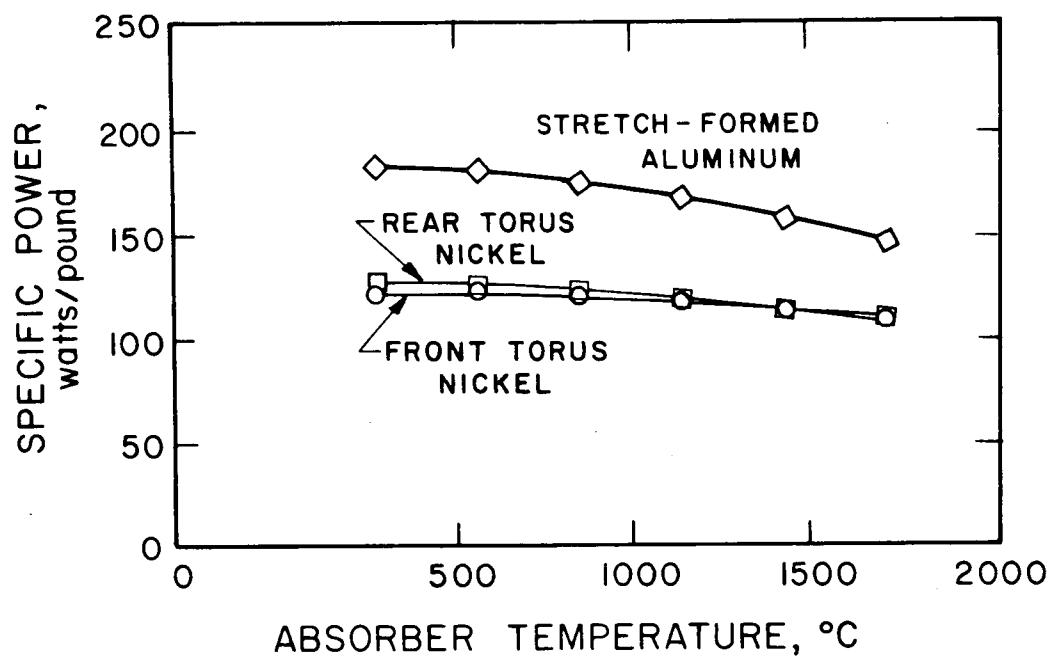


FIG. 7. SPECIFIC POWER OF ONE-PIECE SOLAR CONCENTRATORS\*

\* "NASA SOLAR CONCENTRATOR DEVELOPMENT"  
 BY A. PLATT, JR. AND E. L. GOTTMAN  
 NAA PAT. NO. 1-7, 1967

#### 3.4.1 Optimum Collector Rim Angle

For a given collector diameter, various factors affect the choice of the optimum collector rim angle. These include:

1. Structural integrity of collector shell
2. Total of collector and generator support weight
3. Surface error distribution over collectors of different rim angles, as a function of rim angle
4. Cavity axial misfocus and radial misalignment effects
5. Subtended angle of the solar source and limb darkening effects
6. Thermal distortion effects
7. Angular misorientation as a function of time
8. The effects of rim angle on achievement of uniform heat distribution within the cavity
9. Structural errors caused by orbiting forces
10. Packaging height

For a perfect collector with perfect focus and orientation when 100 percent of the reflected energy is focused into the cavity aperture, the maximum collector-absorber efficiency occurs at a  $45^{\circ}$  rim angle. Based on 6 percent obscuration, a reflectance of 91 percent and a cavity temperature of  $1700^{\circ}\text{C}$ , the variation in total collector-absorber efficiency between a  $45^{\circ}$  rim angle and a  $60^{\circ}$  rim angle "perfect" collector as above would be less than one percent. A qualitative comparison of  $45^{\circ}$  and  $60^{\circ}$  rim angle collectors is given in Table 3-I.

TABLE 3-1

COMPARISON OF HIGH AND LOW RIM ANGLE COLLECTORS  
 TYPIFIED BY 45 AND 60 DEGREE RIM ANGLES

Advantages

45° Rim Angle

Smaller theoretical image

Smaller surface area

Low packaging height

Less efficiency loss due to:

Axial misfocus

Rim errors

Easier to achieve uniform temperature  
 distribution in cavity

60° Rim Angle

More rigidity

Less shell weight for the same  
 rigidity

Shorter and lighter generator  
 support

Less efficiency loss due to:

Random errors

Misorientation

Radial misalignment in the  
 focal plane

#### 3.4.1.1 Optimization of Efficiency

The optimization of collector-absorber efficiency as a function of rim angle is highly dependent on the importance given to each factor affecting efficiency. Many factors which effect optical errors can only be determined by experimental studies of full scale collectors. However, some first approximations can be made to determine the importance of rim angle variation.

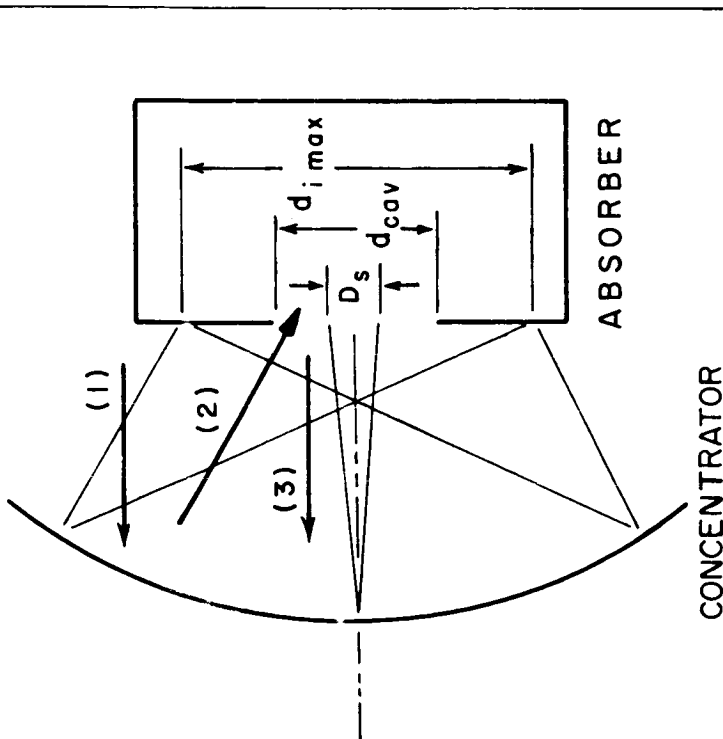
For general background, Fig. 3-8 summarizes many definitions of terms used in concentrator analysis. These terms are general and will be used throughout the concentrator analysis.

Figure 3-9 illustrates the effect of rim angle on the mirror efficiency. Mirror efficiency is plotted as a function of entrance diameter to the cavity for four different rim angles. For a perfect concentrators, it is shown that the highest mirror efficiency can be obtained with a  $45^{\circ}$  rim angle mirror at the smallest entrance diameter. However, the difference between a  $60^{\circ}$  and a  $45^{\circ}$  rim angle mirror is small.

Figure 3-10 illustrates the effect of angular errors in the mirror surface on collector-absorber efficiency. Once again, the difference between a  $45^{\circ}$  and  $60^{\circ}$  rim angle mirror is small.

Figure 3-11 shows the results of a series of calculations in which the maximum collector-absorber efficiency was calculated for varying cavity temperatures, solar intensities, misorientations, and rim angles. A perfect mirror surface was assumed. As shown, misorientation effects on a  $60^{\circ}$  rim angle mirror are less than the effects on a  $45^{\circ}$  rim angle mirror. The difference in effects varies according to the degree of misorientation. For high efficiency systems, misorientation must be within the  $\pm 10$ -minute area. Once again, on the basis of an examination of misorientation, little difference exists between the  $45^{\circ}$  and  $60^{\circ}$





## TERMS USED IN CONCENTRATOR

### ANALYSIS

$$\text{MIRROR EFFICIENCY} = \frac{(2)}{(1)} = \eta_m$$

(Sometimes called collector efficiency)

$$\begin{aligned} \text{COLLECTOR-ABSORBER EFFIC.} &= \frac{(2)-(3)}{(1)} \\ &= \eta_{c-a} \end{aligned}$$

FIG. 3-8 DEFINITIONS OF TERMS USED IN CONCENTRATOR ANALYSIS

## DEFINITIONS

- (1) = ENERGY INCIDENT ON REFLECTOR =  $H A_m$
- (2) = ENERGY ENTERING CAVITY ENTRANCE
- (3) = BLACK-BODY RERADIATION FROM CAVITY ENTRANCE PLUS REFLECTION OUT OF CAVITY

$D_s$  = SUN'S IMAGE DIAMETER

$d_{cav}$  = DIAMETER OF CAVITY ENTRANCE

$d_{i\max}$  = MAXIMUM IMAGE DIAMETER USING MIRROR SURFACE FREE OF ERROR

$D_m$  = MIRROR DIAMETER

$I(r)$  = INTENSITY OF RADIATION IN FOCAL IMAGE

$$\frac{d_{i\max}}{D_m} = \frac{a}{4 \sin \theta_r \cos \theta_r} \left[ 1 + a \tan \theta_r \right]; \quad \begin{array}{l} X = \text{ANGLE SUBTENDED} \\ \text{BY THE SUN} \\ \theta_r = \text{CONCENTRATED} \\ \text{RIM ANGLE} \end{array}$$

## OTHER TERMS USED IN LITERATURE

$$\text{CONCENTRATION RATIO} = \frac{\int_0^{D_s/2} I(r) 2\pi r \, dr}{H \pi D_s^2 / 4}; \quad \begin{array}{l} I(r) = \text{INTENSITY AT} \\ \text{CAVITY ENTRANCE} \\ H = \text{SOLAR INTENSITY} \end{array}$$

$$= \frac{\text{AVERAGE INTENSITY OVER SUN'S IMAGE}}{\text{SOLAR INTENSITY}}$$

$$\text{GEOMETRIC CONCENTRATION RATIO} = \left[ \frac{D_m}{d_{cav}} \right]^2$$

$$\text{CONCENTRATION EFFICIENCY} = \frac{\int_0^{D_s/2} I(r) 2\pi r \, dr}{H \pi D_m^2 / 4}$$

$$= \frac{\text{ENERGY WITHIN SUN'S IMAGE}}{\text{ENERGY ON MIRROR}}$$

$$\text{CONCENTRATION FACTOR} = \left[ \frac{d_{i\max}}{D_m} \right]^2$$

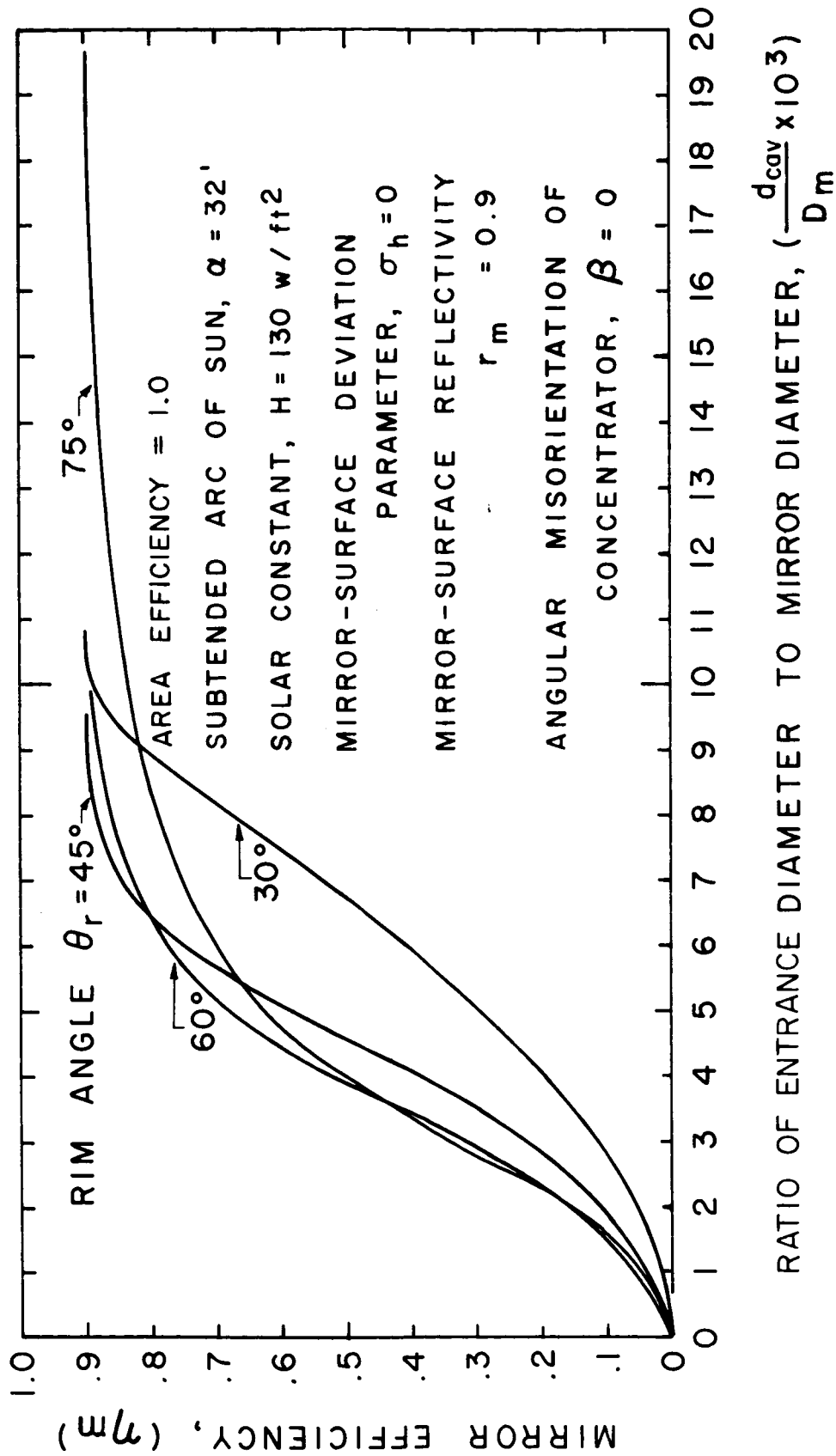


FIG. 3-9 MIRROR EFFICIENCY OF PARABOLOID CONCENTRATOR WITH PERFECT SURFACE ACCURACY AT EARTH'S DISTANCE FROM SUN WITH NO MISORIENTATION

$\sigma_\psi$  = SIGMA VALUE FOR MIRROR SURFACE ANGULAR  
ERROR  
ABSORBER TEMPERATURE,  $T_a = 2000^\circ \text{ K}$

$r_m = 0.9$

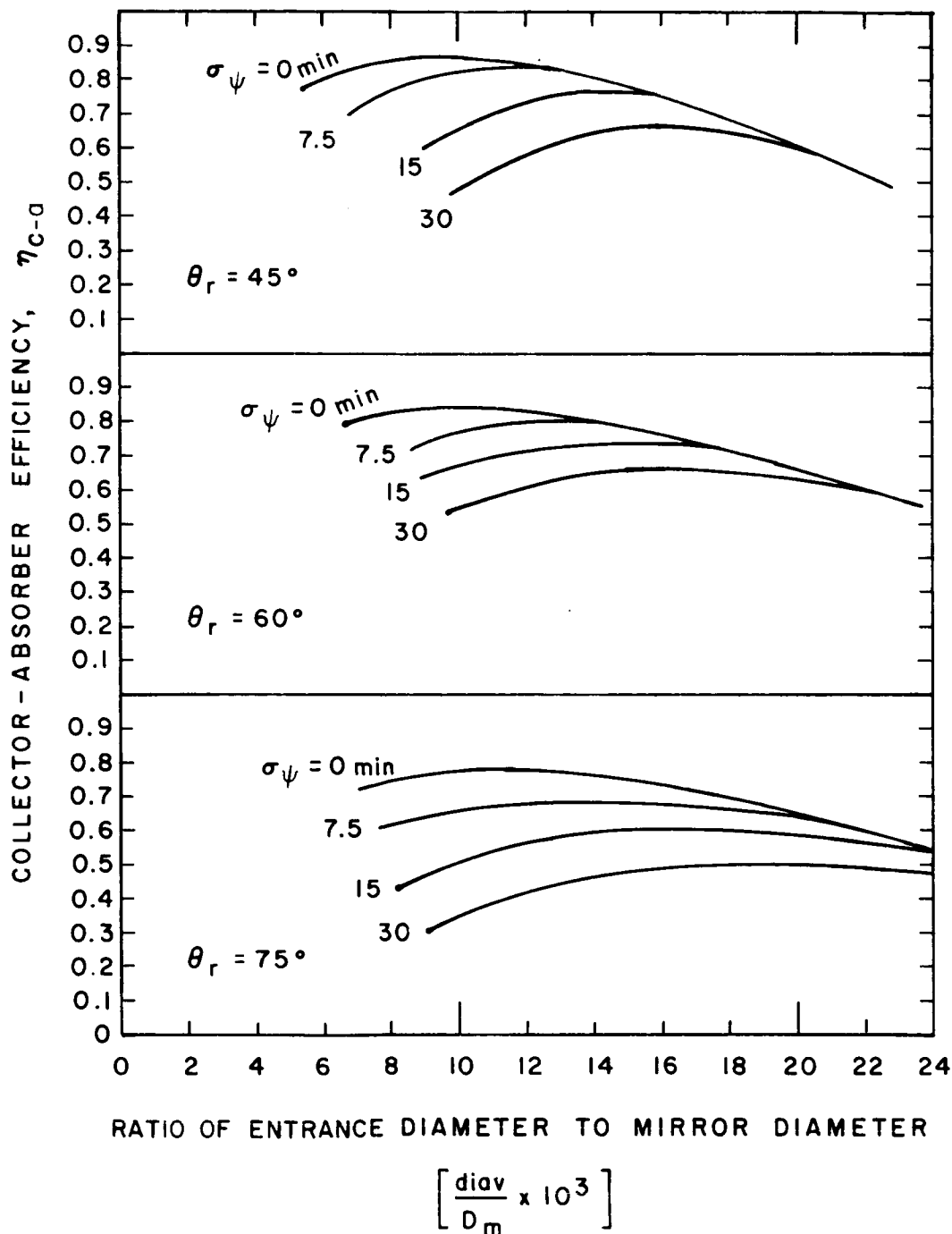


FIG. 3-10 COLLECTOR-ABSORBER EFFICIENCY FOR A PARABOLOID  
CONCENTRATOR WITH SMALL ANGULAR SURFACE  
DEVIATION. DISTANCE FROM SUN = EARTH

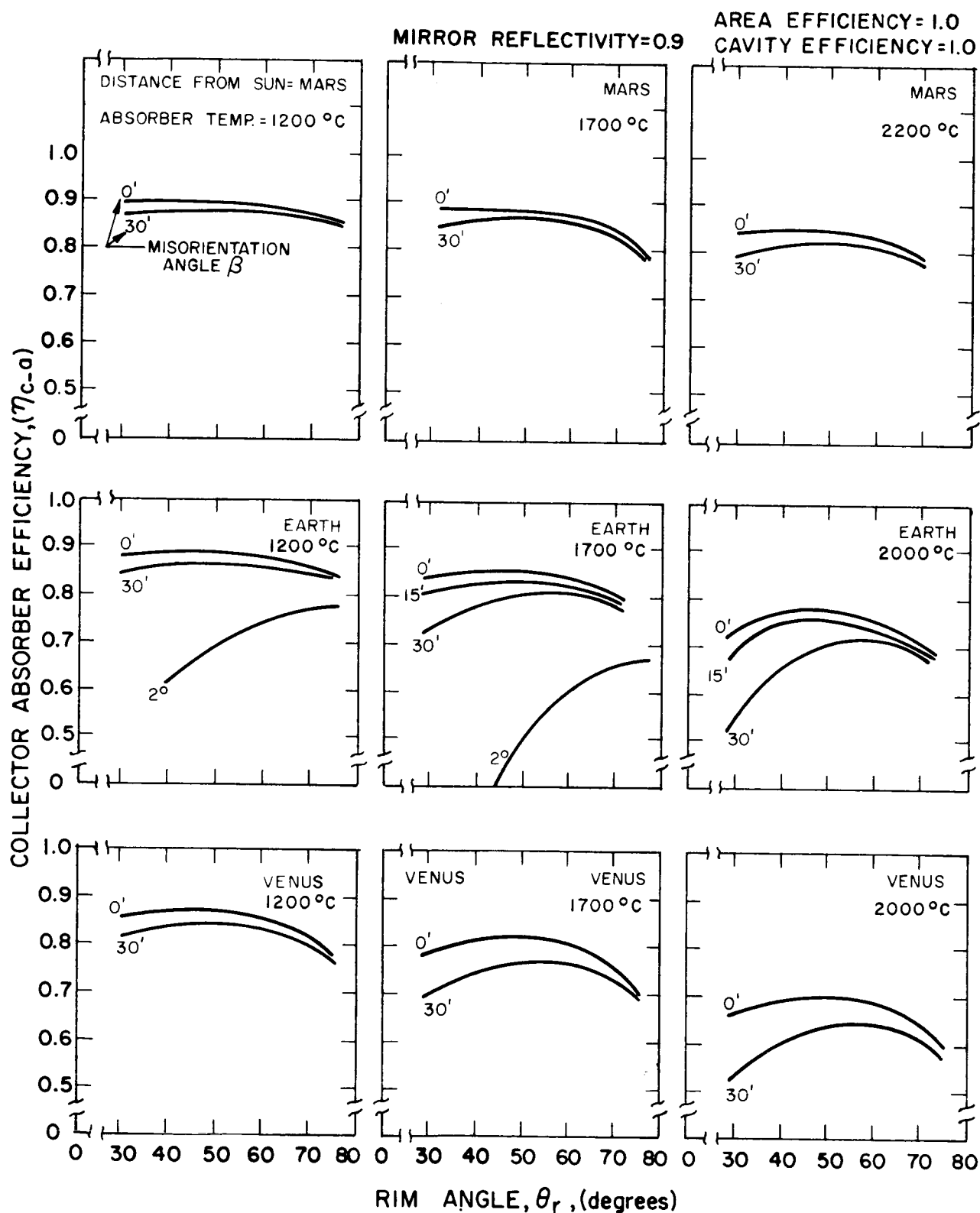


FIG. 3-11 MIRROR COLLECTOR-ABSORBER EFFICIENCY AS A FUNCTION OF RIM ANGLE

rim angle case. The optimum rim angle will depend on solar intensity, distance from the sun, cavity temperature and other factors.

Figure 3-12 is a summary of the optimization of the rim angle vs misorientation for a perfect concentrator. As shown, at the earth's distance from the sun and a cavity of  $1700^{\circ}\text{C}$ , the optimum rim angle is between  $45^{\circ}$  and  $50^{\circ}$ .

The results of Fig. 3-12 must be qualified by the fact that real concentrators will have surface deviation; this will tend to increase the optimum rim angle closer to  $60^{\circ}$ . The other qualification is that none of the calculations in Fig. 3-12 have assumed reflection losses from the cavity. Introduction of reflection losses will tend to make the optimum rim angle smaller.

#### 3.4.1.2 Optimization of Weight

The effect of rim angle on system weight is such that rim angles near  $60^{\circ}$  are more favorable than rim angles near  $45^{\circ}$ .

Figure 3-13 illustrates a typical optimization of collector and generator support weight for a 5 ft and 10 ft system.

Assuming that it is desired to maintain the same resistance through the generator support arms no matter what the length, it can be shown that the weight of the support arms is proportional to the square of the length. The length of the arms is inversely proportional to  $\sin \theta_r$ .

On the other hand, shallower dishes have less surface area per frontal area and a  $45^{\circ}$  skin will weigh less than a  $60^{\circ}$  skin for the same system performance.

The calculations in Fig. 3-13 illustrate a typical optimization. Generator support weight will decrease radically with an increase in rim angle. Collector weight will increase gradually. The optimum point will occur in the range of  $60^{\circ}$  to  $70^{\circ}$  rim angle.

AREA EFFICIENCY = 1.0  
 CAVITY EFFICIENCY = 1.0  
 MIRROR REFLECTIVITY = 0.9  
 DISTANCE FROM SUN = EARTH  
 $T_0 = 1700^\circ\text{C}$

VENUS  
 $1700^\circ\text{C}$

MARS  
 $1700^\circ\text{C}$

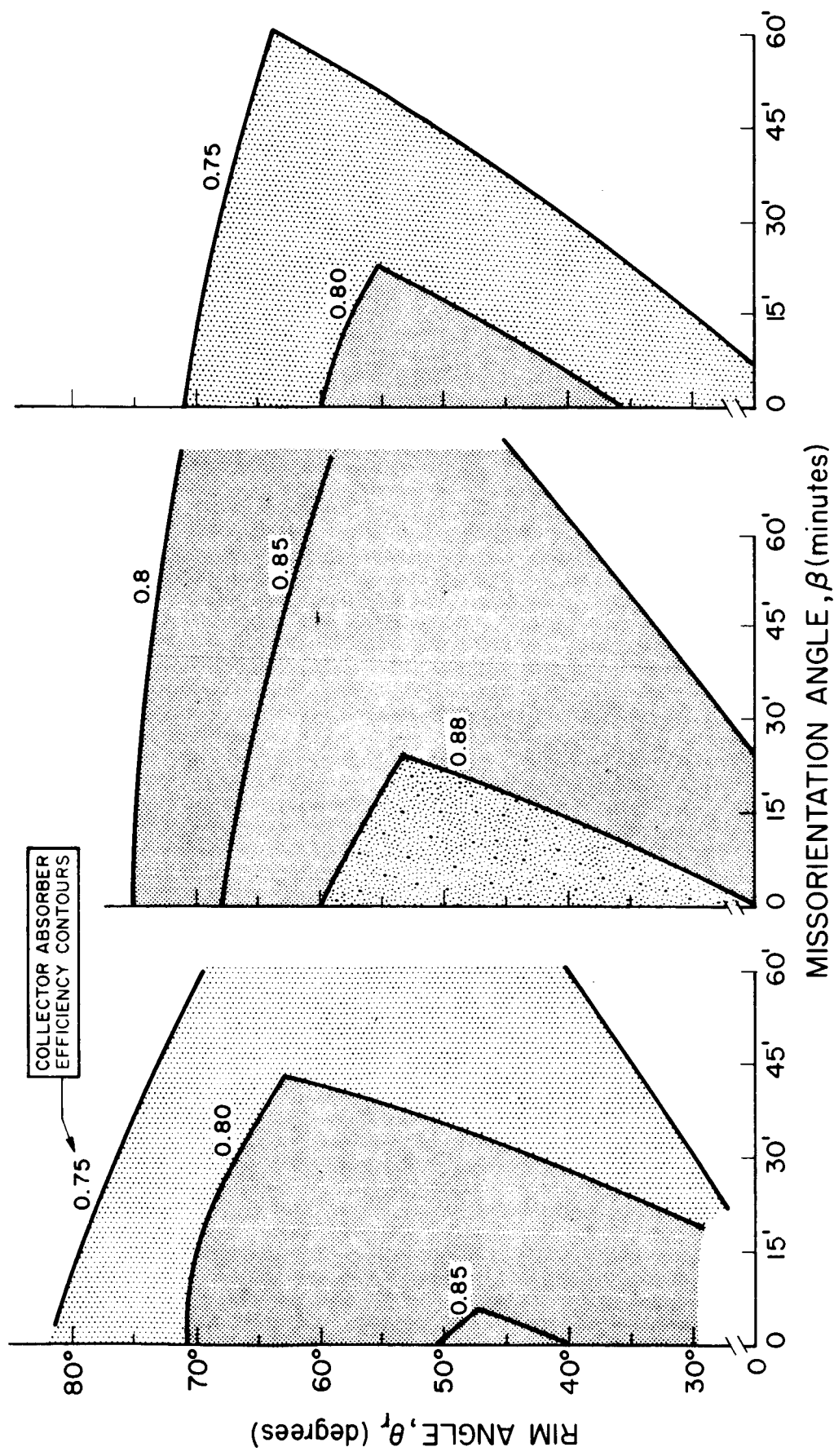


FIG. 3-12 RANGE OF RIM ANGLE AND ORIENTATION REQUIREMENTS FULFILLED TO PROVIDE HIGH COLLECTOR ABSORBER EFFICIENCY USING A PERFECT CONCENTRATOR

# FOR CONSTANT RESISTIVITY

$$W_{\text{SUPPORT}} = \eta \rho_s \cdot \ell = \eta \ell^2 \left( \frac{r \rho_m}{K} \right)$$

$$\ell = \frac{R}{\sin \theta_r}$$

Where: R = Radius of Mirror  
 $\theta_r$  = Rim Angle  
 $\ell$  = Support Length  
 $\eta$  = Number of Arms  
 $\rho_s$  = lb./ft. for arm  
K = Constant Value of resistance  
r = Resistivity  
 $\rho_m$  = Density of material

Total Wt. = Collector & Support

$$W = W_c + W_s$$

$$W_c = W_{\text{SKIN}} + W_{\text{TORUS}}$$

Assume:

1.  $W_{\text{SKIN}} = W_{\text{TORUS}}$
2. Resistance Drop Thru Support Arms is Constant
3.  $\rho_{\text{SKIN}} = 0.25 \text{ lb./ft.}^2$
4.  $\rho_{\text{SUPPORT}} = 0.5 \text{ lb./ft. when } \ell = 3 \text{ ft.}$

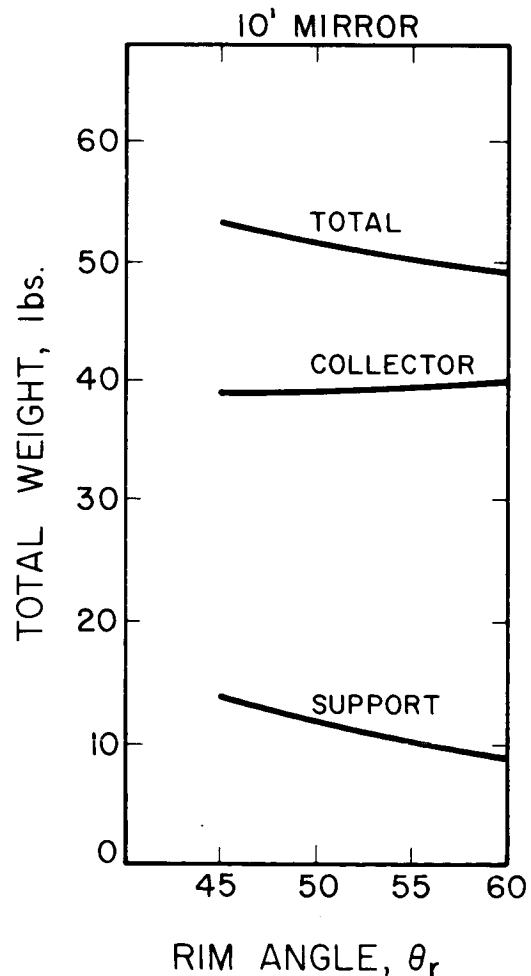
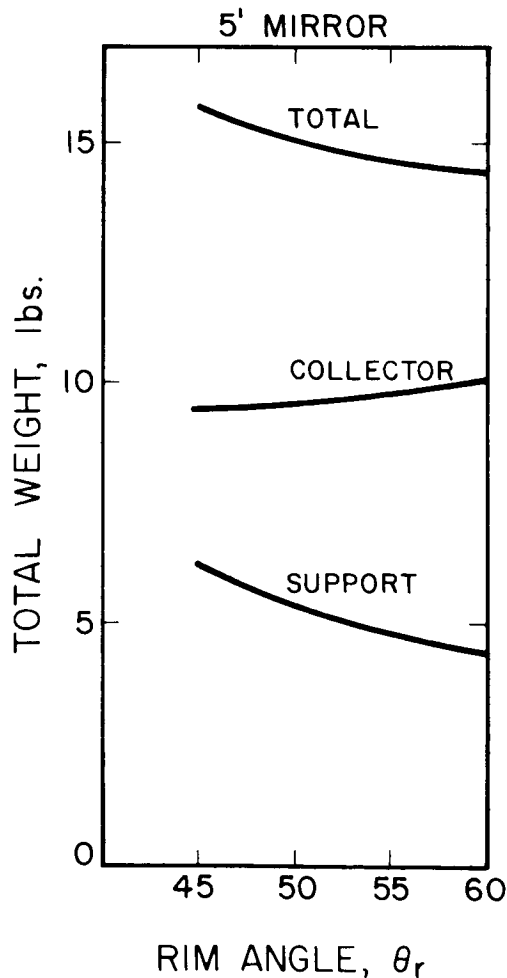


FIG. 1-18 TYPICAL COLLECTION OF COLLECTOR WEIGHT AS A FUNCTION OF RIM ANGLE

In practice, optimization of the rim angle should be accomplished by a computer program which takes into account obscuration, minimum cross section needed for satisfying vibration criteria, thermal conductivity criteria, and etc. Hand-calculations of this type are tedious. However, in one case for a 30 ft mirror it was found the optimum rim angle did occur at about  $55^{\circ}$  from a minimum weight viewpoint.

#### 3.4.1.3 Selection of Rim Angle

As discussed above, the differences in efficiency between a  $45^{\circ}$  and  $60^{\circ}$  rim angle mirror will be small. Weight considerations favor the use of the higher rim angles. Mirrors with rim angles outside of the  $45^{\circ}$  to  $60^{\circ}$  rim angle boundaries will begin to suffer in efficiency.

Final choice of the rim angle will depend a great deal on practical considerations and detailed analysis of the concentrator structure. It is felt at this time that the optimum rim angle should be close to  $55^{\circ}$ .

#### 3.4.2 Mirror Efficiency

Figure 3-14 is a nomograph of mirror efficiency vs mirror diameter and cavity aperture diameter. An example of the nomograph use is shown. For the case of a 5 ft mirror and 0.8 inch cavity entrance diameter, lines A and B form an intersection. Line C is drawn between the zero point of the graph and the A-B intersection to intercept the abscissa at point X. A line parallel to the ordinate is drawn from point X. The example shows for a cavity aperture of 0.8 inch and a 5-ft mirror with a sigma of 10 minutes, mirror efficiency will be about 83 percent.

Figure 3-15 shows an assumed surface distortion vs mirror diameter used in subsequent calculations. The curve for 1964 is based upon judgment regarding what has been demonstrated to date. The curve for 1968 is based upon existing technology with increased experience in fabrication and handling techniques.



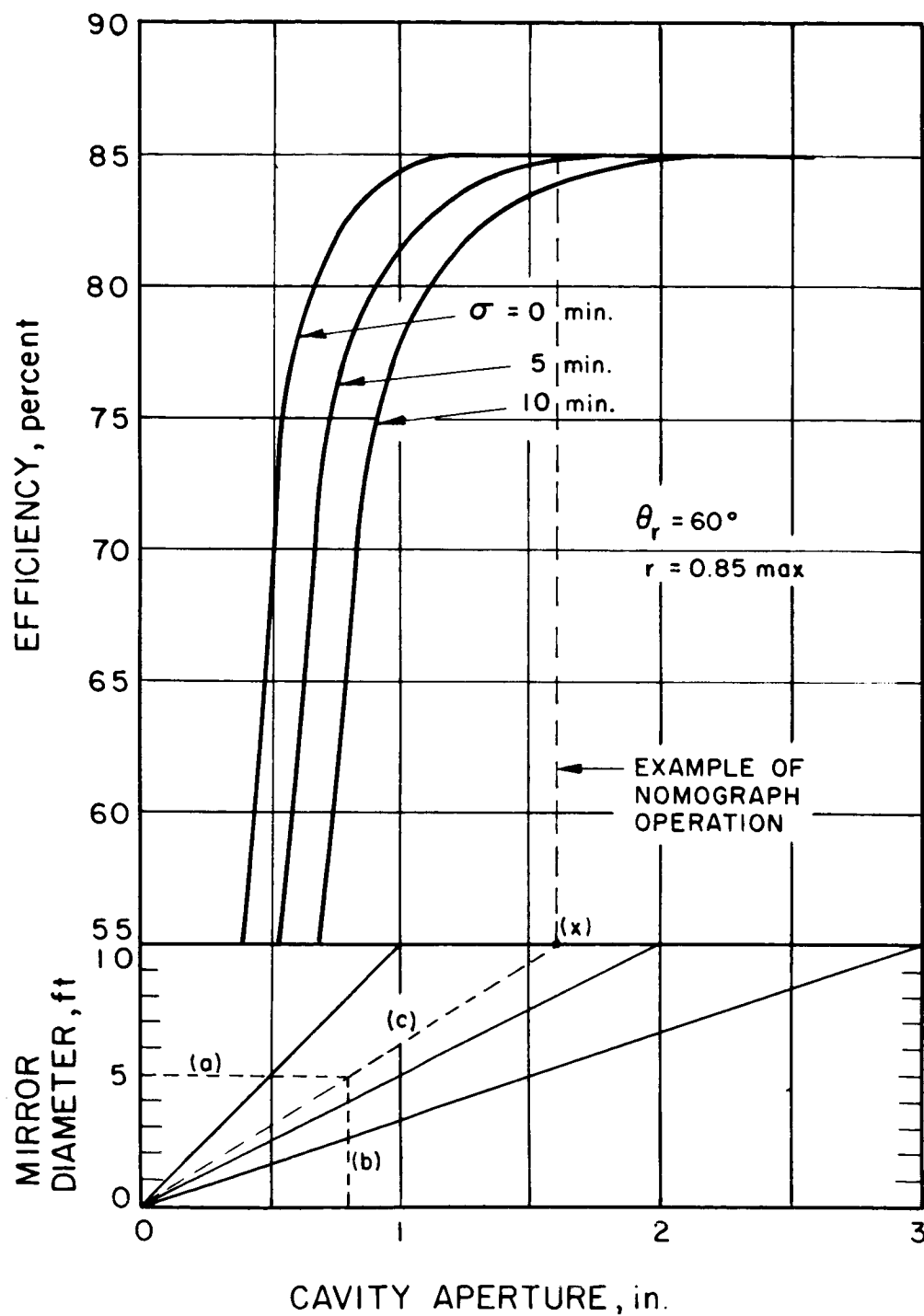


FIG. 14 MIRROR EFFICIENCY VS MIRROR DIAMETER AND CAVITY APERTURE NOMOGRAPH

NOTE: CURVE FOR 1968 BASED UPON EXISTING  
TECHNOLOGY, BUT INCREASED EXPERIENCE  
IN FABRICATION AND HANDLING TECHNIQUES

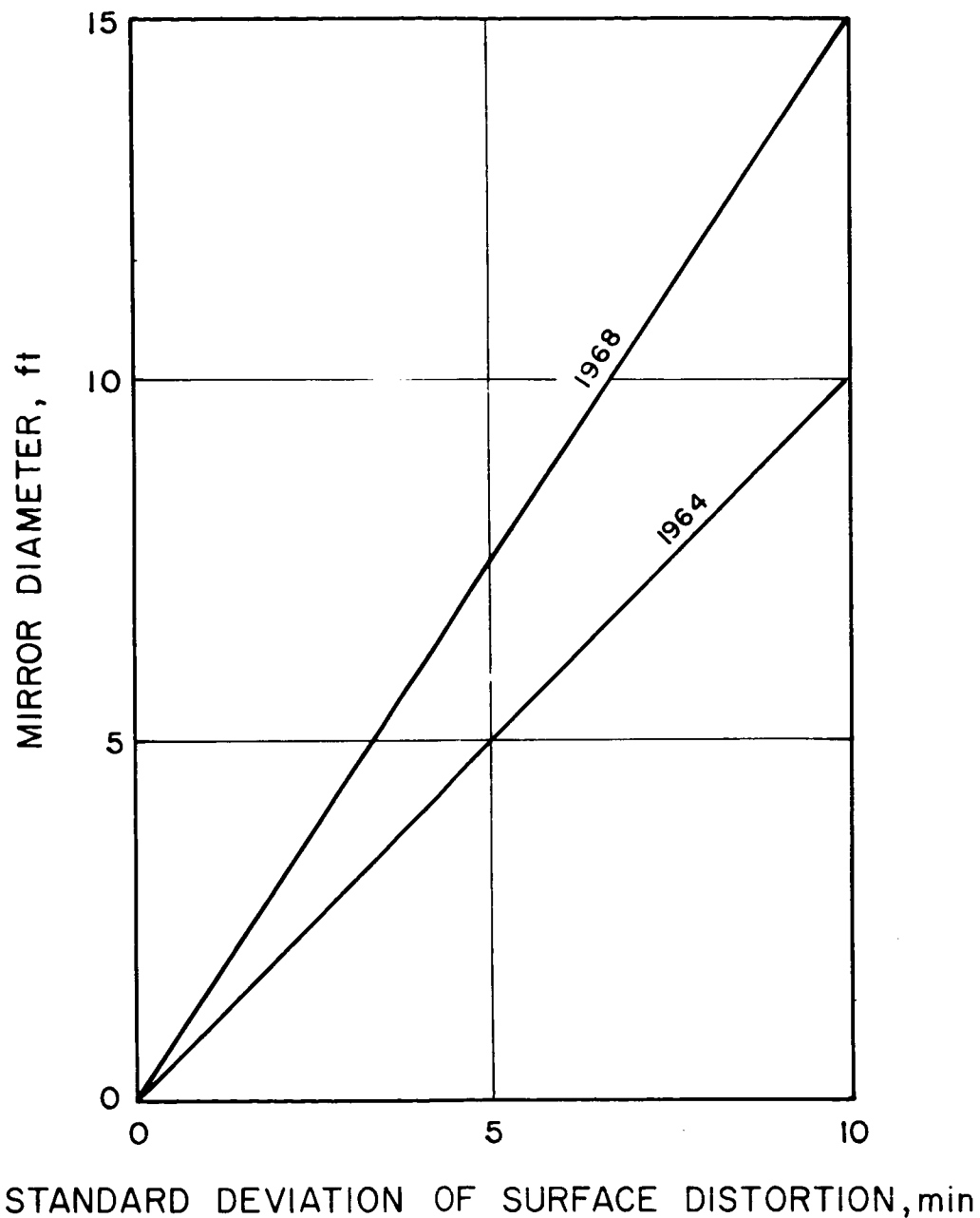


FIG. -1- MIRROR DIAMETER VS PROJECTED DISTORTION

Figure 3-16 shows a maximum power which can be directed into a cavity from a given collector diameter assuming the surface is perfect, the reflectivity is 0.85 and the mirror is at the earth's distance from the sun.

Extrapolating from Figs. 3-14 and 3-15, Table 3-II shows the mirror efficiency for mirror diameters of 5 ft, 7 ft, 8.5 ft and 10 ft assuming a mirror reflectivity of 0.85 at the earth's distance from the sun.

At present, two types of computer programs are available for analysis of concentrator performance. One program is an optical ray trace program with a surface error approximation used to generate mirror efficiency calculations. This program is available at Electro-Optical Systems, Inc., and elsewhere.

A second type of computer program involving a collector, cavity absorber and absorber heat exchanger is being developed by the Aerospace Corporation with the assistance of Dr. George Shrenk. This program can handle entire collector-absorber configurations and can include the effects of:

1. Collectors of any size, shape or configuration
2. Orientation errors
3. Sun of any angular diameter
4. Limb darkening of the sun
5. Surface errors due to thermal distortion
6. Any diameter cavity aperture
7. Absorber surfaces of any configuration

The aerospace program is extremely rigorous and is based on an assumed normal distribution of surface errors. More recent modifications will incorporate the results of actual Hartmann test data to derive the normal distribution. As an example, one case of misorientation using the collector program takes about 60 minutes on an IBM 7094 computer; adequate corrections for limb darkening might have increased the running time four to ten times. For economical

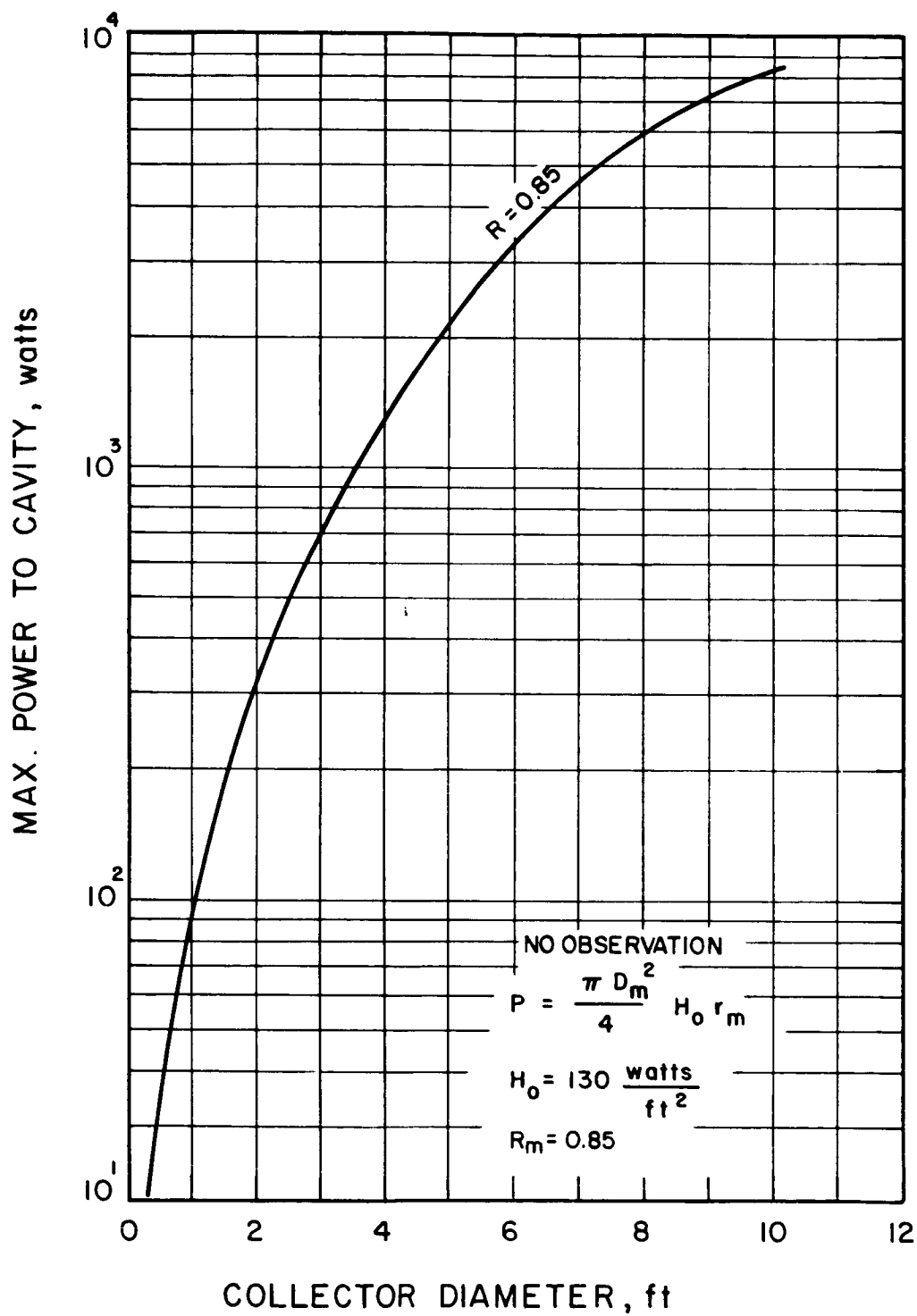


FIG. -16 MAXIMUM POWER INTO CAVITY VS COLLECTOR DIAMETER FOR PERFECT MIRROR

TABLE 3-II

MIRROR EFFICIENCY - 1968

| Cavity Entrance<br>Diameter | Mirror Diameter |      |        |       |
|-----------------------------|-----------------|------|--------|-------|
|                             | 5 ft            | 7 ft | 8.5 ft | 10 ft |
| 0.5"                        | .56             | 51   | 40     | 30    |
| 0.55                        | 62              | 56   | 49     | 42    |
| 0.6                         | 66              | 61   | 57     | 53    |
| 0.65                        | 71              | 67   | 63     | 60    |
| 0.7                         | 75              | 71   | 68     | 65    |
| 0.75                        | 77.5            | 75   | 72     | 70    |
| 0.8                         | 79              | 77   | 75     | 73.5  |
| 0.85                        | 80.5            | 79   | 77     | 76    |
| 0.9                         | 81.5            | 80   | 79     | 77.3  |
| 0.95                        | 82              | 81   | 80     | 79    |
| 1.0                         | 83              | 81.8 | 81     | 80    |
| 1.1                         | 84              | 83   | 82     | 81.5  |
| 1.2                         | 84.5            | 83.8 | 83     | 82.3  |
| 1.3                         | 84.8            | 84.2 | 83.5   | 83    |
| 1.4                         | 85              | 84.6 | 84.1   | 83.5  |
| 1.5                         | 85              | 85   | 84.5   | 84    |

$$R_m = 0.85$$

$$H = 130 \text{ W/ft}^2$$

reasons, therefore, parametric studies are more readily done by the ray trace technique. However, it is expected that the Aerospace program will be developed soon to the point where it is economically feasible to develop a large number of parametric analyses.

Figures 3-16 and 3-17 illustrate results from the ray trace computer calculation which shows the effective solar diameter as a function of focus shift from the focal plane for an 8.5 diameter concentrator. One case is with no misorientation and the other case is with 16 minutes misorientation. As shown, the effects of focal shift can be drastic.

#### 3.4.3 The Nature of Surface Errors

Frequently, for lack of actual data, random gaussian error distributions have been used to represent collector surface errors. The random gaussian distribution does not adequately represent:

1. Radial errors at the collector rim joint
2. Circumferential errors at any radial joints or ribs
3. Zonal defects of the mirror

In actual practice, it appears that the maximum errors of an electro-formed mirror are radial at the collector-torus rim joint or due to zonal defects of the mirror.

For the ray trace program, a tenth order polynomial error representation was chosen for mathematical and computer program simplicity. This error distribution concentrates the errors near the rim and therefore causes a higher efficiency loss, for any standard deviation error, than an equivalent random gaussian error. The tenth order polynomial error distribution appears conservative but provides a good approximation of the actual error distribution for electro-formed mirrors.

Collector surface errors can be classified as: microscopic, macroscopic, and long wave. A collector efficiency cannot be adequately predicted unless each of these surface errors is

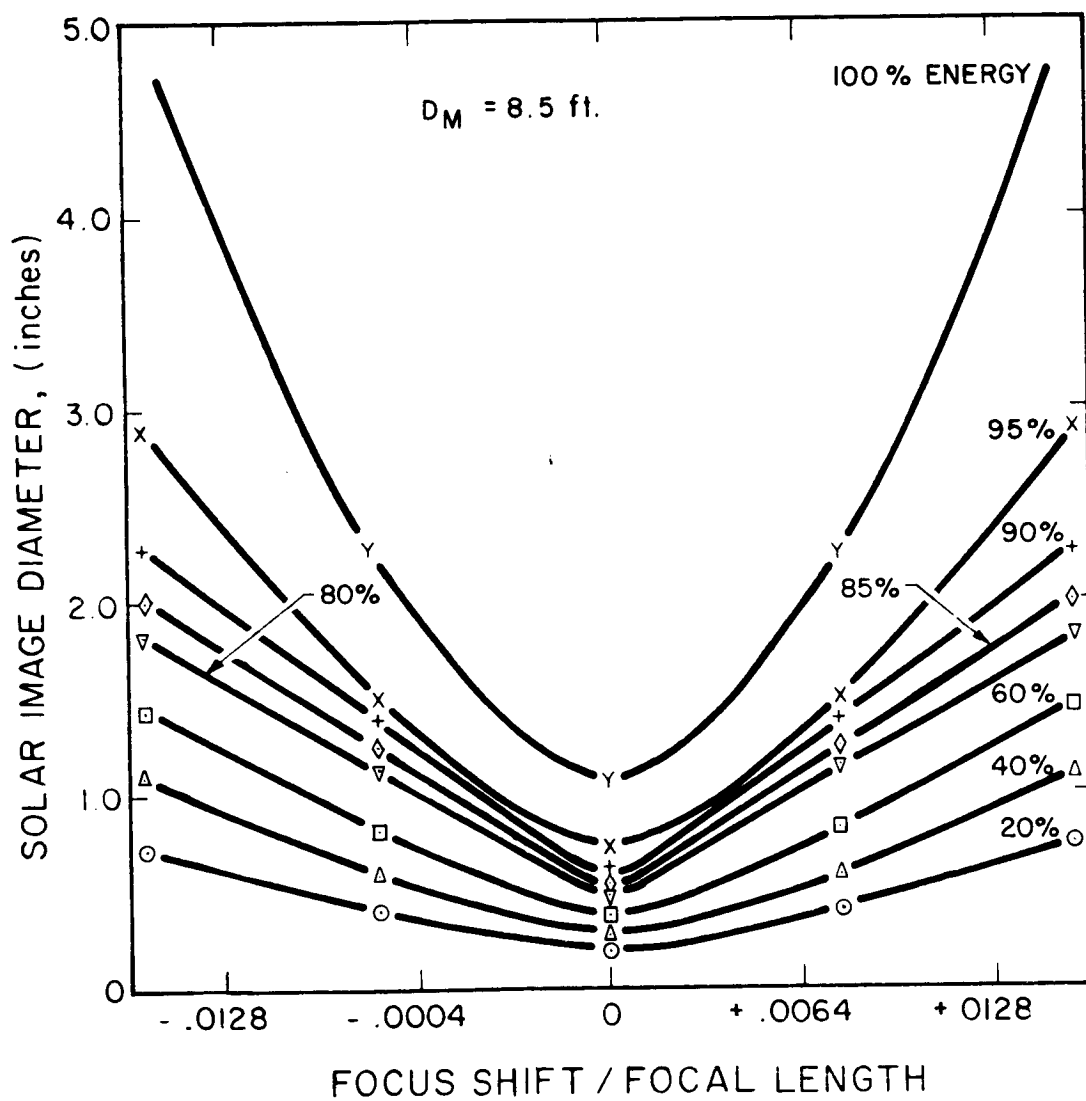


FIG. -17a SOLAR IMAGE DIAMETER VS FOCAL PLANE SHIFT FOR VARIOUS REFLECTED ENERGY LEVELS; A PERFECT  $60^\circ$  RIM ANGLE, CONCENTRATOR WITH NO MISORIENTATION

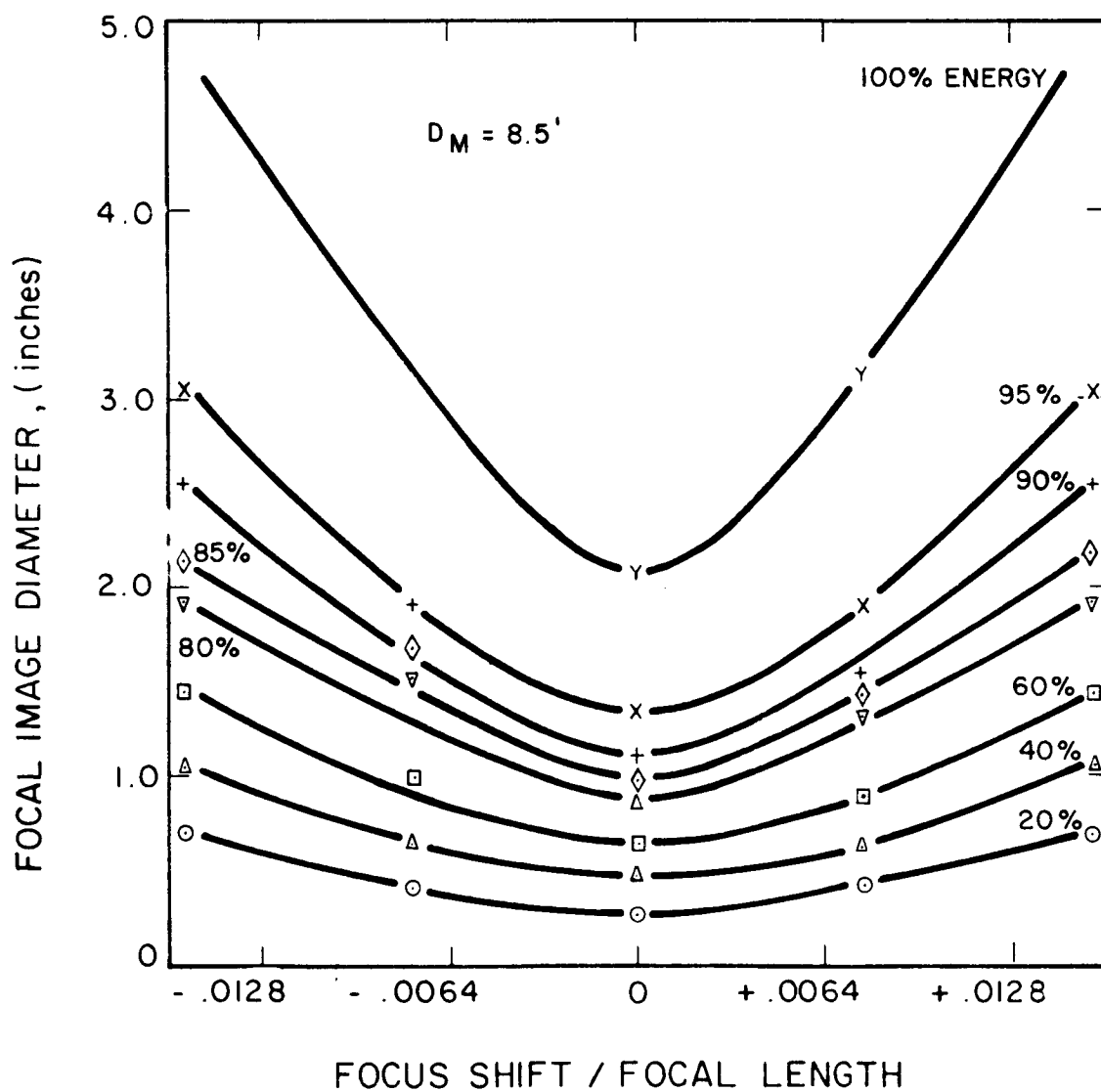


FIG. 3-17b SOLAR IMAGE DIAMETER VS FOCAL PLANE SHIFT FOR VARIOUS REFLECTED ENERGY LEVELS; A PERFECT CO RIM ARC, CONCENTRATOR WITH 16 MINUTES MIS-ORIENTATION



considered. Too often one or two of these types of surface errors are disregarded in the estimation of collector-absorber efficiency. Table 3-III illustrates several examples, and measurement techniques, with comments on these three types of surface errors. If the microscopic surface errors are disregarded, the surface reflectance is often overstated. If surface errors characteristics of macroscopic effects on a collector are neglected, the standard deviation of the collector surface is underestimated.

Microscopic surface errors cause diffuse reflection which results in a lower effective surface reflectance. These errors can result from optical polishing techniques, telegraphing of substrate defects, haziness of free-cast plastic surfaces such as occurs on spuncast masters, or micrometeorite degradation. Microscopic errors explain the difference between the expected collector reflectance (as determined from the reflectance of specially prepared coating samples) and the actual maximum cold calorimeter efficiency of the complete mirror.

Macroscopic errors are those which are individually visible to the unaided eye but which are very small compared with overall mirror dimensions. They can result from gross polishing defects, stress concentrations due to backing structure attachment, or ripples in the surface of plastic spun cast masters. These errors may easily escape notice in standard Hartmann or collimator tests because they may be small compared with the Hartmann spot of the beam from the collimator. These macroscopic errors increase the area of the reflected cone of light whereas the standard Hartmann test measures the displacement of the reflected cone center from the theoretical image point. As shown in Fig. 3-18 macroscopic errors are present when product  $ab$  is greater than the product  $a'b'$  where  $a$  and  $b$ ,  $a'$  and  $b'$  are the minor and major axes of the actual and theoretical images of the reflected light cone on the focal plane.

TABLE 3-III  
COLLECTOR REFLECTIVE SURFACE ERRORS

| <u>Type</u>    | <u>Examples</u>   | <u>Measurement Technique</u>   | <u>Comments</u>  |
|----------------|---|--|--|
| 1. Microscopic | Sleeks, scratches, fine scale orange peel, crazing, micrometeorite damage     | <ol style="list-style-type: none"> <li>1. Cold calorimeter,</li> <li>2. Extremely accurate reflectance measurements</li> <li>3. rms roughness measurement</li> </ol> | Difficult to measure except by calorimetric performance. (Generally the difference between expected reflectance and maximum cold calorimeter performance)      |
| 2. Macroscopic | Backing structure mark off, gross orange peel, short wavelength waviness      | <ol style="list-style-type: none"> <li>1. Precise Hartmann or collimator tests on a macroscale</li> </ol>  | Difficult to differentiate by standard Hartmann or collimator tests - error affects the diameter rather than the locus of the axis of the reflected light cone |
| 3. Long Wave   | Joint edge roll, master waviness residual internal stress, thermal distortion | <ol style="list-style-type: none"> <li>1. Hartmann test</li> <li>2. Collimator test</li> <li>3. Cold calorimeter</li> </ol>  | Easy to measure with Hartmann and collimator test. Error measured by the locus of the axis of the reflected light cone.  |

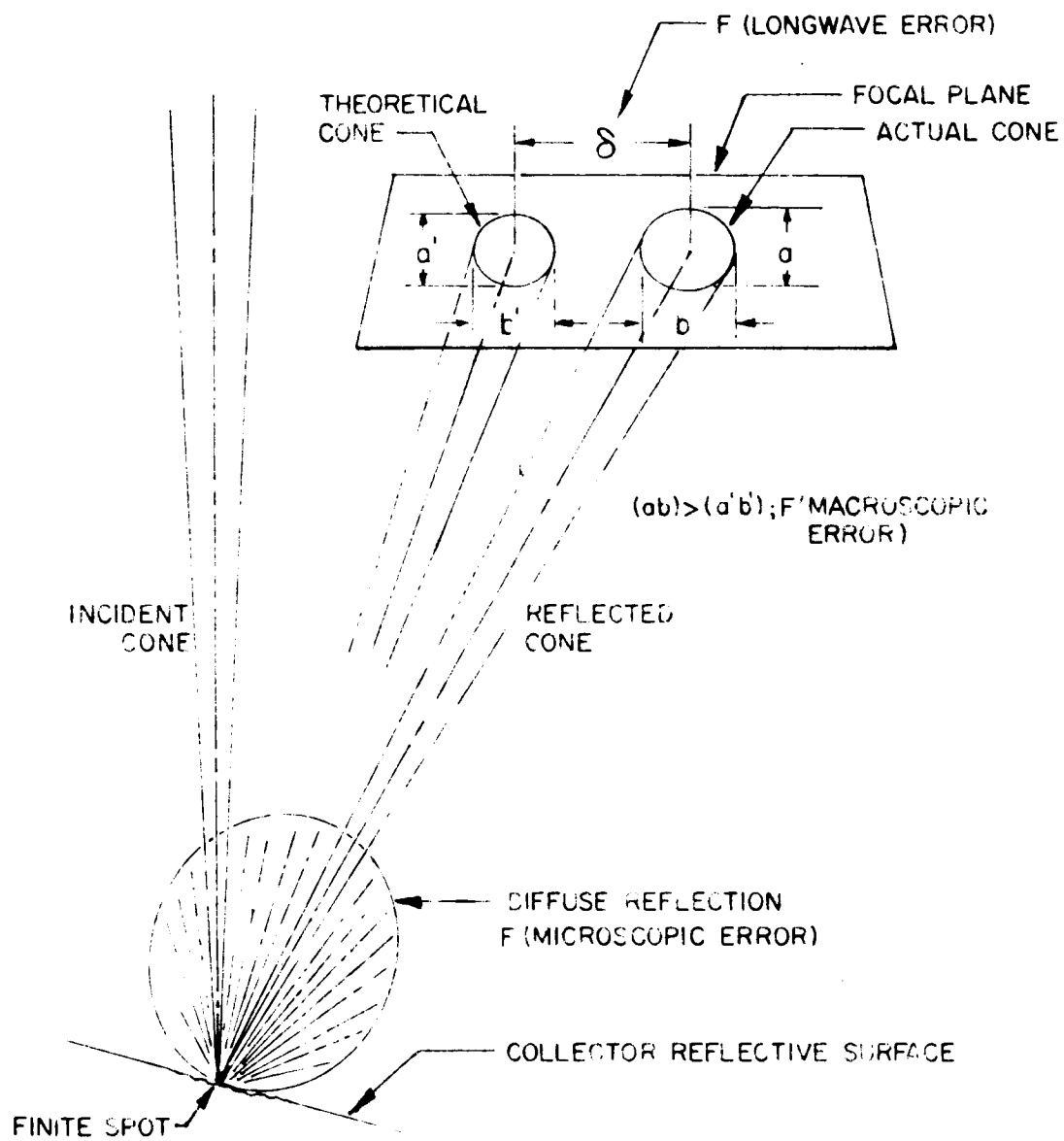


FIG. 1-13 COLLECTOR REFLECTIVE SURFACE ERRORS

Long wave errors are produced by overall collector fabrication errors, gross master distortion and residual or environmental stresses. These errors can be measured readily by Hartmann or collimator test methods.

#### 3.4.4 Misorientation

As shown in Fig. 3-11, small system misorientation (on the order of 15 minutes) does not effect mirror efficiency significantly. The losses are further examined in Figs. 3-19 and 3-20 for several cases of mirror surface error and cavity entrance diameter.

As discussed in Section 5, the loss of generator power drops off with misorientation much faster than mirror efficiency losses would indicate. This is due primarily to temperature distribution within the cavity, an effect far more serious than mirror efficiency losses.

#### 3.5 Thermal Effects

Collector-absorber efficiency is affected by the following temperature effects:

1. Ambient temperature changes of the collector and collector struts
2. Thermal gradient across and through the collector shell
3. Differential thermal expansion effects between the rigidizing torus and collector shell

To determine the transit orbital temperatures on the collector a computer program was written to include the following thermal sources:

1. Solar
2. Earth emission
3. Earth albedo
4. Cavity absorber reradiation
5. Radiator

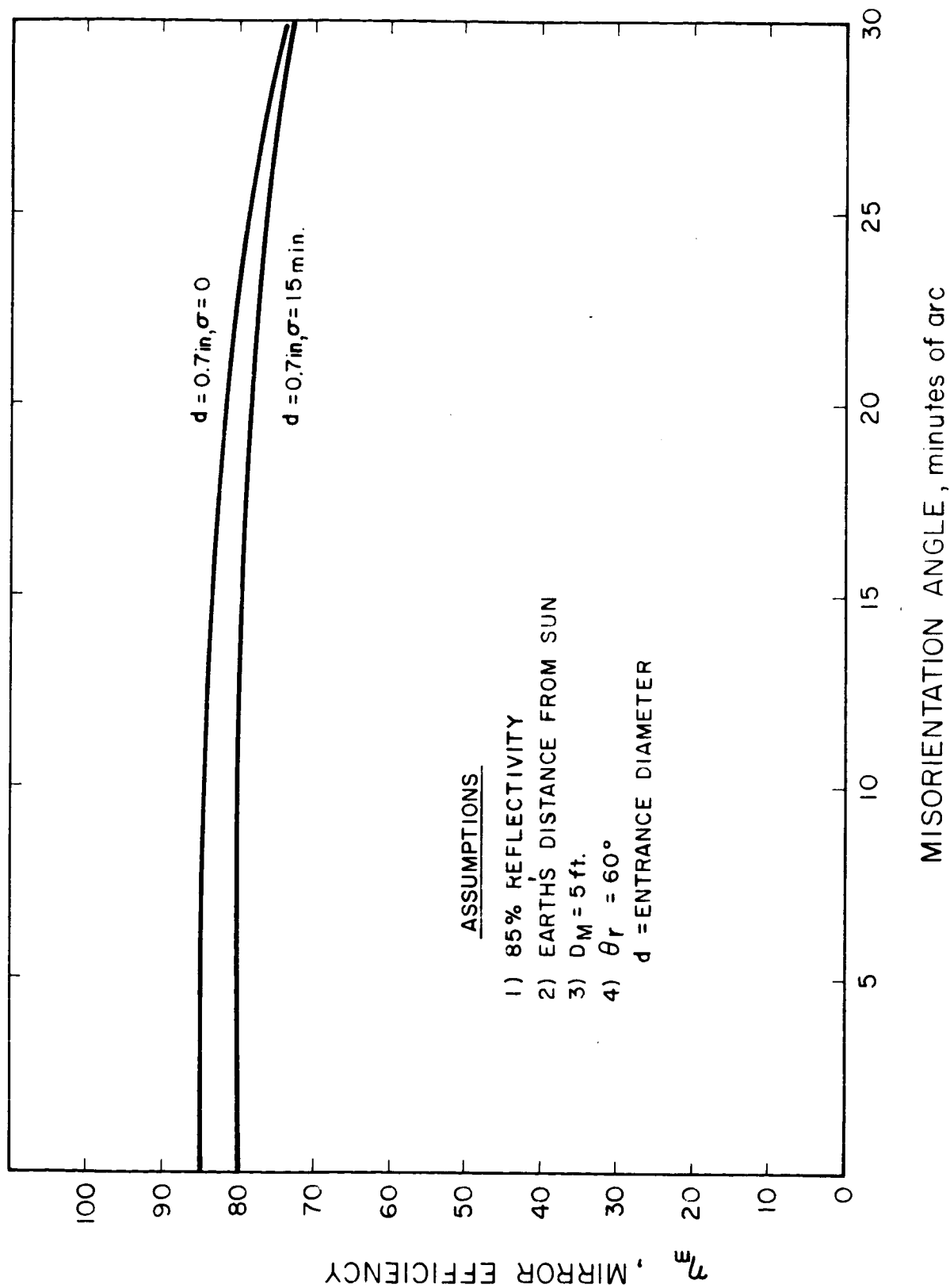


FIG. 1-13 TYPICAL MIRROR EFFICIENCY VS MISORIENTATION

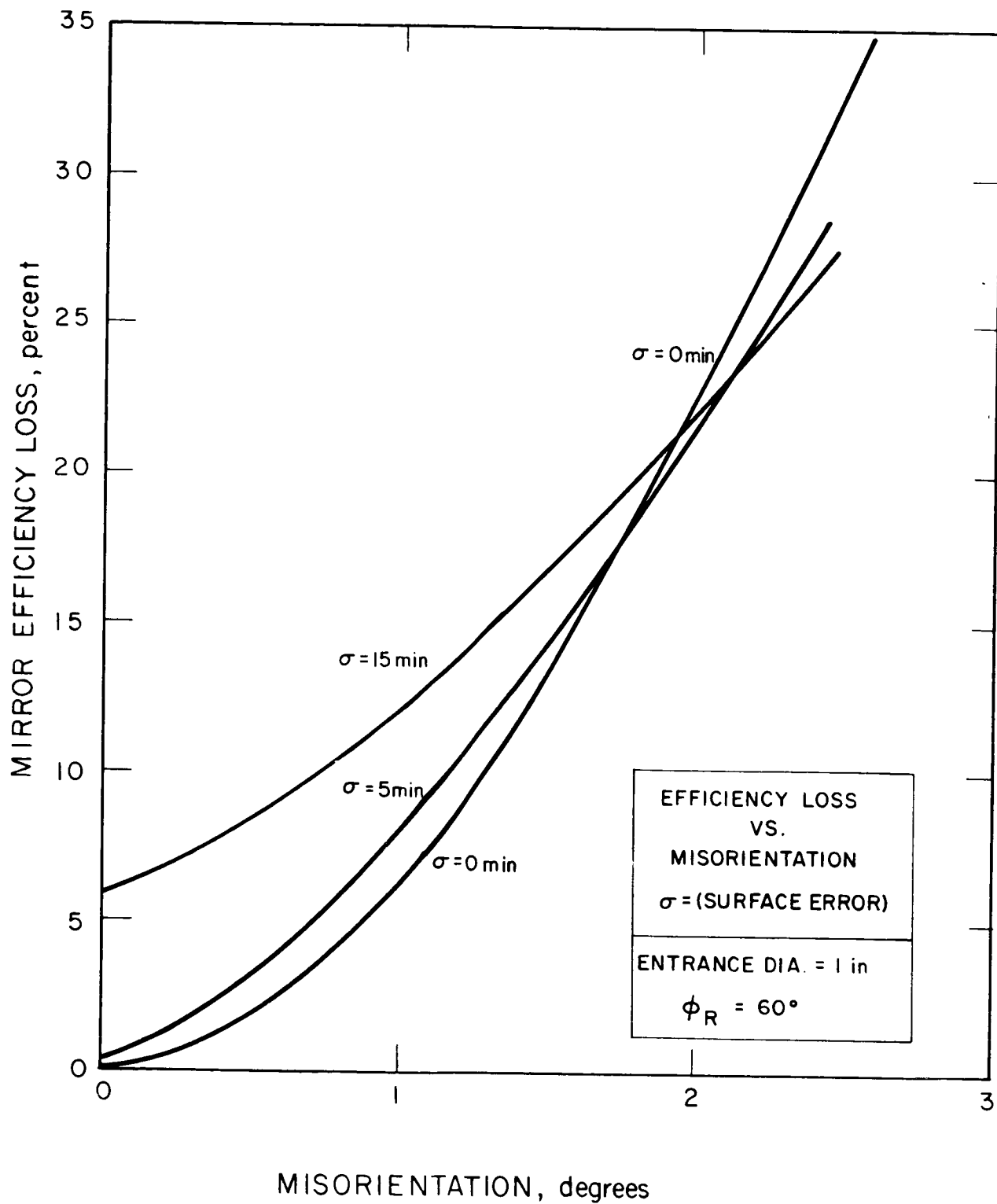


FIG. 1-20 TYPICAL MIRROR EFFICIENCIES VS MISORIENTATION

For simplicity the collector was divided into five different areas, one central area and four rim areas 90 degrees apart. Figure 3-21 shows the various temperature area locations. The input form factors for various thermal sources for a 300 mile equatorial orbit are shown in Figs. 3-22, 3-23, and 3-24. The heat transfer equation used, together with a summary of the constants, emissivities, and absorptivities is given in Table 3-IV. For the temperature calculations of the rim positions, the form factors were adjusted to take into account the variations in incidence angle with respect to all the thermal sources. Figures 3-25, 3-26, 3-27, and 3-28 show the transient temperatures of various surface points neglecting thermal conduction effects. Figure 3-29 shows the central collector temperatures for a 22,000 nautical mile orbit. With thermal conduction between the collector points the plotted temperatures are within 13 degrees centigrade. These analyses indicate that the collector shell temperatures will range from  $-82^{\circ}\text{C}$  to  $+44^{\circ}\text{C}$  during orbit.

Table 3-V depicts the steady state maximum temperature which might be obtained using various combinations of absorptivity and emissivity. A back surface emissivity of 0.9 would require a coating such as chemically deposited platinum black. The 0.3 emissivity value can easily be achieved by electroformed nickel. Coatings having an absorptivity and emissivity of 0.1 can be achieved by spraying chemically deposited silver on the back of the collector surface. A mirror emissivity of 0.02 is probably more realistic than an emissivity of 0.1 for the temperatures at which the collector operates. This change in emissivity counts for a maximum change of 87 degrees and a minimum change of 13 degrees.

Table 3-VI shows the difference in a rear-mounted torus and collector rim temperatures which might be achieved for various cases of absorptivity and emissivity, neglecting conduction effects between the torus and collector shell. Conduction would reduce the  $\Delta T$  by less than 10 percent. This indicates that with a highly emissive and

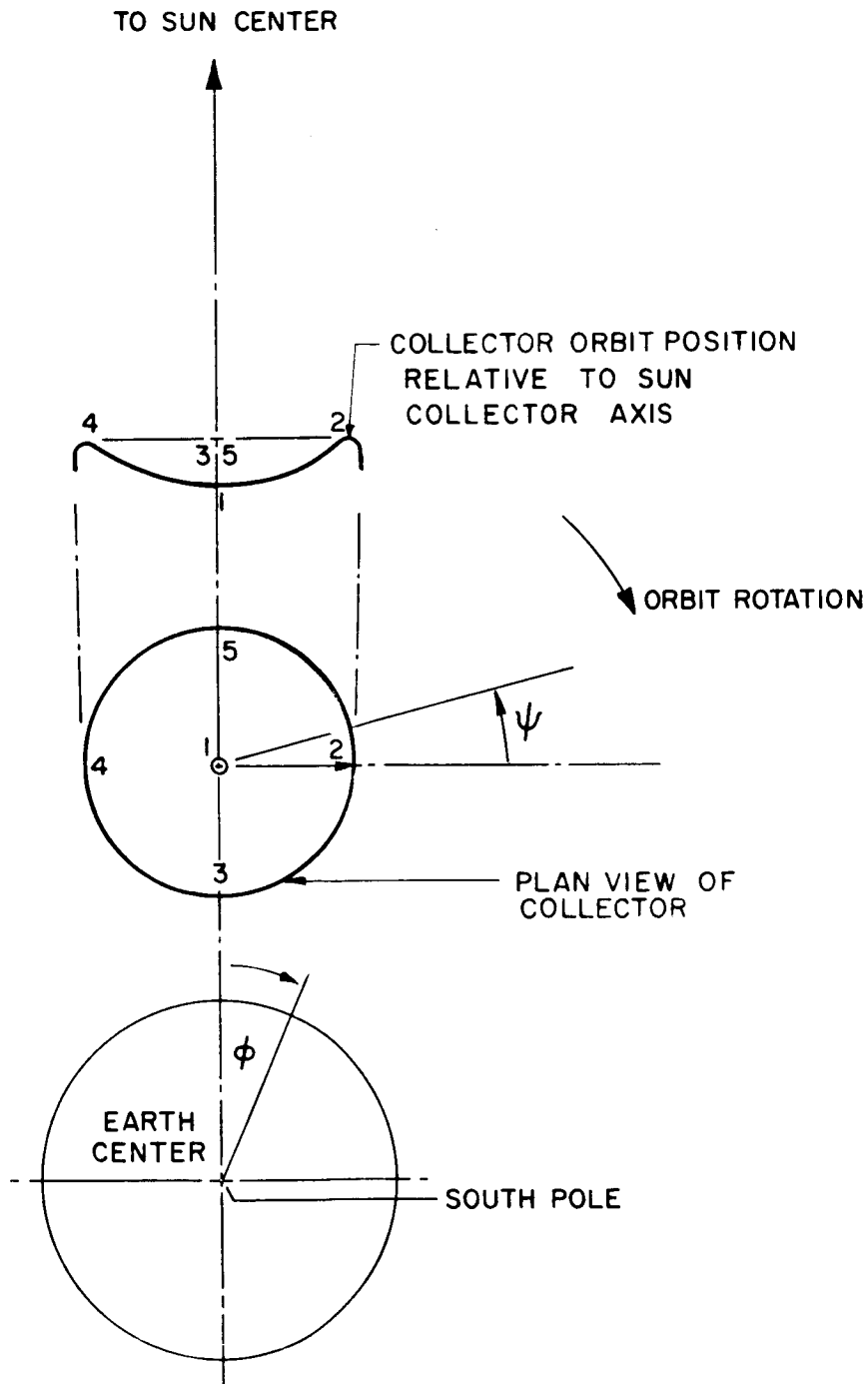


FIG. 3-21 LOCATION OF COLLECTOR TEMPERATURE  
COMPUTATION POINTS WITH RESPECT TO  
THE ORBIT ROTATION AND SUN-EARTH AXIS



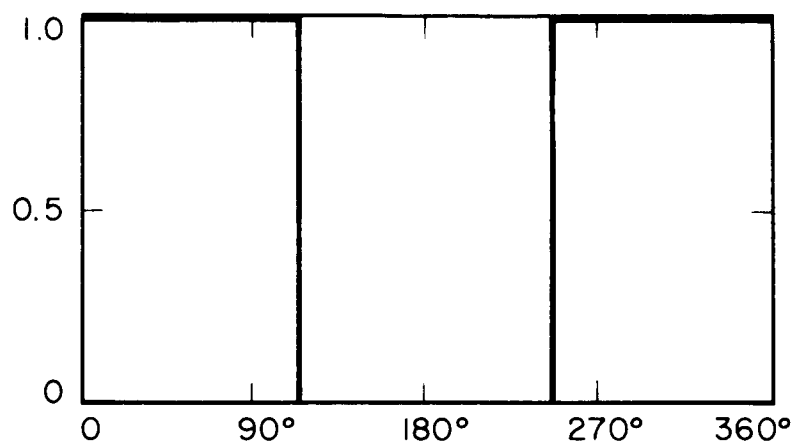


FIG. 22.  $F_{eb}(\phi)$  AND  $F_{em}(\phi)$  AS A FUNCTION OF  $\phi$

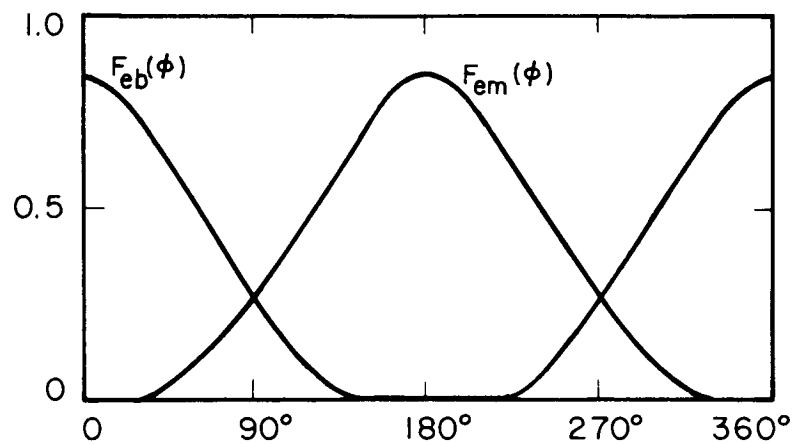


FIG. 23.  $F_{eb}(\phi)$  AND  $F_{em}(\phi)$  AS A FUNCTION OF  $\phi$

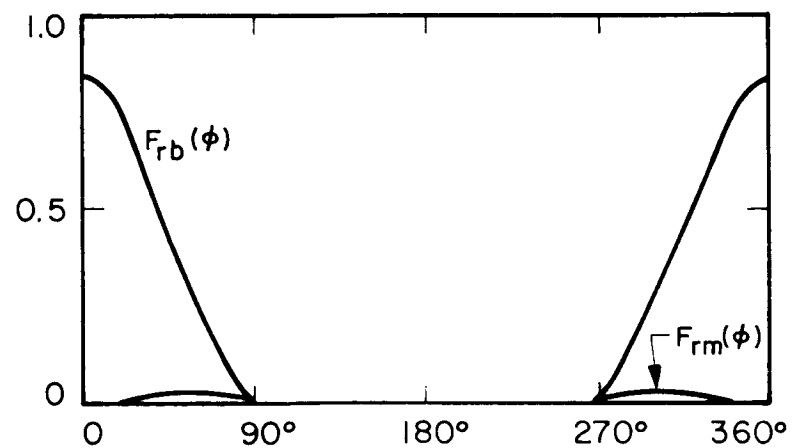


FIG. 24.  $F_{rb}(\phi)$  AND  $F_{rm}(\phi)$  AS A FUNCTION OF  $\phi$

500-KILOHERTZ EQUATORIAL ORBIT FORM FACTOR FUNCTIONS VS ORBIT ANGLE

TABLE 3-IV  
TEMPERATURE EQUATIONS, ASSUMPTIONS AND CONSTANTS

Equation

$$\frac{dT_m}{dt} = \frac{K_{11}}{K_{12}} \left[ -\sigma(F_{ma}e_{ra} + e_b)(T_m^4 - T_o^4) + \epsilon_{ms}H_sF_s(z) + H_e(F_{er}(z)\alpha_{me} + F_{eb}(z)\alpha_{be}) + A\epsilon_s\left(\epsilon_{br}F_{rb}(z) + \epsilon_{mr}F_{rm}(z)\right) + (F_a(z)F_d\alpha_{da} + (T_d^4 - T_m^4) + F_d\sigma\epsilon_d(T_d^4 - T_m^4)) \right]$$

Assumptions and Constants

$K_{11} = \frac{\text{orbit time}}{3600} = 0.00443 \text{ hr}^{\circ}$  and  $0.0783/\text{hr}^{\circ}$  for 300 and 22,000 nautical miles respectively

$K_{12} = \text{cpt}$

$c = 0.11 \text{ Btu/lb}^{\circ}\text{F}$

$\rho = 46.1 \text{ lb/in}^2\text{-ft}^2$

$t = 0.0107 \text{ in}$

$\sigma = 0.1713 \times 10^{-8} \text{ Btu/hr}^{\circ}\text{ft}^2\text{-}^{\circ}\text{R}^4 = 5.672 \times 10^{-8} \text{ w/m}^2 (\text{}^{\circ}\text{K})^{-4}$

$F_{ma} = 1.0$

$\epsilon_m = \alpha_{ms} = \alpha_{me} = \epsilon_{mr} = \alpha_{ma} = \epsilon_{md} = 0.1$

$\epsilon_b = \alpha_{be} = \epsilon_{br} = 0.9$

$T_m = T_b = \text{unknown of the equation}$

$T_o = 0^{\circ}\text{K}$

$H_s = 442.7 \text{ Btu/hr}^{\circ}\text{ft}^2 = 130 \text{ w/ft}^2$

$H_e = 74.4 \text{ Btu/hr}^{\circ}\text{ft}^2 = 21.8 \text{ w/ft}^2$

$A = 0.35$

$F_a = \text{absorber-collector view factor}$

$T_d = 900^{\circ}\text{C}$

$F_d = \text{radiator-collector view factor}$

$T_d = 900^{\circ}\text{R}$

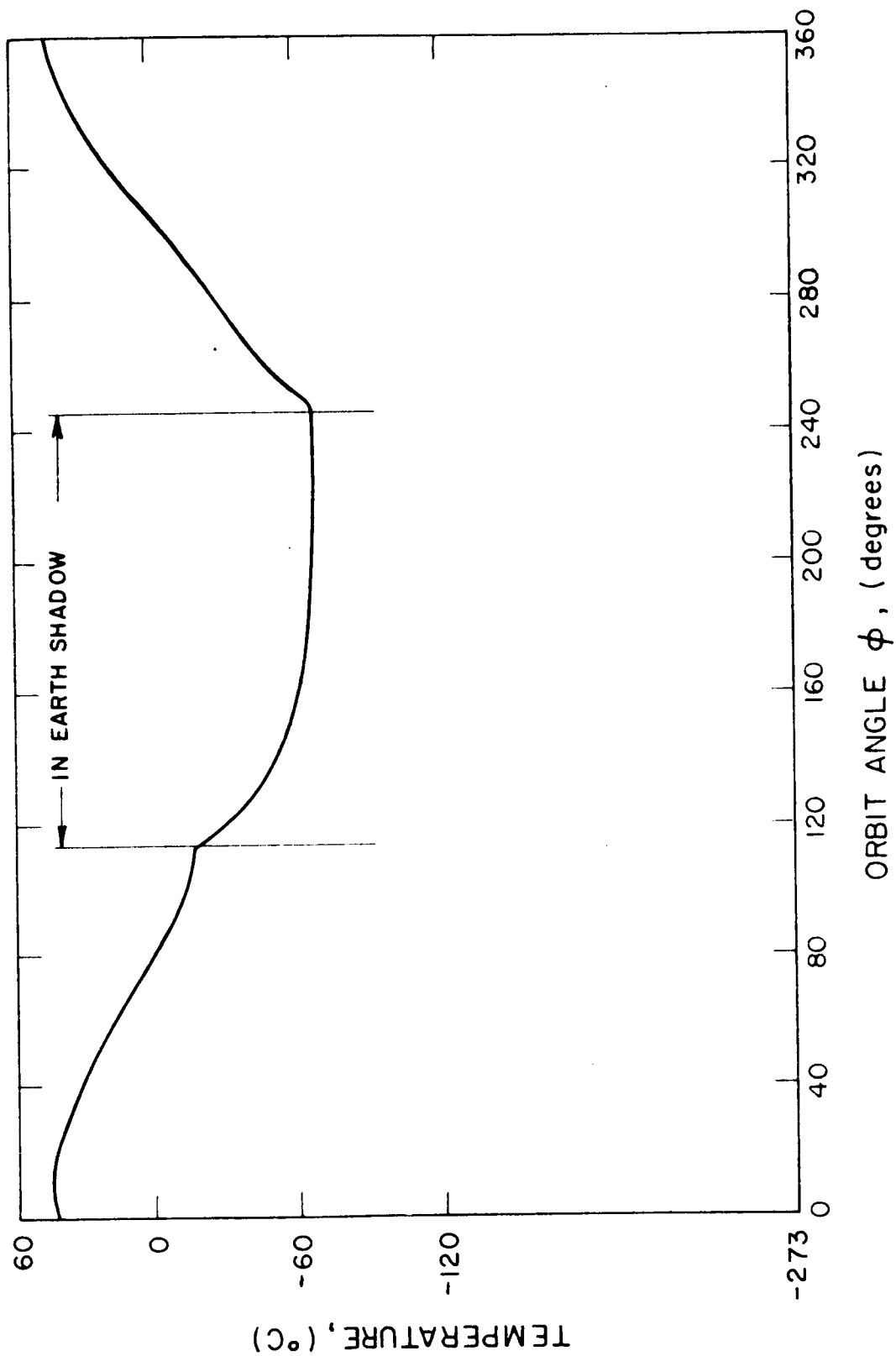


FIG. 10. TEMPERATURE, CENTRAL COLLECTOR SURFACE, TEMPERATURE FOR A 300-NAUTICAL-MILE ORBIT

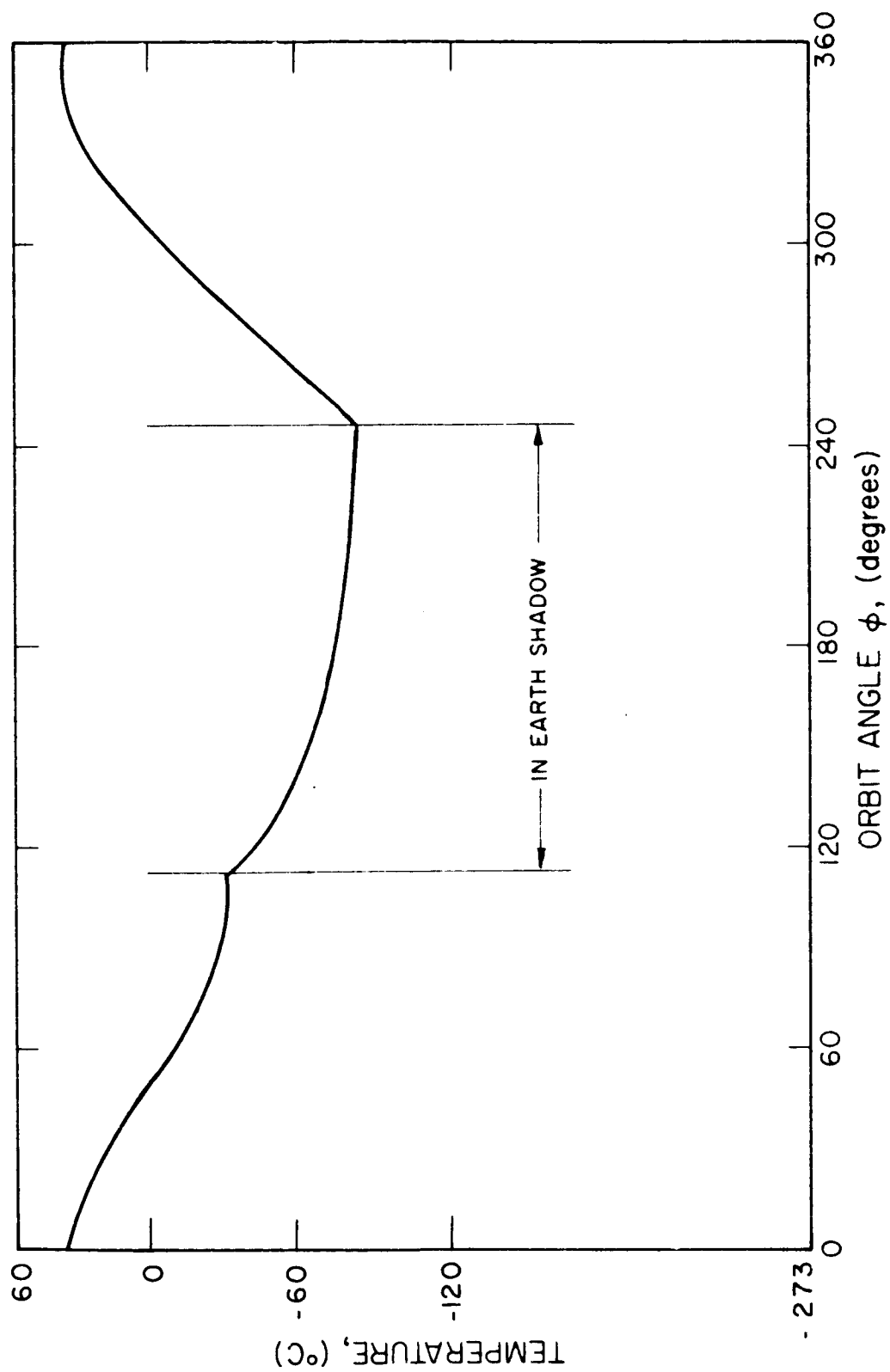


FIG. 1-26. POLAR, COLLECTOR SURFACE TEMPERATURES,  $\psi = 0^\circ$ , FOR 100-KM ALT CIRCULAR ORBIT

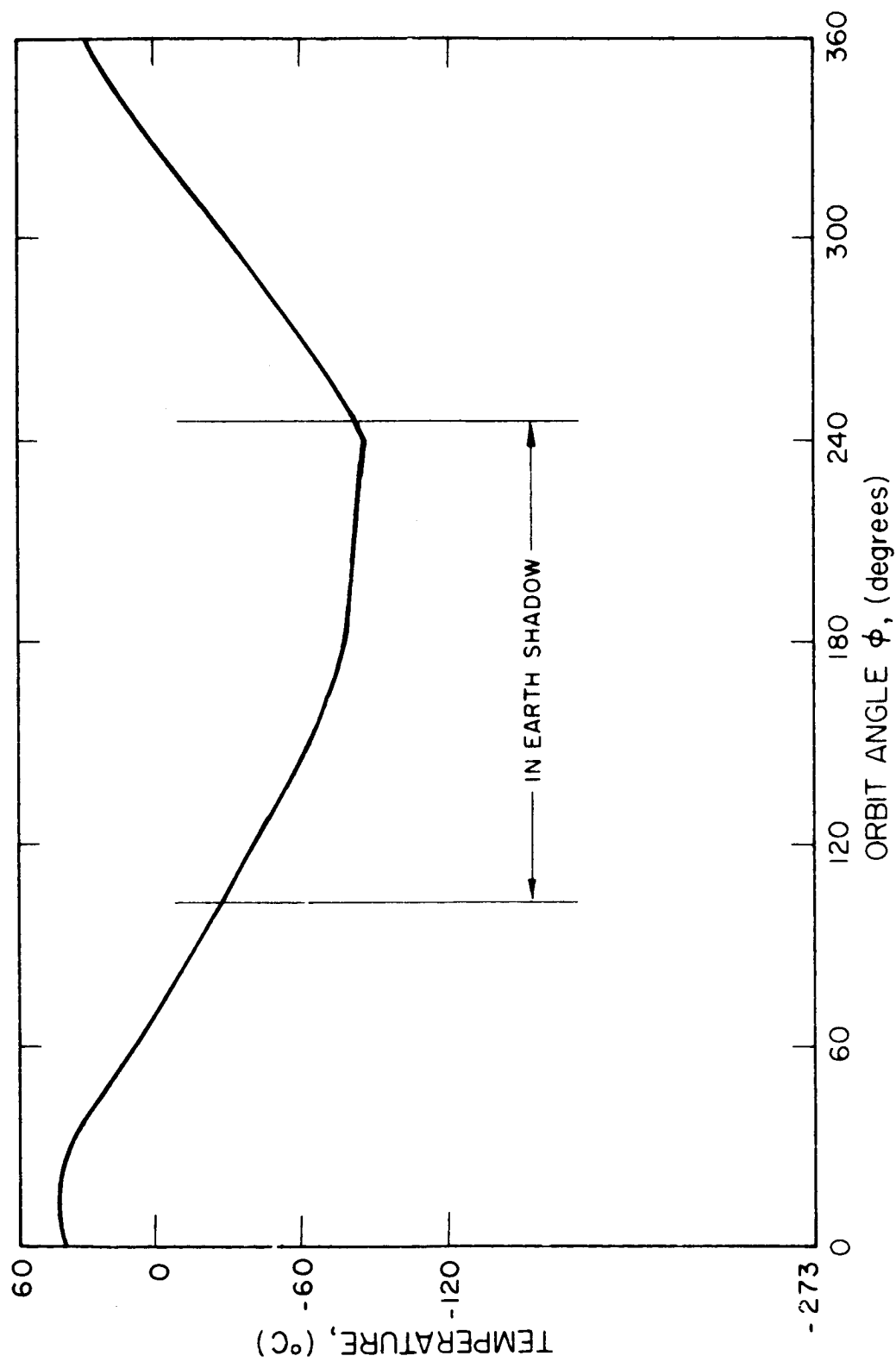


FIG. 4-27 POINT 3 AND 5, COLLECTOR SURFACE TEMPERATURES,  $\theta = \pm 90^\circ$ , FOR A 300-NAUTICAL-MILE ORBIT

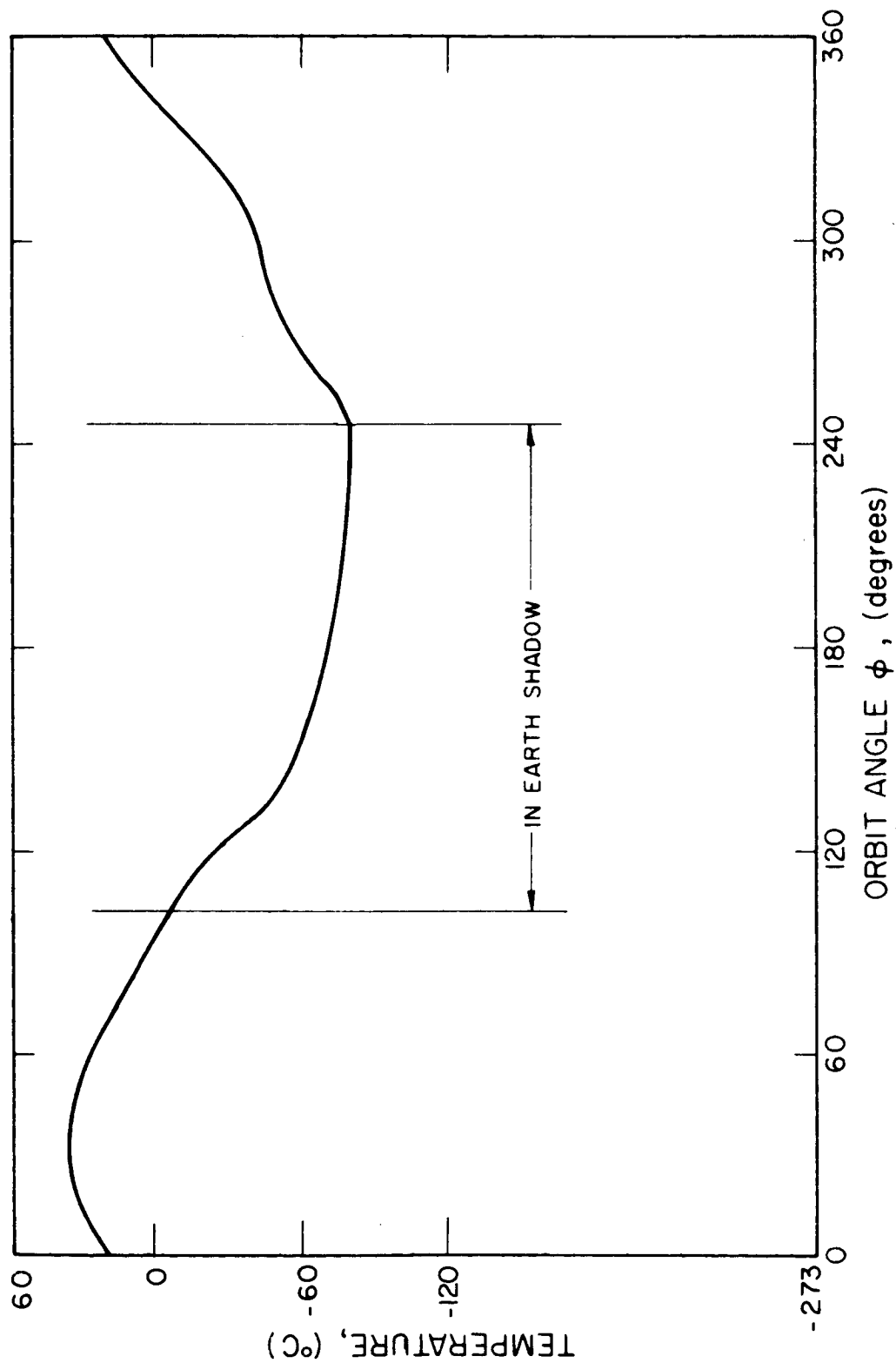


FIG. 1-28 POINT 1, COLLECTOR SURFACE TEMPERATURES,  $\phi = 150^\circ$ , FOR A 300-NAUTICAL-MILE ORBIT

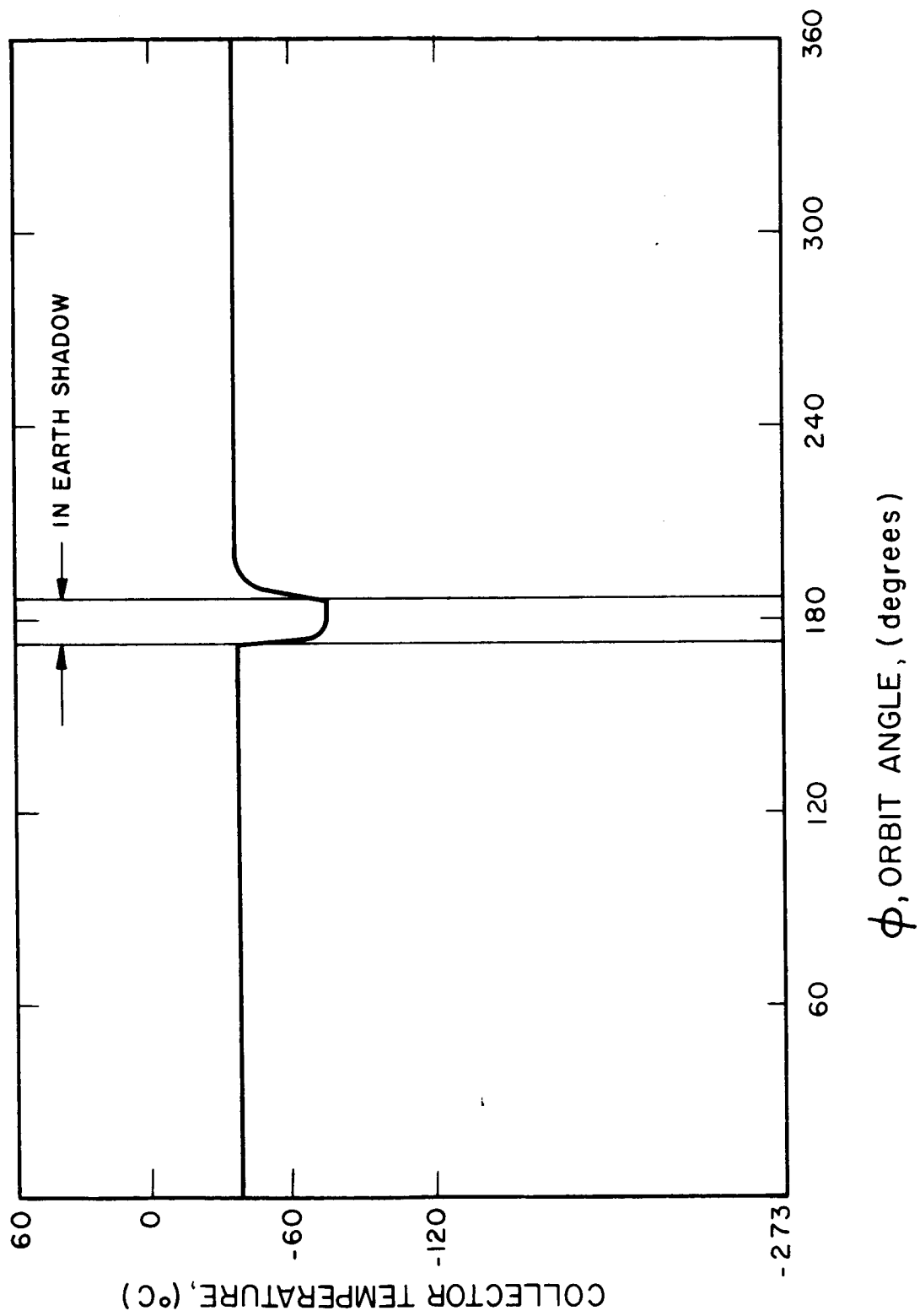


FIG. 1-29 CENTRAL COLLECTOR TEMPERATURE VS  $\phi$  FOR A 22,600-KM ALT CIRCULAR ORBIT

TABLE 3-V  
STEADY STATE MAXIMUM COLLECTOR SHELL TEMPERATURE

| $\alpha_m$ | $\alpha_b$ | $\epsilon_m$ | $\epsilon_b$ | $T_m$<br>°C |
|------------|------------|--------------|--------------|-------------|
| 0.1        | 0.9        | 0.1          | 0.9          | 52          |
| 0.1        | 0.3        | 0.1          | 0.3          | 70          |
| 0.1        | 0.1        | 0.1          | 0.1          | 90          |
| 0.1        | 0.9        | 0.02         | 0.9          | 67          |
| 0.1        | 0.3        | 0.02         | 0.3          | 90          |
| 0.1        | 0.1        | 0.02         | 0.1          | 139         |

Equation:

$$T_m = \left[ \frac{H\phi_m + AH\phi_b + F_{eh}(\phi)_{\max} H\epsilon_b}{\bar{\epsilon}(\epsilon_m + \epsilon_b)} \right]^{1/4}$$

See Table 3-IV and Fig. 3-23 for unspecified constants



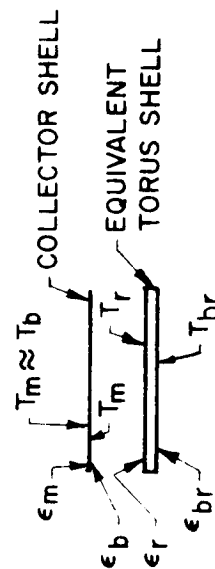
TABLE 3-VI  
COLLECTOR - SHELL-TORUS TEMPERATURE DIFFERENTIALS

| $\epsilon_m$ | $m$  | $b$ | $\epsilon_r$ | $\epsilon_{br}$ | $\Delta T_{m-r}$<br>(°C) |
|--------------|------|-----|--------------|-----------------|--------------------------|
| 0.1          | 0.02 | 0.9 | 0.9          | 0.9             | 45                       |
| 0.1          | 0.02 | 0.9 | 0.9          | 0.9             | 22                       |
| 0.1          | 0.02 | 0.9 | 0.9          | 0.9             | 5                        |

Equation:

$$\Delta T_{m-r} = \frac{H \gamma \cos \theta}{s_m} \left[ 1 - \left( \frac{1}{\epsilon_{br} + \frac{1}{\frac{\epsilon_b \epsilon_r}{\epsilon_r + (1 - \epsilon_r) \epsilon_b}}} \right)^{1/4} \right]$$

where  $Z = \frac{\epsilon_b \epsilon_r}{\epsilon_r + (1 - \epsilon_r) \epsilon_b}$



$$T_r \approx T_{br}$$

Diagram of shell torus radiation model

absorptive coating between the collector shell rim and torus and low absorptive and emissive coatings on the front of the collector shell and rear of the torus, a temperature difference of less than  $5^{\circ}\text{C}$  can be achieved between the collector rim and the collector torus. The desirability of such a low temperature difference and therefore low back and front surface emissivities and absorptivities will be shown in the thermal error analysis below.

Estimated thermal maps derived from the collector surface points are shown in Fig. 3-30 for various orbit positions.

#### Ambient Temperature Effects

The total change in the ambient temperatures from the original alignment temperature is less than  $144^{\circ}\text{C}$  under any conditions. Based on a  $\Delta T$  of  $144^{\circ}\text{C}$  the net change in the focal point due to the change in strut length, mirror expansion, and focal length change is less than 0.05-inch for a 10-foot mirror. This axial misalignment would result in an efficiency loss of less than 1/2 percent. Localized transient temperature differences on the collector shell will produce even smaller efficiency losses due to the smaller incremental  $\Delta T$ .

#### Collector Shell Thermal Gradient

Based on a maximum heat flux of which is appropriately conservative, considering the 0.09 absorptivity of the collector for solar and earth albedo radiation and less for other radiation, a temperature gradient of less than  $0.09^{\circ}\text{C}$  per inch would be produced through the collector shell thickness. If the moment resulting from this temperature gradient is not resisted by a moment at the rim, a maximum error of 0.23 minutes would be produced at the rim. Such a thermal gradient would create a moment of 0.32 lbs/in per lineal inch at the collector rim. The application of an opposite moment at the edge of an equivalent sphere (Timoshenko, Ref. 3-1) neglecting cancellation effects of the thermal moment, would reduce the effective collector area by as much as 3 to 4 percent due to gross distortions of

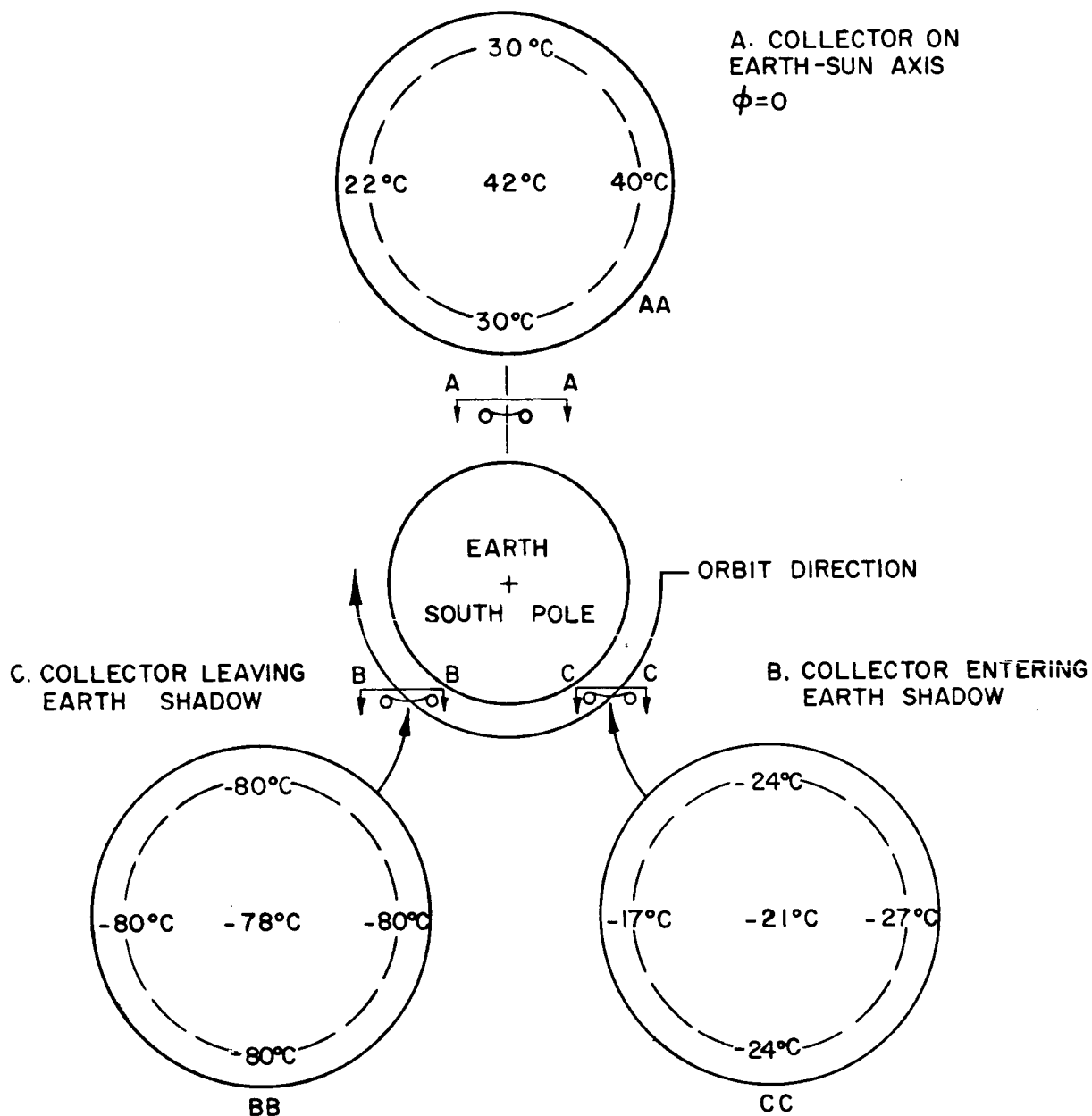


FIG. 1-20 COLLECTOR SHELL TEMPERATURE FOR 3 ORBIT POSITIONS FOR A 300-NAUTICAL-MILE ORBIT BASED ON RESULTS TABULATED IN FIGS. 1-2 THROUGH 1-26

the rim edge. The fact that a restorative moment cancels the thermal gradient moment at the edge lowers the distortion area considerably. Reference 3-2 describes a rigorous thermal analysis of a 9.75-foot diameter all-nickel toroidally supported collector. However, the results of this analysis are not readily adaptable to other diameter collectors because they do not scale with diameter. A computer solution must be developed. Additional work in the collector thermal response area should include a computer analysis using this referenced work.

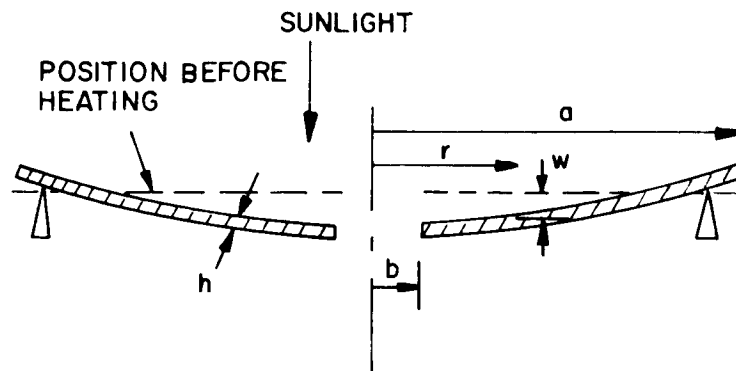
#### Differential Thermal Expansion Effects

Differences between the torus temperature and the integrated shell temperature will result in a differential thermal expansion between the shell and torus. Assuming an entirely rigid connection between these two elements, this difference will cause an edge displacement which would result in shell rim distortions. Using Timoshenko (Ref. 3-1) for an equivalent spherical cap, the maximum area that would be affected by a 9 degree temperature difference would result in a loss of less than 1.7 percent of the collector area due to gross distortion. This analysis, based on a rigid torus acting on a spherical cap, is conservative. The edge effects from the thermal gradient and torus-collector thermal expansion are not additive. In practice an area less than 2 percent of the total area might be affected by the thermal gradient and differential thermal expansion.

An approximate calculation of mirror deflection due to heating by solar radiation is given below:

Assume:

1. Flat plate approximation
2. Temperature is uniform throughout mirror skin when mirror is heated uniformly by sunlight
3. A linear temperature gradient exists through the thickness of the skin
4. Boundary conditions assume a simple support for the outer radius and a free inner radius.



Reference: Newman and Fanay, "Bending Stresses Due to Temperature in Hollow Circular Plates, Part III," Journal of the Aero/Space Sciences, Vol. 27, No. 12, pp. 951-952, December 1960  
per reference; where

$$\frac{wh}{\alpha T_D b^2} = \left( \frac{\frac{r^2}{b^2} - 1}{2} \right)$$

$T_D$  = temperature of the upper face minus temperature of the lower face  
 $\alpha$  = coefficient of linear expansion

Since  $w$  is the deflection which varies as  $r$ , the induced deflection angle,  $\theta$  =

$$\tan \theta = \frac{w}{r} = \frac{T_D b^2}{2\alpha} \left( \frac{2r}{b^2} \right)$$

$$\tan \theta_{\text{edge}} = \frac{T_D r}{\alpha h}$$

This illustrates that deflection is greatest at the edge of the mirror. Assuming that an average  $\theta$  can be expressed.

$$\text{av. } \sigma = \frac{\int \sigma A}{\int A} = \frac{\int_0^a \frac{\sigma T_D}{h} r \cdot 2\pi r dr}{\pi a^2}$$

$$\text{av. } \sigma = \frac{\sigma T_D}{h} \cdot \frac{2}{3}a$$

For nickel: coefficient of expansion  $\approx 14 \times 10^{-6} \text{ } ^\circ\text{C}^{-1}$   
 thermal conductivity  $\approx 0.14 \frac{\text{cal}}{\text{sec } ^\circ\text{C cm}}$   
 $\approx 0.585 \frac{\text{w}}{^\circ\text{C cm}}$

For aluminum: coefficient of expansion  $\approx 26 \times 10^{-6} \text{ } ^\circ\text{C}^{-1}$   
 thermal conductivity  $\approx 0.5 \frac{\text{cal}}{\text{sec } ^\circ\text{C cm}}$   
 $\approx 2.09 \frac{\text{w}}{^\circ\text{C cm}}$

Calculation of  $T_D$

Sunlight  
 $Q_s$

reflected  
 $Q_r$

reradiated  
 $Q_f$

$Q_R$   
 reradiated

$$Q_s = H \cdot A_{\text{mirror}}$$

where

H = solar constant

$$Q_s = Q_r + Q_f + Q_R$$

$$(Q_s = Q_r) = Q_f + Q_R$$

$$Q_f = \sigma T_{\text{mirror}}^4 A_{\text{mirror}} = \epsilon_f$$

where

$\epsilon_f$  = emissivity of the front surface

$\epsilon_R$  = emissivity of the rear surface

$$Q_R = \sigma T_{\text{mirror}}^4 A_{\text{mirror}} \epsilon_R$$

An approximate formula for  $T_D$

$$Q_R = (Q_s - Q_r) - Q_f = \frac{\pi A T_D}{h}$$

where

$\pi$  = thermal conductivity

A = area

assume unit area

$$Q_R \left(1 + \frac{\epsilon_f}{\epsilon_R}\right) = Q_s - Q_r$$

$$T_D = \frac{h}{\pi} \left( \frac{(Q_s - Q_r)}{\left(1 + \frac{\epsilon_f}{\epsilon_R}\right)} \right)$$

Therefore

$$w = \frac{\left(\frac{r^2}{b^2} - 1\right)}{2} \cdot ab^2 \cdot \frac{1}{\epsilon} \cdot \frac{(Q_s - Q_r)}{\left(1 + \frac{\epsilon_f}{\epsilon_R}\right)}$$

$$\theta = r \cdot \frac{(Q_s - Q_r)}{\left(1 + \frac{\epsilon_f}{\epsilon_R}\right)}$$

Assume 0.010-inch nickel skin and a 10-foot mirror

$$\epsilon_f = 0.1, \epsilon_R = 0.9, (Q_s - Q_r) = (0.15) (0.14) w / \text{cm}^2$$

then

$$a = 5\text{-foot}$$

$$\theta = 0.2375 \text{ minute of arc}$$

$$\text{av. } \theta = 0.159 \text{ minute of arc}$$

$$T_D = \frac{10^{-2} \cdot (2.54)}{(0.585)} \cdot \frac{(0.15) (0.14)}{1.11} = 0.0008^\circ \text{C}$$

Assume a 0.010-inch aluminum skin,  $a = 5\text{-foot}$ ,  $\epsilon$ 's are the same

$$\theta = (0.1238 \text{ min. of arc})$$



### 3.6 Structural Aspects

This section deals with the design limits imposed on concentrator structures by various environmental and material conditions.

The subjects are:

1. Weight
2. Membrane stresses imposed by acceleration along the axis and the chances of exceeding material yield levels
3. Compressive buckling as a function of axial acceleration
4. Lateral acceleration effects
5. Shock
6. Aconstical vibration
7. The effects of earth tests

#### 3.6.1 Concentrator Weight

The weight of the concentrator is composed of the skin, torus support, attachments, torus-skin webbing and other components depicted in Fig. 3-1. The specific weight of the concentrator is usually expressed in terms of total pounds per foot<sup>2</sup> of frontal surface area.

The weight of the concentrator is shown in Fig. 3-31 as a function of specific weight and diameter. Also shown are examples of the weight of concentrators fabricated to date.

The state of the art in solar concentrators is limited. Very little optimization of concentrator skin or support has occurred. It is anticipated that specific weights of 0.5 to 0.3 lb/foot<sup>2</sup> can be achieved depending on fabrication technique. The structural analysis presented in this text confirms that no inherent structural limit exists which prevents low specific weights. The primary obstacle is the need to improve manufacturing techniques and the ability to form lightweight, accurate structures.

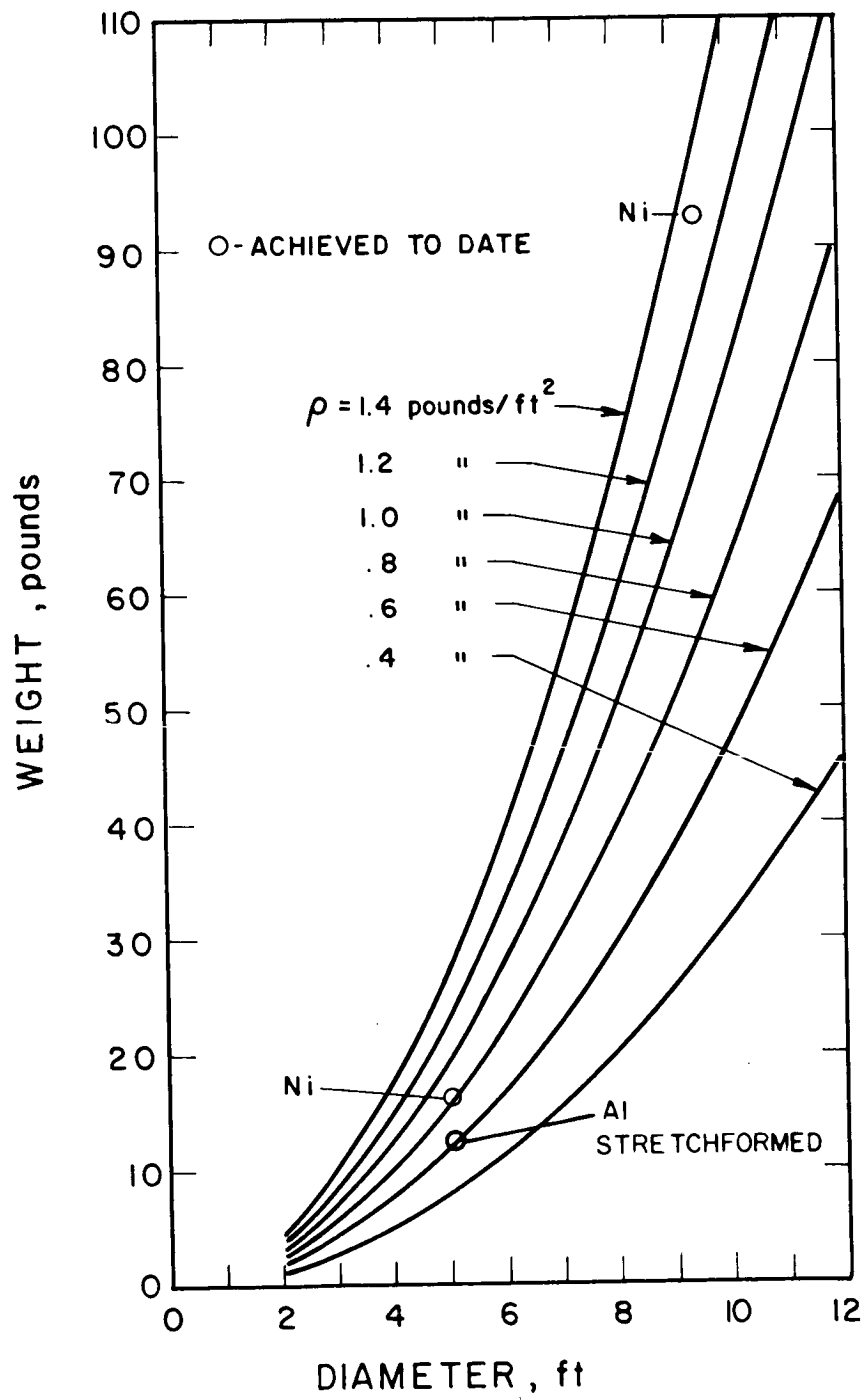
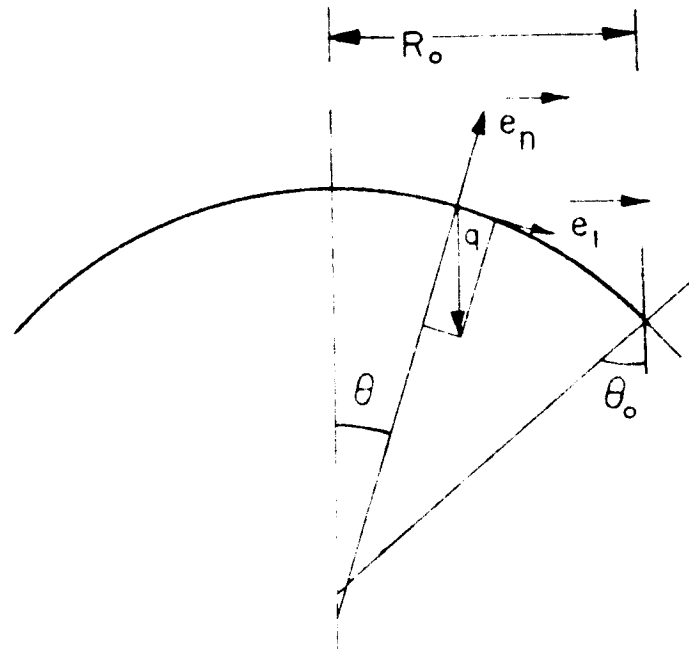


FIG. 3-51 MIRROR DIAMETER VS WEIGHT

### 3.6.2 Membrane Stresses

This section examines the membrane stresses in the skin due to axial loading. Assume the following model



where  $q$  is the unit area shell load:

$$q = \rho g t n$$

and  $q_1$  and  $q_n$  the meridional and normal components:

$$q_1 = q \sin \theta$$

$$q_n = -q \cos \theta$$

and  $R_1$  and  $R_2$  the meridional and hoop radii:

$$R_1 = \frac{2f}{\cos^3 \alpha}$$

$$R_2 = \frac{2f}{\cos \alpha}$$

The acceleration in g's is denoted by n.

From Novoshilov (Ref. 3-5) for a parabolic shell the meridional and hoop forces per lineal inch  $T_1$  and  $T_2$  are:

$$T_1 = -\frac{2qf}{3} \left[ \frac{1}{\cos^2 \alpha} + \frac{1}{1 + \cos \alpha} \right]$$

$$T_2 = -wqf \left[ 1 - \frac{1}{3} \left( 1 + \frac{\cos^2 \alpha}{1 + \cos \alpha} \right) \right]$$

The meridional and hoop stresses are respectively:

$$\sigma_1 = \frac{T_1}{t}$$

$$\sigma_2 = \frac{T_2}{t}$$

or

$$\sigma_1 = -\frac{2}{3} \rho g f n \left[ \frac{1}{\cos^2 \alpha} + \frac{1}{1 + \cos \alpha} \right]$$

$$\sigma_2 = -\frac{2}{3} \rho g f n \left[ 2 - \frac{\cos^2 \alpha}{1 + \cos \alpha} \right]$$

Therefore at the apex,  $\alpha = 0$ , these stresses are: (for nickel)

$$\sigma_1(0) = \sigma_2(0) = 49n \text{ lb/in}^2$$

For a spherical shell covering the same area and having the same height the meridional and hoop stresses are:

$$\sigma_1 = -\rho g n R_o \frac{1}{1 + \cos \theta}$$

$$\sigma_2 = -\rho g n R_o (\cos \theta) - \frac{1}{1 + \cos \theta}$$

Figure 3-32 shows the summary of membrane stresses for the parabolic shell and the spherical approximation for  $\theta$  from 0 to 30 degrees, where  $\theta$  is the angle between the collector axis and radius of curvature. This figure shows that the spherical approximation to the parabolic shell is a fairly good approximation and can be used without significant error. The relatively low stresses per g indicate that the tensile stresses will be less than 570 lb/sq in. for a maximum 10g axial acceleration given in the environmental specifications. However, since the collector shell has a high radius of curvature to thickness ratio a careful investigation of compressive buckling stresses is required.

### 3.6.3 Compressive Buckling Stress

In considering the buckling of the collector subjected to an acceleration during launch along the axis of revolution, it will be assumed that a one g acceleration is equivalent to an external pressure given by the following,

$$p = 1g \rho t = 0.32t \text{ lb/in}^2 \text{ (for Ni)}$$

The buckling pressure of a complete spherical shell under external pressure is given by the following equation,

$$P_{c1} = \frac{2}{\sqrt{3(1-\nu^2)}} E \left( \frac{t}{R} \right)^2$$

where R is the radius of the sphere;  $R = 2f \left( 1 + \frac{R_o^2}{16f^2} \right)$

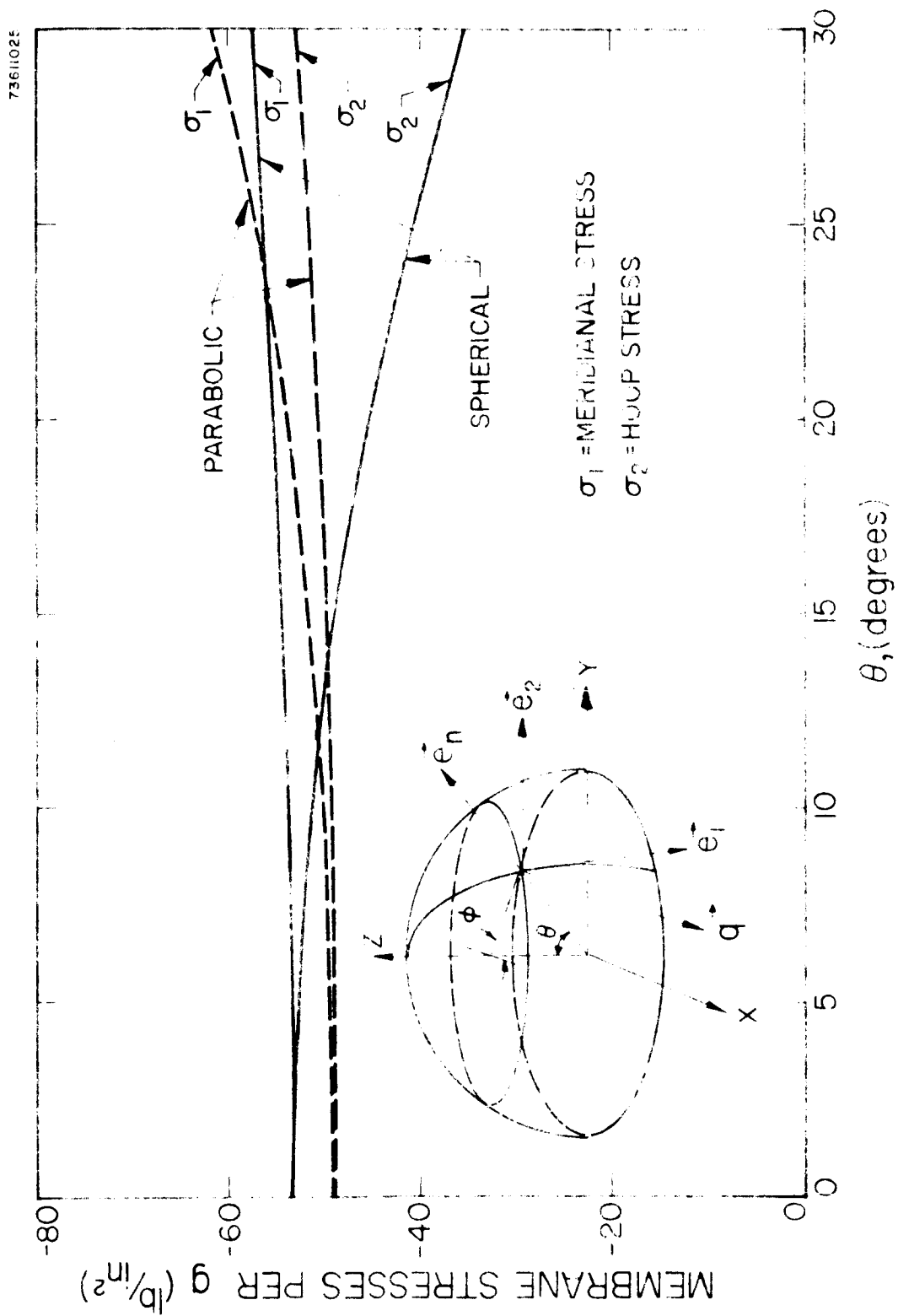


FIG. 1 - 2 MEMBRANE STRESSES DUE TO A LOAD  $q$  ALONG AXIS OF REVOLUTION

In practice structures never can withstand the theoretical buckling pressure. Therefore the fraction

$$\frac{P}{P_{cr}} \equiv \text{"critical buckling factor"}$$

has been used to represent the experimental or predicted buckling pressure where  $p$  is the experimental buckling pressure. There is wide scatter in the experimental buckling pressures of spherical and hemispherical shells. In the range of  $R/t$  from 500 to 2000, the range of  $p/P_{c1}$  is from 0.10 to 0.33. At an  $R/t$  of approximately 85,000 tests on the Echo I spherical balloon gave values of  $p/P_{c1}$  ranging from 0.12 to 0.18 (Ref. 3-6).

If one considers the collector to be a shallow shell, more experimental and theoretical results are available. The shallow shell approximation is violated by the collector, but the information is useful for pointing out trends in the experimental data.

For a shallow spherical shell,

$$\frac{h}{b} \ll 1$$

For the 600 collector,

$$\frac{h}{b} = 0.29$$

where  $b$  = the radius of the shell (2.5 feet for a 5-foot collector).

The only case of a shallow spherical cap subjected to external pressure that has received much attention is the case of clamped edges. For this case the buckling pressure is a complicated function of a parameter  $\lambda$  defined as follows,

$$\lambda = \left[ 12(1-\nu^2) \right]^{1/4} \frac{b}{\sqrt{Rt}}$$

which is

$$\approx \frac{17.9}{\sqrt{E}} \approx 180$$

for the collector.

All of the shallow shell data reported is for  $\lambda$  less than 30. For values of  $\lambda$  greater than 20 the experimental data gives  $p/p_{c1}$  ranging from 0.20 to 0.70, with the higher values given by the more carefully manufactured shells.

As corroborated by Dr. Babcock, the best theoretical analysis now available is Huang's (Ref. 3-7) which gives the following,

$$p/p_{c1} = 0.86 \text{ for large } \lambda.$$

This analysis and related experiments are for the case of clamped edges. The effect of other boundary conditions is unknown, but one would expect this effect to be less in the high  $\lambda$  range as compared to the low  $\lambda$  range.

With the scarcity of theoretical and experimental data available, any prediction of the buckling pressure is somewhat in question. To more accurately predict this pressure, experimental data in the range of parameters corresponding to the collector are necessary.

The large scatter in the buckling pressures obtained from experimental studies can largely be traced to geometric irregularities. In general, it can be said that the better the shell the higher the buckling pressure. From this consideration, one would expect the buckling pressure for the electroformed collector to be quite high. This is borne out by the fact that the data for complete spherical shells, which are hard to manufacture, show low buckling pressures. However, shallow spherical shells with ratios of radius to thickness up to 4,000 show high buckling pressures compared to the classical pressure,  $0.60 \leq p/p_{c1} \leq 0.86$ , if the shell is carefully manufactured, (Ref. 3-8).



Assuming the buckling pressure is given by  $p/p_{c1} = 1/3$ , which is a logical compromise between the data of Refs. 3-6 and 3-8, the required thickness would be,

$$p = \frac{1}{3} p_{c1} = \frac{2 E \left(\frac{t}{R}\right)^2}{3.0(1-\nu^2)} = 3\sigma t$$

$$\begin{aligned} t &= 9.5 \times 10^{-3} \text{ inches for a } 61 \text{ degree rim angle, nickel skin} \\ &= 10.7 \times 10^{-3} \text{ inches for a } 55 \text{ degree rim angle nickel skin} \end{aligned}$$

Figure 3-33 shows the number of g's a collector shell of thickness  $t$  will withstand before buckling for the design  $p/p_{c1}$  ratio and the  $p/p_{c1}$  ratios suggested by the work in Refs. 3-6 and 3-8. Another consideration in the buckling problem is the question of what constitutes failure of the collector.

To assess the structural integrity of the collector, it is necessary to establish a criterion for failure. It is clear that either of the following conditions would constitute local failure:

1. Exceeding the yield stress such that the surface is permanently distorted
2. Buckling to the extent that snap-back does not occur

If a sufficient portion of the mirror area is affected by these conditions, to the extent that performance suffers significantly, the mirror may be considered to have failed. The first task of the structural analysis, then, is to assure that the material yield stress is never exceeded under any unforeseeable conditions. This can be accomplished rather readily for static conditions. Yielding under dynamic conditions is more difficult to determine. It depends on amplification of the vibration under resonance conditions and is strongly dependent on vibration mode shapes, natural frequencies, and damping of the structure, and on the characteristics of the vibration spectrum.

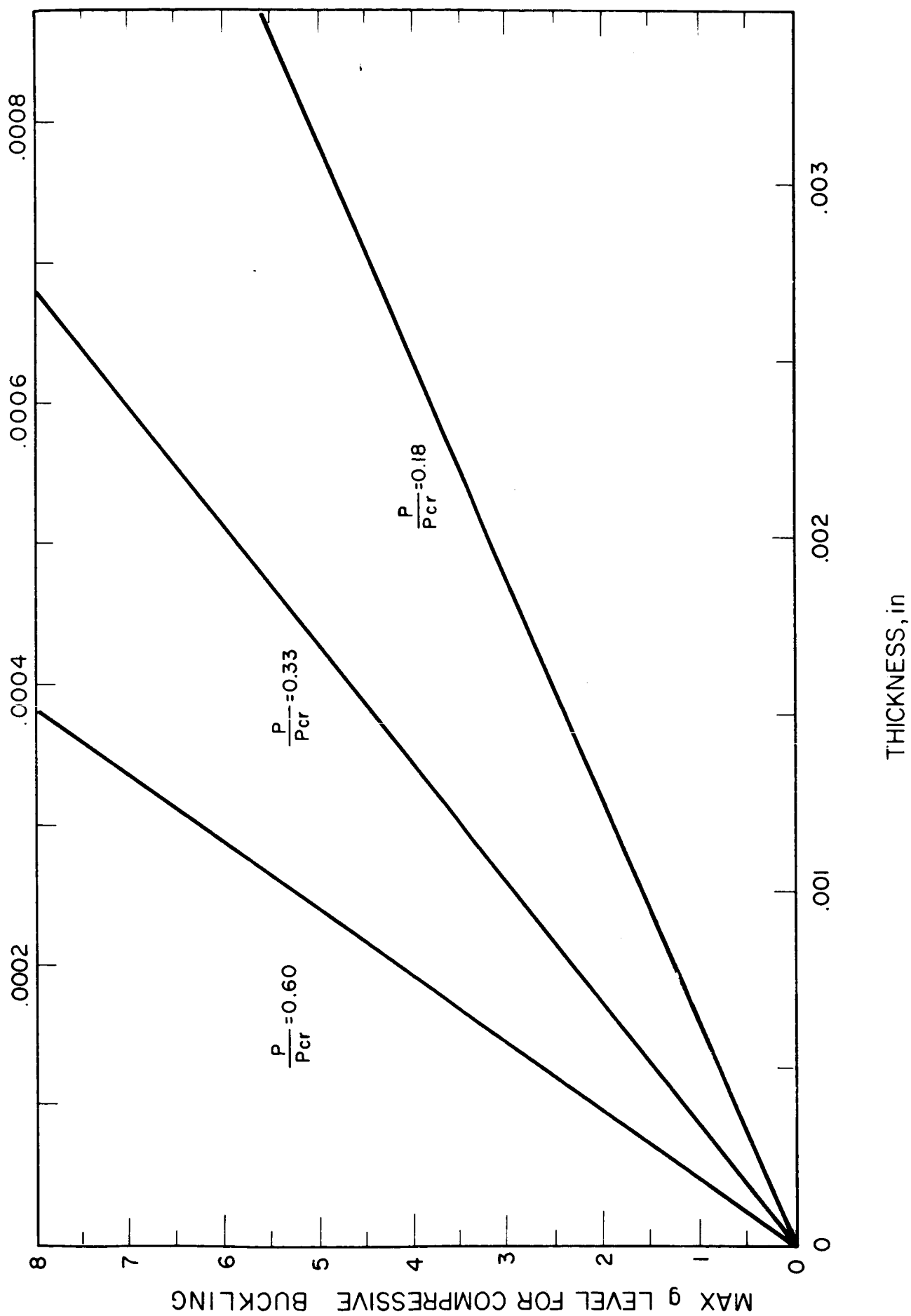


FIG. 10. STATIC BUCKLING RESISTANCE VS. THICKNESS FOR SHELL THICKNESS

Most of the available theory and data on buckling is concerned with determining the stresses or pressures at which buckling begins. However, this does not necessarily represent a good criterion for structural failure. If the local yield stress is never greatly exceeded, and if the buckled area snaps back after the buckling stress is removed, there is no reason to consider that the structure has failed. Experience has been that considerable local buckling of thin concentrator structures can occur under vibration and shock conditions without resulting in any permanent damage to the surface. Unfortunately, little work has been done to determine the extent to which buckling can occur without resulting in permanent degradation of optical properties. At the present rate of development, it is not believed feasible to attack this problem analytically. Some experimental investigation will be required for specific configurations of interest.

#### 3.6.4 Lateral Acceleration Effects

In the membrane analysis of the collector shell subjected to uniform transverse or lateral acceleration, the analysis is simplified by assuming that the collector is a spherical cap having the same base diameter and height as the parabolic shell. The shell diagram in Fig. 3-32 depicts the nomenclature used for the lateral acceleration analysis below.

The unit load vector  $\vec{q}$  is  $\vec{q} = q \vec{1}_x = \text{sgnt } \vec{1}_x$ . The load magnitude is sgnt and  $\vec{1}_x$  is the unit vector in the x direction. Therefore, the meridional hoop and normal loads are:

$$q_1 = \vec{e}_1 \cdot \vec{q} = \cos\theta \cos\phi$$

$$q_2 = \vec{e}_2 \cdot \vec{q} = -q \sin\theta$$

$$q_n = \vec{e}_n \cdot \vec{q} = q \sin\theta \cos\phi$$

Using the notation of Novozhilov, Ref. 3-5

$$q_1 = q_{1,1} \cos\phi \text{ where } q_{1,1} = q \cos\theta$$

$$q_2 = q_{2,1} \sin\phi \text{ where } q_{2,1} = -q$$

$$q_n = q_{n,1} \cos\phi \text{ where } q_{n,1} = q \sin\theta$$

The meridional and hoop and shear forces per lineal inch are respectively

$$T_1 = \frac{1}{R^2 \sin^3 \theta} \left[ \int_0^\theta \bar{r} R \sin \theta \, d\theta \right] \cos \phi = T_{1,1} \cos \phi$$

$$T_2 = \left[ q_{n,1} R + \frac{1}{R^2 \sin^3 \theta} \int_0^\theta \bar{r} R \sin \theta \, d\theta \right] \cos \phi = T_{2,1} \cos \phi$$

$$S = \left[ T_{1,1} \cos \theta + \chi(\theta) \right] \sin \phi$$

where the function

$$\begin{aligned} \bar{r} &= (q_{n,1} \cos \theta + q_{1,1} \sin \theta) R^2 \sin \theta \\ &+ \int_0^\theta (q_{n,1} \sin \theta + q_{1,1} \cos \theta + q_{2,1}) R^2 \sin \theta \, d\theta \\ \chi &= 2qR^2 [\cos \theta - 1] \end{aligned}$$

and

$$\begin{aligned} \chi(\theta) &= \frac{1}{R \sin^3 \theta} \int_0^\theta (q_{n,1} \sin \theta + q_{1,1} \cos \theta + q_{2,1}) R^2 \sin \theta \, d\theta \\ \chi(\theta) &= 2Rq \frac{1 - \cos \theta}{\sin \theta} \end{aligned}$$

The meridional, hoop, and shear stresses are, therefore,

$$\sigma_1 = \frac{T_1}{t} = \frac{c \rho n R \cos \phi}{2} \frac{\sin^2 \theta / 2}{\cos^3 \theta / 2} = \sigma_{1,1} \cos \phi$$

$$\begin{aligned} \sigma_2 = \frac{T_2}{t} &= \frac{c \rho n R \cos \phi}{2} \frac{\sin^2 \theta / 2}{\cos^3 \theta / 2} [1 + 4 \cos^2 \theta / 2] = \\ &= \sigma_{2,1} [1 + 4 \cos^2 \theta / 2] \cos \phi \end{aligned}$$

$$\begin{aligned} \tau_{12} = \frac{S}{t} &= \frac{c \rho n k \sin \phi}{2} \frac{\sin^2 \theta / 2}{\cos^3 \theta / 2} [1 + 2 \cos^2 \theta / 2] = \\ &= \tau_{1,1} [1 + 2 \cos^2 \theta / 2] \sin \phi \end{aligned}$$

Figure 3-34 shows the membrane stresses as a function of  $\theta$  plotted from the above equations. Hoop and meridional stresses are of the same order of magnitude as in axial loading and have opposite signs at the same position. Therefore, compressive buckling will not be a problem.

### 3.6.5 Vibration

The vibration characteristics of this structure will be dominated by the torus mounting since the collector shell and torus are rigidly joined. To better understand the analytical complexities of this problem, the structural frequency response will be broken into three parts:

1. Shell
2. Torus
3. Shell and torus

#### 3.6.5.1 Shell Frequencies

At least four possible edge mountings will determine the lowest natural frequency,  $f_n$ , of the shell. These result from the two alternate methods of supporting the collector in both the launch and orbit phases. These variations and the lowest fundamental nodal response are:

1. Eight-point torus support during launch (four nodal diameters)
2. Continuous torus support during launch (one nodal circle)
3. Tripod support during orbit (three nodal diameters)
4. Quadrapod support during orbit (two nodal diameters)

An example of the fundamental responses for these frequencies is shown in Table 3-V. The fundamental frequencies for Cases 1, 2, and 4 were calculated from the following equation from Reissner (Ref. 3-9):

$$f_n = \frac{t}{2\pi R^2} \frac{E}{12(1-\nu^2)} \left[ \frac{4(1-\nu)(n^2-1)n^2}{n^2} \right]^{1/2}$$

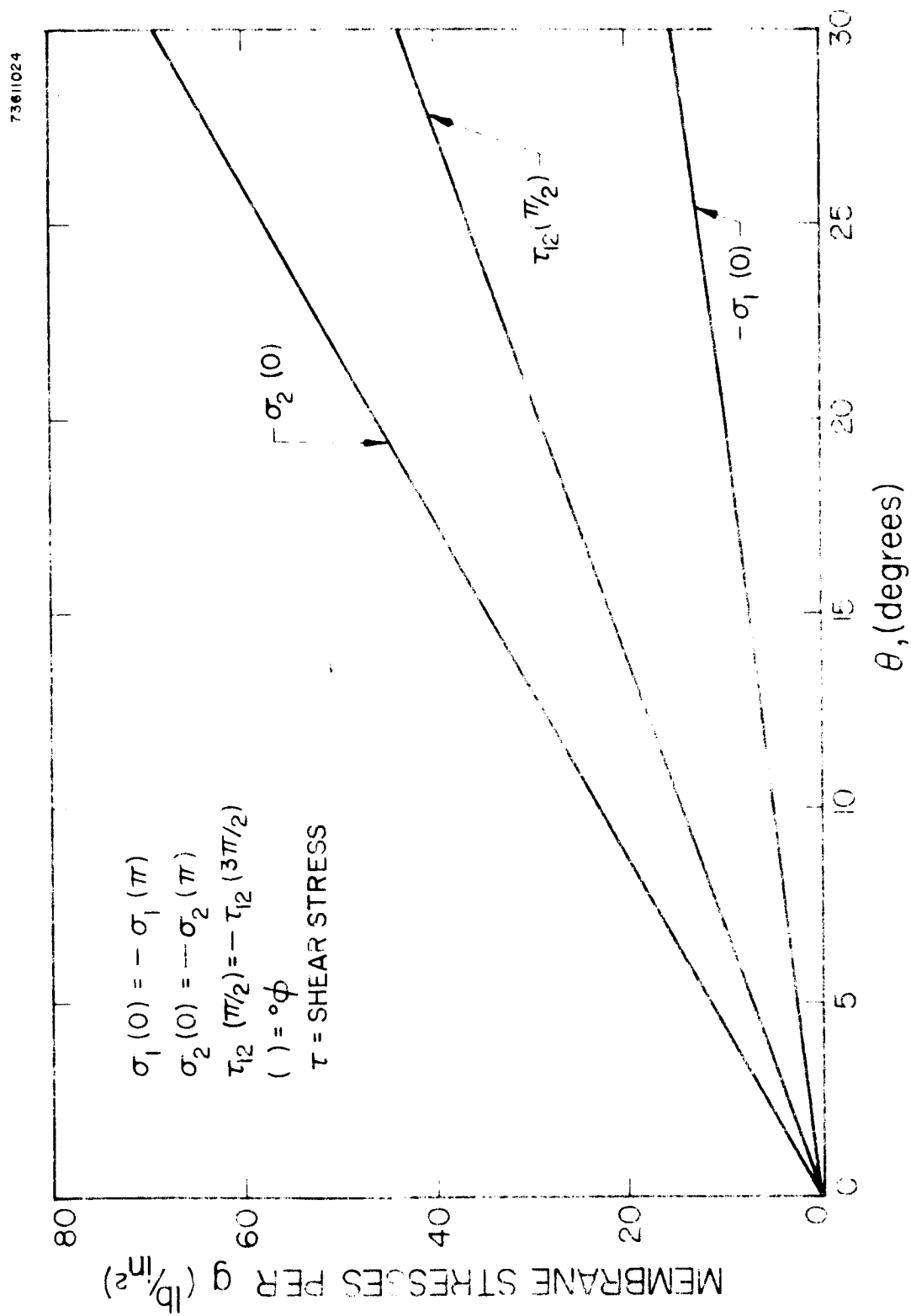


FIG. 3-9. MEMBRANE STRESSES PER g FOR A TRAVERSE OF LOADING

where

n = number of nodal diameters

$\nu$  = Poisson's ratio

$\rho$  = density

R = collector radius

E = modulus of elasticity

The frequencies derived for Cases 1, 3, and 4 are 18, 13, and 8 percent higher than the corresponding frequencies derived from a flat plate of similar diameter and thickness.

Nomographs covering parabolic shells supported as in Cases 3 and 4 are given by Lin and Lee (Ref. 3-10). These results are also included for comparison in Table 3-VII. The paraboloidal frequency for Case 3 may be in error as much as 50 percent since the referenced nomograph was extrapolated to obtain this value. Since the values are close to those evaluated for the spherical cap, the spherical cap approximation appears valid.

In each of the above cases the fundamental frequency is determined largely by the energy stored by inextensional bending. Therefore, frequency is dependent on the shell thickness and almost independent of shell curvature.

The fundamental frequency derived for Case 2 is high because the majority of the vibration energy is stored in stretching the shell. As can be seen in Table 3-VII, the lowest natural frequency for Case 2 is highly dependent on the approximation used. Naghdi (Ref. 3-11) shows that the lowest natural frequency for a thin shell hemisphere is

$$f_n = \frac{0.87}{2\pi R} \sqrt{\frac{E}{\rho}}$$

Therefore, for a hemisphere having the same rim radius as the collector the natural frequency would be 438 cycles per second; with the same radius of curvature as the average spherical radius of curvature, the natural frequency would be 237 cycles per second.

TABLE 3-VII

## 10-FT SHELL NATURAL FREQUENCIES FOR VARIOUS TORUS SUPPORT CASES

| <u>Case</u> | <u>Torus Support</u> | <u>Node</u>                   | <u>Frequency in cps</u> | <u>Reference</u>     |
|-------------|----------------------|-------------------------------|-------------------------|----------------------|
| 1           | 8                    | 4 nodal diameters             | 0.665                   | 3-9                  |
| 2           | Continuous           | breathing - 1<br>nodal circle | 438.                    | 3-11, T              |
|             |                      |                               | 237.                    | 3-11, R <sub>c</sub> |
|             |                      |                               | 384.                    | 3-12                 |
| 3           | 3                    | 3 nodal diameters             | 0.378                   | 3-9                  |
|             |                      |                               | 0.675                   | 3-10, parabola       |
| 4           | 4                    | 2 nodal diameters             | 0.153                   | 3-9                  |
|             |                      |                               | 0.135                   | 3-10, parabola       |

NOTES

Constants used in frequency calculations:

$$E = 30 \times 10^6 \text{ psi}$$

$$n = 2, 3 \text{ or } 4$$

$$R = 60 \text{ in}$$

$$R_c = 111 \text{ in}$$

$$t = 0.010 \text{ in}$$

$$\nu = 1/3$$

$$c = 0.32/386 = 0.00083 \text{ lb} \cdot \text{sec}^2/\text{in}^4$$



The following equation from Reissner (Ref. 3-12) approximates the natural frequency for clamped thin spherical shells:

$$f_n = \frac{2.98}{2\pi} \frac{t}{R^2} \frac{E}{(1-\nu^2)} \left[ 1 + (1+\nu) \left( 0.9 - 0.2(1+\nu) \right) \frac{h^2}{t^2} \right]^{1/2}$$

where h is the collector sagitta.

However, at high h/t ratios this equation may be in error as much as +18 percent as demonstrated by Hoppmann (Ref. 3-13). The calculated frequency of 384 cycles per second is, as one would expect, between the two frequencies calculated for various hemispherical radii above. Based on the questionable assumption of a completely clamped edge, and on the scatter of answers from the analytical solutions for a clamped edge, the natural frequencies calculated for this case may be in error by a factor of 2.

#### 3.6.5.2 Torus

The natural frequencies of the torus,  $f_{n,r}$ , Table 3-VIII were derived assuming that the torus is a complete circular ring whose radius is large with respect to ring thickness in the radial direction (Ref. 3-14). For the four types of mounting described in Cases 1 through 4 in Subsection 3.6.5, the extensional and flexural vibrations, both in the plane and normal to the plane of the torus ring, have been calculated. The flexural vibrations are applicable only to Cases 1, 3, and 4. The equations used to derive frequencies are based on Harris and Crede (Ref. 3-14). Extensional frequencies are derived from the equation:

$$f_n = \frac{1}{2\pi} \frac{E\pi r^4}{m_r R^2} (1+n^2)$$

where  $m_r$  is the torus mass per lineal inch, R the collector radius and r the torus cross sectional radius.

TABLE 3-VIII  
TORUS NATURAL FREQUENCIES  $f_{n,r}$ , FOR VARIOUS SUPPORTS  
FOR A 10-FT MIRROR

| <u>Case</u> | <u>Torus Support</u> | <u>Mode</u>        | <u>Frequency in cps</u> |
|-------------|----------------------|--------------------|-------------------------|
| 1           | 8                    | $4\lambda_{\perp}$ | 516                     |
|             |                      | $4\lambda_{=}$     | 520                     |
| 2           | Continuous           | Extensional        | 2160                    |
| 3           | 3                    | $3\lambda_{\perp}$ | 267                     |
|             |                      | $3\lambda_{=}$     | 273                     |
| 4           | 4                    | $2\lambda_{\perp}$ | 93                      |
|             |                      | $2\lambda_{=}$     | 97                      |

NOTES

Assumed a torus weight of 25 lb;  $\therefore m_r = 0.57 \times 10^{-3} \text{ lb} \cdot \text{sec}^2/\text{in}^2$

$\lambda$  wavelengths, flexural vibration

$\perp$  perpendicular to torus plane

$=$  in torus plane

Flexural frequencies in the plane of the torus ring are derived from:

$$f_n = \frac{1}{2\pi} \frac{E\pi r^4}{4m_r R^4} \frac{n^2(n^2-1)^2}{(n^2+1)}$$

The flexural frequencies normal to the plane of the ring are derived from:

$$f_n = \frac{1}{2\pi} \frac{E\pi r^4}{4m_r R^4} \frac{n^2(n^2-1)^2}{(n^2+1+\nu)}$$

#### 3.6.5.3 Torus-Shell

At present, there is only limited published information on the empirical determination of natural frequencies of toroidally rigidized solar collectors (Refs. 3-15 and 3-16). This work was done on 5-foot diameter mirrors. Although JPL is performing experimental work in this area and although they are developing a computer program which can determine natural frequencies of any paraboloidal shell-torus combination, no simple analytical means are yet available for the calculation of the torus-collector shell natural frequency. Therefore, the determination of this frequency will be based on simplifying assumptions. First, assume that the torus will store all the vibrational energy. Next, a portion of the mass of the collector shell and a part of the shell stiffness will be added to the torus. Experimental work at JPL indicates that approximately 52 percent of the shell mass should be lumped to the torus. If one assumes that the shell stiffness is between 0 and 1 times the torus stiffness, the resultant combined resonant frequency will be from 1 to  $\sqrt{2}$  times the torus frequencies with lumped masses. A summary of the combined shell-torus frequencies for the four cases described above can be calculated from the following equation

$$f_{n,c} = f_{n,r} \left[ \frac{m_r}{m_r + m_s} \frac{D_r + D_s}{D_r} \right]^{(1/2)}$$

where  $f_{n,c}$  is the shell-torus or collector natural frequency,  $m_r$  is the torus mass,  $m_s$  the shell mass,  $D_r$  the torus rigidity, and  $D_s$  the shell rigidity.

### 3.6.6 Vibration Effects

The structural response to vibration effects is dependent on the structural dampening, which determines the resonance amplification factor,  $A_r$ .

$$A_r = \frac{C_{cr}}{2C} = \frac{1}{\eta}$$

where  $C$  is the dampening coefficient,  $C_{cr}$ , the critical dampening coefficient, and  $\eta$  the dissipation factor. Structural dampening is a function of both the air dampening,  $C_a$ , and material dampening,  $C_m$ .

If the collector is approximated by a square plate with the same thickness as that of the collector and with a length and width equal to the collector diameter, the air dampening can be determined by either of two equations. When  $\frac{\omega a}{2c} < 1$  (where  $\omega$  is the frequency in radians/second,  $a$  the length and width, and  $c$  the velocity of sound) or  $f < 12$  cps, the dampening on both sides of the plate is as follows (Ref. 3-17)

$$\frac{C_a}{C_{cr}} = 0.636 \frac{c_m}{c} \frac{\omega}{\rho_m}$$

where  $c_m$  and  $\rho_m$  are, respectively, the speed of sound and density of the plate material. For air dampening on both sides of a nickel shell the air amplification factor  $A_{r,a} = 400$ . However, due to the high diameter to thickness ratio, the amplification factor should be further reduced because of dampening due to inphase air acceleration. This reduction is not easily determined.

When  $\frac{ca}{2c} > 3$  or  $f > 36$  cps, the dampening is determined as follows:

$$\frac{C_a}{C_{cr}} = 0.175 \frac{c}{c_m} \frac{c}{c_m} \frac{D^2}{t^2} \quad (\text{Ref. 3-17})$$

where  $t$  is the shell thickness and  $D$  the collector diameter.  $A_{r,a}$  for this case = 0.00025. The wide amplification variations above 36 cps and below 12 cps are due in part to the exclusion of inphase air acceleration dampening. Tests should be made to verify these formulae for large  $R/t$  ratios.

Mechanical dampening depends on such factors as:

1. Material
  - a. Composition, structure and homogeneity
  - b. Stress and temperature history
2. Internal stress
  - a. Initial stress
  - b. Changes caused by stress in temperature history
3. Stress conditions in use
  - a. Type, i.e., tension, compression
  - b. State of stress, i.e., triaxial and biaxial
  - c. Stress magnitude
  - d. Stress variations
  - e. Environmental characteristics

For most materials, the amplification factor ranges between 6 and 1000. Since nickel is a magnetic material with high internal friction, a material dampening amplification factor,  $A_{r,m}$  of 100 appears conservative. A total amplification factor then is calculated as follows:

$$\frac{1}{A_r} = \frac{1}{A_{r,a}} + \frac{1}{A_{r,m}}$$

Therefore, for frequencies less than 12 cps, the combined amplification factor is much less than 30; for frequencies greater than 36 cps, the amplification is much less than one. The amplification factor for vacuum is 100.

The resonant stress,  $\sigma_r$ , is given by  $\sigma_r = \sigma_{lg} \times A_r \times n$  where,  $\sigma_{lg}$  is the one "g" stress and n the number of g.

Table 3- IX lists the resonant stresses and ratio of yield stress to resonant stress for the four cases of torus mounting in launch and orbit when applied to a 30-foot mirror. In Case 1, the 8-point torus suspension during launch, extremely high resonant stresses are calculated. Reduction of these stresses can be achieved by the following means:

1. Tapering the torus to equalize torus stresses
2. Increasing the torus moment of inertia
3. Designing for friction dampening between the torus and radiator
4. Friction dampening between the radiator mounts and torus brackets
5. Empirically determining the actual dampening of the torus-shell combination

To achieve a safety factor of greater than 1.0, a 40-fold increase in dampening would be required.

Case 2, the continuously supported torus, exhibits extremely low air damped resonant stress. More complete analyses are required to determine whether resonant stresses may be a problem under partial vacuum conditions toward the final boost phases. The torus resonant stresses for the tripod orbit support are high.

The natural frequency for the quadrapod support, Case 4, is lower than the environmental specification and no stress problems should therefore be encountered from orbital vibration.

Since the vibration response is highly dependent on dampening coefficients, natural frequencies, and mounting details, additional empirical studies of the detailed design are necessary.

TABLE 3-IX

## VIBRATION EFFECTS SUMMARY - 30-FOOT MIRROR

| Case | Torus Support | Natural Frequency in cps | Max. Input Acceleration | Amplification Factor |           | Max. Stress at 1 Hz (psi) | Resonance Stress (psi), $\frac{Y}{A}$ |           | Yield Stress $\frac{Y}{A}$ |               |
|------|---------------|--------------------------|-------------------------|----------------------|-----------|---------------------------|---------------------------------------|-----------|----------------------------|---------------|
|      |               |                          |                         | $A_r, a + m$         | $A_{r,m}$ |                           | $A_r, a + m$                          | $A_{r,m}$ | Air Material               | Material Only |
| 1    | 4 points      | 3.6                      | $\infty$                | $< 80$               | 100       | 100                       | 6,376,000                             | 42,000    | 12.5                       | 10            |
| 2    | 4 points      | 14.                      | 19                      | $< 80$               | 100       | 100                       | 2,000,000                             | 3,200,000 | 0.078                      | 0.022         |
| 3    | 3 points      | 3.2                      | 0.25                    | $< 1$                | 100       | 100                       | 13,000                                | 133,000   | 1,000                      | 10            |
| 4    | 4 points      | 2.9                      | -                       | $< 1$                | 100       | 100                       | 37,000                                | 24,000    | 1,500                      | 54            |
| 5    | 4 points      | 2.9                      | -                       | $< 1$                | 100       | 100                       | 37,000                                | 925,000   | 1,500                      | 46.6          |
| 6    | 4 points      | 2.9                      | -                       | $< 1$                | 100       | 100                       | 37,000                                | 925,000   | 1,500                      | 0.119         |

Air - Material - Material Only

By using vibration isolators for the torus support during launch the amplification at the natural resonant frequency can be reduced by at least a factor of two.

The vibration analysis indicates that a continuously supported torus is the preferred design during launch, and that a quadrapod supported torus is preferred during orbit.

The effects of dynamic loading on compressive buckling have not and cannot be readily determined from available analytical or empirical studies.

#### 3.6.7 Shock

A typical critical shock specification is the 35g shock loading by either a 10 millisecond triangular pulse, an 8 millisecond half sine wave pulse, or a rectangular pulse of 5 milliseconds. Table 3-X summarizes the results of this launch shock on the critical components for Cases 1 and 2. If the natural period of the element in question is greater than the shock period, the displacement of the element governs the ultimate stress. If the period of the element is less than the shock period the acceleration governs.

For the continuously mounted torus the maximum shell stress would be  $< 2,100$  pounds. In this case the high shell dampening will prevent any resonance amplification and limit the maximum g to 35 or less.

TABLE 3-X  
SHOCK SUMMARY, 10 FEET MIRROR

| <u>Torus Support</u> | <u>Natural Period Seconds</u> | <u>Maximum Acceleration Determined by</u> | <u>Maximum Stresses psi</u> |
|----------------------|-------------------------------|---|-----------------------------|
| Continuous           | 0.001                         | Acceleration - 35g                        | Shell 2,100                 |



### 3.6.8 Acoustical Noise

The effect of the 148 db acoustical noise field of the Saturn must be studied both from the standpoint of static buckling and dynamic stress.

The sound pressure level of 148 db Re 0.0002 microbar is equivalent to an rms pulsating pressure of  $0.07 \text{ lb/in}^2$ . From Olson, Ref. 3-18, the net radiation pressure (assuming the shell is an infinite wall) from acoustical noise striking the shell from one side is given by the following relationship:

$$p_n = (\gamma + 1) \frac{p}{2c^2}$$

where

- $p_n$  = the net radiation pressure
- $\gamma$  = the ratio of the specific heat of air at constant pressure to the specific heat at constant volume = 1.4
- $p$  = the pulsating acoustical noise pressure
- $\rho$  = the air density
- $c$  = the velocity of sound in air

Therefore at a 148 db acoustical noise level the net radiation pressure is  $6 \times 10^{-4}$  psi which is an order of magnitude less than the critical buckling pressure for the shell. Since the acoustical noise level will be approximately constant on both sides of the collector shell, there will effectively be no net radiation pressure. Therefore, from a static standpoint no buckling should occur.

For a flat plate the mean square stress value is given by the following equation from Ref. 3-17:

$$(\bar{\sigma})_n^2 = \frac{K_{14} c_m^2 a^2}{E_t^2 3\pi} \rho_p (p_n)$$

where

$(\bar{\sigma})_n^2$  = mean square stress value

$K_{14}$  = proportionality constant

$c_m$  = velocity of sound in material

$a$  = minimum plate or shell width

$E$  = modulus of elasticity

$t$  = plate, shell thickness

$\xi = \frac{C}{C_{cr}}$

$\phi_p(\omega_n)$  = pressure function of natural frequency,  $\omega_n$ , and acoustical noise level

Some experimental data is available on the stresses arising from a 148 db acoustic noise pressure level on aluminum flat and curved plates (Ref. 3-19). The stress in a similar nickel plate can be inferred by dividing the stress equation for nickel by that of aluminum, thereby cancelling  $K_{14}$  and  $\phi_p(\omega_n)$  so that

$$\overline{(\sigma^2)}_{n,ni} = (\bar{\sigma})_{n,al}^2 \frac{c_{m,ni}^2 a_{ni}^2}{c_{m,al}^2 a_{al}^2} \frac{E_{al}^2 t_{al}^3 \xi_{al}}{E_{ni}^2 t_{ni}^3 \xi_{ni}}$$

For the nickel shell  $\xi$  is determined from the air dampening equations in Subsection 3.6. In the case of the clamped shell, where the natural frequency is above 36 cps,  $\xi$  is  $2 \times 10^3$ . For an aluminum plate of these dimensions the ratio of structural and air dampening to critical dampening  $\xi$  is less than 0.01. A summary of constants used follows.

| Item                 | Units                            | Nickel<br>(Ni)    | Aluminum (Ref. 3-19)<br>(Al) |
|----------------------|----------------------------------|-------------------|------------------------------|
| $(\bar{\sigma})_n^2$ | lb <sup>2</sup> /in <sup>4</sup> |                   | 25,000                       |
| $c_m$                | in./sec                          | $1.9 \times 10^5$ | $1.97 \times 10^5$           |
| a                    | in.                              | 360               | 9.36                         |
| E                    | psi                              | $30 \times 10^6$  | $10 \times 10^6$             |
| t                    | in.                              | 0.0107            | 0.032                        |
| $\mu$                | —                                | $2 \times 10^3$   | $\sim 10^{-2}$               |

Therefore, the nickel shell stress due to a 148 db acoustical noise level will be less than 230 psi. Even if the air dampening factor of the collector shell were in error by a factor of 200 to 300, the fatigue strength of nickel would not be exceeded.

In the proposed design, additional resistance to stress fatigue is provided by the curvature of the shell and the predominantly tensile loading provided by the launch acceleration. The improvement in resistance to acoustical failure as a function of shell curvature and static pressure, equivalent to static acceleration, on the concave side of curved plates is also discussed in Ref. 3-19.

From the experimental data of Ref. 3-19 the edge mounting design is very important. Therefore design details which increase friction dampening and which reduce localized edge stresses, will reduce any edge effects of acoustical noise.

#### 3.6.9 Thermal Effects

The all-nickel collector structure has a high resistance to thermal stress and thermal shock. At no time will the temperature over the entire collector vary by more than 120°C. Based on a thermal expansion coefficient of  $7.3 \times 10^{-6}$  and a modulus of elasticity of  $30 \times 10^6$ , for nickel, the maximum possible thermal stress even

assuming a completely rigid torus would be of 44,400 psi which gives a safety factor of greater than 1.5 relative to a 70,000 psi yield strength.

The resistance of this structure to thermal shock will be high. While no standard thermal shock resistance test exists, good thermal shock resistance appears to be a function of the ratio  $Ks/\sigma E$ , where  $K$  is the thermal conductivity,  $s$  the tensile strength,  $\sigma$  the linear coefficient of thermal expansion, and  $E$  the modulus of elasticity. This ratio shows that thermal shock resistance is favored by high tensile strength, high thermal conductivity, low modulus of elasticity at failure and low thermal expansion. Based on comparative values of the above coefficients, for comparable structures and thermal variations nickel has a thermal shock resistance comparable to that of aluminum.

No structural degradation is therefore expected from either thermal stress or shock.

### 3.7 Concentrator Coatings

The nature of the reflective qualities of the mirror will be determined by:

1. Substrate
2. Undercoating
3. Reflective layer
4. Overcoating

Figure 3-35 illustrates the reflective properties of silver, aluminum, and aluminum with a  $\text{SiO}_2$  overcoat, coated on glass, as a function of wavelength.

For solar radiation, the maximum reflectance measured to date has been 94 percent and 89 percent for vacuum-coated silver and aluminum.

In some cases it may be necessary to use a coating between the substrate and the reflective layer for one of the following reasons:

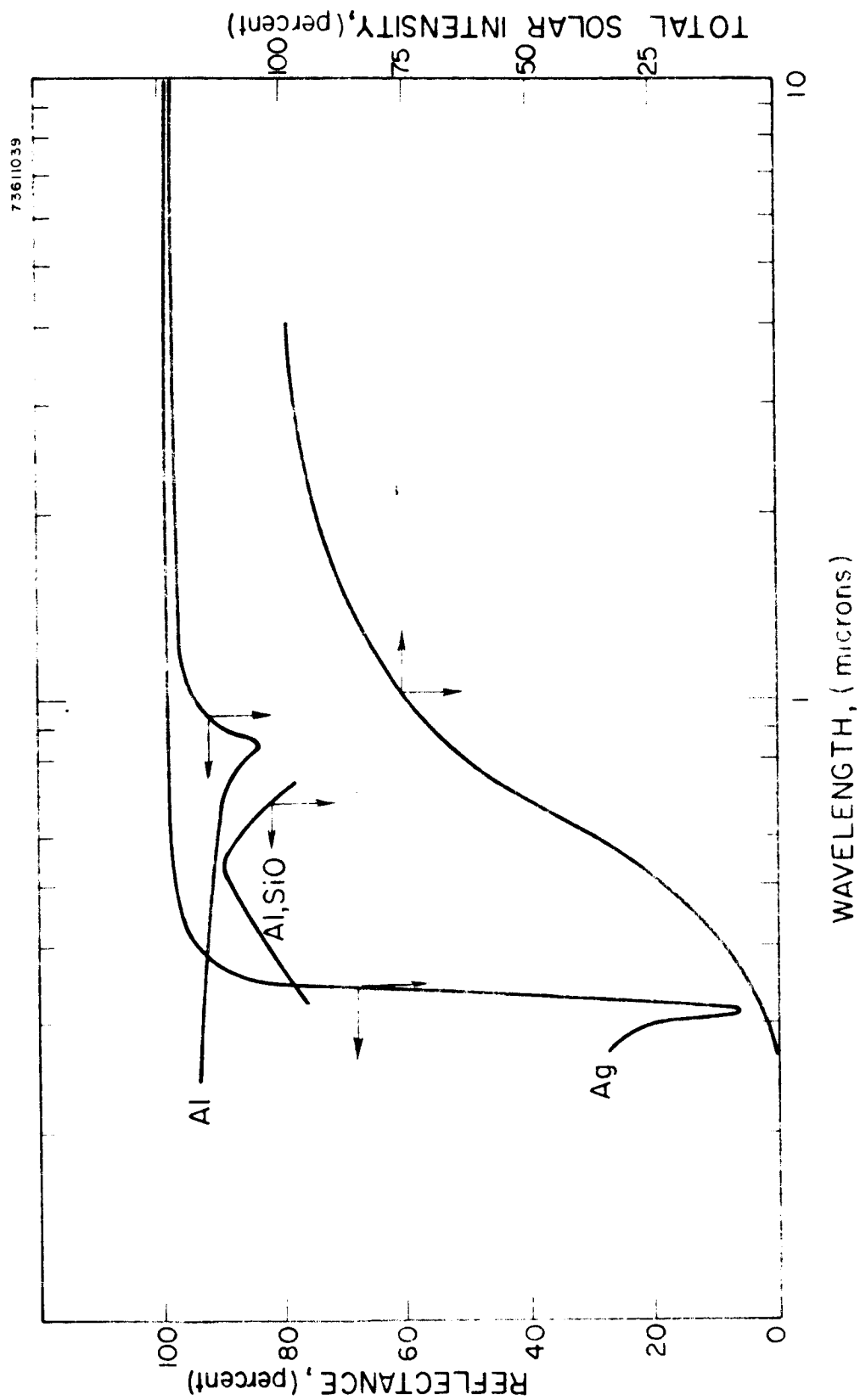


FIG. 1-75 REFLECTANCE AND TOTAL SOLAR INTENSITY VS WAVELENGTH

1. To improve adhesion of the reflective layer
2. To prevent diffusion of the reflective layer into the substrate or vice versa.

Depending on the substrate and reflective layer, one or both of these functions often can be satisfied by a vacuum deposited layer of a dielectric such as silicon monoxide or cerium dioxide.

Only two pure metals, aluminum and silver, have reflectances high enough for solar concentrators. It is also possible to obtain high reflectance using multilayer interference filters of alternating and metallic and dielectric materials. However, the art of applying these coatings to large area curved surfaces has not been developed. Therefore, they will not be considered further.

Aluminum. Vacuum deposited aluminum on an optically smooth substrate has a reflectance of approximately 89 percent for the total solar spectrum. Aluminum is a chemically durable material. Immediately after exposure to the atmosphere a thin, transparent layer of aluminum oxide forms on the surface that prevents further oxidation. Aluminum is rather soft and easily abraded and may require some protective overcoating if extensive ground handling or cleaning is anticipated.

Silver. Silver can be deposited either by vacuum deposition or by chemical reduction. The latter approach is used as an integral part of the process of fabricating electroformed nickel concentrators. Either type of silver has an average reflectance of 93 percent or more for the total solar spectrum. Silver tarnishes when exposed to certain chemical contaminants such as sulfides and must be protected during ground storage. However, if adequately protected, the reflectance of silver can be maintained at a high level indefinitely, thus offering a worthwhile performance advantage over aluminum for solar concentrator applications. This protection is relatively simple and can take one of the following forms:

1. Storage in a clean atmosphere (clean air, nitrogen, argon, etc.) in a plastic bag or box
2. Coating with a plastic surface layer that would be removed prior to launch
3. Coating with a sublimating plastic layer that would evaporate in space after deployment

Chemically-deposited silver is much more durable than vacuum-deposited silver. It has been found that vacuum-deposited overcoatings do not satisfactorily protect silver against corrosion. Furthermore, they lower the reflectance to the extent that the advantages of silver are lost.

In many cases it may be desirable to protect aluminum reflecting layers with a transparent overcoating of a dielectric such as silicon oxide of  $\text{SiO}_2$ . Several oxides of silicon have been investigated.  $\text{Si}_2\text{O}_3$  appears to give the best optical properties. The primary purpose of such a coating is to prevent damage of the reflective layer prior to launch by providing a hard, durable surface that can be easily cleaned. Some chemical protection will also be obtained from the overcoating. The real necessity for such a coating is problematical, since a reasonable degree of care in handling the mirror should obviate the necessity for cleaning between fabrication and launch. Protection afforded by a silicon-oxide overcoating in space has not been determined. However, preliminary experiments have shown that such a coating might provide some protection against degrading effects.

A second type of dielectric overcoating is obtained by anodizing the aluminum reflecting layer to form a thicker aluminum-oxide coating. This technique was developed by the group under Dr. Hass at Fort Belvoir and has been further developed at Boeing. When properly formed, such a layer can provide protection and optical properties comparable to those of the silicon-oxide coatings. Goodyear is experimenting with a proprietary coating that can be put on aluminized Mylar to increase the infrared emittance for temperature control purposes. The composition of this coating is not known.

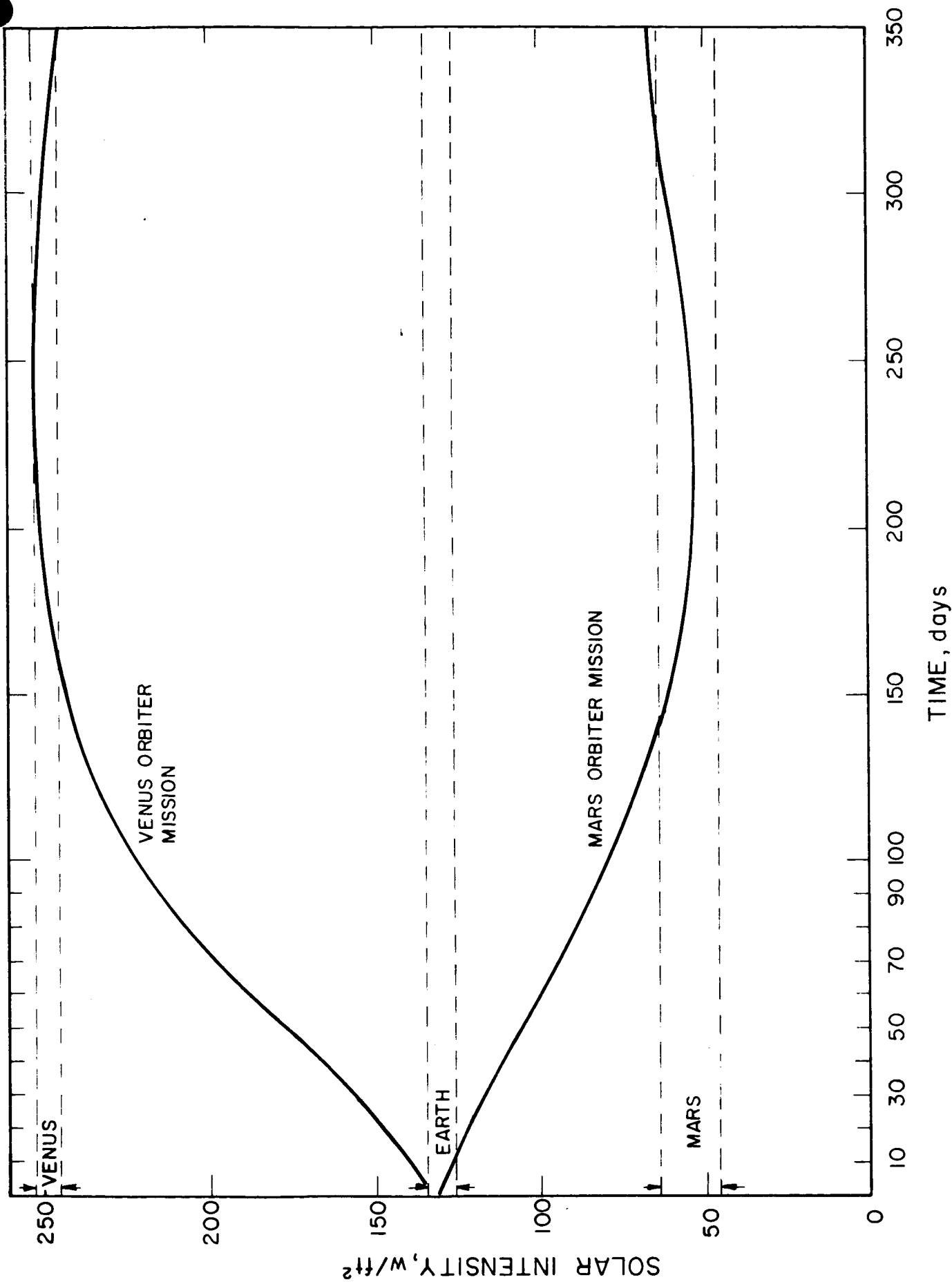


FIG. 1 - SOLAR INTENSITY VS. TIME



### 3.7.1 Solar Intensity

Figure 3-36 illustrates the solar intensity typically encountered on a Mars and Venus mission as a function of time.

Table 3-XI summarizes the solar intensity at various locations.

TABLE 3-XI  
PLANET DISTANCES

|       | <u>Distance (AU)</u> |         | <u>Solar Intensity (<math>\text{J}/\text{ft}^2</math>)</u> |       |
|-------|----------------------|---------|--|-------|
|       | Min                  | Max     | Min  | Max   |
| Earth | 0.983AU              | 1.017AU | 125.5  | 134.5 |
| Lunar | 0.98                 | 1.02    | 125  | 135.2 |
| Venus | 0.718                | 0.728   | 245  | 252   |
| Mars  | 1.42                 | 1.67    | 46.5   | 64.5  |

### 3.7.2 Reflective Surface Degradation

As discussed in Appendix A, it is difficult to predict the effects of the space environment on reflective surfaces with the limited experimental evidence available. Figure 3-37 shows a model used for reflection degradation in system calculations which appears reasonable. It was assumed that UV and proton damage accounted for 8 percent degradation in a year's time at Earth. The degradation at Mars and Venus varies as the inverse square law.

Meteoroid degradation of 2 percent was assumed for each orbiting conditions (300 nautical mile) meteoroid. The flux density profile will vary as the distance from the earth and sun vary. A relative meteoroid density profile is shown for typical Venus and Mars mission based on calculations performed by JPL (Ref. Fig. 3-38). As shown, meteoroid flux away from gravity centers such as the earth is expected to be small.

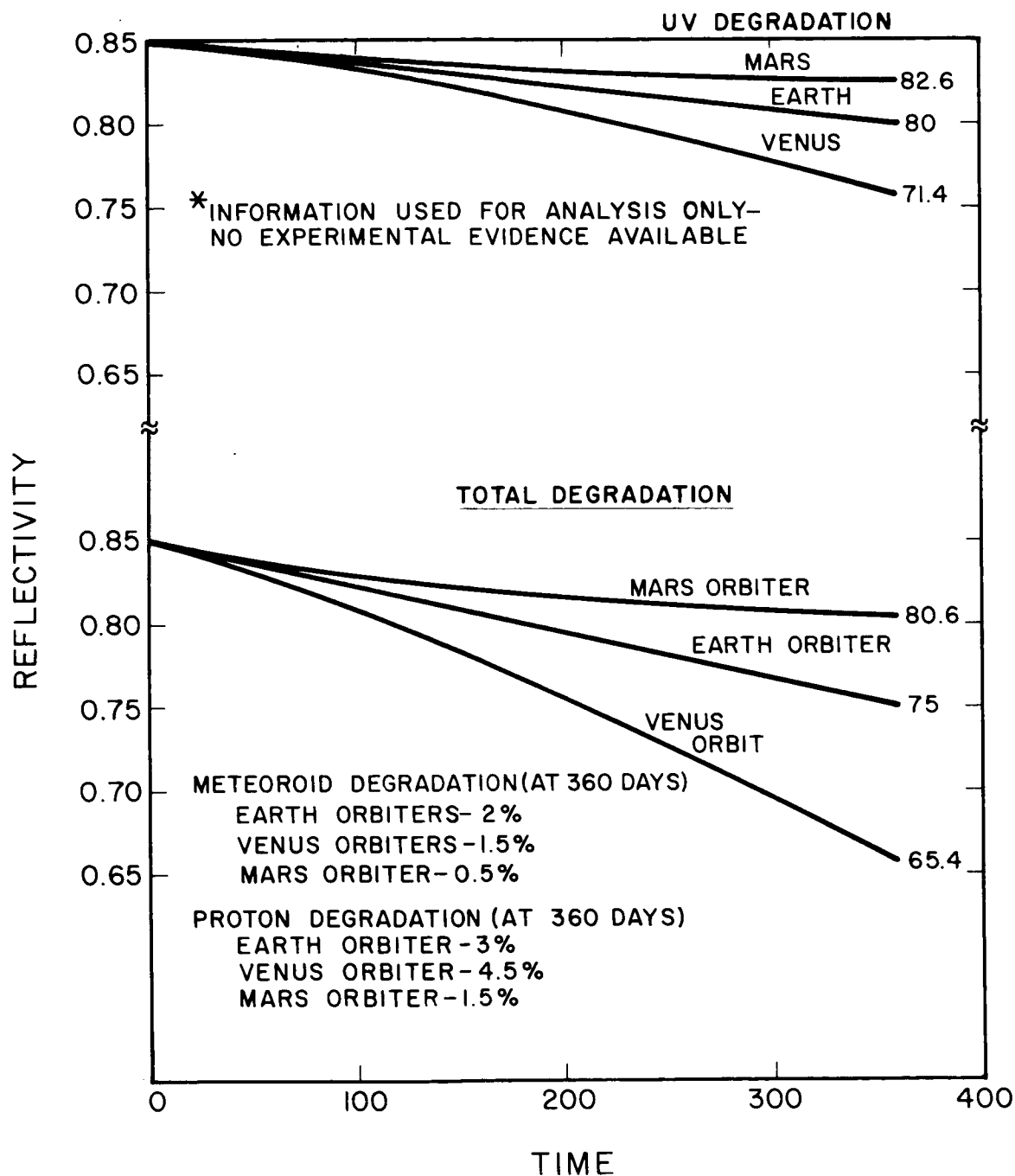
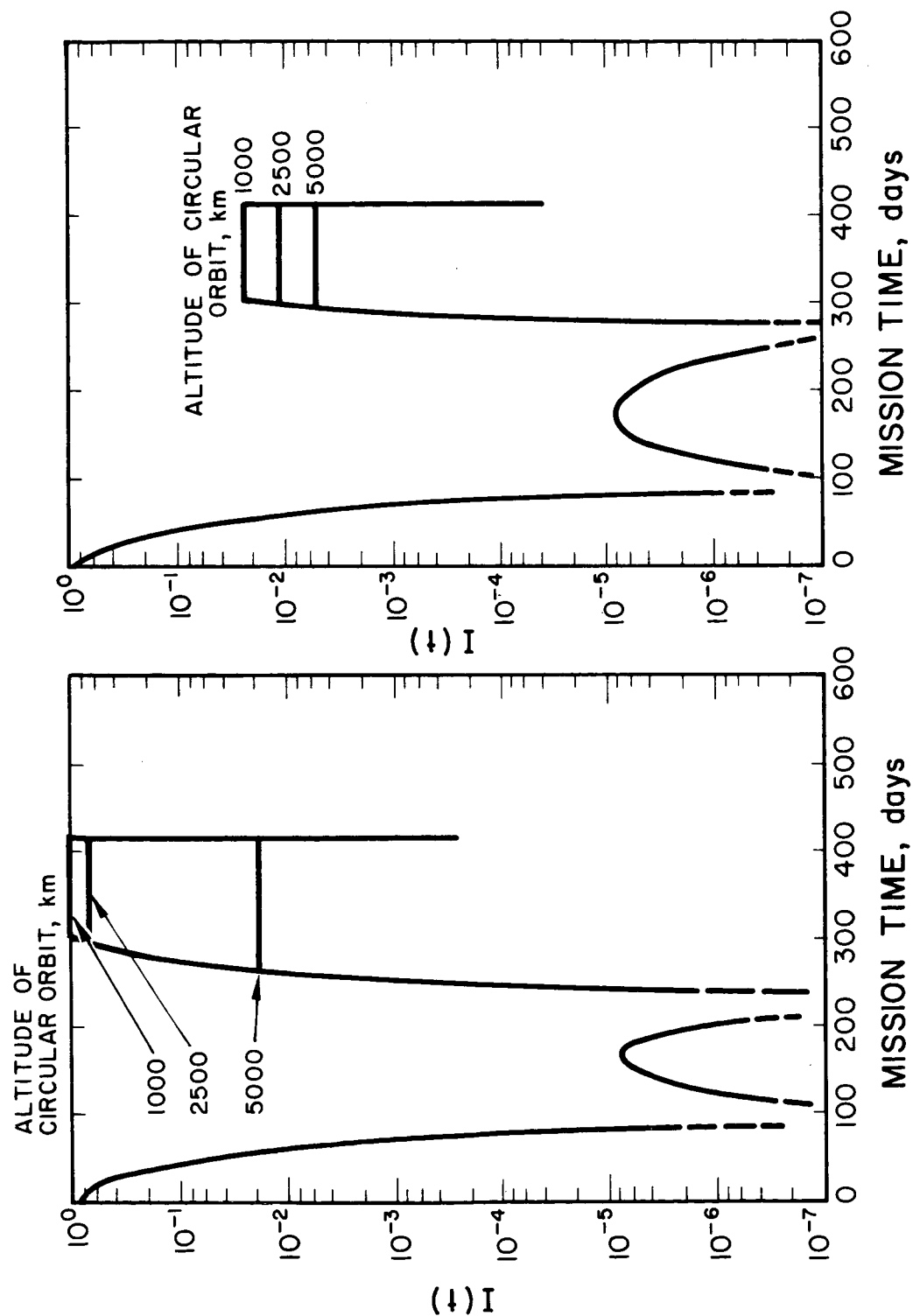


FIG. 3-27 MODEL REFLECTIVITY DEGRADATION WITH TIME



MARS ORBIT PER FLUX-INTENSITY PROFILE  
FOR VARIOUS CIRCULAR ORBITS

VARIABLE FLUX-INTENSITY PROFILE  
FOR VARIOUS CIRCULAR ORBITS

FIG. 3-18. MARS ORBIT PER FLUX-INTENSITY PROFILE

### 3.8 Collector-Absorber Efficiency

The collector-absorber efficiency of the concentrator-generator combination is a function of many parameters. Given below is a general expression for collector-absorber efficiency which involves various parameters of the concentrator and cavity.

$$\eta_{c-a} = \frac{P_{\text{absorbed by cavity}}}{P_{\text{on mirror}}} = r \cdot \eta_m F_a - F_r \cdot \frac{\sigma T_c^4 A_c}{H \cdot \pi \frac{D_m^2}{4}}$$

where

- $F_a$  = fraction of flux which enters the cavity which is reflected back out the entrance
- $F_r$  = fraction of flux emitted by surface which escapes from the entrance
- $\eta_m$  = mirror efficiency ( $r = 1.0$ )
- $r$  = mirror reflectivity
- $T_c$  = temperature of cavity walls
- $H$  = solar constant
- $A_c$  = surface area of cavity interior
- $D_m$  = diameter of mirror
- $\epsilon$  = effective emissivity of cavity walls

$$F_a = \frac{\epsilon}{1-(1-\epsilon)(1-\theta)} ; F_r = \frac{\epsilon\theta}{1-(1-\epsilon)(1-\theta)}$$

where

- $\epsilon$  == emissivity of interior surface
- $\theta$  = average view angle of interior surface towards cavity entrance

$$\theta \approx \frac{\pi d_c^2}{4 A_c} \cdot (A) + B \approx \frac{A_o}{A_c} \cdot A + B$$

where

- $A_o$  = cavity opening area
- $d_c$  = diameter of entrance to cavity
- $A$  = constant
- $B$  = constant

The collector-absorber efficiency is strongly affected by the parameters  $F_a$  and  $F_r$  which are a function of cavity geometry and interior emissivity. Rough calculations in the past have assumed that the cavity operates as a blackbody with  $F_a$  equal to 1 and  $F_r$  equal to the ratio of entrance area to cavity surface area. As shown later in the text, this approximation can lead to very optimistic results with regard to reflection losses.

The most serious problem lies in the term  $F_a$ ; i.e., significant losses result from direct reflection out of the cavity entrance.

The expressions for  $F_a$  and  $F_r$  are given in terms of the emissivity of the interior surface and the average view angle of the generator surface toward the cavity entrance. This view angle is generally given in the literature as a function of the ratio cavity opening area to surface area of the cavity interior and several constants assuming diffuse reflection from the surface. The constants generally depend on the nature of the cavity geometry. For a hemispherical cavity, the view angle  $\theta$  is equal to the ratio of cavity opening area to interior surface area of the hemisphere.

Typical cavity shapes are shown in Fig. 3-39. Shown are the cylinder, cone, hemisphere, sphere, and double cone. For the geometries of interest, the hemisphere demonstrates the most losses and the double cone configuration demonstrates the least loss.

A comparison of cavity shapes is shown in Table 3-XII. Given is the ratio of cavity opening area to cavity interior surface area as a function of geometrical parameters. In general, the ratio of cavity opening to cavity surface area should be small. In this respect, the comparison of the sphere and double cone in Table 3-XII illustrates the superiority of the double cone.

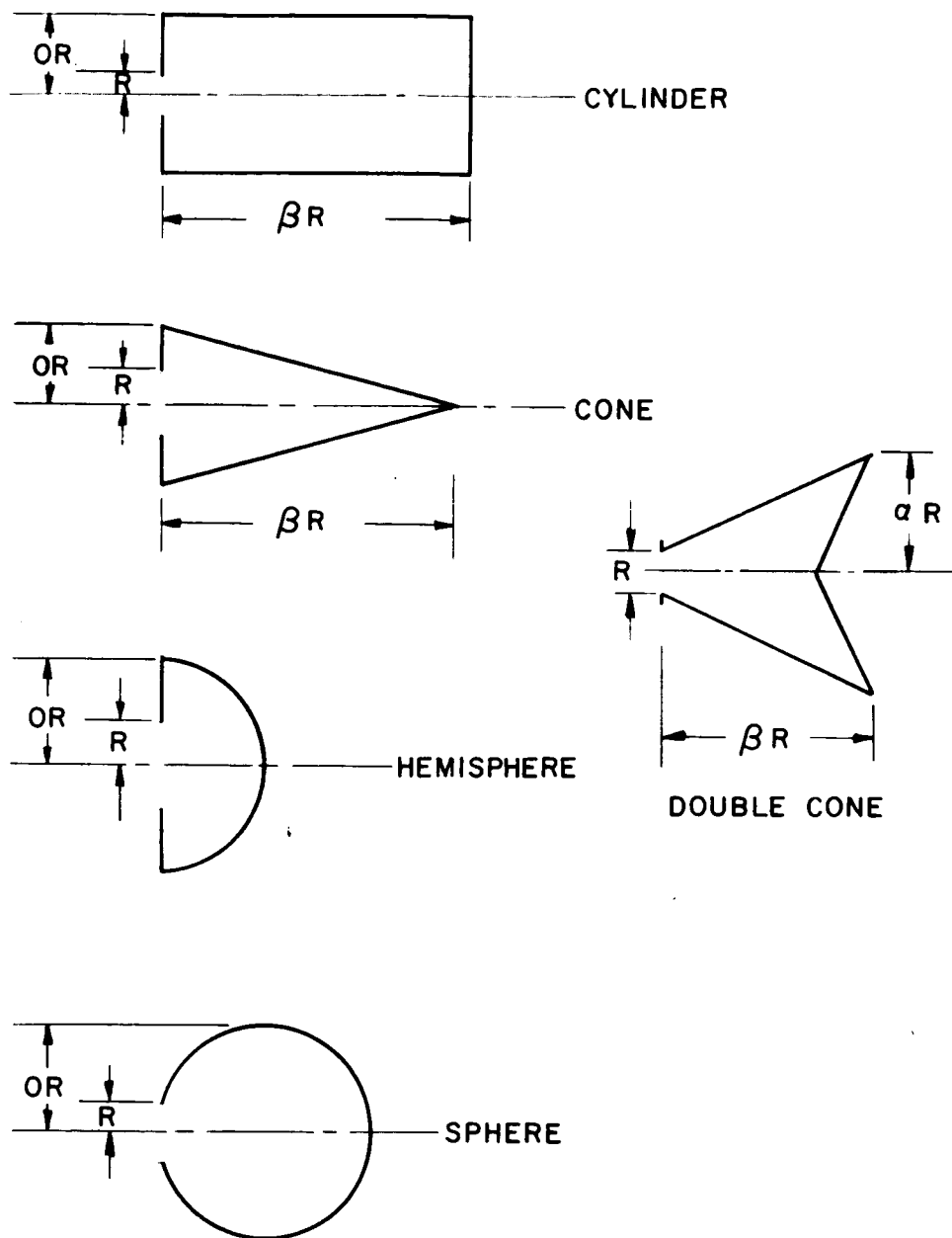


FIG. 2-39 TYPICAL CAVITY SHAPES

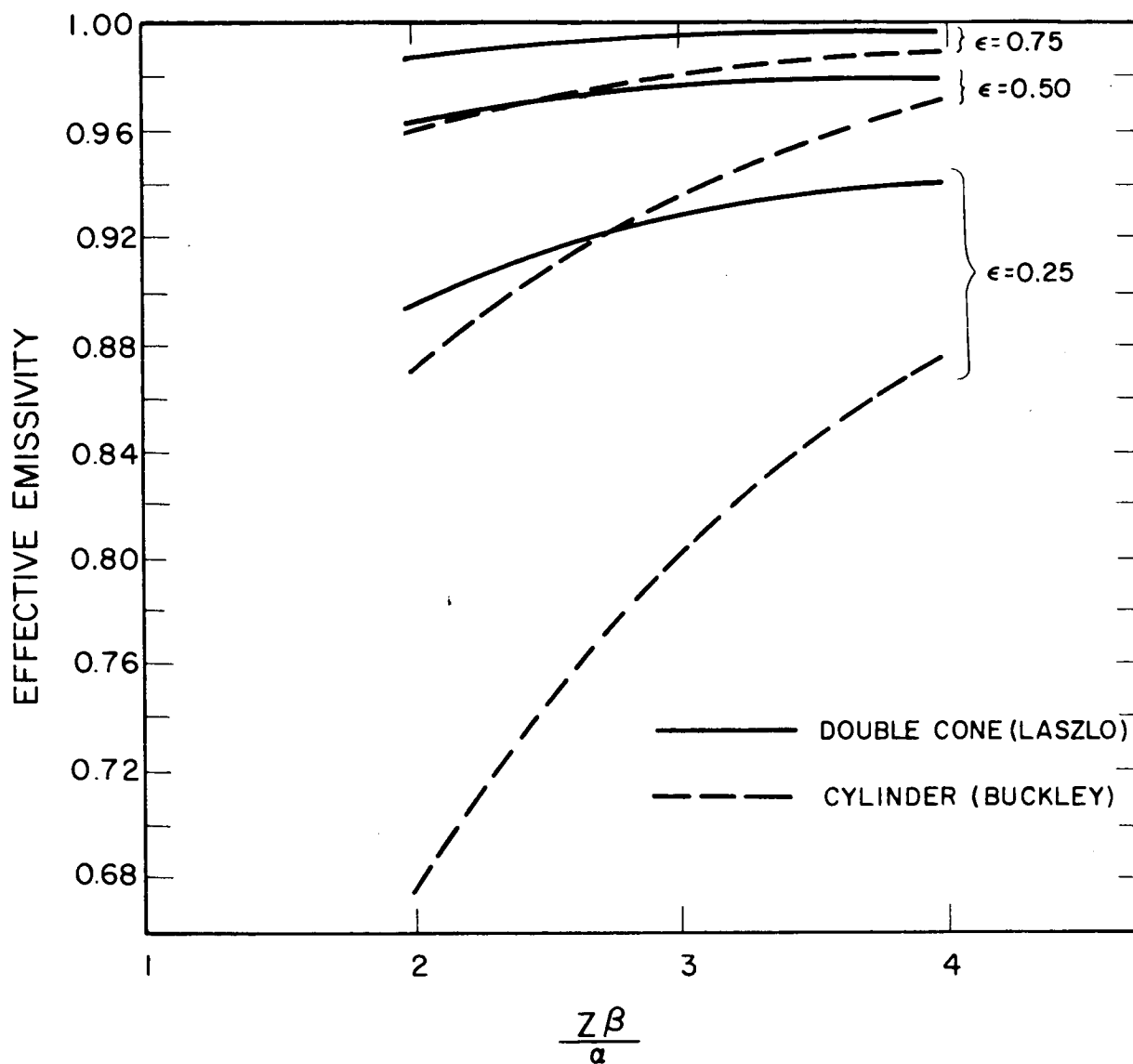


FIG. 3-40 COMPARISON OF THE EFFECTIVE EMISSIVITY OF THE CYLINDER WITH THAT OF THE DOUBLE CONE

TABLE 3-XII  
COMPARISON OF ARTIFICIAL BLACKBODY SHAPES

| $\frac{2\beta}{\alpha}$ | $\frac{A_o}{a_c}$ |                 |             | Double<br>Cone | $A_o/A_c - (A_o/A \text{ Sphere})$ |               |                        |
|-------------------------|-------------------|-----------------|-------------|----------------|------------------------------------|---------------|------------------------|
|                         | <u>Sphere</u>     | <u>Cylinder</u> | <u>Cone</u> |                | <u>Cylinder</u> *                  | <u>Cone</u> * | <u>Double<br/>Cone</u> |
| 1                       | 0.500             | 0.250           | 0.415       | 0.175          | -0.250                             | -0.085        | -0.325                 |
| 2                       | 0.200             | 0.167           | 0.309       | 0.094          | -0.033                             | +0.109        | -0.106                 |
| 3                       | 0.100             | 0.125           | 0.241       | 0.059          | +0.025                             | +0.141        | -0.041                 |
| 4                       | 0.059             | 0.100           | 0.195       | 0.041          | +0.041                             | +0.136        | -0.018                 |
| 5                       | 0.039             | 0.083           | 0.164       | 0.036          | +0.044                             | +0.125        | -0.009                 |
| 6                       | 0.016             | 0.056           | 0.111       | 0.015          | +0.040                             | +0.095        | -0.001                 |

\* Comparison of shapes with sphere

Figure 3-40 compares the effective emissivity of the cylinder cavity with that of the double cone cavity.

Figure 3-41 illustrates numerical calculations which were performed on several cavity shapes to determine the average view angle,  $\theta$ . As shown, the sphere, cylinder, and cone all demonstrate view angles which fall in a narrow bandwidth as a function of opening area to the interior surface area. The hemisphere demonstrates an unfavorable average view angle. Figure 3-42 illustrates the factor  $F_a$  as a function of cavity surface emissivity and average view angle. As shown,  $F_a$  is a strong function of  $\theta$ . Figure 3-43 illustrates the factor  $F_r$  as a function of surface emissivity and view angle  $\theta$ . As shown in Fig. 3-42, low cavity emissivities can result in a low  $F_a$  which will dramatically decrease collector-absorber efficiencies. In general, with the type of cavities and generator structures used in high-efficiency systems, the cavity wall emissivity should be as close to 1.0 as possible to decrease reflection losses.



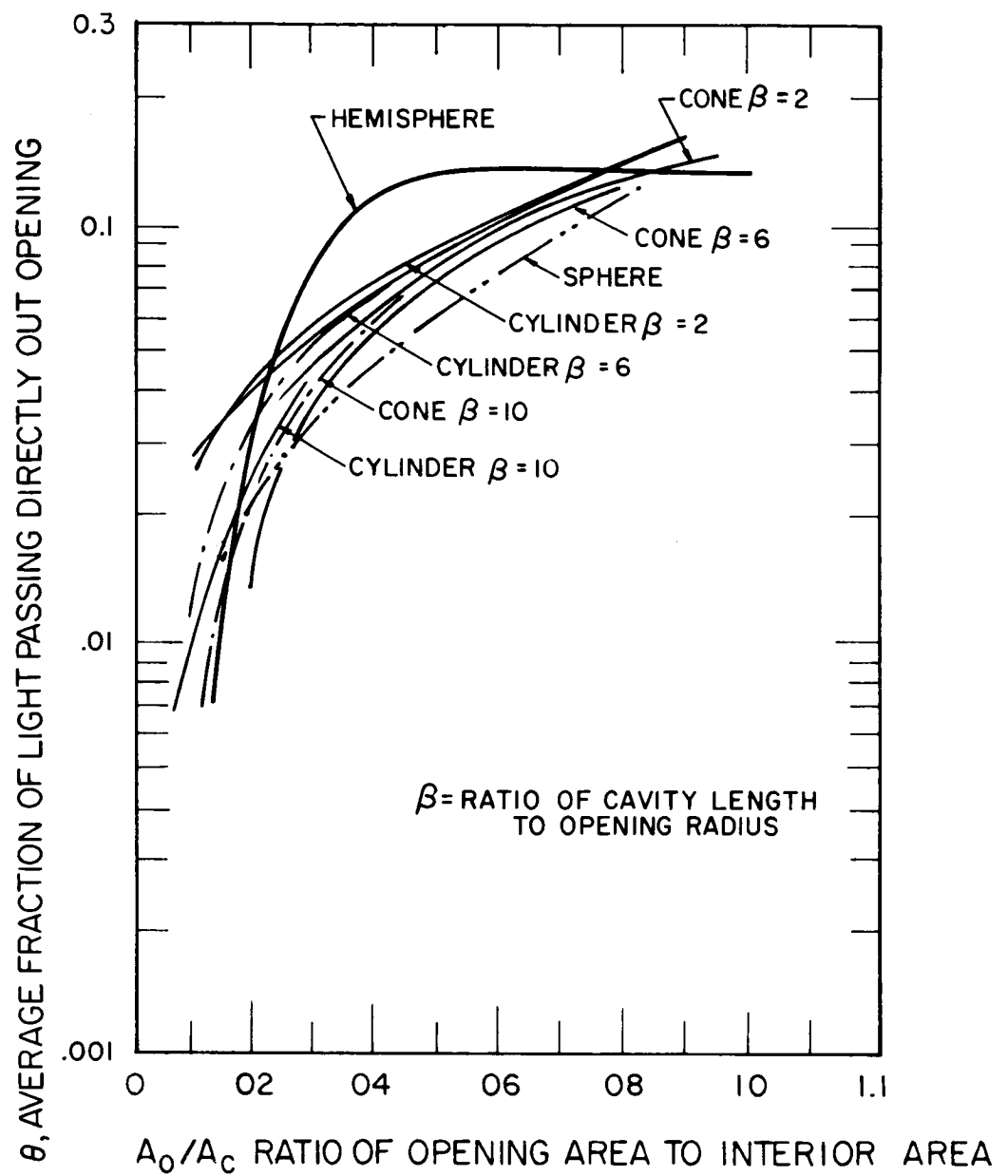


FIG. -11 LIGHT PASSING OUT OPENING OF VARIOUS CAVITIES

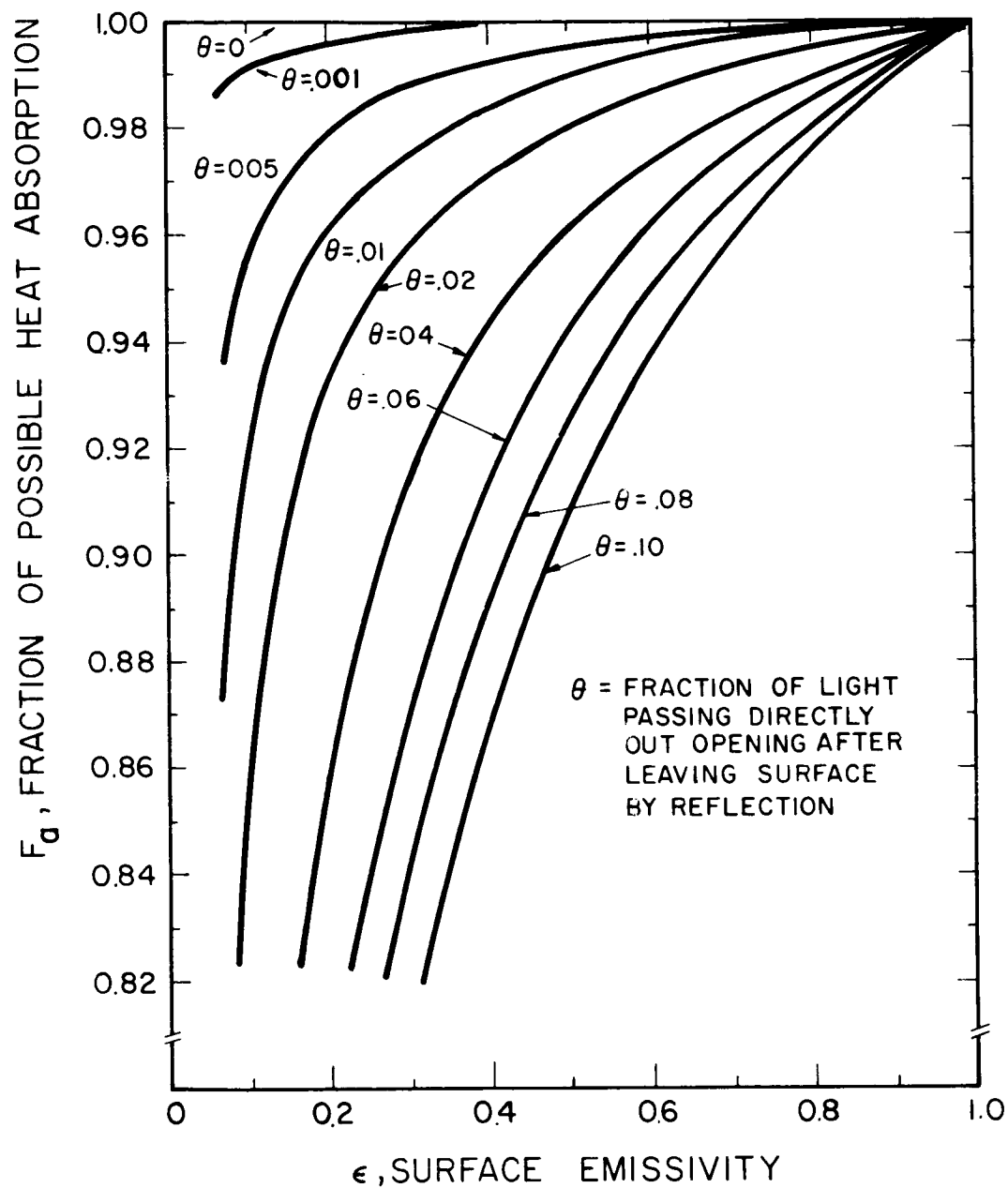


FIG. 1-42 CAVITY HEAT ABSORPTION VS SURFACE EMISSIVITY

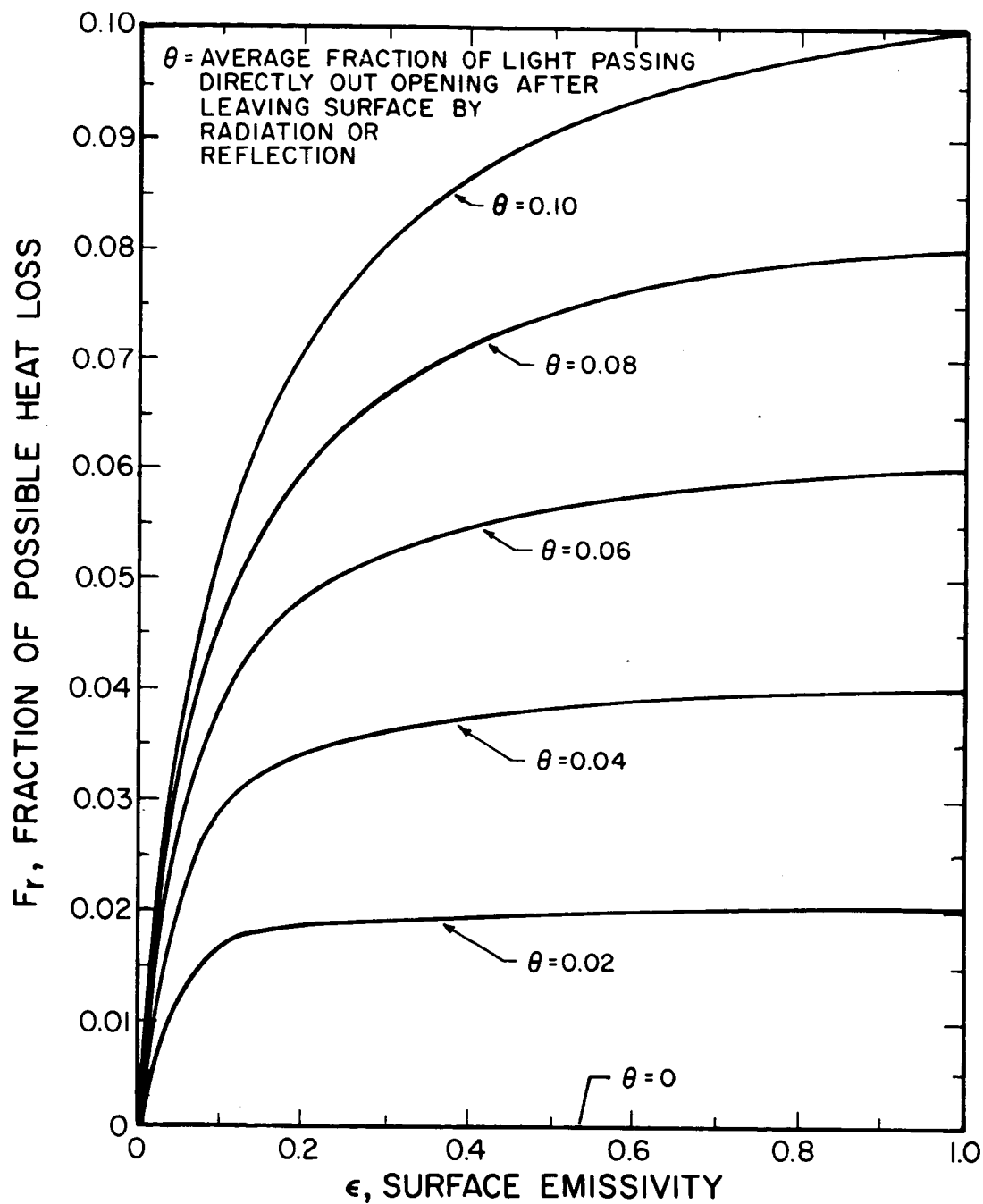


FIG. 3-43 CAVITY HEAT LOSS VS SURFACE EMISSIVITY

The optimum cavity entrance diameter is a strong function of cavity emissivity. This is shown in the example of Fig. 3-44.

Figure 3-44 illustrates the importance of reflection losses from the cavity. Collector-absorber efficiency is dramatically reduced at the optimum entrance diameter. Also, the optimum entrance diameter is smaller than would be obtained using a blackbody approximation. While specific conclusions depend on concentrator characteristics, it appears that good cavity design would demand surface emissivities greater than 0.6.

A matter of great concern to the cavity designer is the equalization of temperatures within the cavity. The magnitude of the problem is illustrated in Fig. 3-45 which shows the distribution of incoming solar flux on the rear of several cavity shapes; flat, spherical and conical. As shown, the distribution is a strong function of concentrator rim angle. For rim angles of 60 degrees, the flux intensity at the center of the flat plate is eight times the flux intensity at the flat plate edge. This situation is much better using a 45 degree rim angle concentrator. Flux distribution is uniform on a hemisphere. For a cone, the flux is maximum at the cone apex and minimum at the edges of the cone.

The distribution shown in Fig. 3-45 can be misleading with regards to temperature distribution if within the cavity. Reflection and reradiation from cavity walls is a principle mechanism for temperature equalization.

The effect of cavity shape on the redistribution of energy within the cavity is illustrated in Fig. 3-46. For the calculations of Fig. 3-46, it was assumed that the cavity was divided into two symmetrical parts. One half would receive a different amount of incoming solar flux than the other half. Assuming that each half of the cavity had the same view angle towards the entrance and the same emissivity, the redistribution in energy was calculated and is shown in

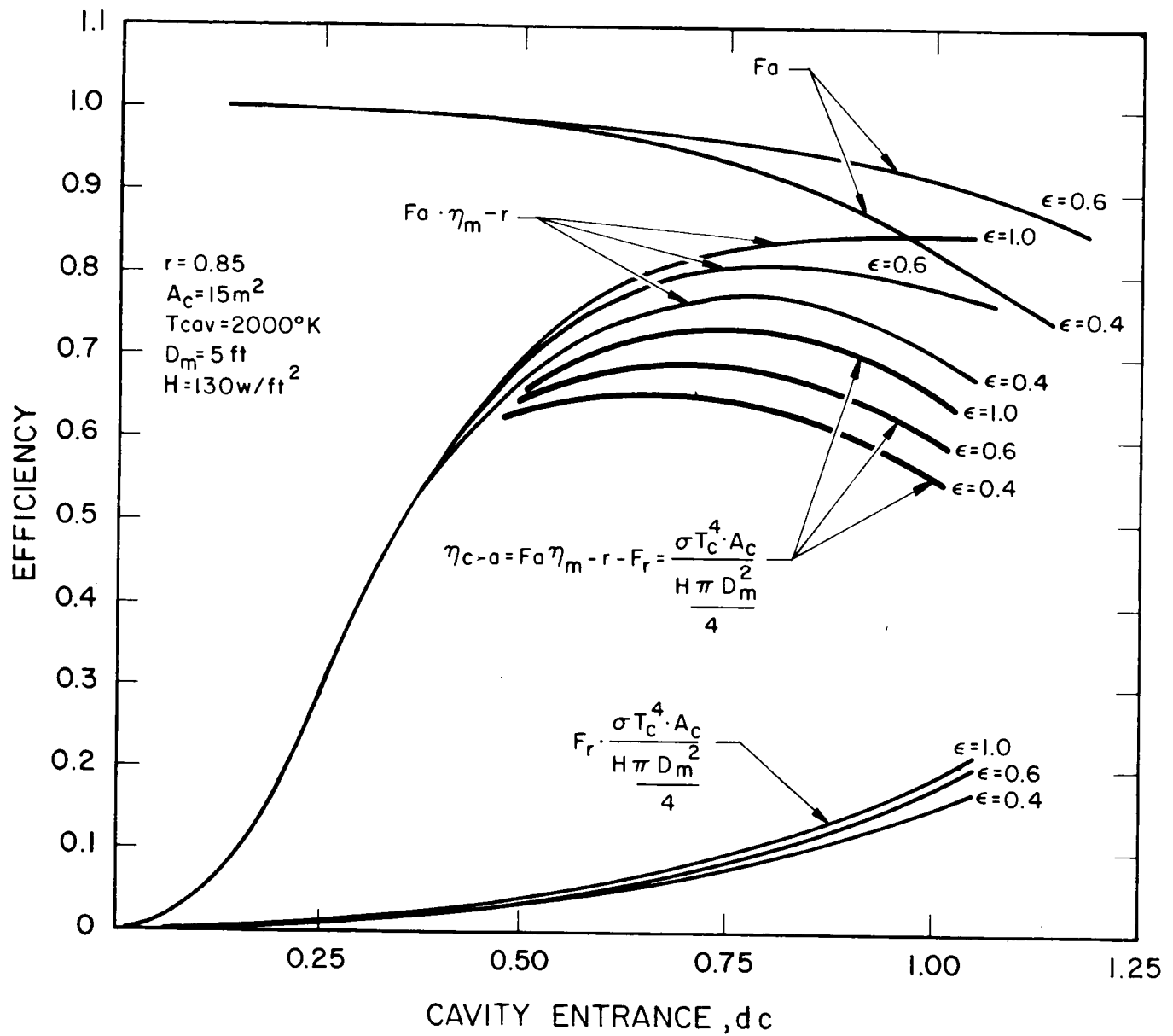
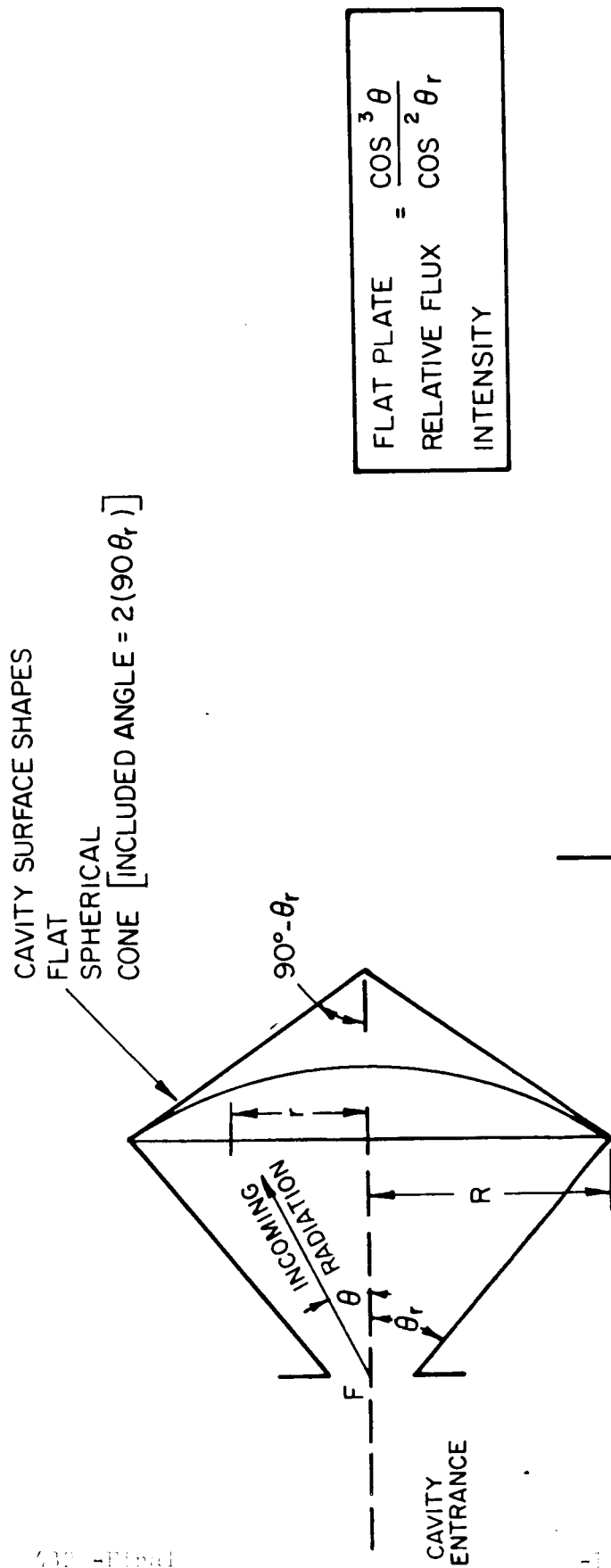


FIG. 3-54 TYPICAL OPTIMIZATION OF CONCENTRATOR CAVITY DESIGN



$$\frac{\text{FLAT PLATE}}{\text{RELATIVE FLUX}} = \frac{\cos^3 \theta}{\cos^2 \theta_r}$$

INTENSITY

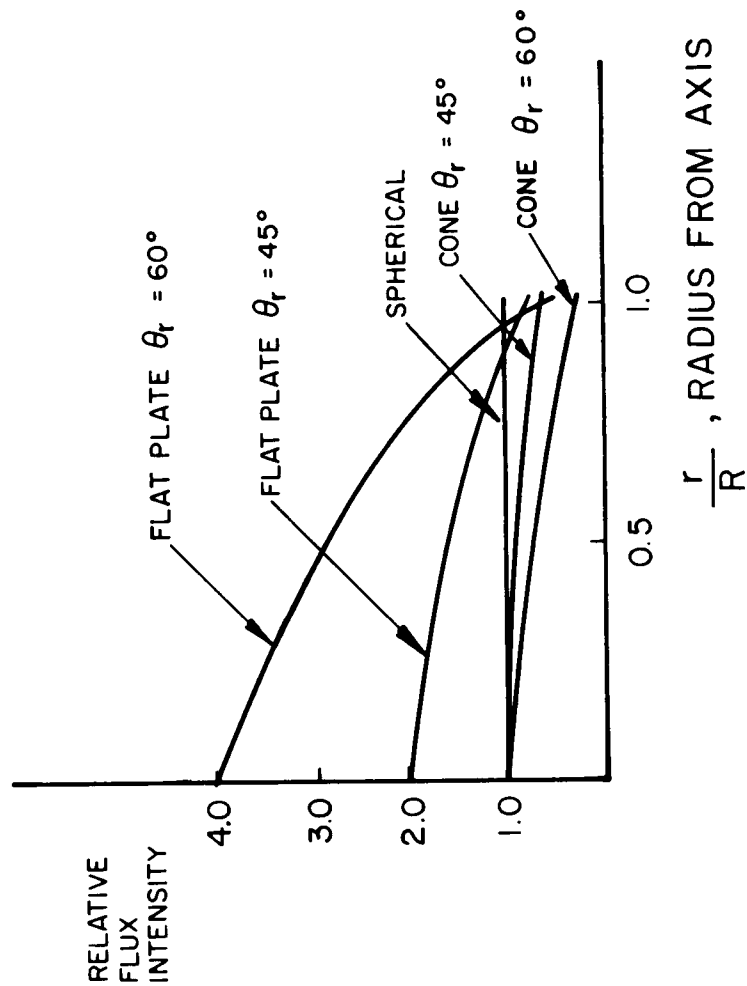


FIG. 4-10 FLUX DISTRIBUTION ON REAR OF CAVITIES

Fig. 3-46 as a fraction of possible difference in heat absorption; i.e., assuming that the difference in heat absorption is one, what fraction of this difference remains after redistribution of energy within the cavity.

Figure 3-46 shows that the redistribution of energy is a function of the view angle  $\theta$  and surface emissivity. For small view angles, and a surface emissivity of 0.6, the fraction of difference in heat absorption will be 0.4 of the original difference in heat absorption. Figure 3-46 shows that low surface emissivities are desirable from a temperature distribution viewpoint, in contrast to the desire for high surface emissivities for high cavity efficiency.

A series of calculations were performed, using a computer program set upon the IBM 1620 machine, to determine the maximum collector-absorber efficiencies obtainable at earth, Mars and Venus, for different size concentrators, different reflectivities and varying cavity temperatures. Figures 3-47 and 3-48 are typical results from the calculation.

Calculations assumed a constant interior surface area, a constant surface emissivity of 0.6, and a mirror efficiency table given in Subsection 3.1 of this report.

Also, it was assumed that  $\theta$  was equal to the ratio of cavity entrance area to interior surface area. This approximation is adequate for ball park answers but must be refined in detailed system design.

Figure 3-47 illustrates the effect of cavity temperature on maximum collector-absorber efficiency. The entrance diameter was varied for each cavity temperature and the optimum entrance diameter was selected by the computer for each temperature. Collector-absorber efficiency is shown as a function of mirror reflectivity and diameter. The efficiency obtainable with a 10-foot mirror is higher than can be obtained with a 5-foot mirror; this is primarily due to the decreased importance of the reradiation loss as a percent of the incoming radiation to the cavity.

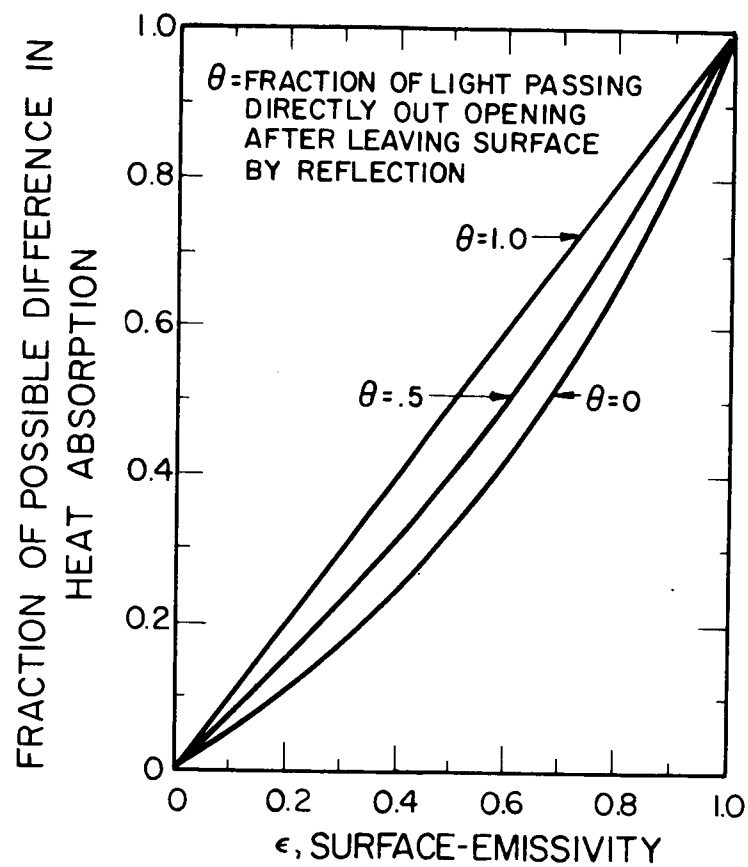


FIG. 2-46 DIFFERENCES IN HEAT ABSORPTION VS SURFACE EMISSIVITY



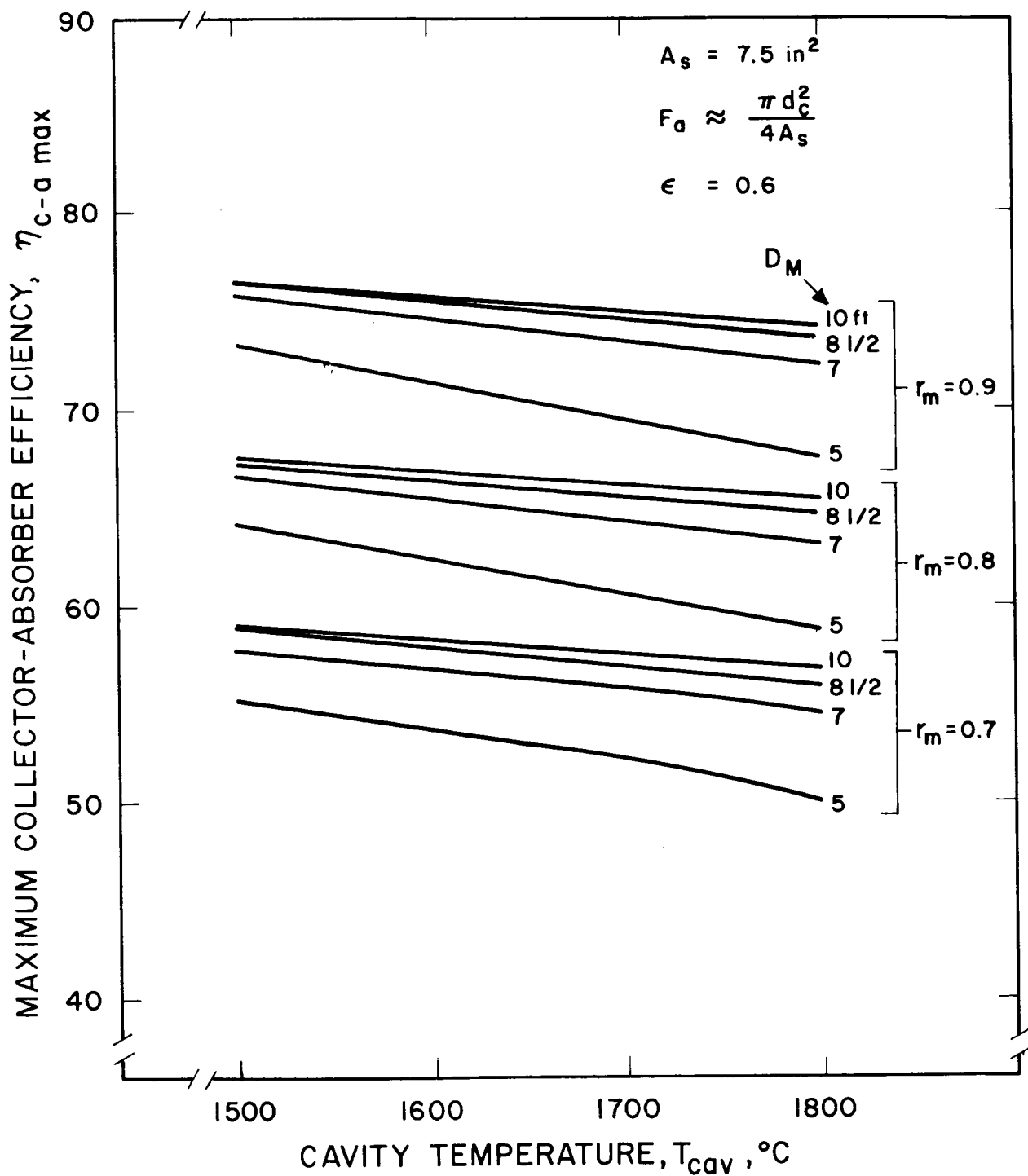


FIG. -47 MAXIMUM COLLECTOR-ABSORBER EFFICIENCY AT EARTH

Figure 3-48 shows the collector-absorber efficiency at Venus, Mars, and earth for a cavity temperature of  $1700^{\circ}\text{C}$  and a mirror reflectivity of 0.8. As shown, the efficiency at Mars drops considerably based on the assumptions of computer program. It should be pointed out, however, that the mirror efficiency used in the computer calculation was pessimistic with regards to Mars in that the effects of the decreased sun's image diameter were not taken into account.

However, the trend in collector-absorber efficiency shown in Fig. 3-48 will remain the same; i.e., mirror-absorber efficiencies at Mars will generally be less than those at earth and at Venus efficiencies will be higher. This change is due to the fact that while the incoming radiation to the cavity changes, the reradiation remains constant. The importance of cavity design is once again illustrated.

Several important conclusions can be drawn from the preceding discussion:

1. Cavity design is extremely important in determining collector-absorber efficiency. Blackbody approximations will not give a true picture of cavity losses.
2. The double coned and/or spherical cavity appear best from a loss viewpoint. However, this is primarily due to the increase of surface area compared to cavity opening area. A tradeoff analysis must be made between generator losses and reradiation and reflection losses to determine the best cavity shape.
3. Distribution of energy within the cavity can be more equalized with low cavity emissivities. This is in contrast to the need for high emissivities for high cavity efficiencies.
4. Even though the surface quality of larger mirrors is generally poorer than the smaller mirrors, the effects of reflectivity losses from the cavity entrance far overshadow the slight increase in mirror efficiency obtained by the smaller mirrors. It would appear that larger mirror systems can be more efficient than smaller mirror systems.
5. Because of cavity design, solar-thermionic system efficiencies will probably be higher at Venus than at Mars.

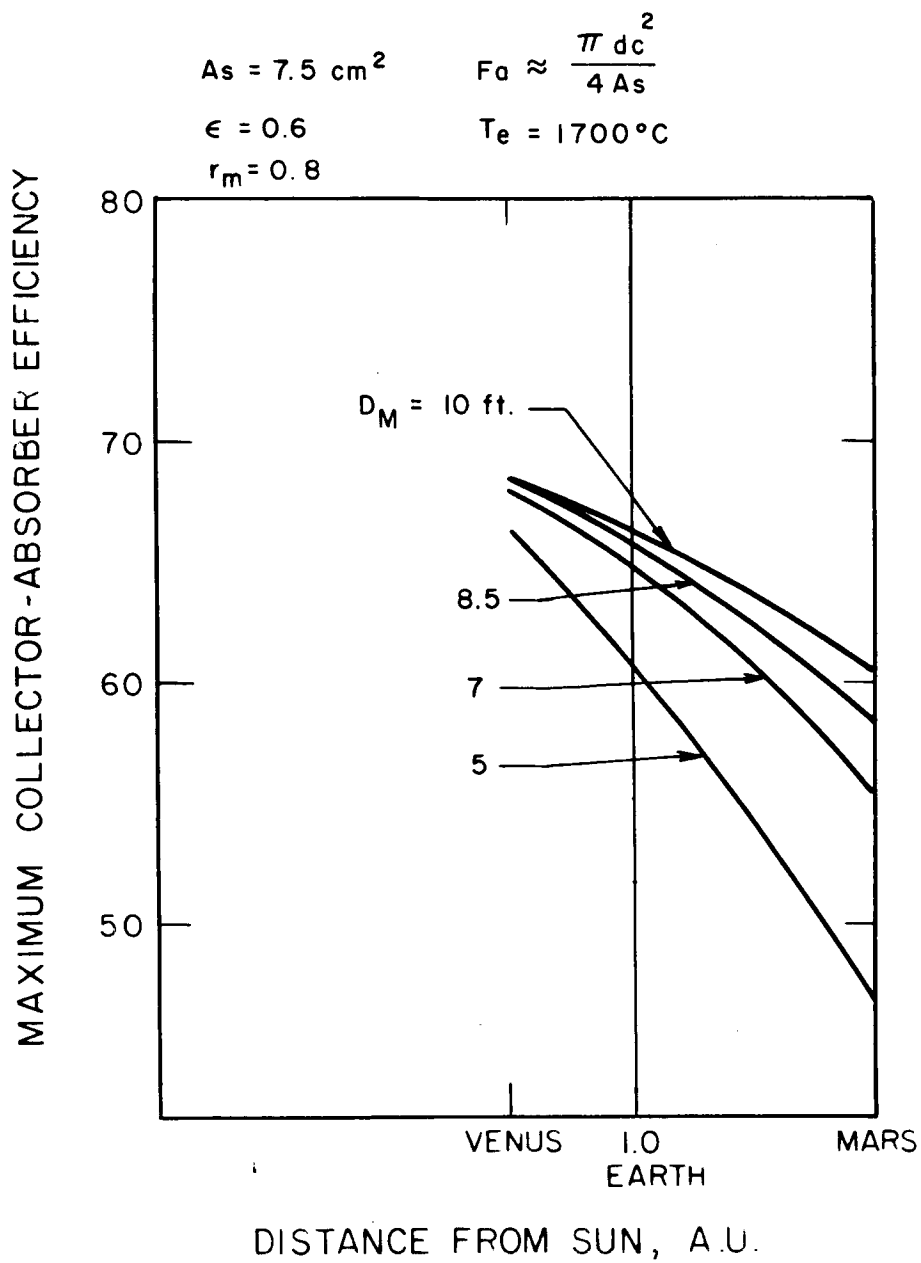


FIG. 2-48 MAXIMUM COLLECTOR-ABSORBER EFFICIENCY AT VENUS, MARS, AND EARTH

## REFERENCES

### SECTION 3

- 3-1 S. Timoshenko and S. Woinowsky-Krieger, "Theory of Plates and Shells," McGraw-Hill Book Co., Inc., 1959
- 3-2 G. S. Stern, "Thermal Elastic Analysis of a Parabolic Shell," Jet Propulsion Laboratory Technical Report No. 32-479, Aug 1963
- 3-3 Raymond J. Roark, "Formulas for Stress and Strain," McGraw-Hill Book Co., Inc., 1954
- 3-4 Robert R. Parmerter, "The Buckling of Clamped Shallow Spherical Shells Under Uniform Pressure," Aeroelasticity and Structural Dynamics, SM 63-53, AFOSR 5362, Nov 1963
- 3-5 V. P. Novozhilov, "The Theory of Thin Shells," P. Noordhoff, Ltd., Groningen, the Netherlands, 1959
- 3-6 Harvey G. McComb and Wilbur B. Fichter, "Buckling of a Sphere of Extremely High Radius - Thickness Ratio," from "Collected Papers on Instability of Shell Structures - 1962," NASA Technical Notes D-1510, 561, Dec 1962
- 3-7 Nai-Chien Huang, "Unsymmetric Buckling of Clamped Spherical Shells," American Institute of Aeronautics and Astronautics Journal, Vol. 1, Apr 1963, p. 945
- 3-8 Charles D. Babcock and Ernest D. Sechler, "The Effect of Initial Imperfections on the Buckling Stress of Cylindrical Shells," NASA Technical Note D-2005, Jul 1963
- 3-9 Millard W. Johnson and Eric Reissner, "On Transverse Vibrations of Shallow Spherical Shells," Quarterly of Applied Mathematics, Vol. 15, Apr 1958, p. 367
- 3-10 Y. K. Lin and F. A. Lee, "Vibrations of Thin Paraboloidal Shells of Revolution," J. Appl. Mech., Vol. 27, Dec 1960, p. 743
- 3-11 P. M. Naghdi and A. Kalnis, "On Vibrations of Elastic Spherical Shells," J. Appl. Mech., Vol. 29, Mar 1962, p. 65
- 3-12 Eric Reissner, "On Vibrations of Shallow Spherical Shells," J. Appl. Phys., Vol. 17, Dec 1946, p1038
- 3-13 W. H. Hoppmann, II, "Frequencies of Vibration of Shallow Spherical Shells," J. Appl. Mech., Vol. 28, Jun 1961, p. 305

## REFERENCES (contd)

### SECTION 3

- 3-14 William F. Stokey, "Vibration of Systems Having Distributed Mass and Elasticity," Section 7-1 of "Shock and Vibration Handbook - Volume 1," Cyril M. Harris and Charles E. Crede, McGraw-Hill Book Co., 1961
- 3-15 Jet Propulsion Laboratory, "Appendix B - Vibration Survey - Mariner B, Nickel Solar Energy Thermionic Reflector," 1961
- 3-16 "Solar Energy Thermionic Conversion System - Appendix B - Concentrator Test Data and Observations," JPL Contract 950109, 1962
- 3-17 Harvey H. Hubbard and John C. Houbolt, "Vibration Induced by Acoustical Waves," Section 48 of "Shock and Vibration Handbook - Volume 3"
- 3-18 Harry F. Olson, "Acoustical Engineering," Van Nostren Co., 1957
- 3-19 Robert W. Hess, Robert W. Herr, and William H. Mayes, "A Study of the Acoustical Fatigue Characteristics of Some Flat and Curved Aluminum Panels Exposed to Random and Discrete Noise," NASA Technical Notes D-1, Aug 1959

#### 4. SYSTEM STRUCTURE AND MECHANISMS

The elements of the systems structure can be defined as follows:

1. Support arms for the generator
2. Electrical and mechanical connections for the support arms at the generator and mirror ends
3. Vehicle adapters - a rigid or deployable structure which holds the solar-thermionic system to the vehicle and locates it in the proper position during the unfolding sequence
4. Electrical leads to the system electronics from the generator support
5. Launch support structures such as dampers, pylons for holding the generator, etc.

All of these items contribute to system weight. Design details depend significantly on the adaptation of the system to the vehicle; for example, the location of the electronics, field of view limitations, etc.

This section is primarily concerned with the tradeoffs to be considered in the design of generator support structure. The generator support design is a critical item in solar-thermionic system design. The choice of the support arm configuration and the methods of integrating into the system will depend on:

1. Vibration characteristics of the structure
2. Packaging and deployment possibilities
3. Effect on system design

The design of the arms should represent an optimum tradeoff between the following factors:

1. Minimization of heat conducted to electrical components
2. Obscuration of the concentrator
3. Power losses in the leads due to high resistance

4. Ability to accurately place the generator without movement due to thermal gradients
5. Minimum weight
6. Ability to hold instrumentation, leads, etc.
7. Elimination of magnetic field

From a systems viewpoint, perhaps the most serious problem is the conductivity of heat down the relatively thick leads to the DC/DC converter. Temperatures above 50°C at the DC/DC converter will result in lower efficiencies and reliability; 30°C is desirable. For larger concentrators, on the order of 10 ft, minimum first-mode resonant frequency requirements may result in rather thick arms and limit tradeoff possibilities.

The choice of materials was examined and it was found that beryllium was probably the best material from a tradeoff viewpoint for the generator support arms; however, further examination is warranted into the joining techniques for beryllium structures.

Two sets of generator support arms for a 5-foot concentrator have been assembled in prototype flight form. The first concept consisted of a three-arm generator support in which one of the members was telescoping and hinged at each end so that the support arm structure could be folded during launch. The two rigid arms served as current conductors. This concept is illustrated in Fig. 4-1. Generator support arms consisted of riveted aluminum truss structures with the following characteristics:

Weight (three-arms) - 3 lbs

Obscuration - 3 percent

IR efficiency ~ 0.5 percent

Minimum resonant frequency ~ 1,000 cps

A second set of arms for a 5-foot concentrator was assembled in 1964 and is shown in Fig. 4-2. The structure holds the generator rigidly in place and consists of six arms each of which consists of two coaxial tubes. All of the arms carry electrical current. The six arms are formed in groups of two to create an equivalent three-armed structure.

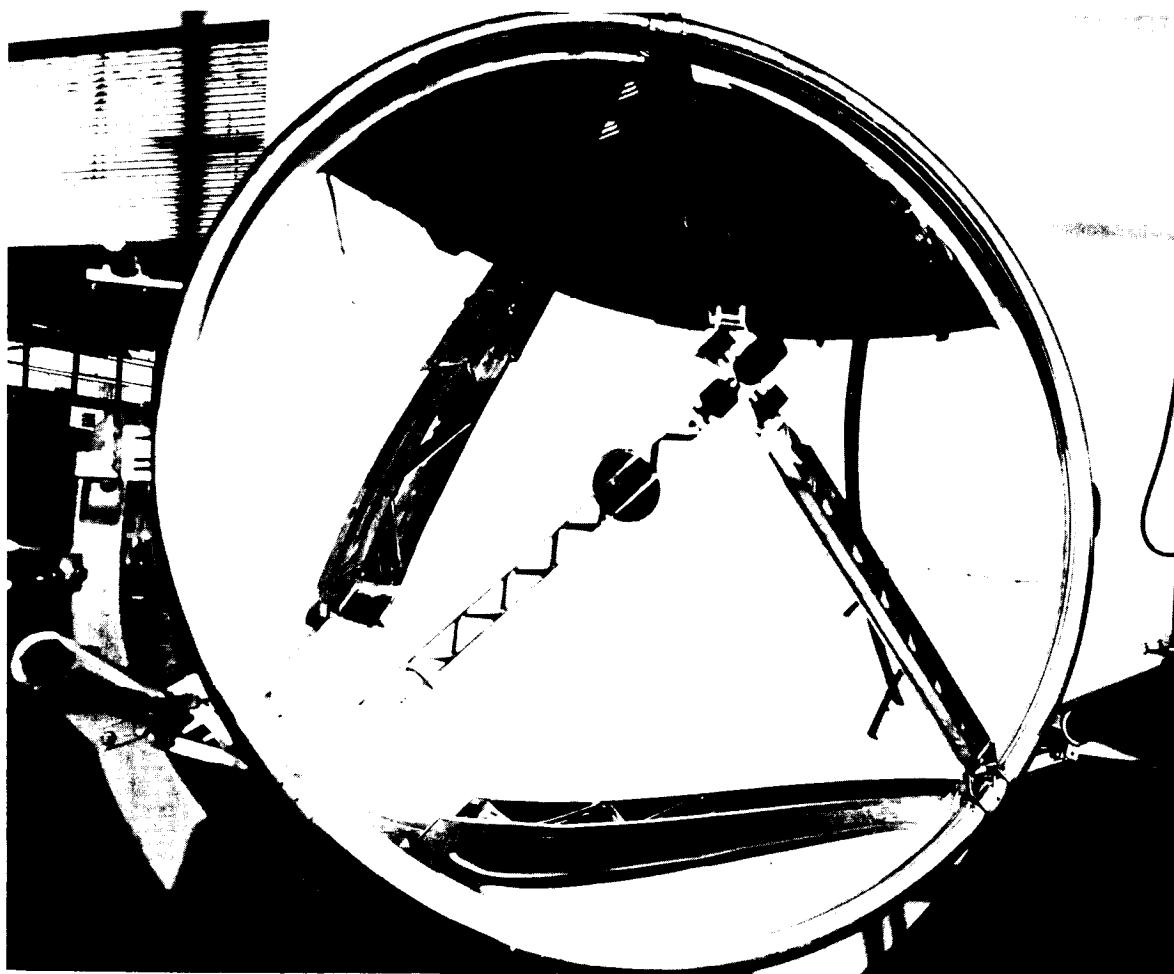


FIG. 4-1 PHOTOGRAPH OF THREE-LEGGED UNFOLDING SUPPORT ARMS



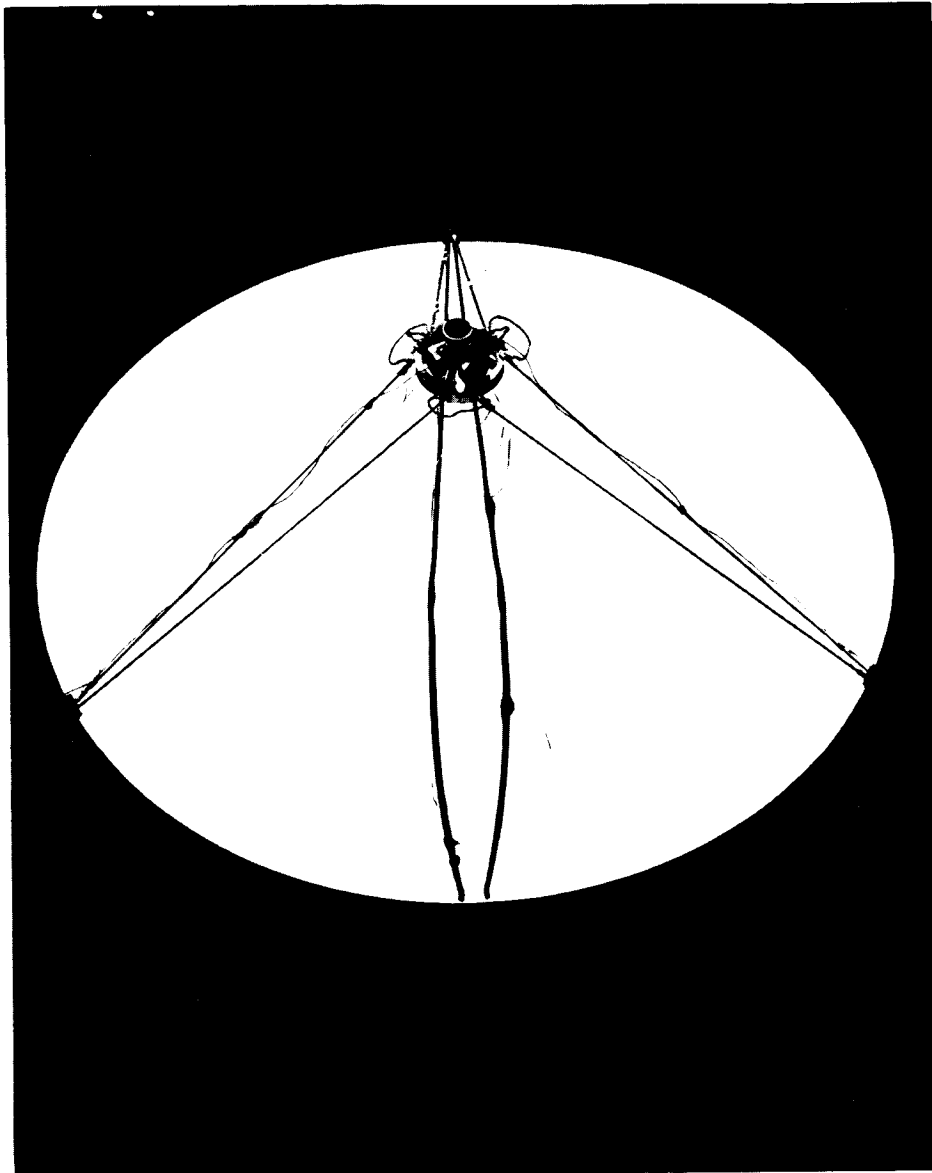


FIG. 4-2 - PHOTOGRAPH OF RIGID, COAXIAL,  
3-LENNED SUPPORT ARMS

The arms are made of aluminum and exhibited the following characteristics:

Weight - 1.3 lbs

Obscuration - 3 percent

IR loss - about 1 percent

The structure shown in Fig. 4-2 was subjected to the Atlas-Centaur flight acceptance vibration tests in March, 1965; no degradation or failure was observed. Amplification of the acceleration forces imparted to the generator was on the order of 3 to 5.

The structures shown in Figs. 4-1 and 4-2 illustrate the state of the art in generator support structures. A great deal of work remains in this area to result in an optimum system and to understand the design limitations imposed by the generator structure. Empirical and analytical data of a variety of types is required prior to final design of a system. Many of the items required for an investigation are discussed in this section.

#### 4.1 Rationale for Generator Support Design

Figures 4-3 and 4-4 illustrate the factors in consideration of the generator support design. As shown in Fig. 4-3, vehicle constraints and concentrator/system constraints of many kinds must be considered in the initial generator support configuration study. The configuration study leads into the optimization and material selection for the arms.

A more detailed program is shown in Fig. 4-4 which involves the generator support arms design after vehicle constraints are considered. Most of the factors to be considered in generator support design are listed.

#### 4.2 Design for Nonmagnetic Characteristics

An important requirement of a solar-thermionic system structure is to minimize magnetic fields and magnetic field variation. This is due to the desire for minimization of interference with magnetometer or other field measurements, and to avoid problem areas in attitude control introduced by magnetic torque. This can be accomplished most successfully with a coaxial arrangement for the generator support where two opposing currents create magnetic fields which cancel each other as illustrated in Fig. 4-5.

The net magnetic field with the coaxial arrangement will be a function of the differences in current between inner and outer tubes.

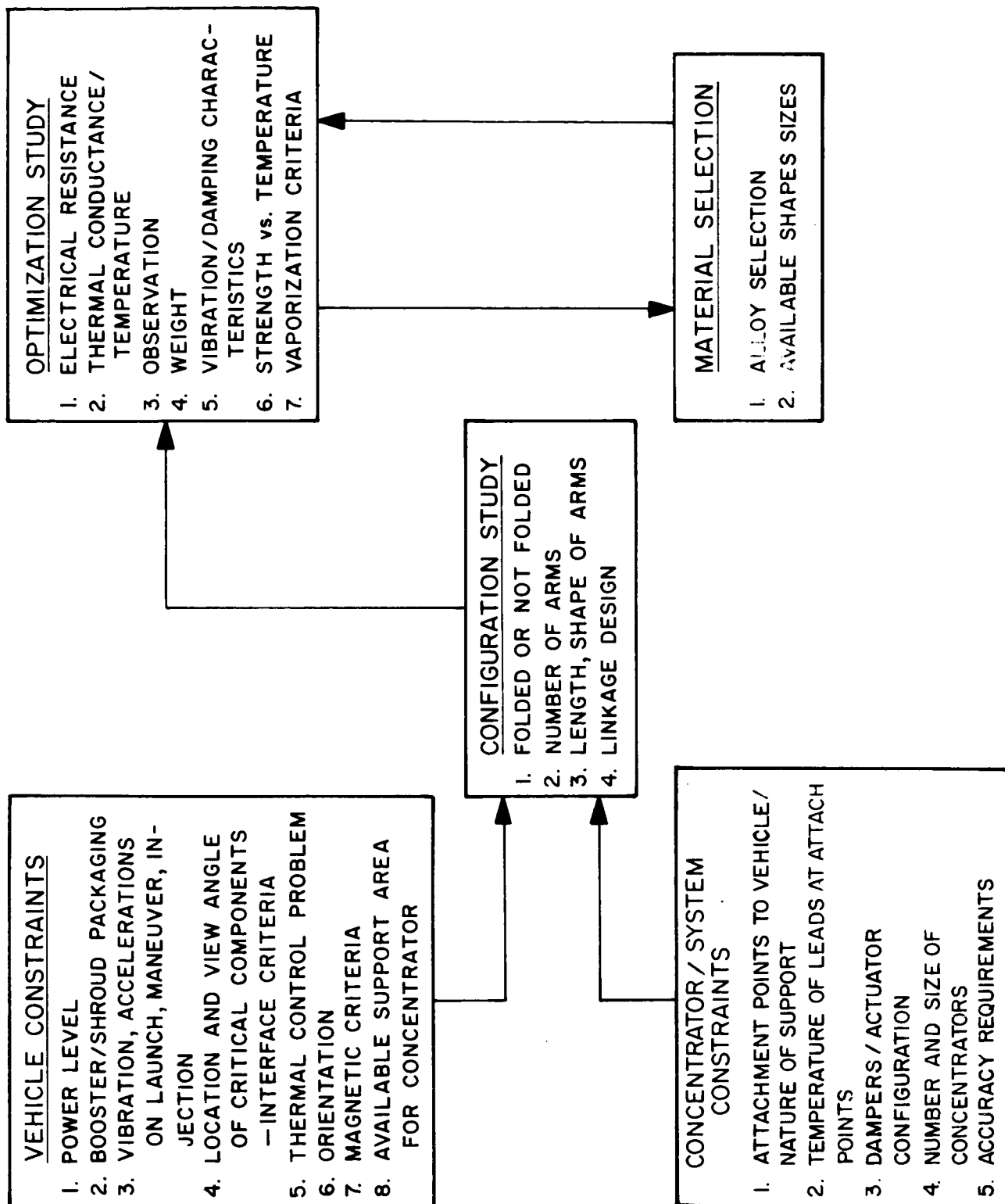


FIG. 4- GENERATOR SUPPORT REQUIREMENTS

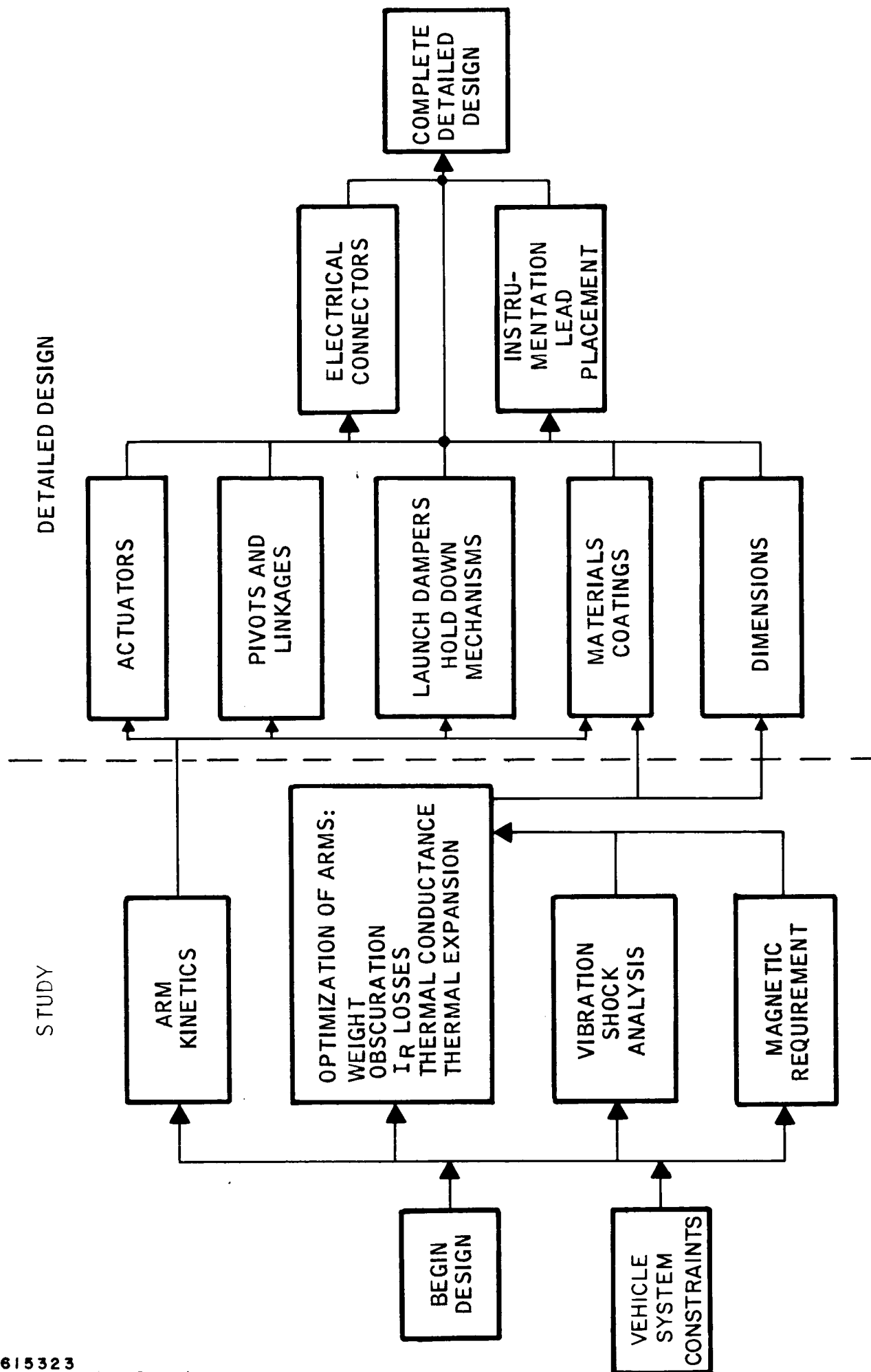
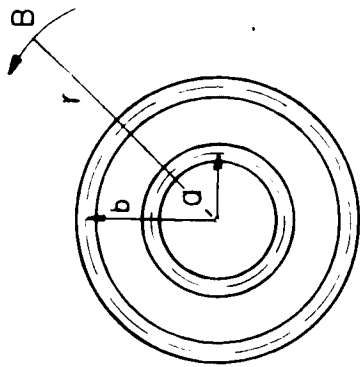
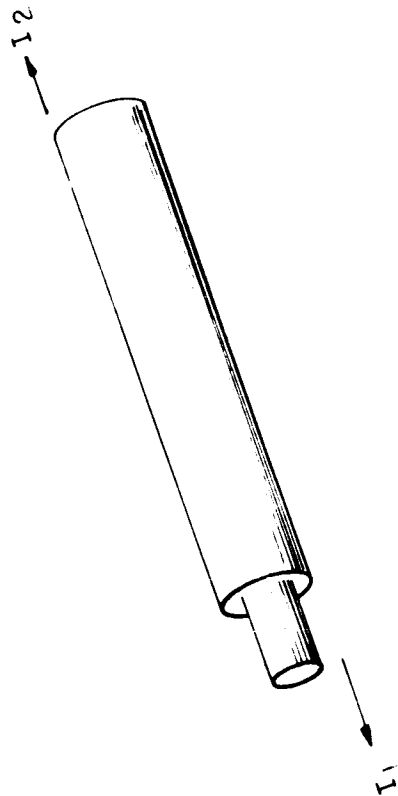


FIG. 1-4 DESIGN PROGRAM FOR GENERATOR SUPPORT



MAGNETIC FIELD  $-B = \left( \frac{I_2 - I_1}{2\pi r} \right) H_0 \times 10^9$  GAMMA

$$H_0 = 4\pi \times 10^{-7}$$

$r$  IS IN METERS

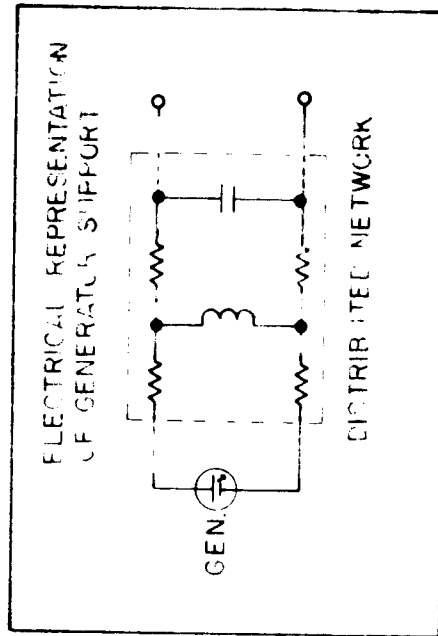
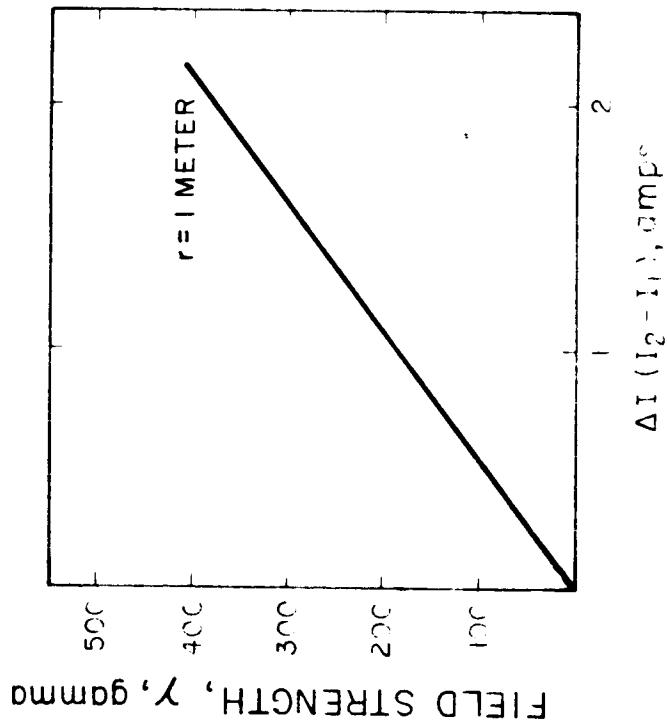


FIG. 1-3 MAGNETIC CHARACTERISTICS OF COAXIAL GENERATOR SUPPORT

The magnitude of this field is illustrated in Fig. 4-5. For example, at a distance of 1 meter from the generator support arm (perpendicular to the axis) a current difference of 1 amp will result in a magnetic field of 200 gamma (based on the infinitely long tube approximation).

Differences in the current between the inner and outer tube will exist no matter how carefully the tubes are matched. This difference will result from differences in temperature and therefore different resistivities, differences in the materials used, effects on resistivity at temperature for long periods of time, surface effects, etc. Therefore, in a tube carrying 100 amps, a 1 percent difference in current between the inner to outer tube would result in a one amp difference in current. The specification for the Mariner panel was 3 gamma at 3 feet. Therefore, the seriousness of the magnetic field problem and the importance of careful matching of the tubes is well illustrated.

The coaxial tube arrangement represents a distributed electrical network shown in Fig. 4-5. There exists the self-inductance of the tube, the mutual inductance between tubes, and the capacity between tubes along with the electrical resistance. The amount of energy stored within this distributed network is fairly low. When a sudden change of current in the tube occurs, for example, during a temporary misorientation, this energy will be discharged to the DC/DC converter. A detailed investigation must be made of the energy within the distribution network, the effect of discharging this energy into the low impedance DC/DC converter, and the maximum changes in current which can be tolerated as a result.

Another specification which is pertinent to the power system used on space vehicles is the change in magnetic field which can be expected as a function of time. Thus, larger changes can saturate the magnetometer. This is another reason why the current from the generator must be carefully controlled to be constant. Small but fast variations in generator current may create magnetic field disturbances which are detrimental to magnetometer operation.

#### 4.3 Generator Support Length

Figure 4-6 illustrates the length of the generator support arm as it varies with the mirror diameter and concentrator rim angle. Exact length will depend on generator diameter and end attachments to the generator support arm. Figure 4-6 can be considered as a good approximation.

#### 4.4 Typical Unfolding Schemes

There are many generator support configurations and unfolding mechanisms which can be conceived. Some of these are illustrated in this text and include:

1. Rigid support arms illustrated in Fig. 4-2. The number of arms can vary according to design optimization but will be in the range of 2 to 6. The system in Fig. 4-2 shows six support arms grouped in pairs to form a three-arm support. In the investigation no particular advantage was found going beyond the three-armed structure; the aid in vibration characteristics is not worth the cost and obscuration of the concentrator. Two-armed and one-armed rigid generator supports introduce vibration problems.
2. A second concept is that of a three-legged generator support with folding arms illustrated in Figs. 4-1 and 4-7. The folding could be in one arm, as shown, with hinges on all three arms. The unfolding sequence implies an actuator and greater reliability problems. Because of the difficulty of maintaining electrical continuity, the best approach might be to have the electrical leads in the two rigid supports and the instrumentation on the unfolding member.
3. Figure 4-8 illustrates a two-legged unfolding system where the arms are hinged at the mirror torus. The minimum length of the arms is defined by the geometry of the system as shown. For a  $45^{\circ}$  rim angle mirror, the generator entrance would be located about at the edge of the mirror when folded.

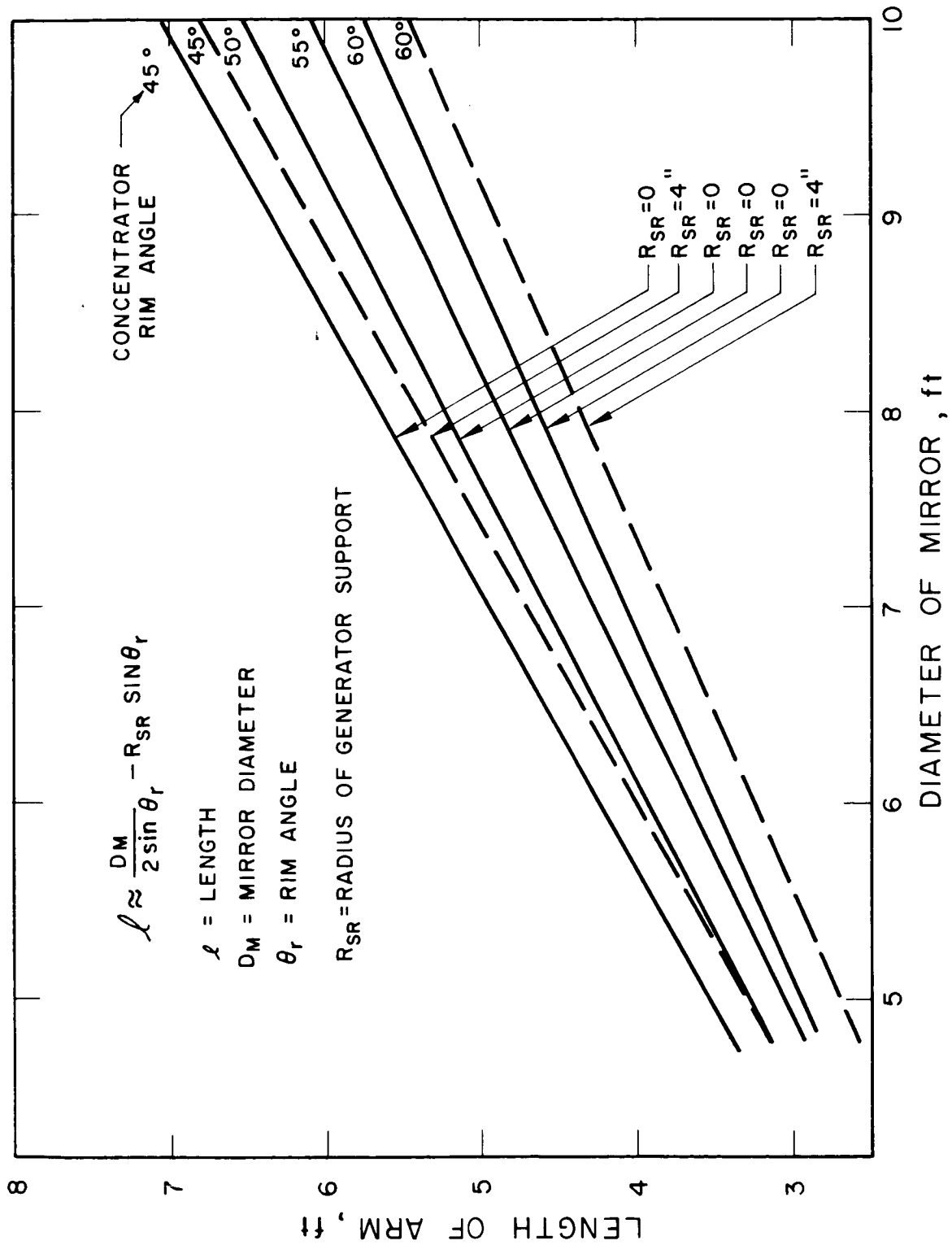
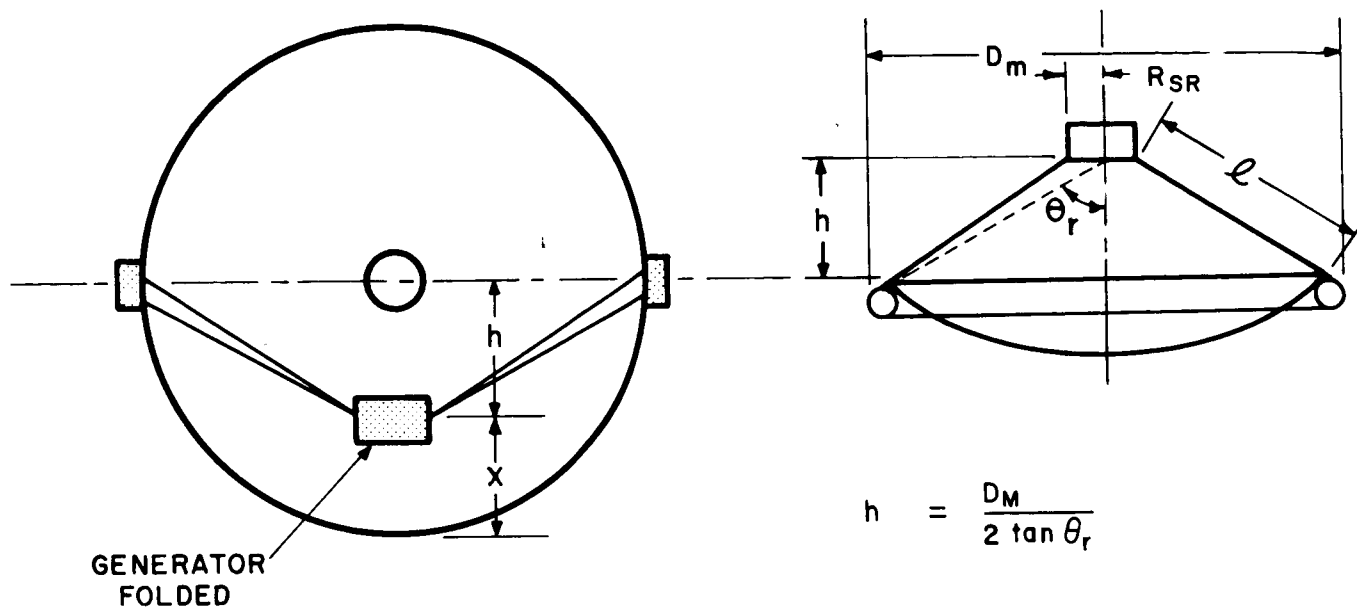


FIG. 4-6 LENGTH OF GENERATOR SUPPORT ARM







$$l \approx \frac{D_M}{2 \sin \theta_r} - R_{SR} \sin \theta_r$$

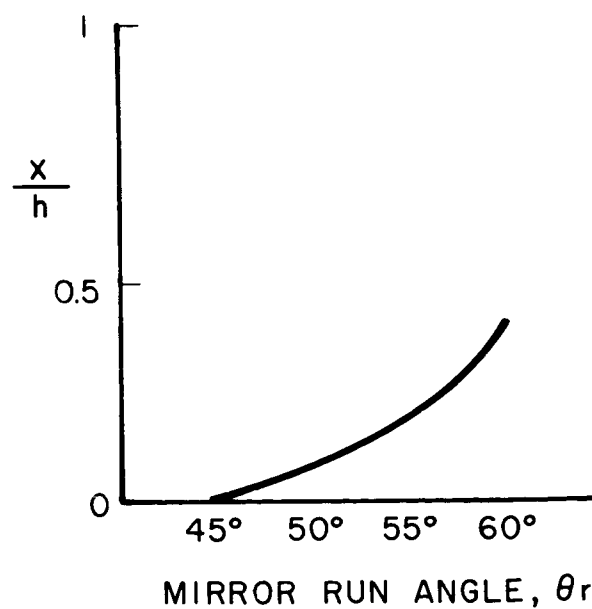
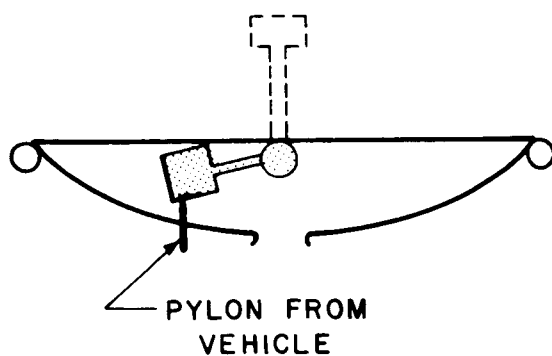


FIG. 4-8 DIAGRAM OF "TWO-LEGGED UNFOLDING" GENERATOR SUPPORT ARMS

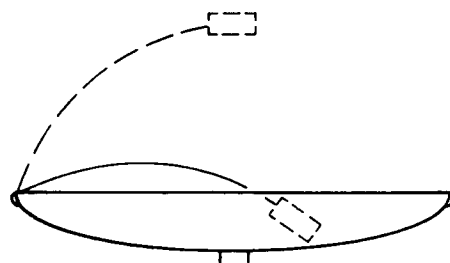
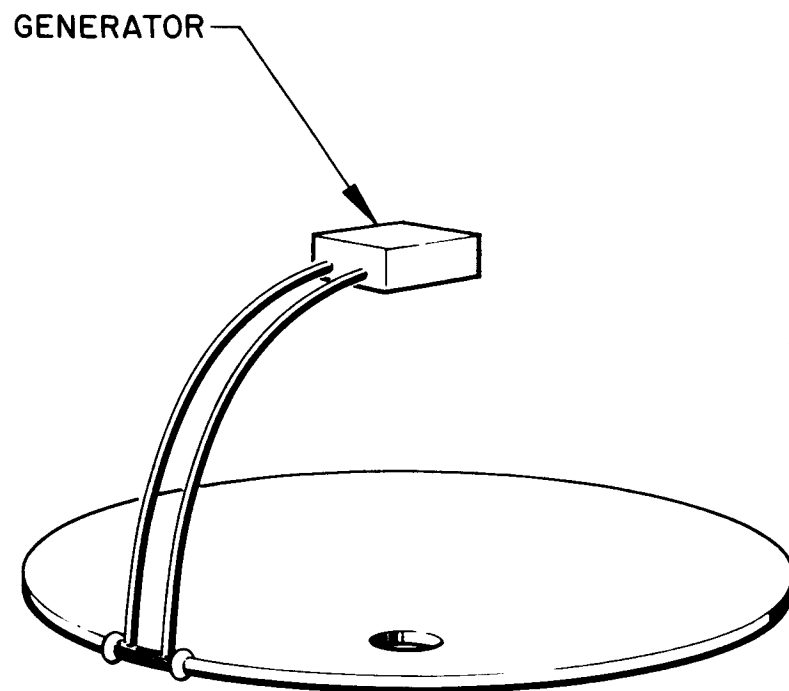


FIG. 4-9 ILLUSTRATION OF ONE-ARMED GENERATOR SUPPORT

For a  $60^\circ$  rim angle, mirror, the generator would necessarily be folded in a position between the center and edge of the mirror. For this reason, a  $45^\circ$  rim angle mirror might be advantageous from a structural viewpoint when using the two-legged generator support approach. One problem with the two-legged approach is the greater difficulty in accurate location of the cavity entrance after unfolding.

4. Figure 4-9 illustrates a one-arm generator support which is unfolded and rotated into position. Accuracy and folding problems are similar to the two-armed approach.
5. Figure 4-10 illustrates a "bucket handle" approach which is unique in that the generator support arms position the concentrator with regards to the generator instead of vice versa. The bucket handle approach has several interesting possibilities: first, the optimization of the generator support arms no longer depends on tradeoffs between thermal conductivity and resistivity. Second, packaging arrangements appear somewhat more flexible. It should be noted, however, that the problem of the leads to the DC/DC converter remains the same, i.e., the leads must minimize the temperature of the DC/DC converter while decreasing the losses. Because obscuration is no longer a factor in the tradeoff in lead design, it appears possible to decrease overall system losses in the leads.

Advantages between rigid and unfolded schemes cannot be determined until detailed designs are made. Rigid support arms are difficult to package but offer fewer problems where the shroud may be significantly larger than the vehicle. Any unfolding scheme introduces a reliability consideration and increases the possibility of mislocating the generator upon unfolding.

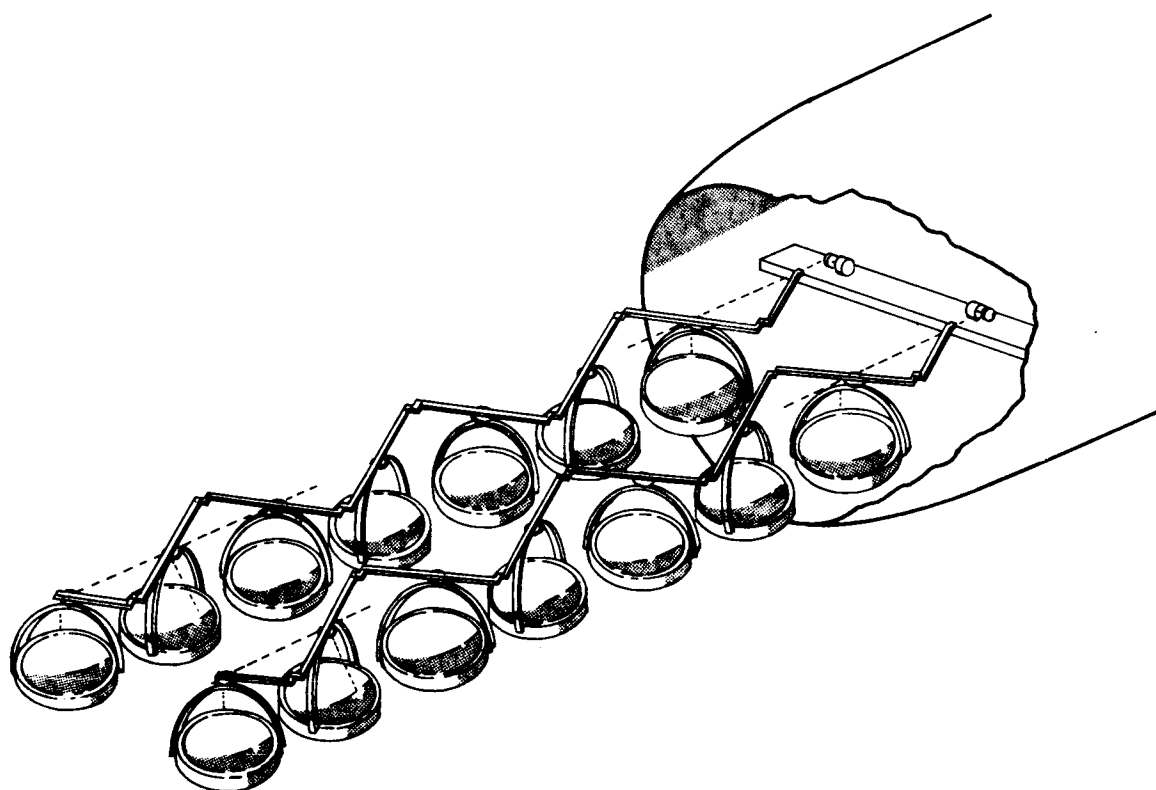
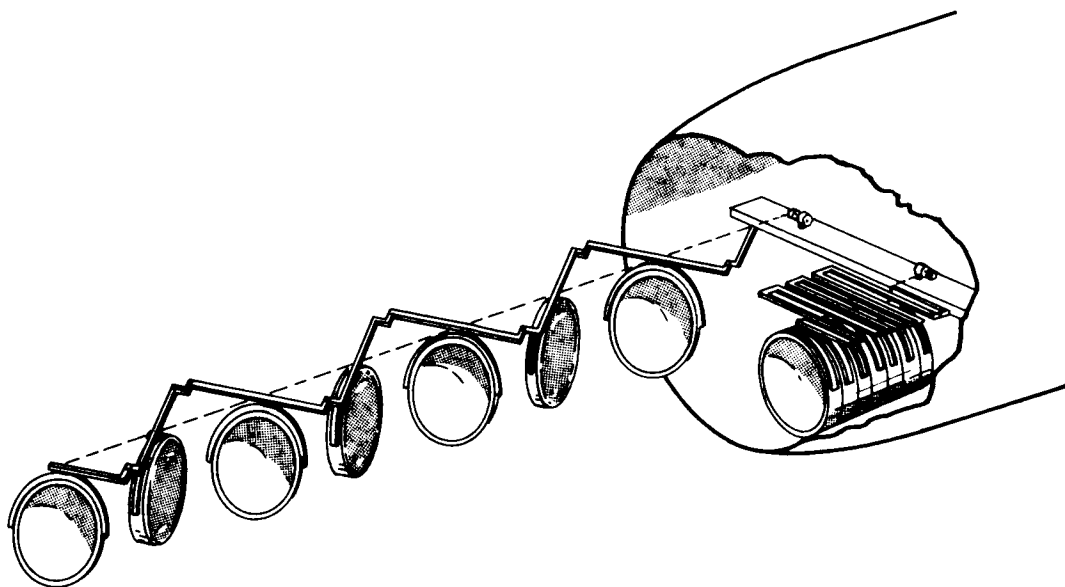


FIG. 4-10 BUCKET HANDLE GENERATOR SUPPORT CONFIGURATION

#### 4.5 Material Considerations

An investigation was made of various materials which were relatively light in weight and appeared suitable for use in the generator support configuration. Table 4-I summarizes the properties of these materials as derived from a variety of handbooks, manufacturer's information, etc.

The selection of materials depends on a large number of factors. Several of these are discussed below.

1. Thermal Conductivity

Thermal conductivity should be small to minimize heat flow down the support. Aluminum, beryllium, and beryllium alloys all exhibit about the same degree of thermal conductivity. Titanium, however, has a relatively small thermal conductivity.

2. Vibration Characteristics

The vibration characteristics of the generator support will be determined by the EI factor and the density of the arms. EI should be high and density should be low. Beryllium and Be-Al are superior to other materials in this characteristic.

3. Electrical Resistivity

Resistivity should be low to decrease electrical losses. Aluminum, beryllium, magnesium and various alloys exhibit low resistivity. Titanium, however, exhibits very high electrical resistivity and for this reason the use of titanium will introduce prohibitive electrical losses.

4. Coefficient of Expansion

Coefficient of thermal expansion should be low to minimize the chance of mislocation of the generator. Furthermore, the change in coefficient with temperature should be minimum in order to allow adequate prediction of arm location.

TABLE 4-I  
MATERIAL SUMMARY

| Material                   | Yield Strength<br>1000 psi | Modulus of Elasticity<br>Tension<br>10 <sup>6</sup> psi | Electrical Resistivity<br>ohm-cm x 10 <sup>6</sup> | Thermal Conductivity<br>w-in/in <sup>2</sup> °C | Density<br>lb/in <sup>3</sup> | Poisson's Ratio $\mu$ | Coefficient of Linear Expansion<br>(per °C) x 10 <sup>6</sup> | Modulus of Elasticity<br>Torsion<br>10 <sup>6</sup> psi |
|----------------------------|----------------------------|---|--|---|-------------------------------|-----------------------|---|---|
| Aluminum                   |                            |   |  |   |                               |                       |   |   |
| 2014-O                     | 14                         | 10.6  | 3.45   | 4.89  | 0.101                         | 0.33                  | 23 at 40°C  |   |
| 2014-T4                    | 42                         | 10.6  | 5.07   | 3.4   | 0.101                         | 0.33                  | 31 at 600°C   |   |
| 2014-T6                    | 60                         | 10.6  | 4.3  | 3.93  | 0.101                         | 0.33                  |   |   |
| Copper                     |                            |   |  |   |                               |                       |   |   |
| 99% + Cr<br>(heat treated) | 45                         | ~ 16<br>(drawn)   | 9  | 9.6   | 0.315                         |                       | 17.64   |   |
| Nickel                     |                            |   |  |   |                               |                       |   |   |
| Monel 400                  | 70                         | 26  | 22   | 0.732   | 0.319                         | 0.32                  | 15.84   |   |
| Titanium                   |                            |   |  |   |                               |                       |   |   |
| Ti-6Al-4V                  | ~ 70                       | 16.5  | 187 at 800°F                                       | 0.298   | 0.16                          |                       | 9.5   | 6.1   |
| Ti-75A                     | ~ 26                       | 15.1  | 60   | 0.43  | 0.16                          |                       | 9.2   | 6.5   |
| Beryllium                  | 60                         | 40  | 5 at 680°F   | 3.82  | 0.066                         |                       | ~ 16  |   |
| Magnesium                  |                            |   |  |   |                               |                       |   |   |
| ZK60A-T5                   | 38                         | 6.3   | 0.7  | 3.08  | 0.066                         | 0.28                  | ~ 28  | 2.5   |
| Be-Cu                      |                            |   |  |   |                               |                       |   |   |
| Alloy 165AT                | 125                        | 18  | 8.2  | 3.02  | 0.292                         |                       | 16.2  |   |
| 10AT                       | 80                         | 17  | 3.8  | 5.85  | 0.311                         |                       | 18  |   |
| Be-Al                      |                            |   |  |   |                               |                       |   |   |
| 62% Be                     | 40                         | 28.7  | ~ 5  | 5.3   | 0.0756                        |                       | 16.6  |   |
| 38% Al                     |                            |   |  |   |                               |                       |   |   |

#### 5. Workability

It is likely that an optimum generator support structure will involve shapes and sizes which are not standard. The selected material should have the ability to be worked into various shapes using thin skin materials. Beryllium has difficulty in this respect. The beryllium alloys (Be-Al) are highly superior to beryllium in this respect.

#### 6. Joining Properties

Reliable bonds and joints must be made with the generator support material with low resistance losses.

#### 7. Vapor Pressure

The end of the generator support nearest the generator is likely to become quite hot. The vapor pressure of the material will rise and it is important to select a material which will not deposit relatively thick coatings on the concentrator. Figure 4-11 shows the vapor pressure of various materials which can be considered for use. As shown, magnesium is probably out of the question for use in a generator support structure. Beryllium and aluminum exhibit much higher vapor pressures than titanium. As a rule of thumb, at  $10^{-12}$  mm mercury vapor pressure, about 0.001 cm of material will leave the surface every thousand hours. The use of beryllium and aluminum, therefore, has to be carefully examined in order to determine the effect of this evaporation on mirror characteristics. However, a preliminary examination indicated that the concentrator would receive a total layer of about  $10^2$  angstroms per 10,000 hours. This interference coating would probably not significantly affect reflectivity.

#### 8. Recrystallization

All materials are subject to recrystallization phenomena at high temperatures. For example, aluminum and magnesium have



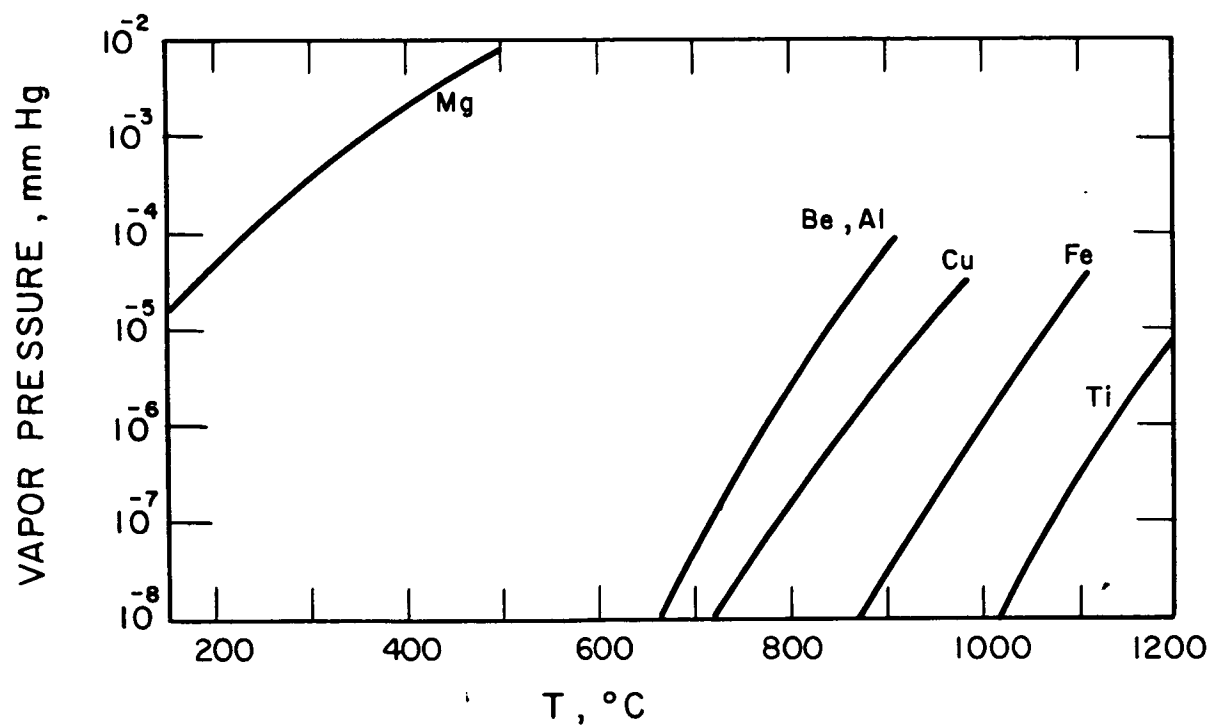


FIG. 4-11 VAPOR PRESSURE OF VARIOUS MATERIALS

recrystallization temperatures ranging from 350° to 500°C. The effect of recrystallization depends intimately on the strain in the support structure, the temperature and related phenomena. Effects could include a change in thermal conductivity, a change in electrical resistivity, and other extreme conditions exceeding the yield point of the material.

#### 9. Changes with Temperature

All materials will change with temperature. One particular area of interest is the change of material yield point with temperature and time. Tubes, for example, are made by cold working in many cases. Cold working effects will be largely eliminated in areas which are held at high temperatures for a long period of time. For example, the ductile fracture characteristics of a material could change to brittle fracture characteristics. This is another area which bears investigation before final selection of a material.

#### 10. Melting Point and Eutectics

The melting point of several materials of interest is close to the expected temperature of one end of the generator support. Aluminum, for example, melts at approximately 650°C. If there exists any danger of a "hot spot" on the generator support, materials used close to their melting point region should not be considered. Another consideration is the eutectic melting point of materials. For example, beryllium-aluminum alloys have a eutectic melting point of 640°C.

#### 4.6 Thermal Expansion Effects

For a 5-foot concentrator and a 60° rim angle, a coefficient of linear expansion of  $20 \times 10^{-6}$  inches/inch/degree C, averaged over the entire length of the generator support arm, assuming a linear distribution of temperature from 600°C to 100°C over the generator support arm would result in a displacement of 0.14 inch.

The example above illustrates the importance of thermal expansion considerations. The thermal expansion calculations can never be extremely accurate due to the inaccuracies of known thermal conductivity of material as a function of temperature, chances for recrystallization and other phenomena effecting thermal conductivity, the temperature distribution down the support arms, the temperature profile in the support arms, etc.

An examination of the materials indicates that titanium exhibits the least expansion of the materials considered. Beryllium has a reasonable expansion of about  $16 \times 10^{-6}$ .

The 0.14-inch displacement can be tolerated as this will mean approximately less than 1 percent loss in mirror efficiency. The real danger lies in a accumulation of errors in the concentrator structure, support structure, and thermal characteristics such that the expansion becomes three to four times this amount. Then decreases in efficiency on the order of 5 to 10 percent could be expected.

#### 4.7 Thermal Conductivity Effects

The temperature of the low voltage DC/DC converters is considered to be a serious problem in system efficiency and reliability. Temperatures of less than  $50^{\circ}\text{C}$  are desired. The temperature of the DC/DC converter will be determined by the amount of heat conducted into it by the generator support leads and the internal heat generated.

An examination was made of the expected temperatures along the generator support arms and the amount of heat that would be flowing down the arm into the DC/DC converter. Calculations involved the solution of differential equations in a rather complex program that will not be described here.

Calculations were concerned only with the generator support arm from the generator to the edge of the mirror. It should be recognized that additional electrical loss and cooling will occur in the electrical leads from the edge of the mirror to the DC/DC converter. The inclusion of this consideration is left for a more detailed study.

Figure 4-12 illustrates the results of some of the analysis. Shown is the temperature at the end of the support arm versus a support parameter which is defined in Fig. 4-12. The use of the curve is self-explanatory. If the temperature at the generator is known, (say  $600^{\circ}\text{C}$ ), and a given temperature at the mirror end is desired (say  $60^{\circ}\text{C}$ ), then the ratio of  $T_0/T_L$  can be found (for this example, 2.6). From this, the value of the support parameter  $X_T$  can be found and, knowing the characteristics of the support arm, the ratio of radiating surface per unit length to the cross sectional area can be found. For thin-walled tubes, this is equivalent to finding the thickness of the wall needed to satisfy the end temperature conditions. ( $\frac{A_s}{A_c} = \frac{1}{t}$ )

In a similar manner, calculations were performed to determine the amount of heat flowing into the strut as a function of heat parameter shown in Fig. 4-13. An examination of this figure indicates that the amount of heat flowing into support arms with reasonable wall thicknesses is not excessive.

The mechanism by which thermal conductivity and the temperature of the generator ends are introduced in the optimization analysis is illustrated in Figs. 4-14 and 4-15.

Figure 4-14 shows the temperature at the end of the generator support as a function of tube wall thickness. A coaxial arm was assumed where each tube had the same cross sectional area and the entire structure behaved similar to a single tube with twice the cross sectional area of the outer tube. As shown, the wall thickness of titanium can be much greater than that of aluminum to maintain the same temperature of the generator support end. For a 5-foot mirror, under the given conditions, it appears possible to maintain the thickness of 0.025 inches to maintain an end temperature of  $60^{\circ}\text{C}$ .

After selection of the end temperature (say  $60^{\circ}\text{C}$ ), optimization of the generator support dimensions can be made. The parameter which varies is the diameter of the outer tube. As the diameter of

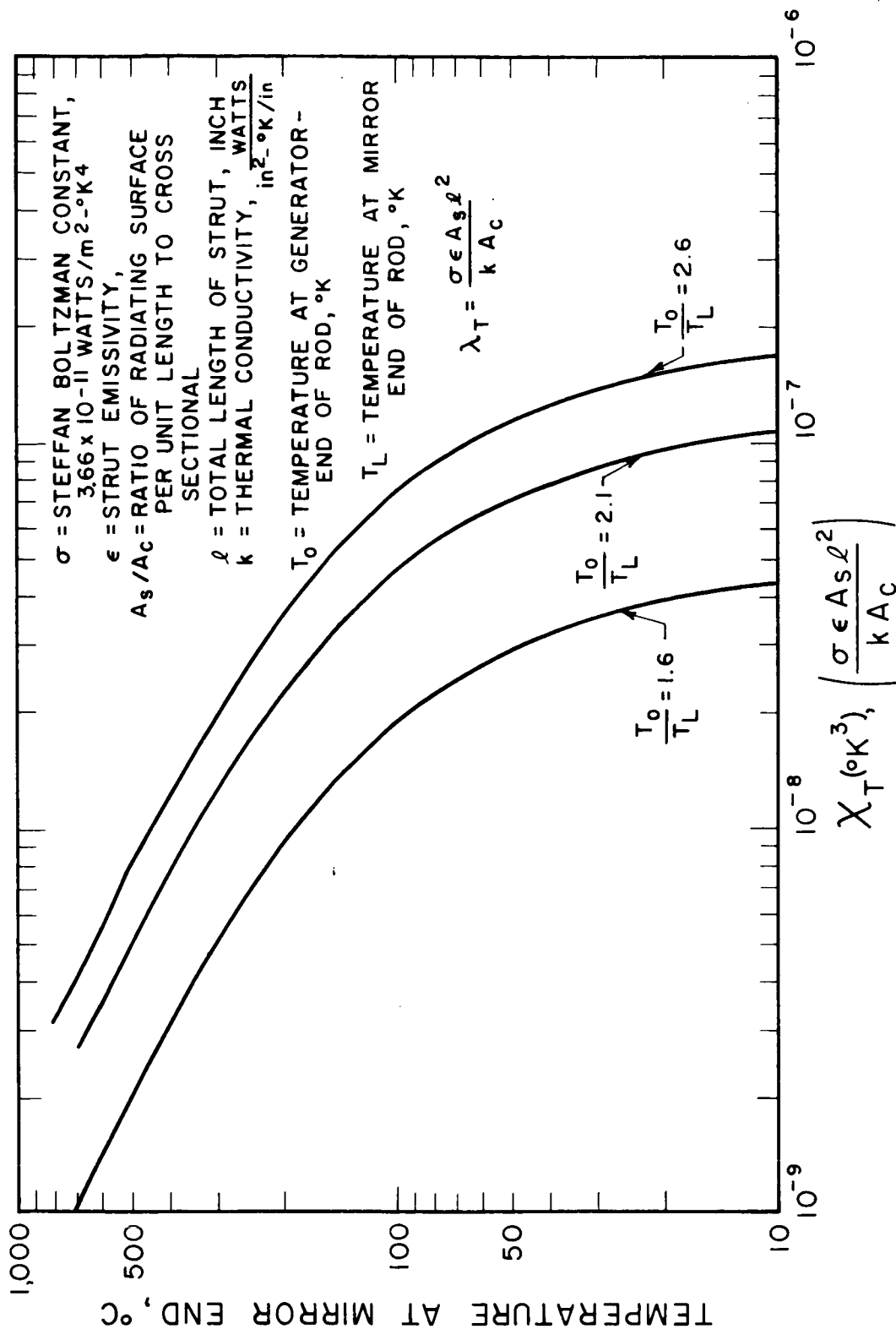


FIG. 1-12 TEMPERATURE AT MIRROR END VS SUPPORT PARAMETER  $X_T$

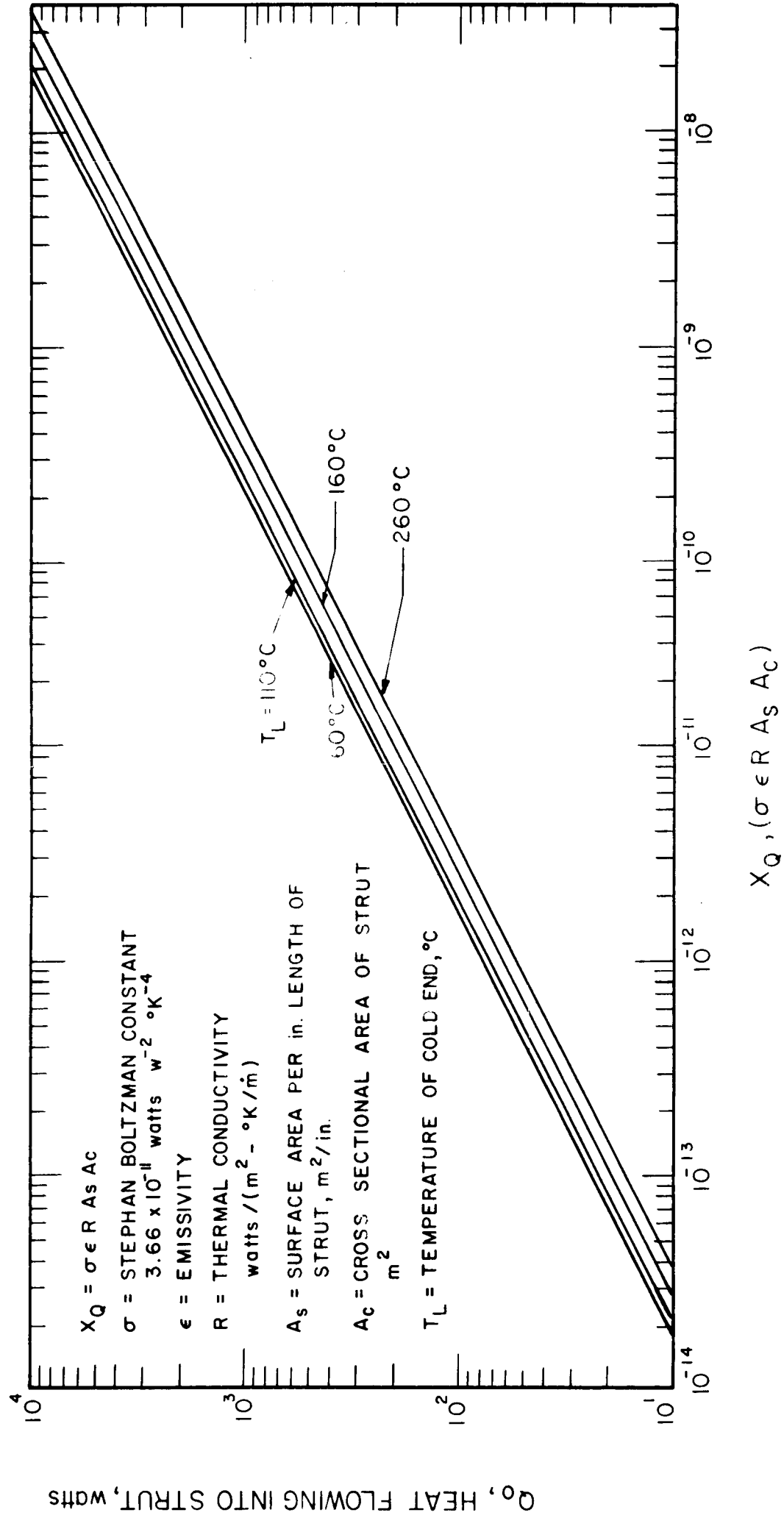
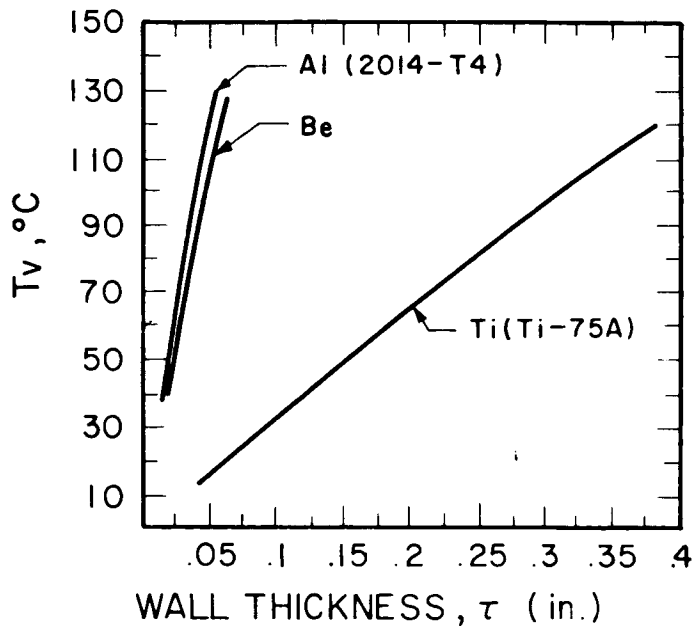


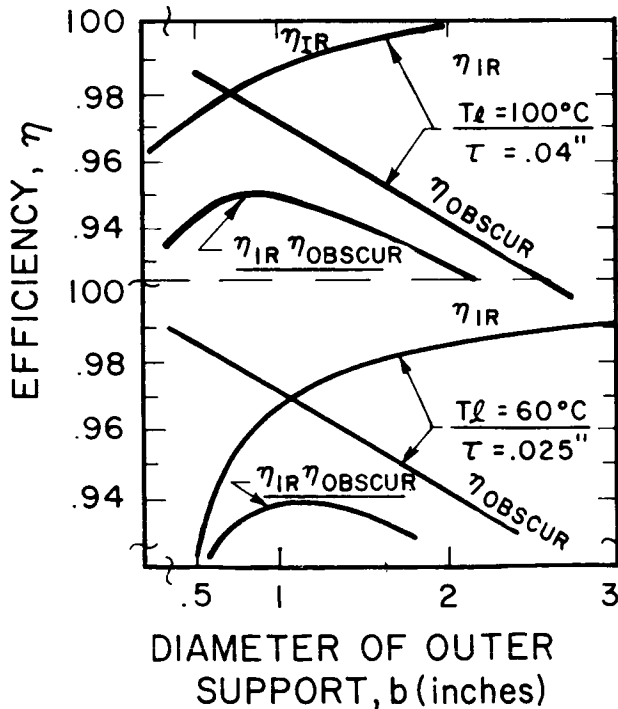
FIG. 4-13 HEAT FLOWING INTO STRUT AS THE TEMPERATURE  $T_L$  OF COLD END TEMPERATURE = 6000°C, SELECTED VALUES OF COLD END TEMPERATURES

FIG. 4-14 TEMPERATURE AT STRUT END OF GENERATOR SUPPORT  
FOR 5ft. MIRROR



SEE FIG. 4-12  
FOR DERIVATION  
OF  $T_L$

$T$  AT GENERATOR END  
=  $600^\circ\text{C}$   
 $\epsilon = 0.9$  - EMISSIVITY  
OF WALLS  
 $T_L$  = TEMPERATURE OF  
SUPPORT END AT  
CONCENTRATOR



$N = 3$  COAXIAL LEGS  
 $I_{gen} = 60$  AMPS  
 $V_{gen} = 4.2$  VOLTS  
MATERIAL = Al (2014-T4)

$$\eta_{IR} = 1 - \frac{I_{gen} r \ell^2}{N V_{gen} \pi b t}$$

$$\eta_{OBSCUR} = 1 - \frac{b \cdot N}{H \pi \ell \sin \theta_r}$$

WHERE  $r$  = RESISTIVITY  
 $\ell$  = SUPPORT LENGTH  
 $b$  = SUPPORT DIAMETER  
 $\tau$  = WALL THICKNESS  
 $\theta_r$  = CONCENTRATOR  
RIM ANGLE

FIG. 4-15 TYPICAL EFFICIENCY TRADE-OFF FOR GENERATOR SUPPORT  
ARMS - 5ft. CONCENTRATOR

the outer tube increases, the resistivity will go down and the obscuration will go up. This is illustrated in Fig. 4-15.

Figure 4-15 shows that the optimum diameter of the generator support arm will vary significantly with the change in desired temperature of the generator support. For  $T_L = 100^\circ\text{C}$ , the maximum combined obscuration and electrical loss efficiencies are 95.5 percent, while for a  $T_L$  of  $60^\circ\text{C}$ , combined efficiencies are 94 percent.

The results in Fig. 4-15 would change with a change in generator support emissivity. With a decrease in emissivity by one-half, the wall thickness would be halved. This would mean an increase in electrical losses and an optimum diameter support which would be larger in diameter and would result in lower combined efficiency.

The use of a different number of legs other than three would not affect the optimization results significantly. However, for a large number of legs, wall thicknesses would become too small to be practical.

The calculations in Fig. 4-15 are based on a 250-watt generator operating in a 5-foot system. It was assumed that the current output was 60 amps and the voltage output was 4.2 volts. Lower voltages and higher current would result in decreased generator support efficiency and the optimum support diameter which would become larger.

Figure 4-15 assumed the use of aluminum. Since the thermal conductivity and electrical resistivity of beryllium is quite similar, the results would be roughly the same for the use of beryllium.

Figures 4-16 and 4-17 show the same type of tradeoff optimization for 10-foot concentrator. It would be noted that the generator support efficiency can be higher with a 10-foot concentrator. In Fig. 4-17, a 1000-watt generator was assumed operating at 120 amp output.

The optimization of the generator support dimensions from a generator support efficiency viewpoint will not result in the optimum dimensions from a system viewpoint. The lowest lb/KW for the system



FIG. 4-16 TEMPERATURE AT END OF GENERATOR SUPPORT FOR 10ft. MIRROR

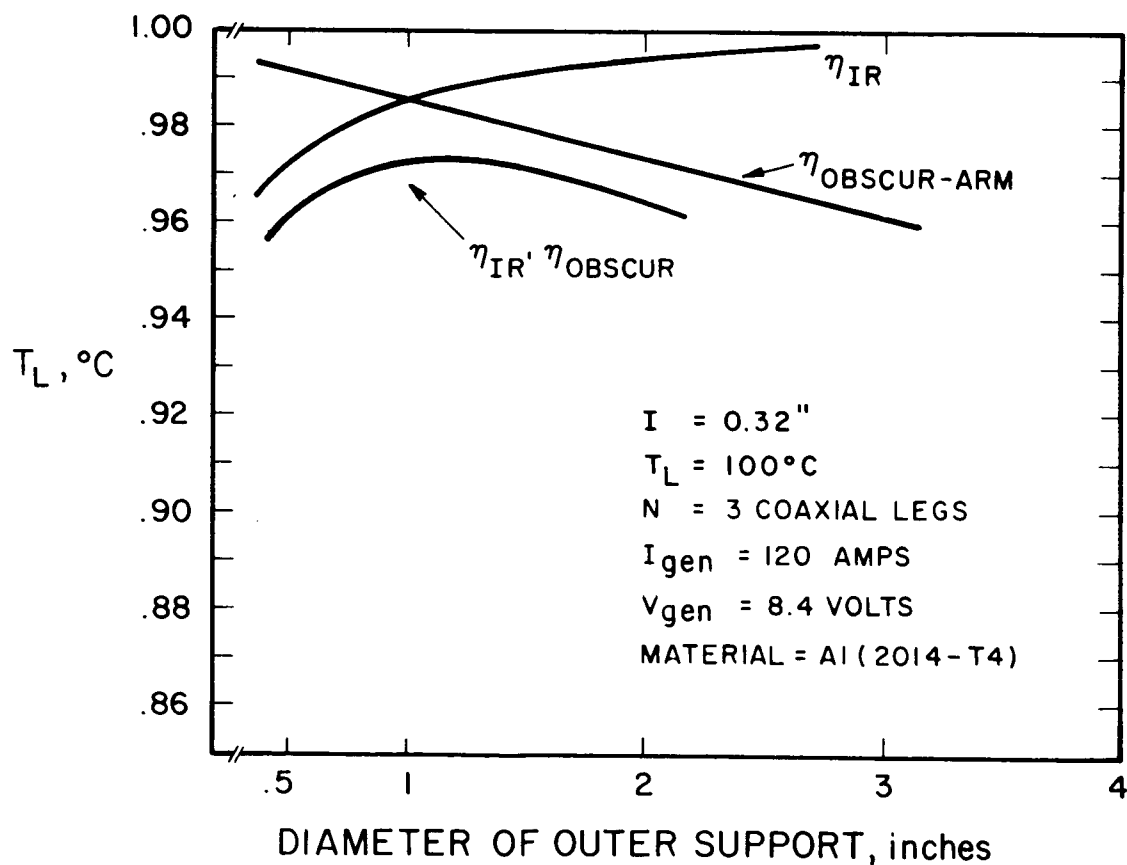
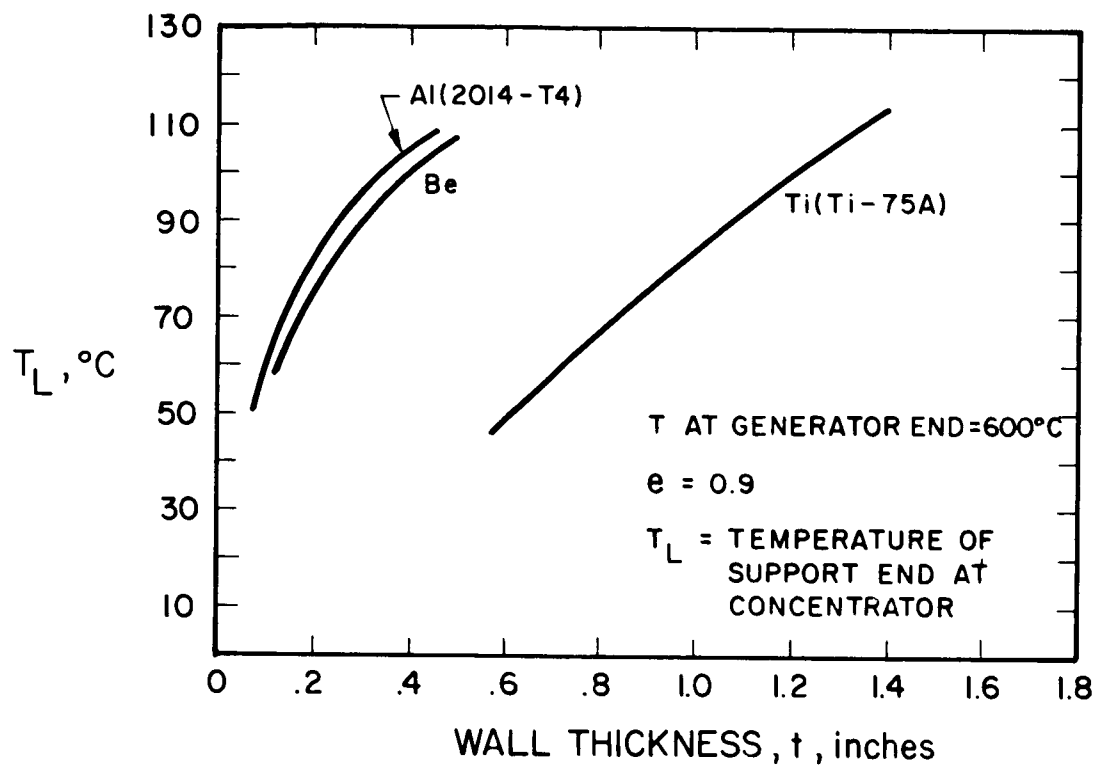


FIG. 4-17 TYPICAL EFFICIENCY TRADEOFF FOR GENERATOR SUPPORT ARMS - 10ft. MIRROR

will occur using a smaller outer support diameter that results in a "less than-optimum" generator support efficiency.

The illustrations in Figs. 4-14 through 4-17 show the complexity of the optimization problem in the generator support area. A large number of variables is involved, each of which can drastically affect the results. It is recommended that design limits be established with the use of a computer program. The generator support is as critical a component to the system as a generator or concentrator and must be carefully analyzed.

#### 4.8 Vibration Considerations

Vibration of the generator support must be considered in the launch mode and cruise mode. For the folding systems, the problem during launch is that of resonance induced into the generator support which is fixed at each end. The fixation can be adequately represented by a beam held at each end by pin joints. For nonfolding structures, the vibration analysis is much more complex. An analysis was made of the three-legged and four-legged generator support structure in terms of resonant frequencies which would be expected.

The limits on resonant frequency are rather indefinite and depend on specific vehicle design and the accompanying guidance and control system. For example, the Mariner 64 panels were limited in frequency response during cruise to a bandwidth of 0.5 to 5 cps. The lower limit was based on attitude control system interaction and the upper limit on resonance considerations during the midcourse maneuver. The objective during launch was to obtain as high a first mode resonance as possible; for the Mariner panel this was about 14 cps. A minimum first mode resonance of 35 cps was used on the Ranger panel in order to avoid resonant coupling to the vehicle structure.

##### 4.8.1 Launch Vibration Mode

Figure 4-18 illustrates typical transverse vibration of the generator support arm in the launch mode assuming that the arm is clamped at one end and hinged on the other. Only "first mode" resonance is treated here. Figure 4-18 assumes the use of beryllium with an outer

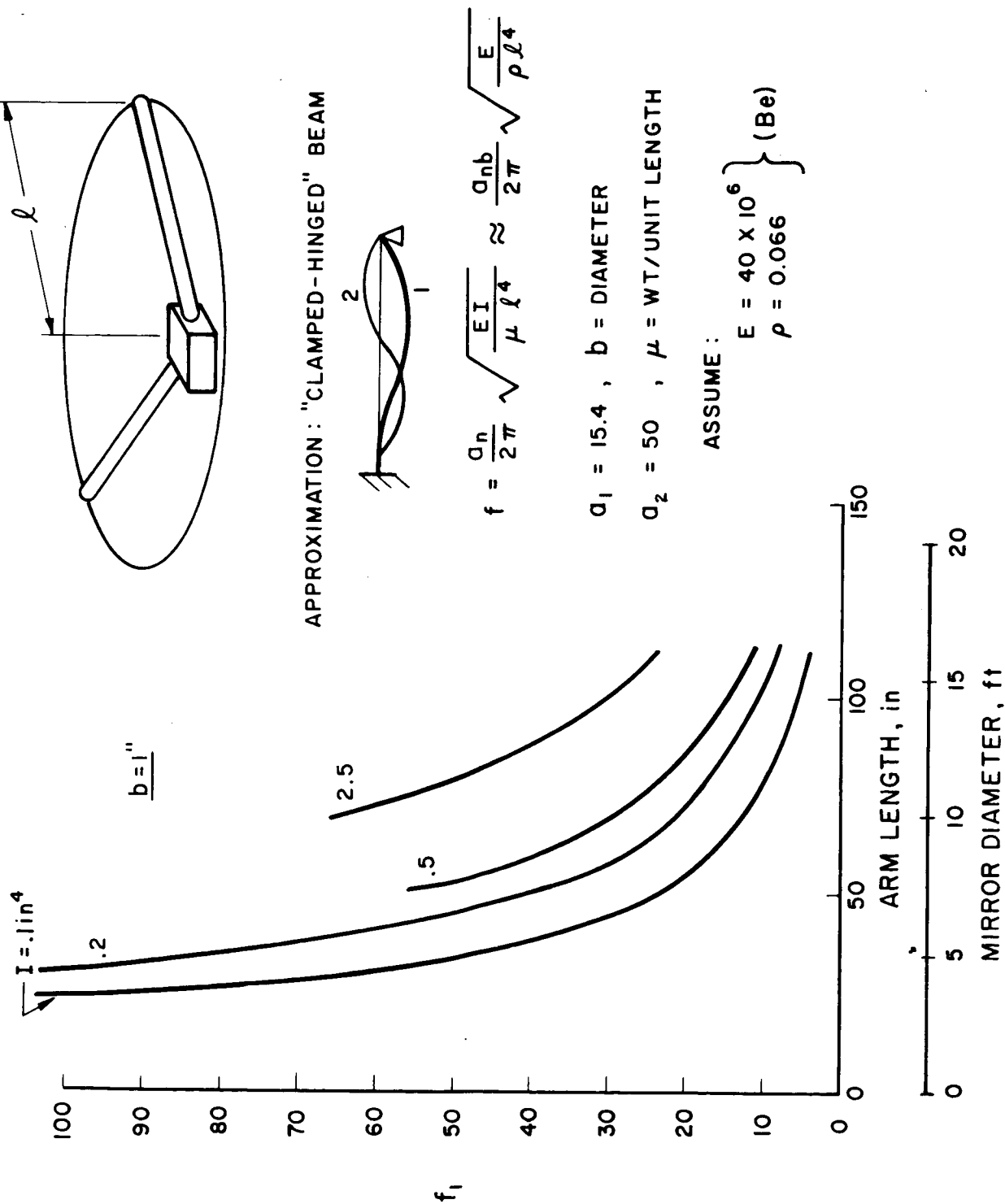


FIG. 1-18 TYPICAL TRANSVERSE VIBRATION OF GENERATOR SUPPORT IN LAUNCH MODE

support diameter of 1 inch. As shown, for a 5-foot mirror a 1-inch support diameter with reasonable wall thicknesses will result in relative high first mode resonances. However, for 10-foot mirrors, the moment of inertia of the arms must be an order of magnitude higher. This can be shown by examination of the equation for first mode resonance in Fig. 4-18.

Figure 4-19 shows the moment of inertia for a thin-walled cylinder as a function of wall thickness and outer support diameter. As shown, the same moment of inertia can be obtained with different wall thicknesses and diameters; however, the moment of inertia is a strong function of the support diameter. For the examples in this text, the coaxial configuration is assumed to behave as a single tube; i.e., the inner and outer tubes behave as a single tube with twice the thickness of the outer tube. This is reasonable if the coaxial tubes are attached by means of insulators.

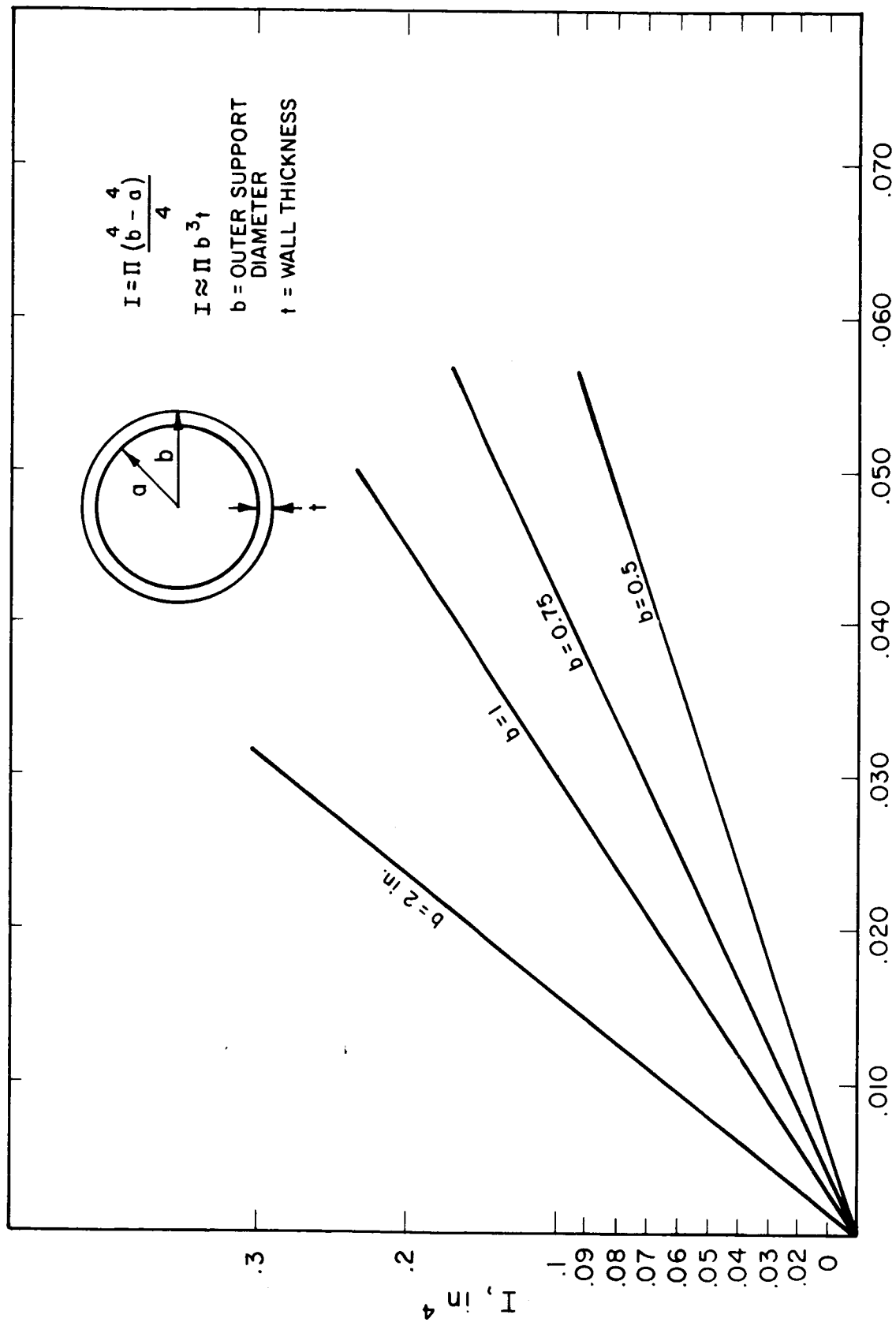
Figure 4-20 illustrates the minimum outer diameter of the support arm required for a minimum first mode resonance during launch of 35 cps. As illustrated, the minimum outer diameter is a function of the square of the length of the arm and becomes relatively thick for a 10-foot concentrator. Also, the minimum diameter is a strong function of the ratio of density to elastic modulus. Beryllium is far superior to other materials in this respect. The use of aluminum, for example, would increase the minimum diameter by a factor of 2.5.

Figure 4-21 illustrates the minimum weight of the generator arm required for a minimum resonance of 35 cps during launch. The weight is a direct function of wall thickness and the cube of the length. Once again, beryllium far outstrips the use of other materials with regard to minimum generator support weight.

#### 4.8.2 Vibration of the Solar-Thermionic Generator and Generator Support in the Deployed Position

The generator-strut arrangement present in a solar-thermionic system may be described structurally by means of the theory of frames.

All the supports are assumed to be capable of storing potential energy in bending and torsion only and the ends are assumed



WALL THICKNESS,  $t$ ,

FIG. 1-19 MOMENT OF INERTIA FOR THIN-WALL CYLINDER

$$b = \frac{W}{l\pi\rho t} = \frac{K}{l\pi\rho}$$

$$b = l^2 \sqrt{\frac{\rho}{E}} \left( \frac{2\pi f}{a_1} \right)$$

$$\left. \begin{array}{l} a_1 = 15.4 \\ \rho = 0.066 \\ E = 40 \times 10^6 \end{array} \right\} \text{Be}$$

$$f = 35 \text{ cps}$$

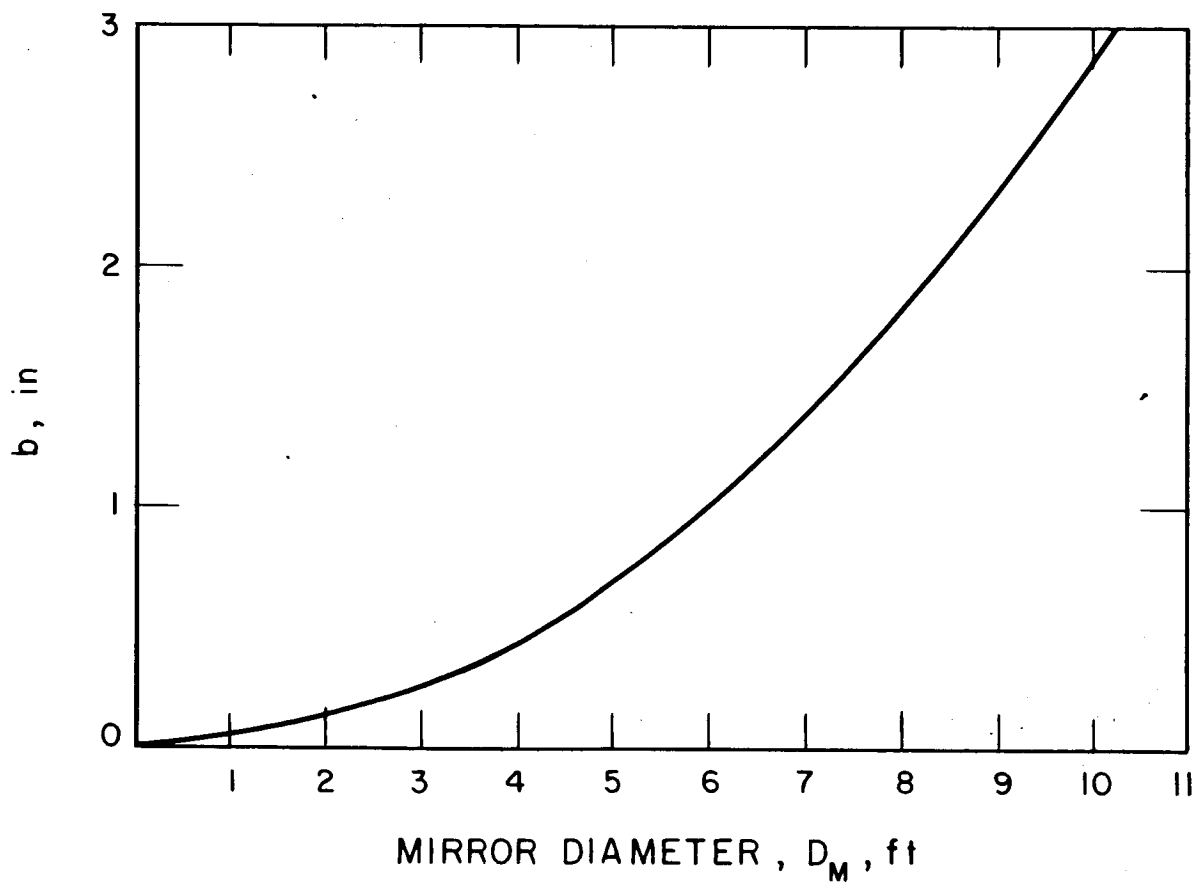
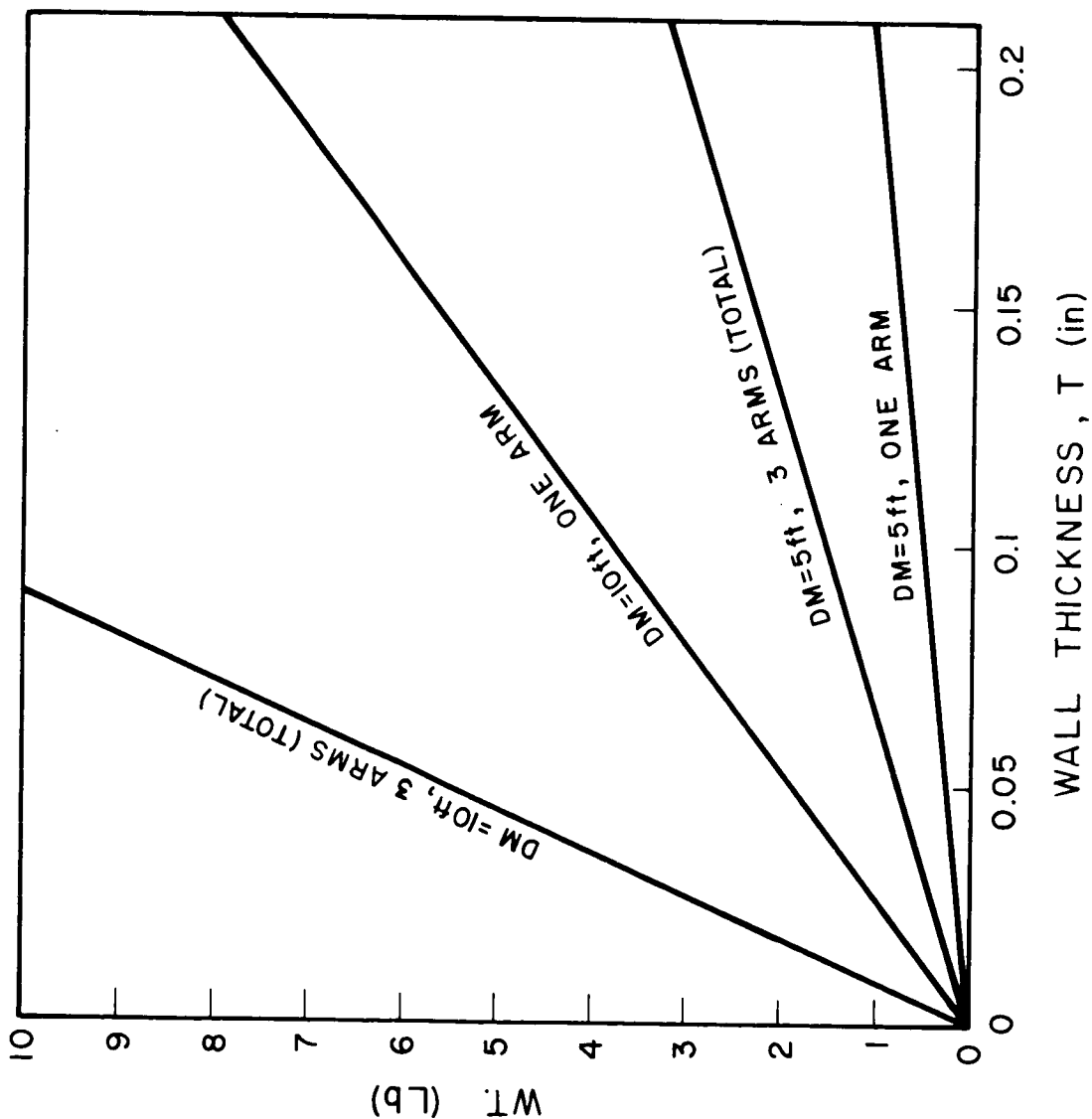


FIG. 4-20 MINIMUM OUTER DIAMETER OF SUPPORT ARM REQUIRED FOR FIRST MODE RESONANCE IN LAUNCH MODE OF 35 CPS



W = WEIGHT

$W = \ell \cdot \pi \cdot b \cdot \tau \cdot \rho$

$W = \frac{\ell I \rho}{b^2}$

$\ell$  = LENGTH OF ARM

I = MINIMUM MOMENT OF INERTIA

$\rho$  = DENSITY

b = ARM OUTER DIAMETER

$$W = \ell^3 \pi \tau \rho \sqrt{\frac{\rho}{E}} \left( \frac{f \cdot 2 \pi}{a_1} \right)$$

$\tau$  = WALL THICKNESS

$a_1 = 15.4$

f = MINIMUM RESONANT FREQUENCY

MATERIAL = Be

FIG. 1-21 MINIMUM WEIGHT OF GENERATOR ARM REQUIRED FOR MINIMUM RESONANCE IN LAUNCH MODE OF OSC'S

to move due to translation and rotation of the generator. The support inertia is assumed negligible.

The frequency equation for the system is obtained by assuming that the modes vibrate with a frequency  $\omega$  and is written directly from the potential and kinetic energy expressions. The six values of frequency found from the frequency equation are the six natural frequencies for the system. Using the diagonal terms of the frequency equation determinant, the frequency estimates are fair to good depending on the amount of cross coupling.

For a complete solution to the problem the eigenvalues of the frequency equation must be determined with the effect of the coupling terms taken into account. These frequencies may then be used to determine the vibration modes corresponding to each frequency. The approximate method adopted by this study is to assume the vibration mode, then find the corresponding frequency, hence, once the frequency has been estimated both the frequency and the mode shape are known approximately.

#### The Kinetic Energy Matrix

The following definitions are now made:

- $X_1, X_2, X_3$  = translation in X, Y, Z directions respectively  
 $X_4, X_5, X_6$  = rotation with respect to  $X_1, X_2, X_3$  respectively

With these definitions the kinetic energy T may now be written as

$$T = 1/2 (W_g/g)(\dot{X}_1^2 + \dot{X}_2^2) + 1/2 \left(\frac{J_G}{g}\right)(\dot{X}_4^2 + \dot{X}_5^2 + \dot{X}_6^2) \quad (4-1)$$

$W_g$  = generator weight, lbs

$g$  = gravity constant, 386 in/sec<sup>2</sup>

$J_G$  = polar moment of inertia of the generator (this is not the area moment, the generator mass is included)

The first set of terms has the kinetic energy contribution resulting from generator translation and the second set of terms has the contributions due to generator rotation. Note that the factor one-half in



the second set of terms is due to the polar moment of inertia being twice the moment of inertia with respect to  $X_1$  or  $X_2$  axes.

#### The Stiffness Factor, K

The resonant frequencies for all modes are directly proportional to  $(W_G/K)^{1/2}$ . Once the material has been chosen then E is known. The modulus of rigidity I depends on the strut cross section geometry and so may not be known exactly until a strut design has been agreed upon. The strut design depends on factors other than those of a purely structural nature and hence will not be elaborated on here. Suffice it to say that materials under consideration are aluminum, beryllium, and titanium and that current estimates of I range from 0.1 to 2.5 in<sup>4</sup>.

The kinetic energy expression may be written in the form of a matrix

$$T = 1/2 \sum_{i=1}^6 \sum_{j=1}^6 M_{ij} \dot{X}_i \dot{X}_j$$

Only the diagonal terms of the matrix are present. The symbols have meanings similar to those for the potential energy matrix.

$$M_{11} = M_{22} = M_{33} = W_G/g$$

$$M_{44} = M_{55} = (J_G/2) = 4W_G/g, \text{ (See footnote)}$$

$$M_{66} = J_G = 8W_G/g, \text{ (See footnote)}$$

where

$$W_G = \text{generator weight}$$

#### The Potential Energy Matrix

The entire system may be regarded as a frame with energy stored due to twisting and bending. The elongation in the members may be neglected as trivial as is the practice in the Theory of Frames.

Note:  $J_G = (W_G/2g) (\text{generator radius})^2$ , hence

$M_{44} = M_{55} = 4W_G/g$  and  $M_{66} = 8W_G/g$  only for the case where the generator radius is 4 inches as in this study.

Consider the beam shown in Fig. 4-22 in the plane xy with length L, angles  $\theta_1$ ,  $\theta_2$ ,  $\phi$  and end deflections  $y_1$ ,  $y_2$ . The  $\theta$  values are the slopes at both ends of the beam and  $\phi$  is the average rotation of the beam element ( $\phi = (y_2 - y_1)/L$ ). A beam deformed as shown above has a potential energy U given by

$$U = K \left[ \theta_1^2 + \theta_1 \theta_2 + \theta_2^2 - 3\phi (\theta_1 + \theta_2) + 3\phi^2 \right] \quad (4-2)$$

K = stiffness factor,  $2EI/L$

I = moment of inertia of beam cross section with respect to the neutral axis perpendicular to the xy plane

E = modulus of elasticity of beam

Equation 4-2 is for each of the two planes in which bending occurs.

The beam may also be subject to torsion about its longitudinal axis. The potential energy for a twisted beam is

$$U_T = GJ\psi^2/(2L) \quad (4-3)$$

G = modulus of shear

J = polar moment of inertia of beam cross section

$\psi$  = angular displacement of beam tip

The struts are prismatic hence,

$$GJ = 0.75EI \quad (4-4)$$

hence

$$U_T = 0.188 (2EI/L)\psi^2 = 0.188 K\psi^2 \quad (4-5)$$

To find the potential energy for the system, sum the potential energy for each strut subject to bending in each plane and twisting about its own axis. Next find the geometrical relationships between each  $\phi$  and  $\theta$  and the coordinate system adopted.

The coordinate system used is translation in three directions and rotation about the three translation axis.

The transformations from  $\phi$  and  $\theta$  values to the six degree of freedom system referenced to above is a linear one hence the

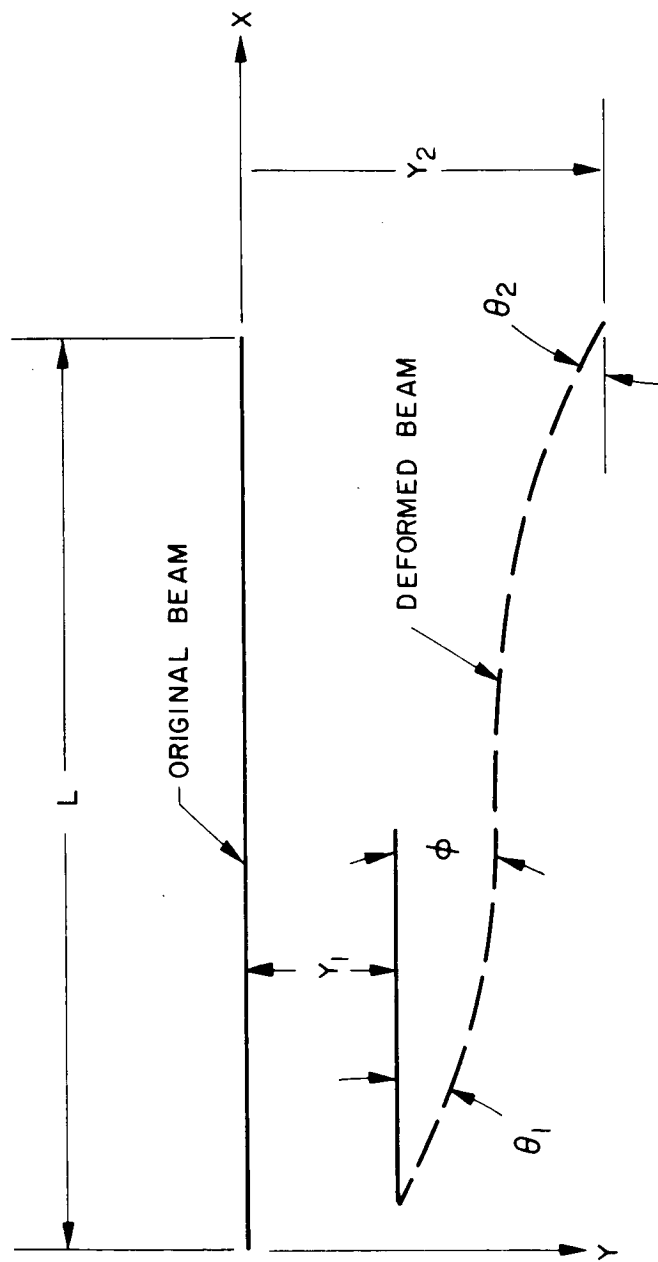


FIG. -22 BEAM DEFORMATION IN  $XY$  PLANE

potential energy which is quadratic in  $\phi$  and  $\theta$  will also be quadratic in terms of the six generalized coordinates. The potential energy term may therefore be written in the general form

$$U = 1/2 \sum_{i=1}^6 \sum_{j=1}^6 a_{ij} X_i X_j \quad (4-6)$$

$i, j$  = summation indices

$X_1, X_2, \dots, X_6$  = generalized coordinates to be designated later on

$a_{ij}$  = coefficients which allow  $U$  to be written in the prescribed fashion above

### The Frequency Equation

Assume that each generalized coordinate vibrates with a circular frequency\*  $\omega$  and amplitudes  $\ell_1, \ell_2, \dots, \ell_6$  then

$$\begin{array}{c} X_1 \\ X_2 \\ \vdots \\ X_6 \end{array} = \begin{array}{c} \ell_1 \sin \omega t \\ \ell_2 \sin \omega t \\ \vdots \\ \vdots \end{array} = \begin{array}{c} \ell_1 \\ \ell_2 \\ \vdots \\ \ell_6 \end{array} \sin \omega t$$

$$\text{i.e. } \underline{X} = \underline{\ell} \sin \omega t \quad (4-7)$$

where the bars below the letters symbolize a matrix. It can be shown (See Toug "Theory of Mechanical Vibrations" pp. 176-176, Wiley)

that

$$(-\omega^2 \underline{M} + \underline{A}) \underline{\ell} = 0 \quad (4-8)$$

$\underline{M}$  = matrix for kinetic energy terms i.e., of  $M_{ij}$

$\underline{A}$  = matrix of potential energy terms i.e., of  $a_{ij}$

and that

$$\text{Determinant of } |\underline{A} - \omega^2 \underline{M}| = 0 \quad (4-9)$$

Equation 4-5 gives the six values of the frequency which satisfy Eq. 4-7. After the frequencies have been found from Eq. 4-9 the mode shapes may be found directly from Eq. 4-8.

\* $2\pi\omega = f$ , where  $f$  = cycles/sec.

It is very difficult to solve Eq. 4-9 directly and a computer solution is the best approach unless the system is sufficiently uncoupled so that reasonably good frequency estimates may be obtained by using the diagonal terms only.

#### The Three-Strut Arrangement

The three-strut arrangement consists of three struts each 120 degrees apart. Each strut has two numbers associated with it. An odd number which represents the base (at the collector) and an even number for the end at the generator.

The generator motion is prescribed by the vectors  $\vec{p}$ ,  $\vec{\alpha}$ . The vector  $\vec{p}$  describes motion due to translation and has components (X, Y, Z). The vector  $\vec{\alpha}$  describes rotation and has components ( $\alpha_x$ ,  $\alpha_y$ ,  $\alpha_z$ ). In the analysis generalized coordinates ( $X_1$ ,  $X_2$ , -- $X_6$ ) are used. Their definitions are given in Fig. 4-23.

In subsequent pages the potential energy for member 1-2,  $U_{12}$ , is derived by means of Eq. 4-1 and geometrical considerations. The potential energy for the other two members is derived by means of coordinate transformations.

#### Potential Energy for Member 1-2

The following terms are defined:

- $\psi_{2,12}$  = angular twist of end 2 with respect to end 1. The positive sense is the same as that of the vector from pt1 to pt2.
- $\theta_{2,z}$  = rotation of end 2 in the 1-2-Z plane.
- $\theta_{2, \text{cone}}$  = rotation of end 2 in the tangent plane to the axis of the cone formed by the struts.

$\phi_{12, Z}$  = average rotation of spar 1-2 in the 1-2-Z plane.  
See note on Fig. 4-23 for determination of positive sense.

$\phi_{12, \text{cone}}$  = average rotation of spar 1-2 in the tangent plane to the cone formed by the struts. See note on Fig. 4-23 for determination of positive sense.

From geometrical considerations

$$\psi_{2, 12} = (a/L) X_6$$

$$\alpha_{2, Z} = X_4 + (\sin \alpha_5) X_2/L - X_3/L$$

$$\alpha_{2, \text{cone}} = X_2 + X_1/L$$

$$\phi_{12, Z} = \frac{a X_4 - X_3}{L \cos \alpha_5}$$

$$\phi_{12, \text{cone}} = (a/L) X_6 + X_1/L$$

From geometry  $L = 35$  inches and  $\alpha_5 = 63.5$  for a 5-foot diameter collector with a 60 degree rim angle and a 4-inch radius generator. Using Eqs. 4-1 and 4-8 the total potential energy for a four strut case was found to be

$$U = 10^{-2} K \times \begin{aligned} &200 X_1^2 + 4.74 X_1 X_5 \\ &200 X_2^2 - 4.74 X_2 X_4 \\ &1.04 X_3^2 \\ &106 X_4^2 \\ &106 X_5^2 \\ &6 X_6^2 \end{aligned}$$

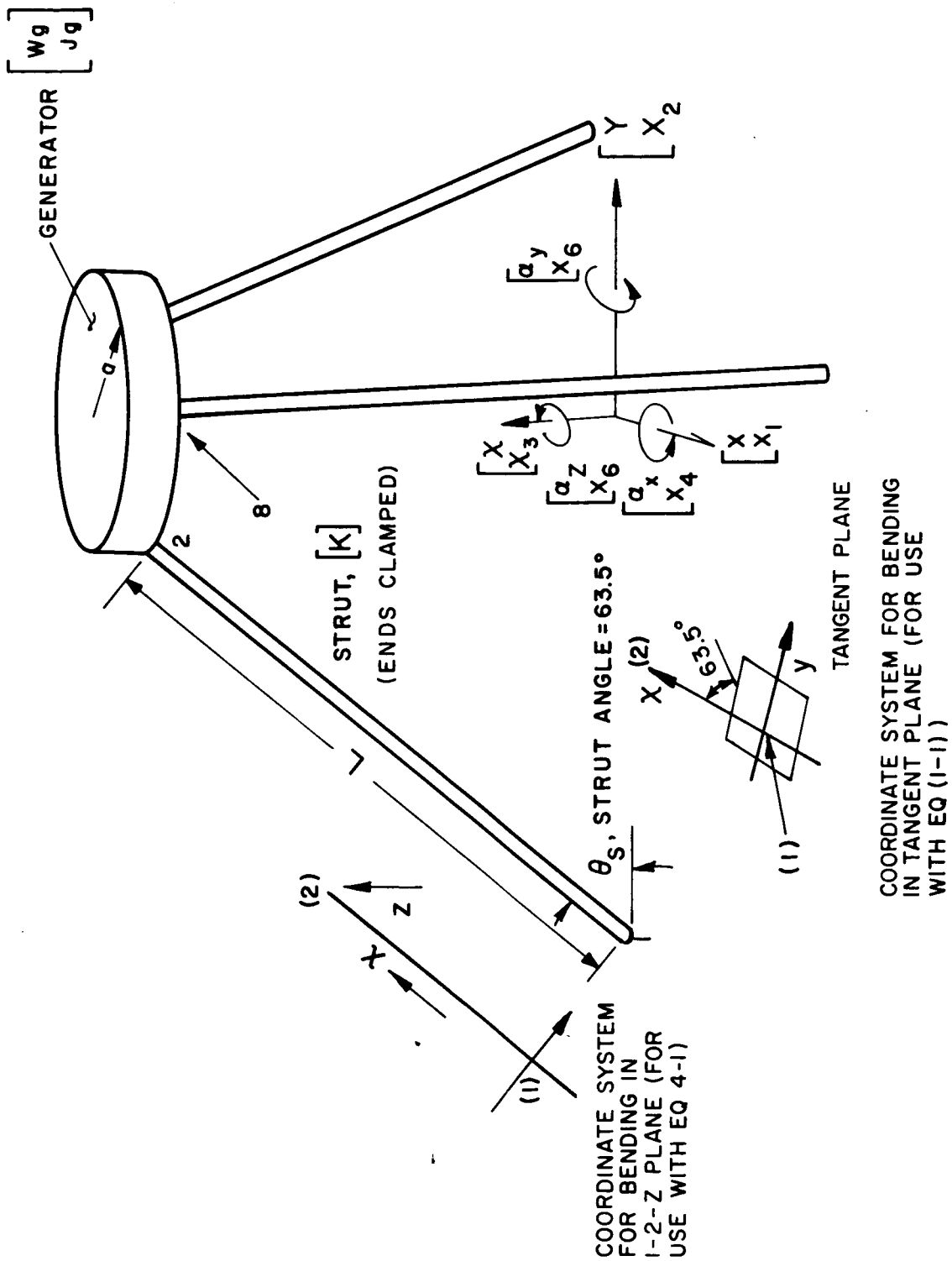


FIG. 4-23 THREE-STRUT SOLAR-THERMIONIC GENERATOR. COORDINATE SYSTEMS USED. IDENTIFICATION OF REFERENCE POINT 5)

and the frequency equation is:

|                   |                   |                    |                    |                    |                    |
|-------------------|-------------------|--------------------|--------------------|--------------------|--------------------|
| (200- $\lambda$ ) | 0                 | 0                  | 0                  | 1.19               | 0                  |
| 0                 | (200- $\lambda$ ) | 0                  | -1.19              | 0                  | 0                  |
| 0                 | 0                 | (1.04- $\lambda$ ) | 0                  | 0                  | 0                  |
| 0                 | -1.19             | 0                  | (26.5- $\lambda$ ) | 0                  | 0                  |
| 1.19              | 0                 | 0                  | 0                  | (26.5- $\lambda$ ) | 0                  |
| 0                 | 0                 | 0                  | 0                  | 0                  | (0.75- $\lambda$ ) |

where

$$\lambda = 10^2 W_G / (gK) \cdot \omega^2$$

$$K = 2EI/L$$

Observe that the coupling appears light for all rows except the sixth so that reasonable approximations to the exact frequencies may be made by assuming  $X_1, X_2, X_3, X_4$ , uncoupled and a poor approximation can be made for the X-axis rotational frequency by assuming the sixth row uncoupled.

Frequency estimates based on the uncoupling assumptions are shown in Table 4-II.

#### Conclusion

The resonant frequencies in the translational and rotational modes of several typical cases have been shown to have lowest frequencies in the neighborhood of 40 to 60 cps for a 5-foot mirror, 60 degree rim angle and 100 to 150 cps for a 10-foot, 60 degree rim angle using reasonable numbers for strut physical parameters.

The most serious problem exists in the rotational vibration about the concentrator axis. However, using the physical constants shown, the resonant frequencies are high enough to be usable in typical vehicle structures. However, it is clear that the situation could easily change. For example, the use of aluminum (assuming all other physical parameters remain the same) would decrease the resonant frequency by half, which may cause difficulty in typical vehicle structures.



TABLE 4-II  
TYPICAL RESONANT FREQUENCIES OF SUPPORT ARMS  
IN UNFOLDED POSITION

|   |        | Frequency, cps    |                   |                   |                   |                   |                   |
|---|--------|-------------------|-------------------|-------------------|-------------------|-------------------|-------------------|
|   |        | $\underline{f_1}$ | $\underline{f_2}$ | $\underline{f_3}$ | $\underline{f_4}$ | $\underline{f_5}$ | $\underline{f_6}$ |
| $D_m = 5$ ft.   | 4 arms | 945               | 945               | 68                | 343               | 343               | 58                |
| $I = 0.13$  | 3 arms | 720               | 720               | 51                | 261               | 261               | 44                |
| $E = 40 \times 10^6$ (Be)   |        |                   |                   |                   |                   |                   |                   |
| $W_G = 5$ lb  |        |                   |                   |                   |                   |                   |                   |
| $D_m = 10$ ft.  | 4 arms | 2,650             | 2,650             | 178               | 900               | 900               | 152               |
| $E = 40 \times 10^6$  | 3 arms |                   |                   | 134               |                   |                   | 114               |
| $I = 3.4$   |        |                   |                   |                   |                   |                   |                   |
| $W_G = 10$ lb   |        |                   |                   |                   |                   |                   |                   |
| -----   |        |                   |                   |                   |                   |                   |                   |
| $f^2 = \frac{1}{(2\pi)^2} \cdot g \cdot \frac{2EI}{L} \cdot \frac{\lambda}{10^2 W_g}$ |        |                   |                   |                   |                   |                   |                   |

The situation with three arms is roughly the same. Assuming the same physical constants for the struts, the resonant frequency decreases as shown and care must be taken to select a high enough EI factor.

The pairing of two smaller arms to make one, as shown in Fig. 4-2, will aid considerably in raising the EI factor which affects  $f_6$ , and can lead to overall weight savings. The benefit in terms of vibration must be traded against the small losses expected in obscuration and IR losses.

#### 4.9 Weight

As discussed in previous paragraphs, the weight of the generator support arms will be a function of:

1. The tradeoff between resistance losses and obscuration of the concentrator
2. Design limits imposed by the temperature at the end of the generator support
3. Design limits imposed by vibration problems during launch or cruise

The maximum value of the generator support efficiency is shown in Fig. 4-24 based on previous assumptions. The maximum value is a function of many parameters as shown.

Figure 4-25 shows a typical generator support optimization for a 5-foot mirror. The lb/KW figure for the system (including support arms) and the arms themselves are shown. Assumptions for calculations are typical and are listed.

As shown, the minimum outer support diameter for first mode resonance in a "folded" launch mode of 35 cps is 0.72 inch. In the case shown, the limitation due to thermal conductivity down the support arm is more severe than limitations due to vibration. In the case shown, a wall thickness of 0.050 inch resulted in a temperature at the end of the generator support arm of 100°C which is considered to be the maximum limit. This, therefore, is a maximum wall thickness which can be used and for outer support diameters of less than 0.8 inch, the losses in electrical resistivity rapidly decrease overall system efficiency. This decrease in system efficiency results in a sharp increase in lbs/KW for the entire system (as illustrated).

Figure 4-26 illustrates the same optimization using aluminum instead of beryllium arms. As shown, the minimum resonance criteria become much more important.

Figure 4-27 illustrates the same type of optimization for a 10-foot mirror. In this case, the vibration problem overshadows the thermal conductivity problem. As shown, the minimum outer support diameter is 2.8 inches for a resonance frequency of 35 cps. For aluminum arms, shown in Fig. 4-28, the situation becomes much worse.

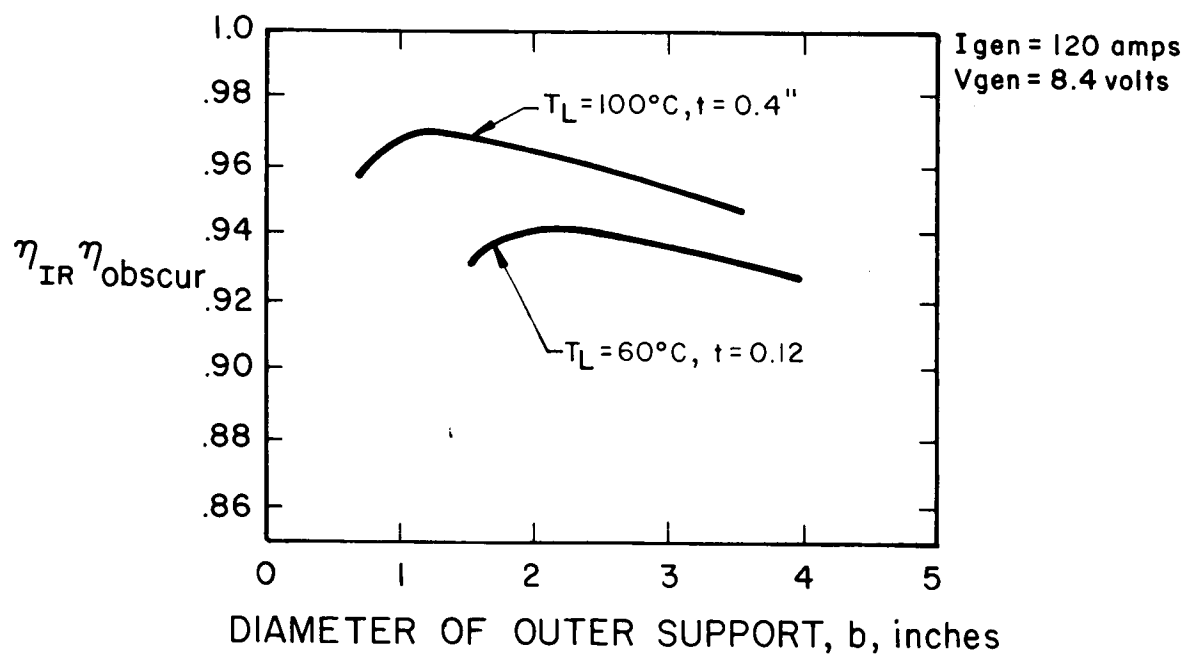
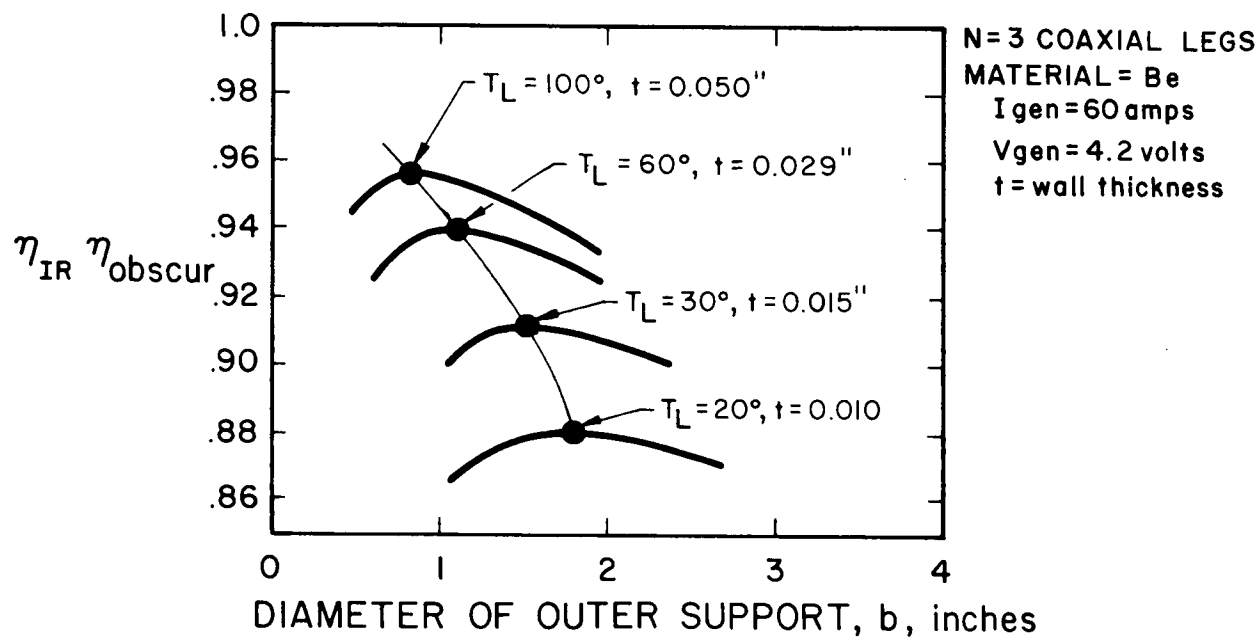


FIG. 4-24 MAXIMUM VALUE OF GENERATOR SUPPORT EFFICIENCY

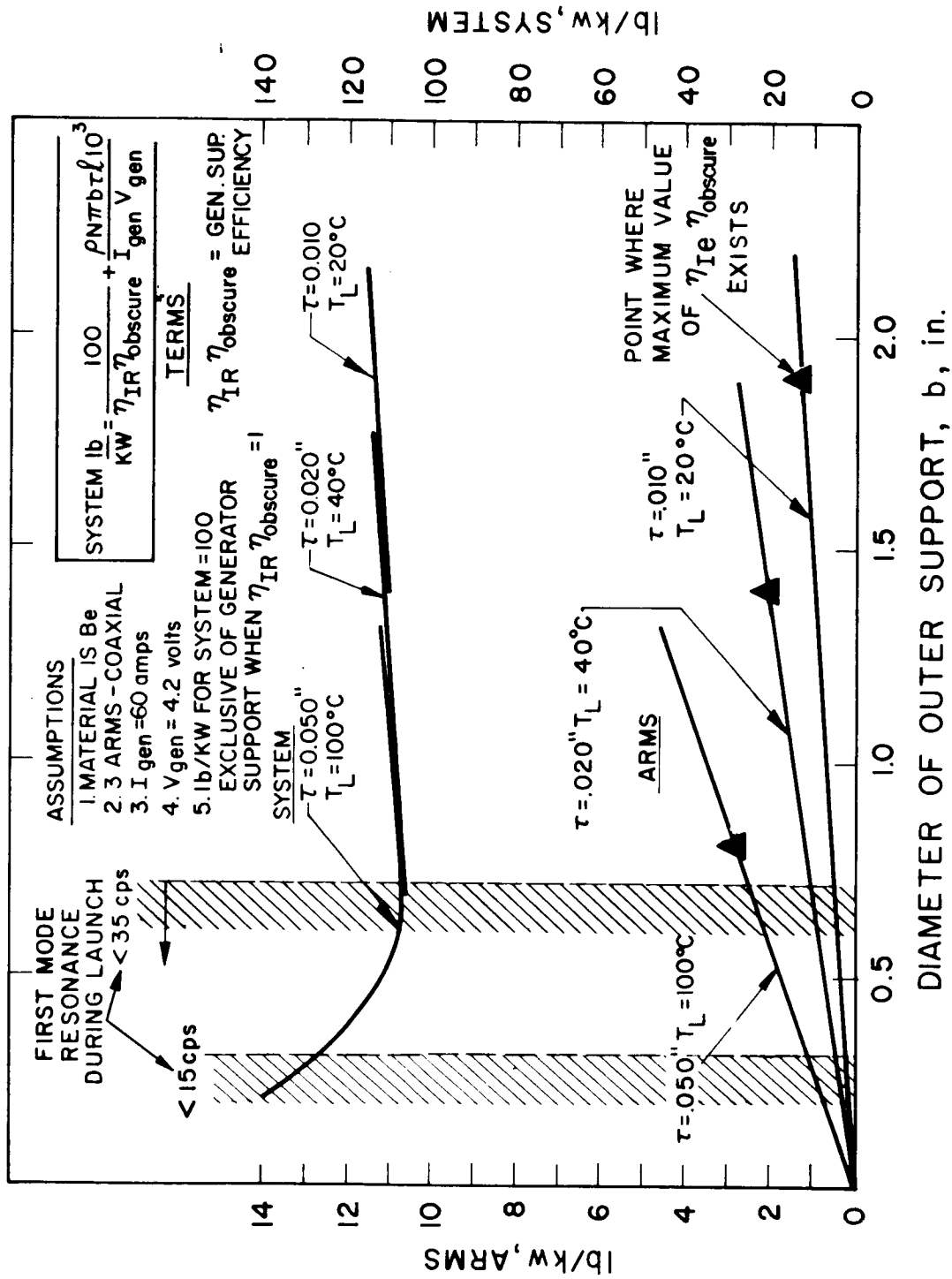


FIG. 4-25 TYPICAL GENERATOR SUPPORT OPTIMIZATION FOR 5ft. MIRROR

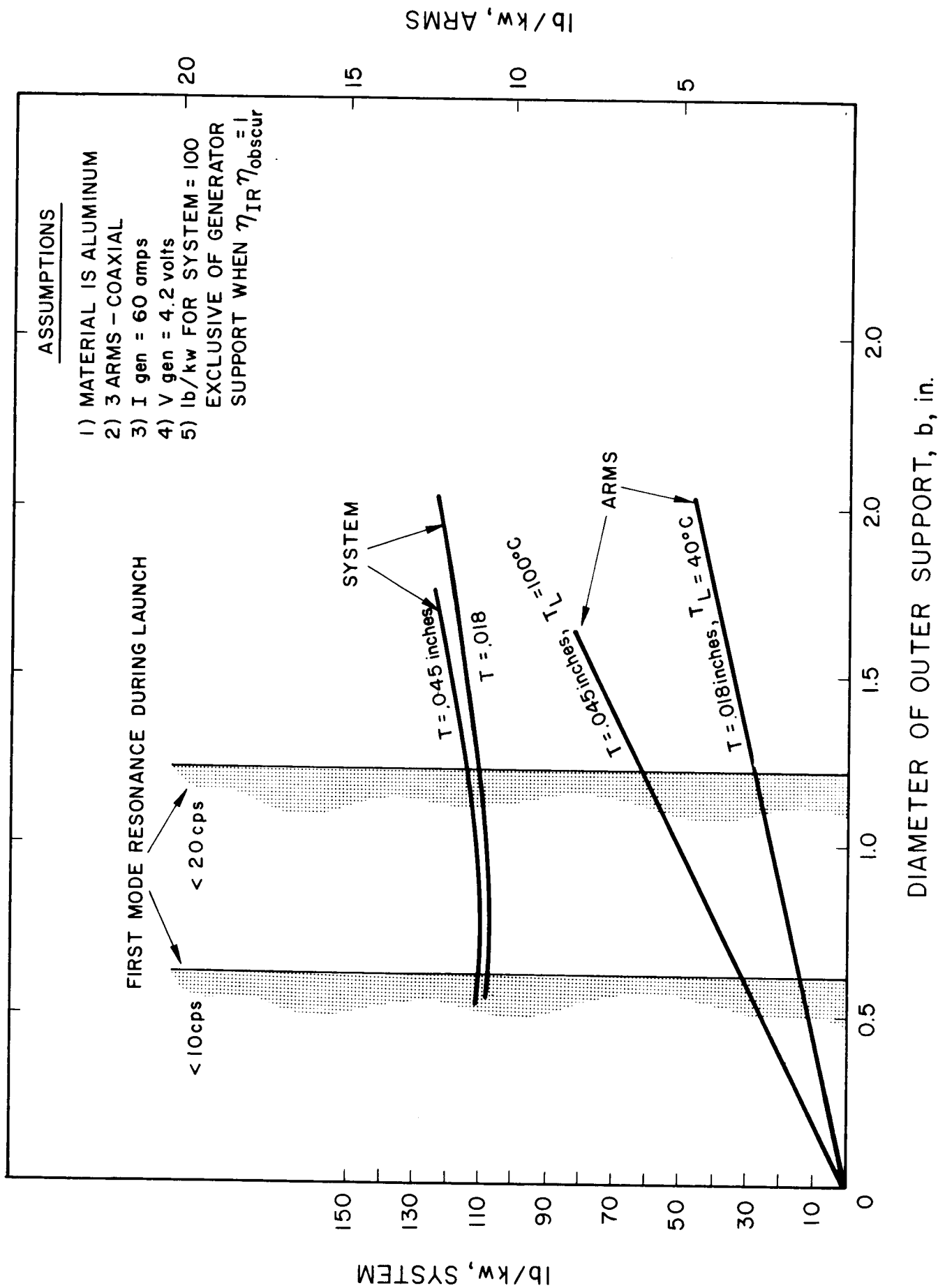


FIG. 4-26 TYPICAL GENERATOR SUPPORT OPTIMIZATION FOR 5FC SYSTEM

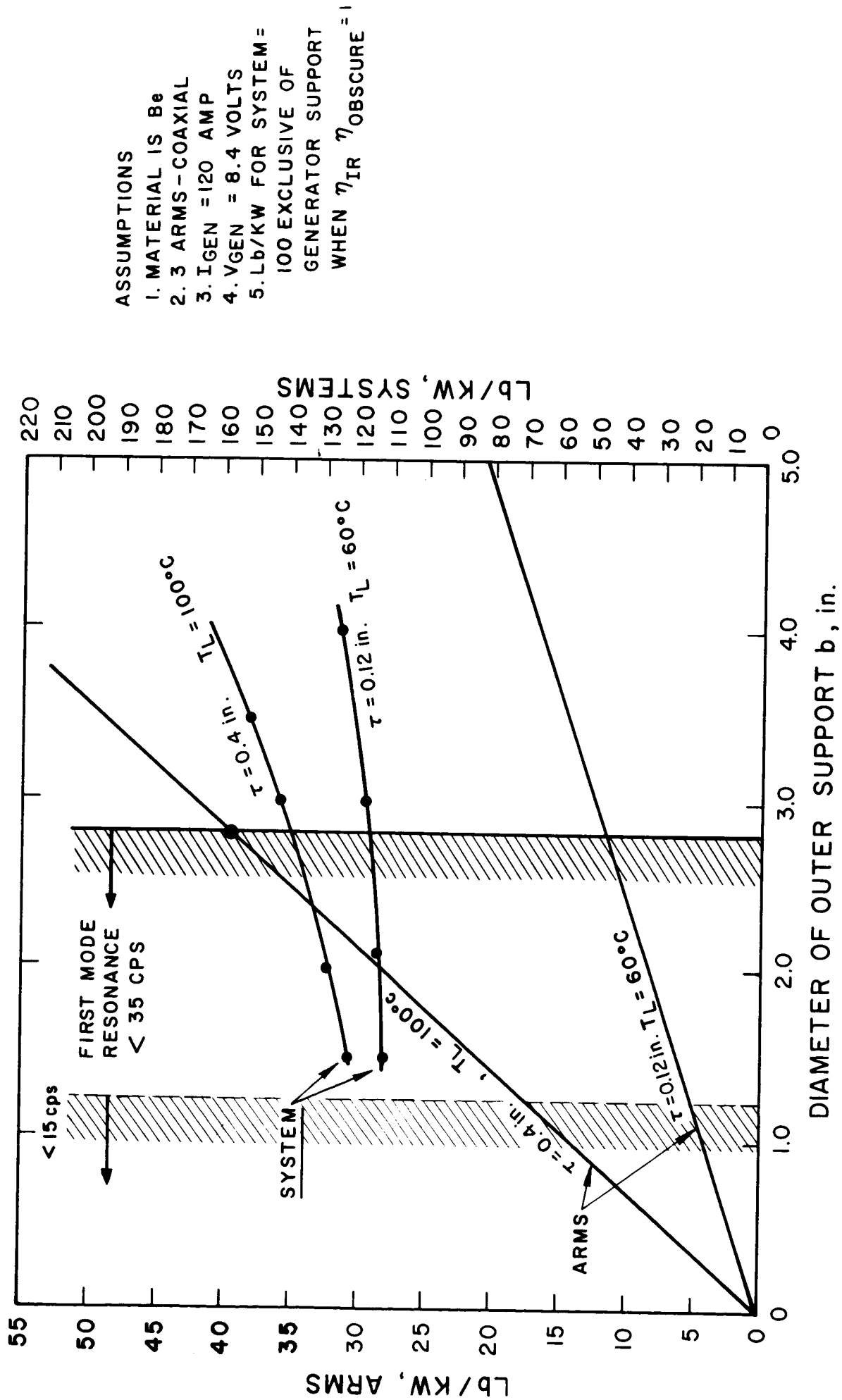


FIG. 4-27 TYPICAL GENERATOR SUPPORT OPTIMIZATION FOR 10FL SYSTEM

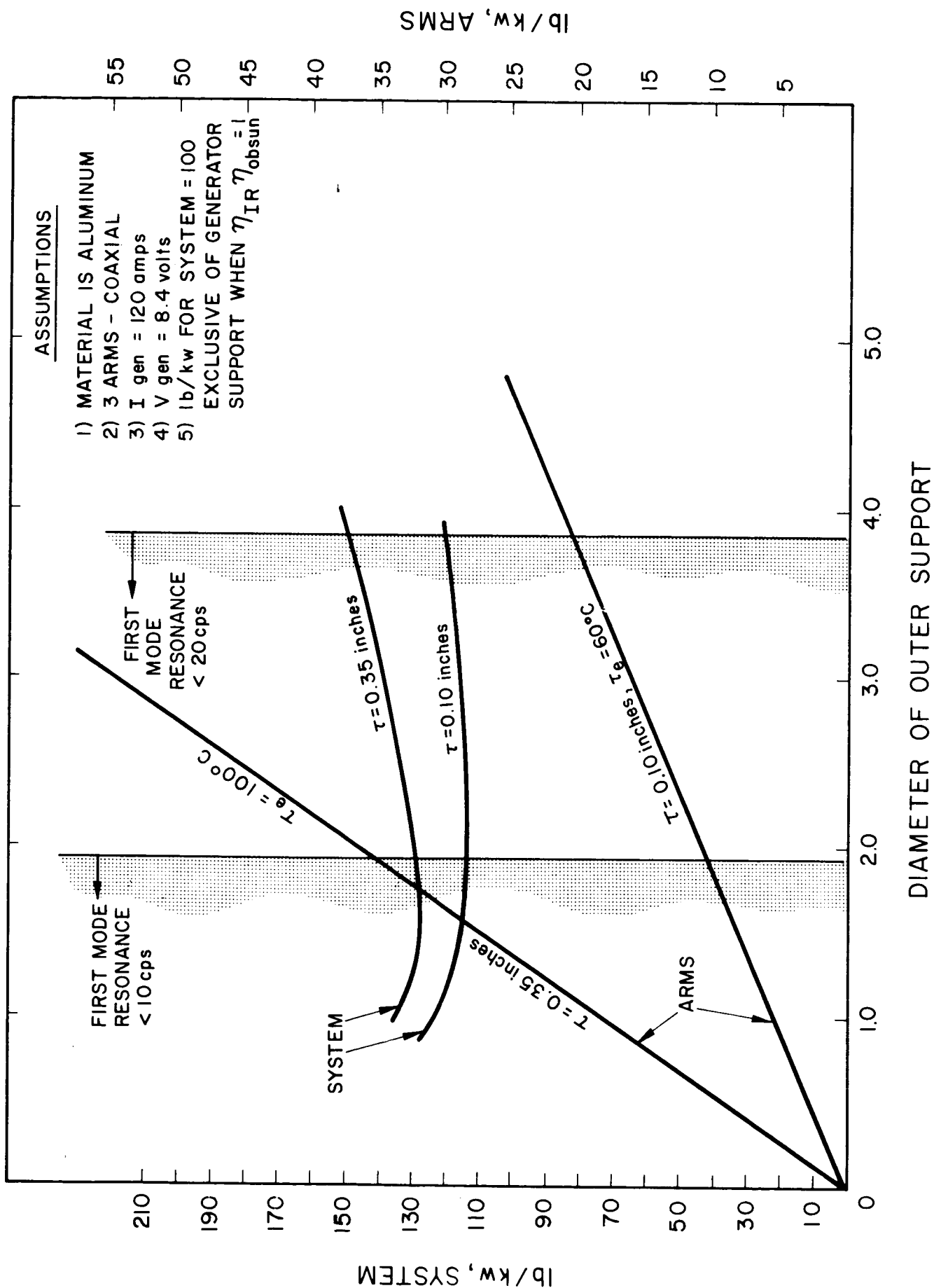


FIG. 4-28 TYPICAL GENERATOR SUPPORT OPTIMIZATION FOR 100% SYSTEM

In conclusion, the optimization of generator support arms has been shown to be a complex problem involving the performance of other components of the system. The weight of the arms by themselves is not as important as the effect of generator support design on overall system efficiency. Thermal conductivity and vibration characteristics are important design criteria. Unfortunately, the knowledge of these effects and the methods for calculating these effects are still relatively approximate.

#### 4.10 Other Thermal Effects

In addition to thermal expansion, mislocation of the generator can result from bimetallic effects. These arise from (1) absorption of radiation from the sun, concentrator, generator, and nearby planets (2) differing fields of view towards the concentrator and generator.

At  $300^{\circ}\text{C}$  a blackbody will emit  $0.6 \text{ watts/cm}^2$  and at  $100^{\circ}\text{C}$ ,  $0.11 \text{ watts/cm}^2$ . With high emissivity, say 0.9, the generator support skin will absorb  $0.12 \text{ watts/cm}^2$  at normal incidence to the sun. Thus, at the generator support end close to the concentrator, the impinging solar radiation is an important contributor to the overall temperature of the generator support arm.

The bimetallic effects are expected to be small. Preliminary calculations indicated a maximum temperature differential from one side of the generator support arm to the other of less than  $5^{\circ}\text{C}$ .

Of more importance, however, is the effect of the radiation absorption on the design calculations for the generator support. As discussed above, a primary factor in the tradeoff optimization was the thickness of the wall which was limited by the maximum temperature allowed at the end of the generator support. As a result of other incident radiation, the maximum allowable wall thickness will decrease.

If the wall thickness must decrease, electrical resistivity will increase, and in general, the effect will be to decrease overall system efficiency.



## 5. THERMIONIC CONVERTER

An investigation was made into the state of the art in thermionic converters and their performance characteristics. This section will describe the converter and its operation, and summarize the performance characteristics.

During the study, I-V, P-V and efficiency curves were derived for converters operating at 15, 20 and 25 watts/cm<sup>2</sup> at 0.7 volt and emitter temperatures of 1500 to 1800°C; extrapolation was based on performance of current laboratory converters.

Several different types of I-V curves can be derived depending on power input conditions. Almost all the converter I-V curves measured in the laboratory maintained conditions of constant emitter temperatures and "optimized" reservoir and radiator temperatures. This type of curve, while useful as an indication of potential performance, cannot be used in systems analysis where constant power input is the governing condition in converter operation.

If a converter is designed for 1700°C emitter temperature at a specific voltage, operation at other voltage levels with constant power input will vary the temperatures within the converter. Higher current and lower voltage results in higher seal and collector temperatures. Lower current and higher voltage results in higher emitter temperature and lower collector and seal temperature. Until adequate reliability data is gathered regarding the effects of varying the load, it is assumed that the optimum design condition from a system viewpoint is to maintain the output of the converter close to the design point.

Limited life information on converters is available; several converters have reached 3000 hr. life steady state at relatively low power outputs. The avoidance of rapid increases or decreases in temperature is desirable. Also, laboratory experiments indicate that startup will

require load adjustment to short-circuit conditions along with a maximum input of solar energy to the generator in order to open the emitter-collector gap.

### 5.1 Converter Description

A thermionic converter is a device which converts heat into electricity by utilizing the tendency of metals to emit electrons at high temperature. A typical device is shown in Fig. 5-1. The components of the converter are:

1. An emitter which typically operates at temperatures from  $1500^{\circ}$  to  $1800^{\circ}\text{C}$ .
2. A spacer which consists of a thin-walled cylinder which serves to support the emitter and, in present converter designs, separate the emitter from the collector at operational temperatures.
3. A collector which is cooler than the emitter, typically at  $700^{\circ}$  to  $800^{\circ}\text{C}$ , and collects the electrons emitted by the emitter. Typical spacings between the emitter and collector at operational temperatures may range from 0.00025 to 0.010 inch. Optimum spacing depends on temperatures, materials, geometry and related phenomena.
4. A leadthrough ring which supports the spacer and carries current to an electrical lead; also, it can provide a support for the insulation between collector and emitter.
5. A radiator for radiating the energy from the collector to maintain a cool collector.
6. A cesium reservoir and tubulation into the emitter collector space in order to provide a cesium plasma.
7. Electrical leads.
8. A support structure for mounting the converter onto a practical generator structure. The converter can be mounted in several ways which may or may not utilize individual support structure.

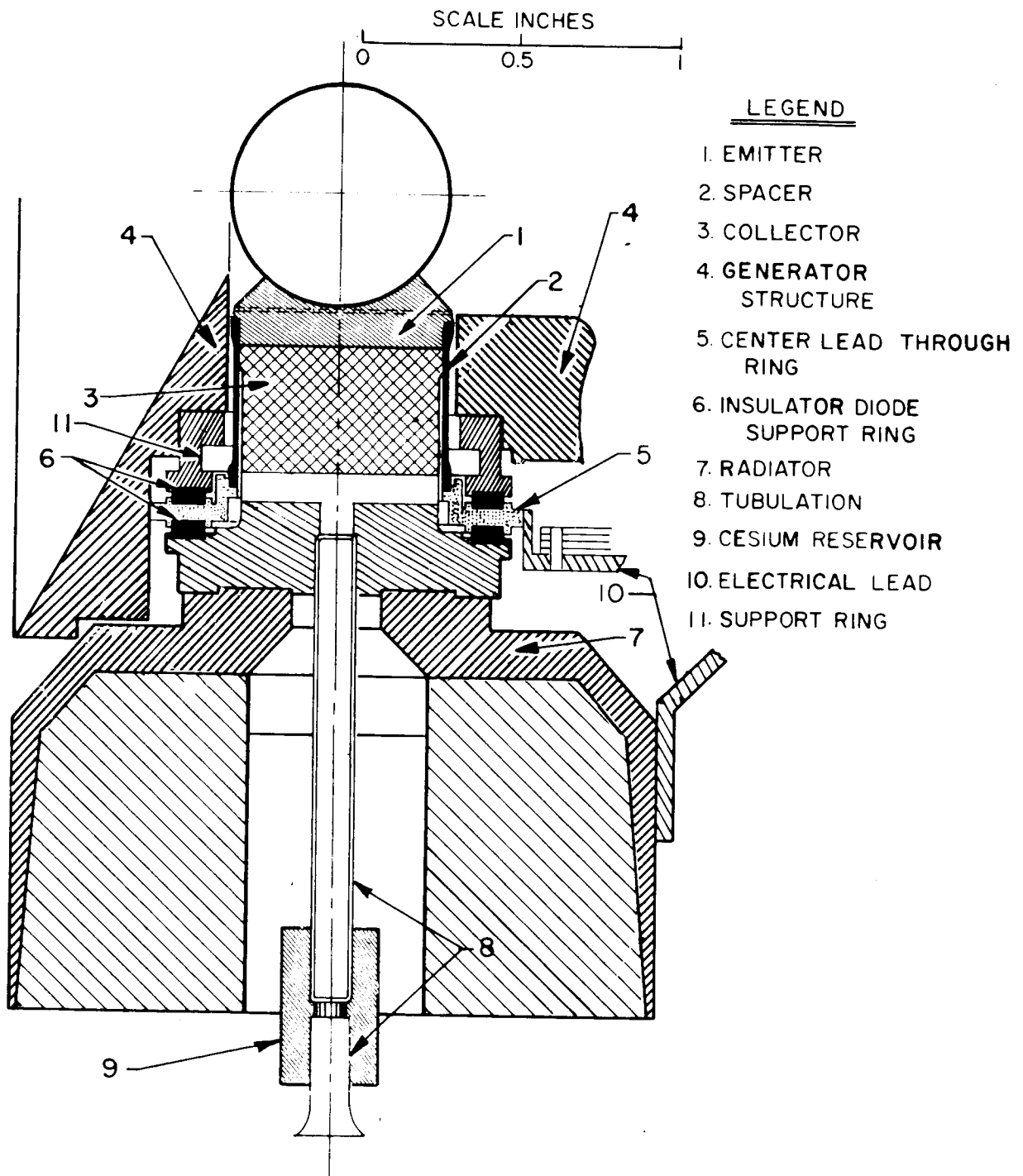


FIG. 5-1 TYPICAL DIODE CONFIGURATION

Figure 5-2 is an illustration of converters which have been assembled in the years 1961 through 1965. The basic configuration is the same; i.e., a round flat emitter is heated on one end and is supported by a thin wall cylindrical spacer. The weight of the converters has remained about the same ranging from 0.5 to 0.75 lb per converter. As described later, the performance characteristics have increased significantly during the past years.

Figure 5-3 shows the potential energy diagram as it exists in an operational converter. An expression for converter efficiency is given in Eq. 5-1. The efficiency depends on electron cooling losses and other losses which depend to a large degree on converter collector temperature. Typical converter, cesium conduction, electrode radiation, and conduction losses are given in Table 5-1 for a range of emitter temperatures. These losses are relatively small compared to the power drain from the emitter from electron cooling.

Figure 5-4 shows typical electron cooling power losses from the emitter at various emitter temperatures. The electron cooling power is described by Eq. 5-2.

The power output of the device is described in Eq. 5-3 and is given by the product of the current plus the summation of the voltage potentials described in Fig. 5-3. It is desirable to maintain a high emitter work function and a low collector work function in order to maximize the voltage out from the device. Other voltage losses include the plasma loss and the potential fall at the cathode.

$$\text{Converter Efficiency} = \frac{\text{Power Output}}{\text{Electron Cooling} + \text{Cs Conduction Loss} + \text{Inter-electrode Radiation} + \text{Lead and Envelope Conduction \& Radiation}} \quad (5-1)$$

$$P_{\text{electron cooling}} = I \left[ \phi_e + 0.173 \frac{T_{\text{emitter}}}{1000} \right] \quad (5-2)$$

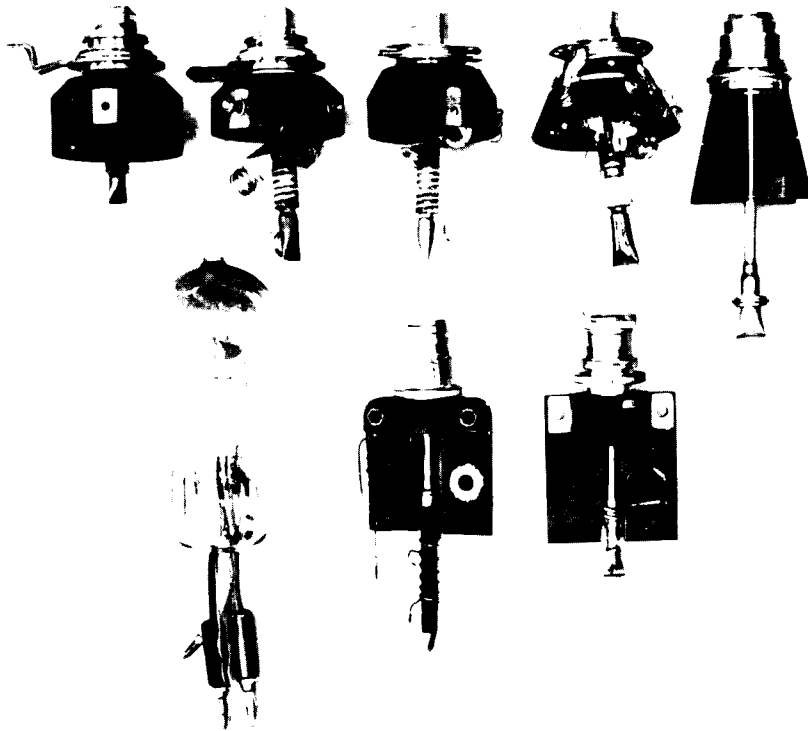
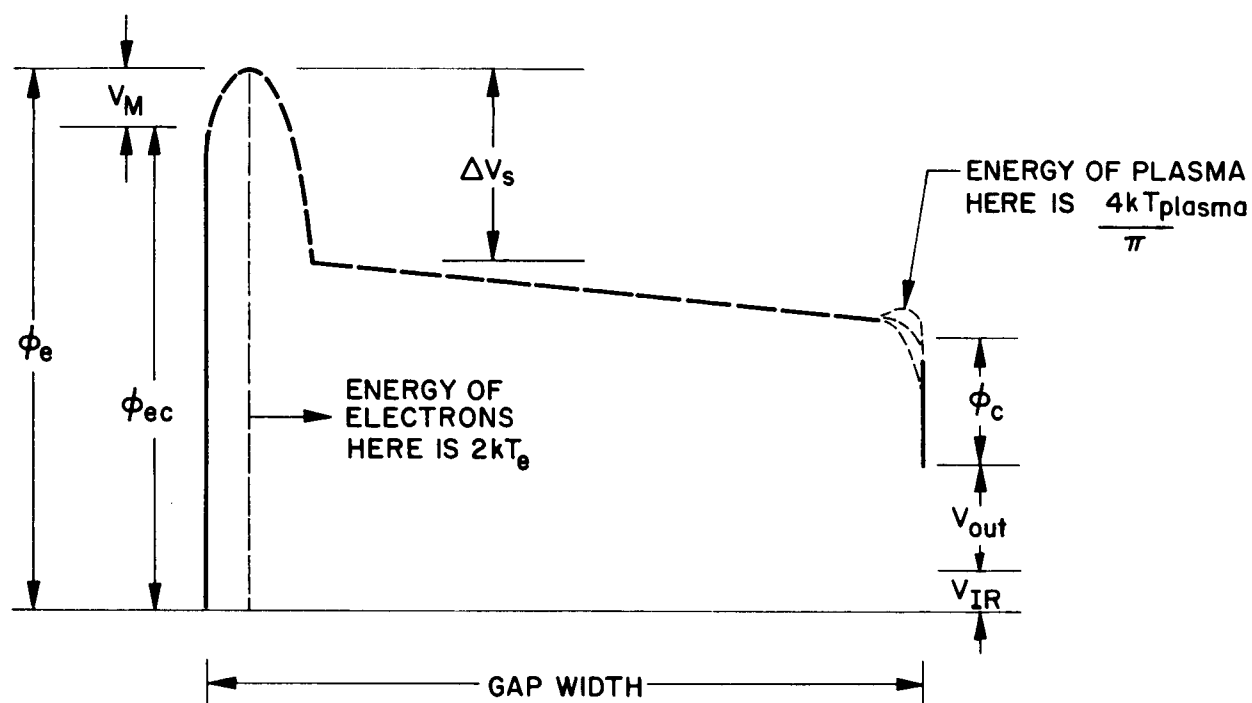


FIG. 5-2 CONVERTER ITERATIONS



$T_e$  = EMITTER TEMPERATURE, abs  
 $T_{\text{plasma}}$  = PLASMA TEMPERATURE  
 $V_n$  = POTENTIAL MINIMUM  
 $\phi_e$  = "EFFECTIVE" EMITTER POTENTIAL  
 $\phi_{e,0}$  = EMITTER POTENTIAL UNDER ZERO ELECTRIC FIELD CONDITIONS  
 $\Delta V_s$  = POTENTIAL FALL AT CATHODE, volts  
 $V_{out}$  = OUTPUT VOLTAGE OF CONVERTERS AT CATHODE  
 $\phi_c$  = COLLECTOR POTENTIAL  
 $V_{IR}$  = LEAD VOLTAGE DROP

FIG. 5-3 CONVERTER POTENTIAL ENERGY DIAGRAM

TABLE 5-I  
TYPICAL CONVERTER CESIUM CONDUCTION  
INTERELECTRODE RADIATION, AND CONDUCTION LOSSES

|  | Emitter Temperature, °C |             |             |             |
|--|-------------------------|-------------|-------------|-------------|
|  | <u>1500</u>             | <u>1600</u> | <u>1700</u> | <u>1800</u> |
| Cesium Conduction Loss<br>(w/cm <sup>2</sup> )         | 6                       | 7           | 8           | 9           |
| Interelectrode Radiation* Loss<br>(w/cm <sup>2</sup> ) | 13                      | 17          | 20          | 25          |
| Conduction Loss<br>(w/cm <sup>2</sup> )                | 33                      | 37          | 40          | 43          |

\*emissivity of 0.4 assumed for both surfaces.

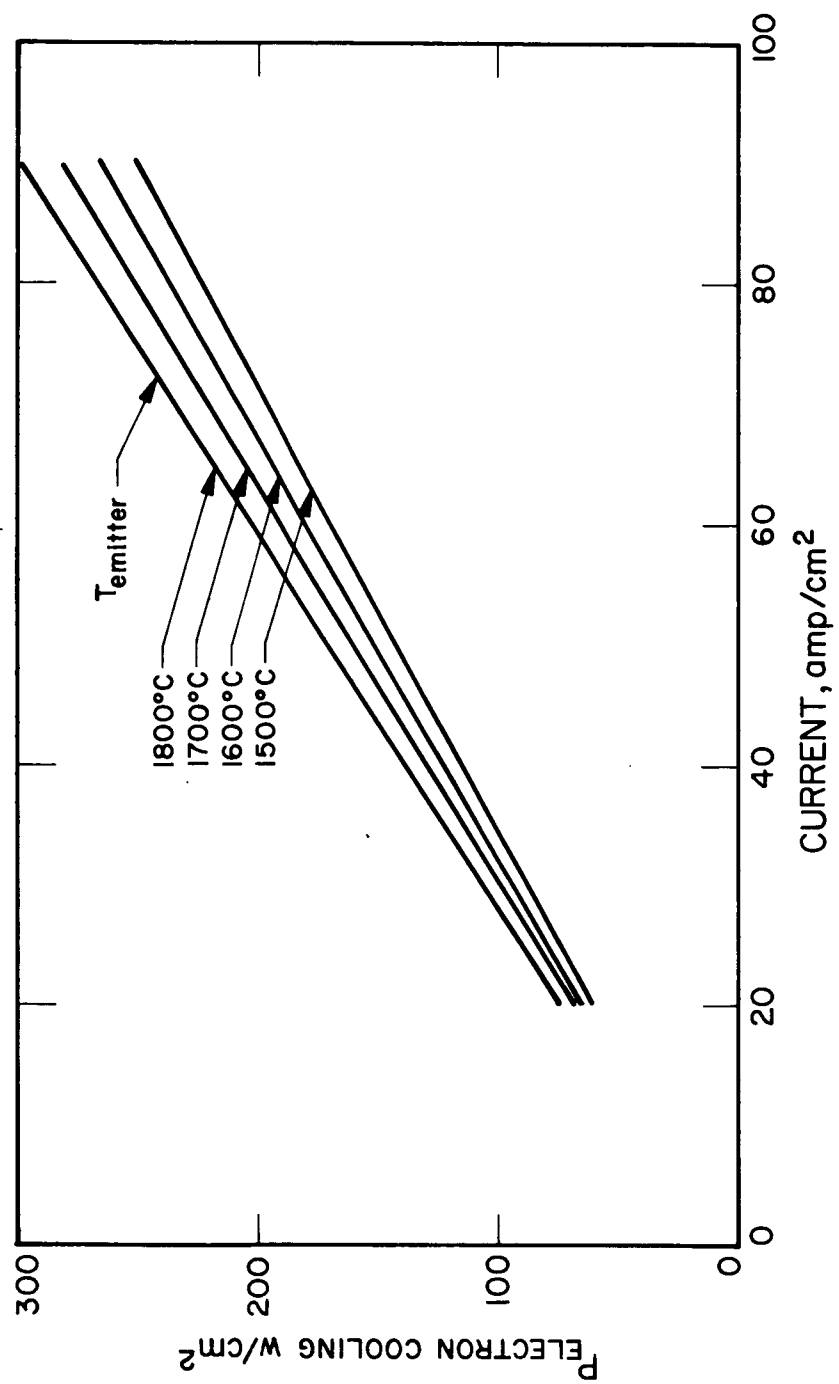


FIG. 5-4 ELECTRON COOLING FROM EMITTER



where  $I$  = current

$\phi_e$  = emitter surface work function

$T_{\text{emitter}}$  = emitter surface temperature ( $^{\circ}\text{K}$ )

$$P_{\text{output}} = I \left\{ \phi_e - \Delta V_s - \phi_c - V_{\text{IR}} - \frac{4 k T_{\text{plasma}}}{\pi e} \right\} \quad (5-3)$$

(see Fig. 6-3 for explanation of terms)

## 5.2 Performance Characteristics

The output of the thermionic converter depends on a large number of variables including spacing between emitter and collector, emitter temperature, collector temperature, cesium temperature, material work functions, losses and related phenomena.

In general, at a given emitter and collector temperature, the converter has an optimum power output for any given cesium reservoir temperature. This is illustrated in Fig. 5-5 which shows typical DC performance of a converter which is really the envelope of a number of optimum I-V curves at each cesium reservoir temperature.

"Optimum" DC performance as illustrated in Fig. 5-5 can be misleading. Figure 5-6 shows three types of converter I-V curves and two types of converter P-V curves which can be used to describe converter characteristics. These are:

1. Curve A is an I-V curve with constant emitter temperature and optimized cesium reservoir radiator temperature at each point. This is the "DC" performance curve usually obtained in laboratory tests. This curve is only an indication of performance and is not directly applicable to system design.
2. Curve B is an I-V characteristic where constant power input is given to the converter and the temperatures of the converter are allowed to vary as a function of load. This is the nature of the operation of the converter in a system mode and is the curve most useful in system design. Limits on the load changes which can be withstood by the converter will depend on the temperatures achieved by the seal and emitter.

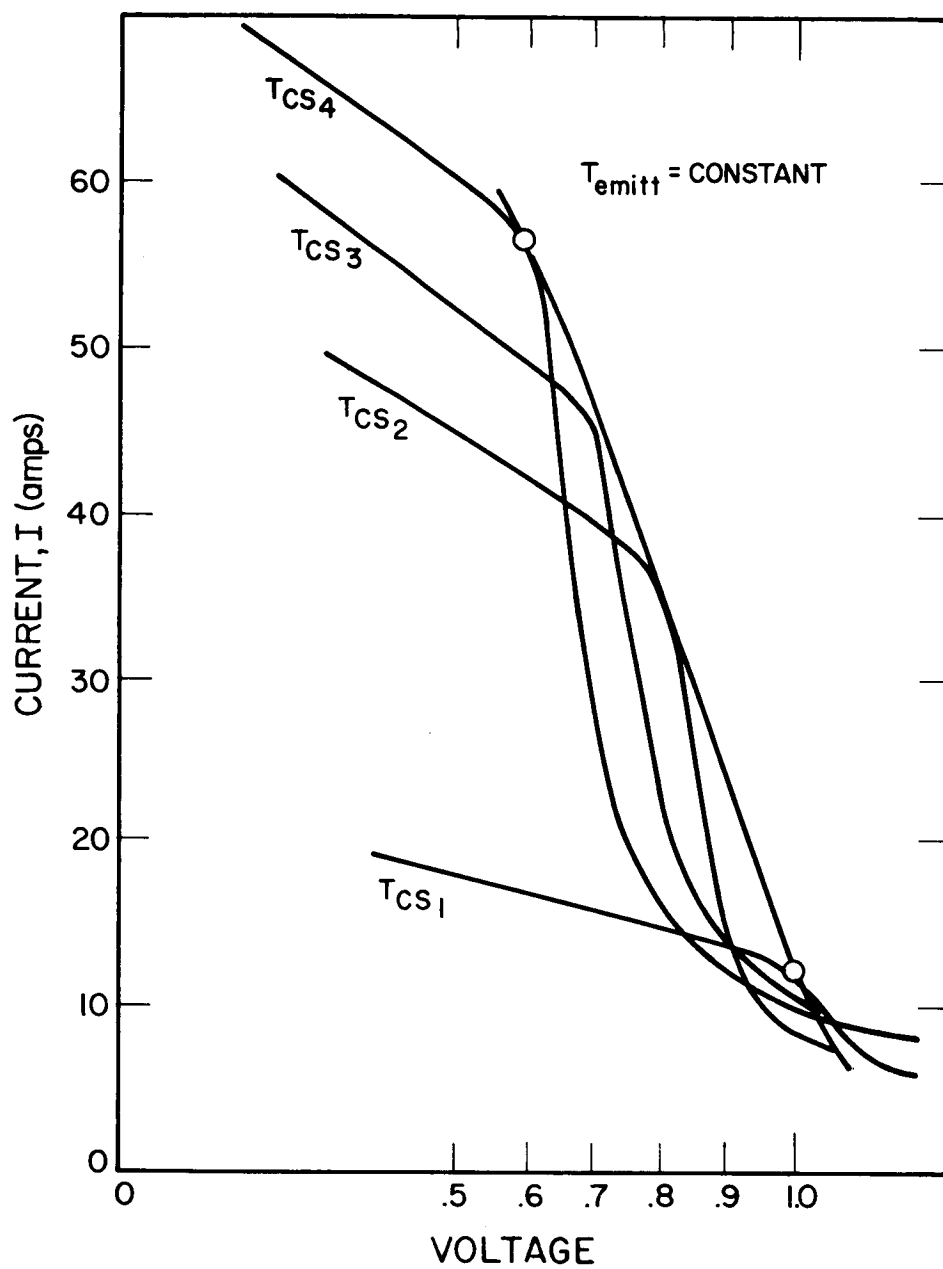


FIG. 5-5 TYPICAL D.C. PERFORMANCE, SHOWING ENVELOPE OF OPTIMUM IV CURVES

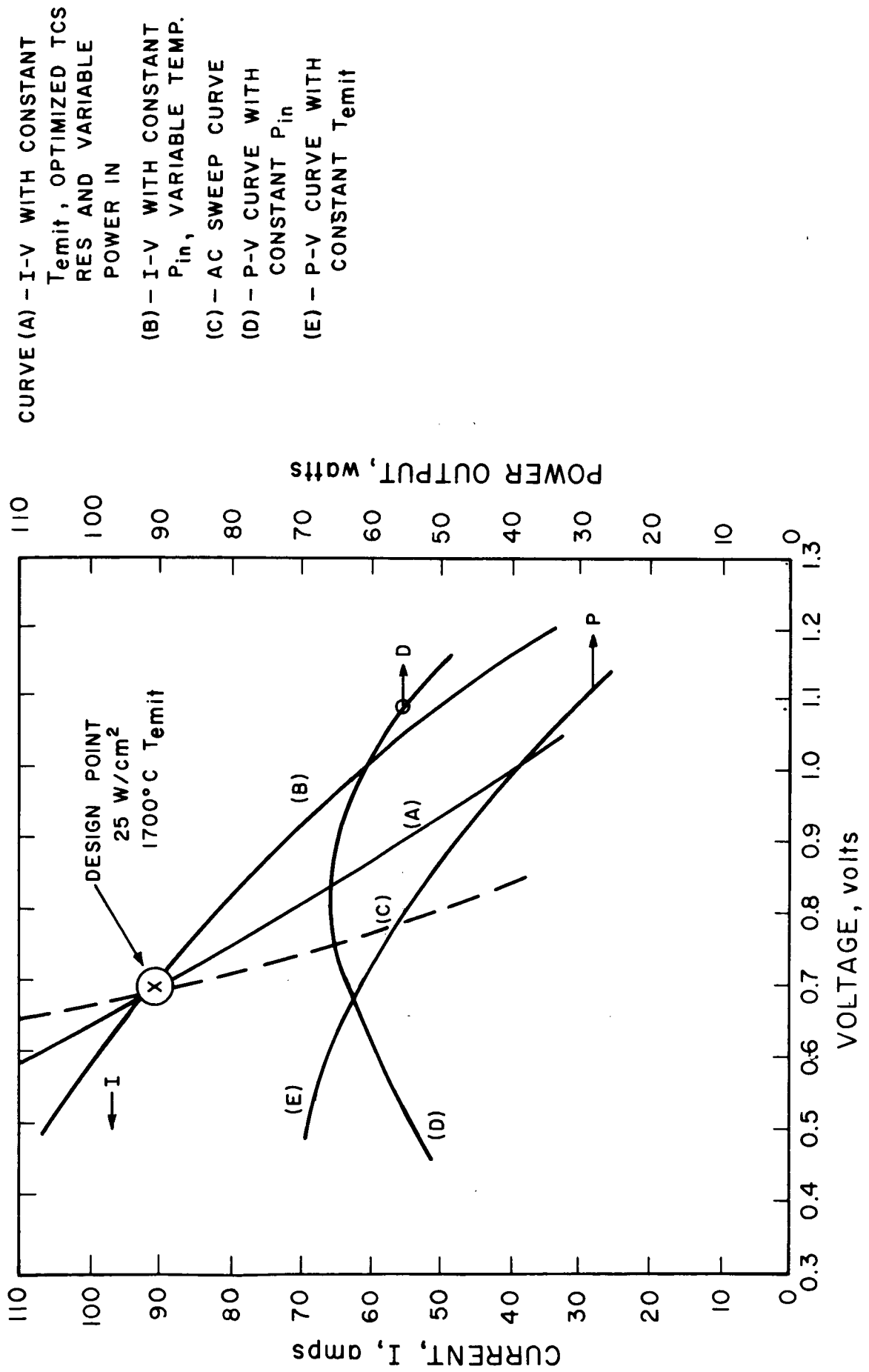


FIG. 5-6 TYPES OF CONVERTER CHARACTERISTICS

3. Curve C is an AC sweep curve which is obtained by swiftly varying the load about a given design point such that the converter performance curve is obtained without changing any temperatures in the system and maintaining a constant power input. This curve is useful for determining potential performance.
4. Curve D is a P-V curve with constant power input to the converter. This curve is characteristic of the operation of the converter in a system.
5. Curve E is a P-V curve with constant emitter temperature corresponding to Curve A. This curve is not directly applicable to system design.

It should be noted in Fig. 5-6 that the optimum power point for a converter with constant power input is at a much higher voltage than the maximum power output of a converter operated at constant emitter conditions.

Figures 5-7 through 5-15 present I-V, P-V and efficiency curves for thermionic converters operating at emitter temperatures of 1500°, 1600°, 1700°, and 1800°C. Three types of converters are assumed; these are capable of 15 watts/cm<sup>2</sup>, 20 watts/cm<sup>2</sup> and 25 watts/cm<sup>2</sup> at 0.7 volt with an emitter temperature of 1700°C. Performance and efficiency characteristics were derived using Eqs. 5-1, 5-2, and 5-3 and other information available in the literature.

The curves in Figs. 5-7 through 5-15 are considered to be reasonable extrapolations of the state of the art. Several converters have exhibited greater than 20 watts/cm<sup>2</sup> at 0.7 volt although these cannot be characterized yet as production converters.

Figures 5-16, 5-17, and 5-18 show I-V curves for the three types of converter for the case where constant power input is given to the converter. The constant power curves are compared with the constant emitter temperature curves and significant differences can be seen. The constant power curves are consistent with the use of Eqs. 5-1, 5-2, and 5-3 and analysis of the change in conduction losses, temperature losses, etc.

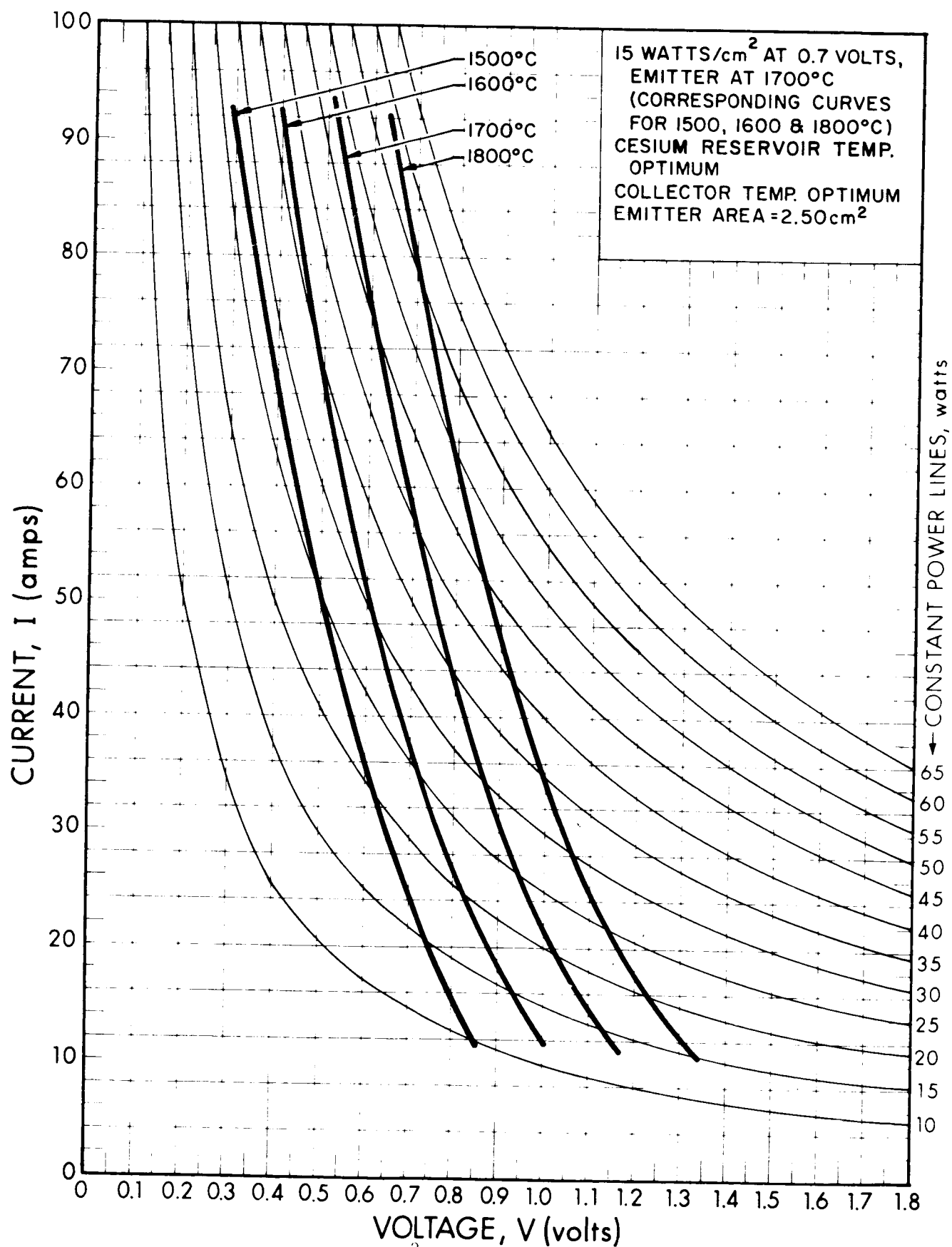


FIG. 5-7 I-V CURVE - 15 w/cm<sup>2</sup> CONVERTER

4326-Final

5-13

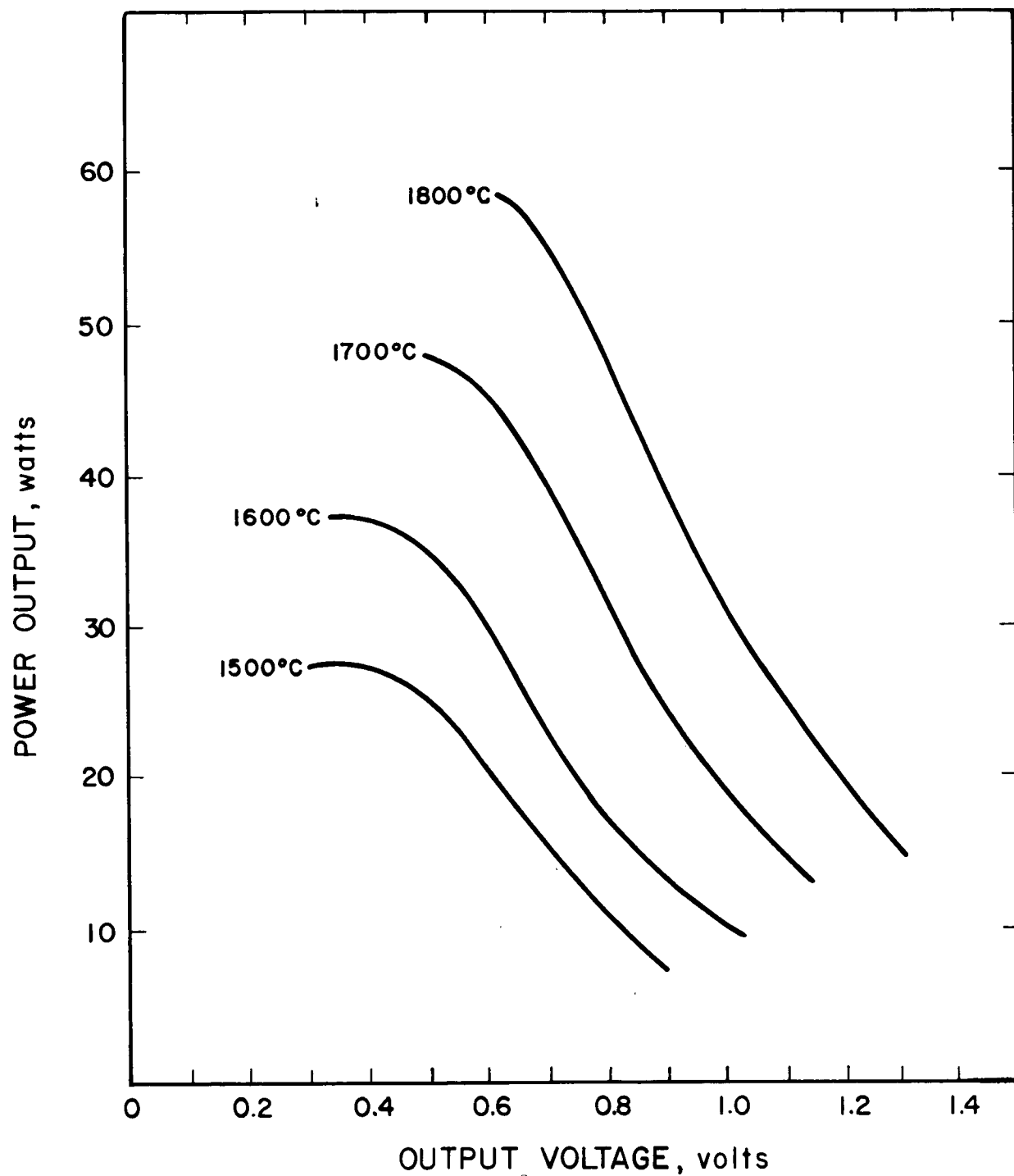


FIG. 5-8 P-V CURVE -  $15 \text{ w/cm}^2$  CONVERTER

4326-Final

5-14

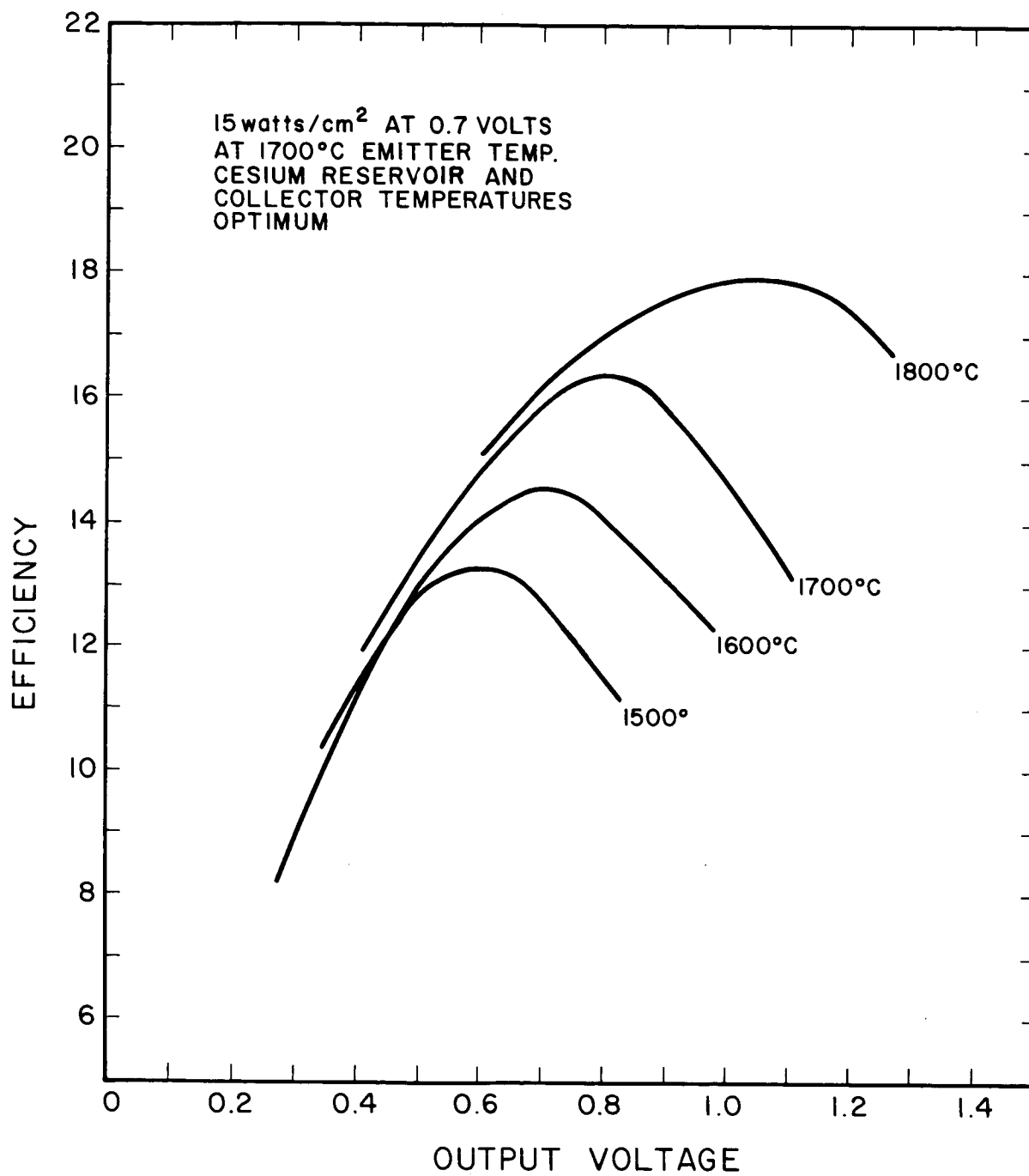


FIG. 5-9 EFFICIENCY CURVE - 15 w/cm<sup>2</sup> CONVERTER

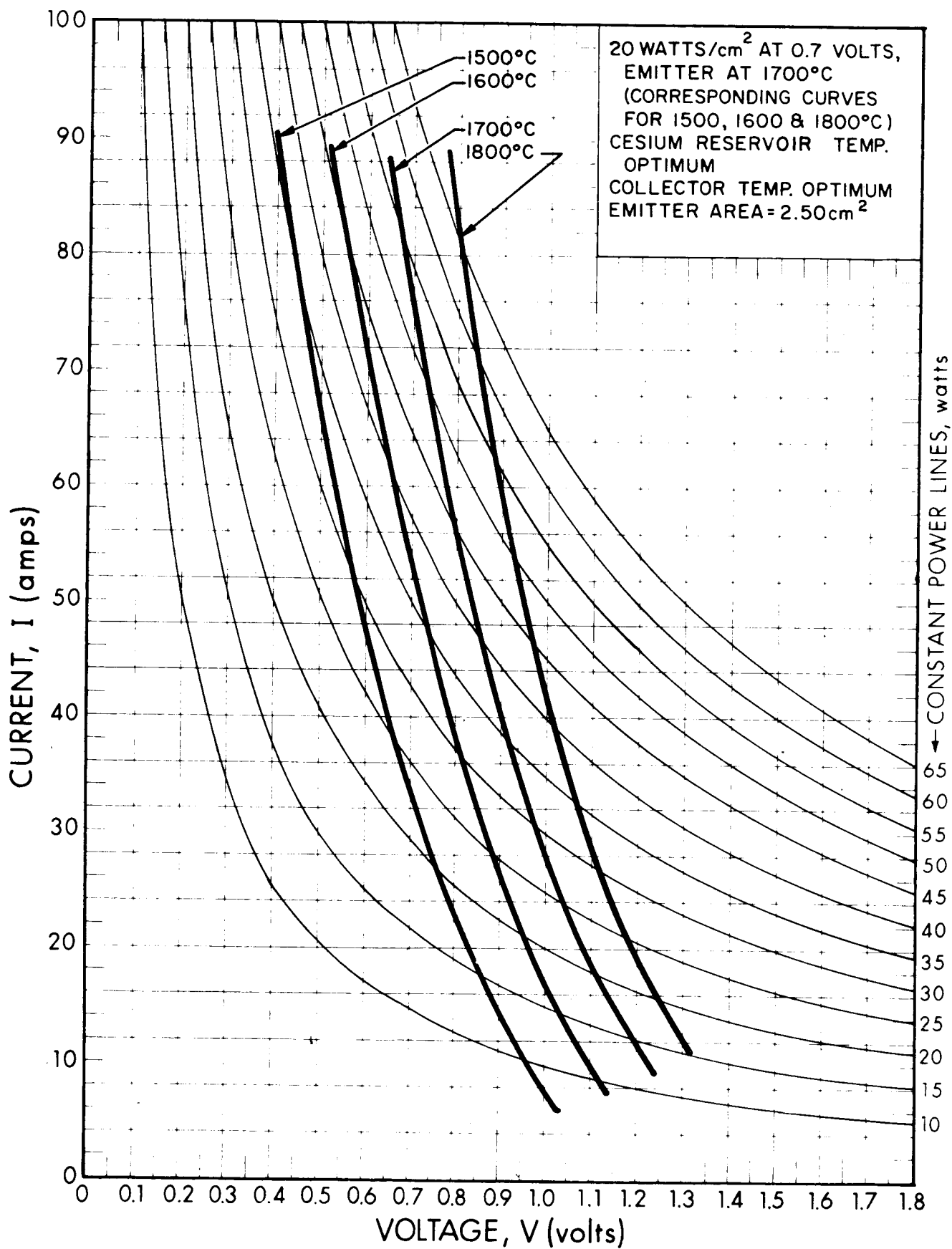


FIG. 5-10 I-V CURVE - 20 w/cm<sup>2</sup> CONVERTER  
4321-Final 5-16



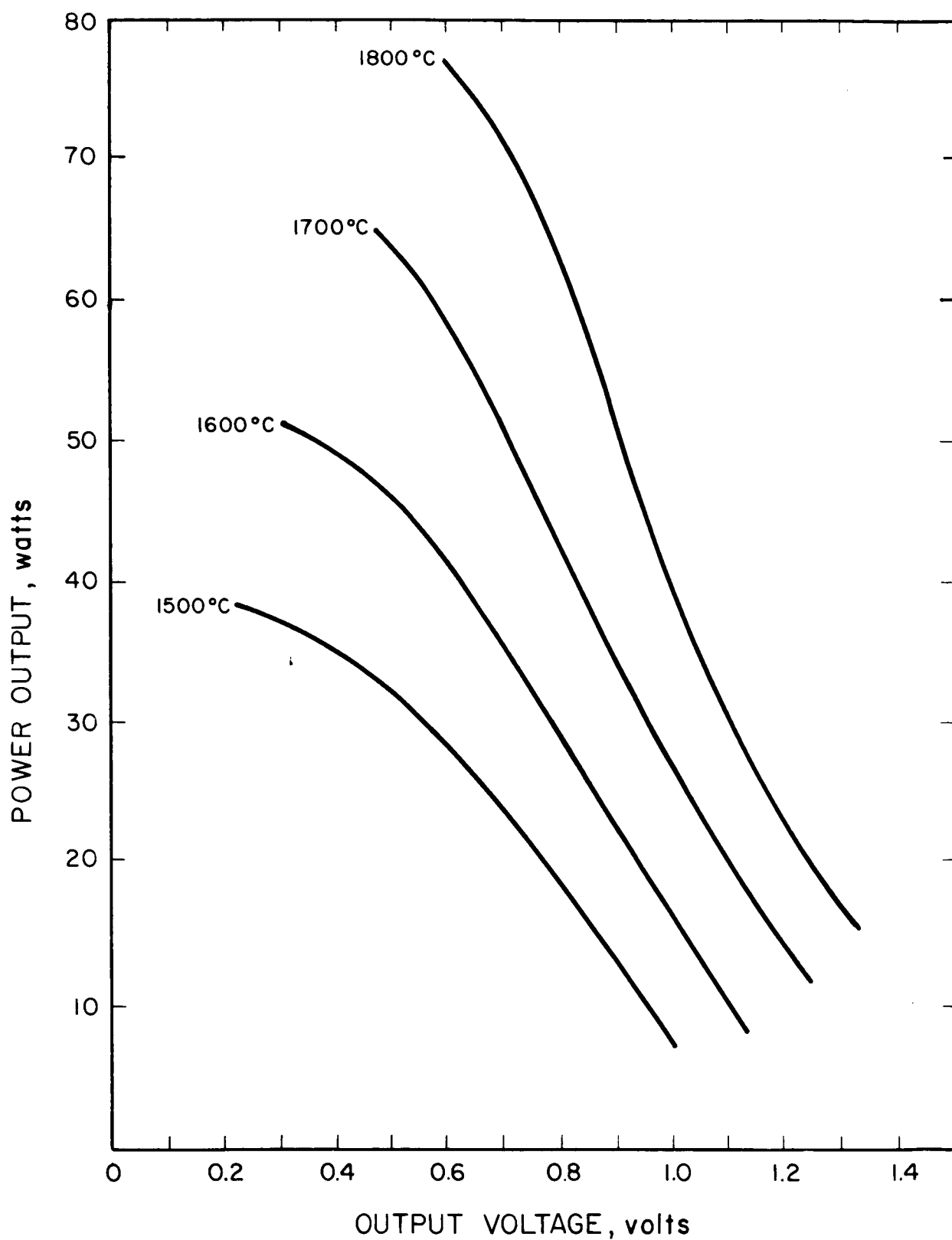


FIG. 5 -11 P-V CURVE - 20 w/cm<sup>2</sup> CONVERTER

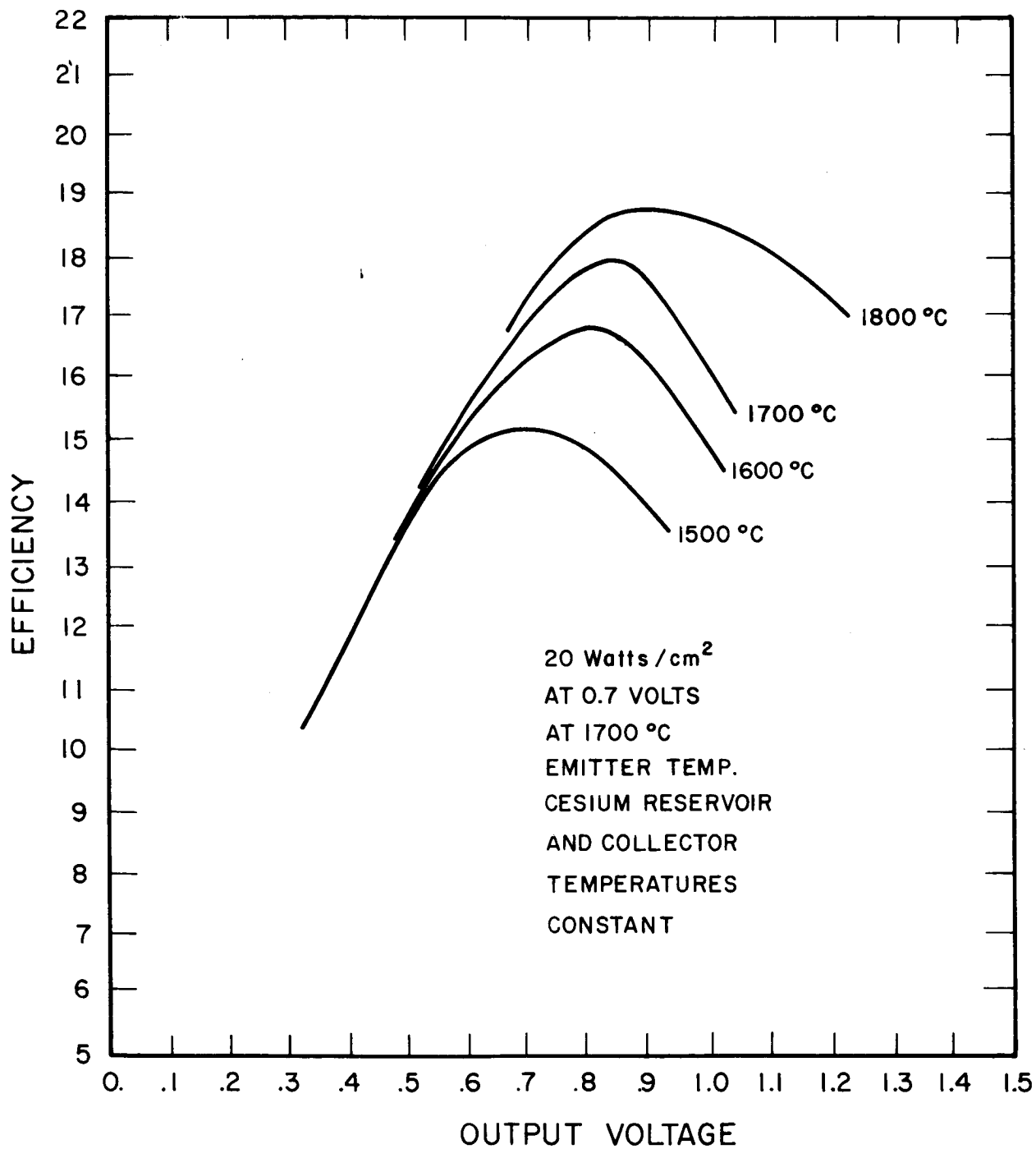


FIG. 5-12 EFFICIENCY CURVE - 20 w/cm<sup>2</sup> CONVERTER

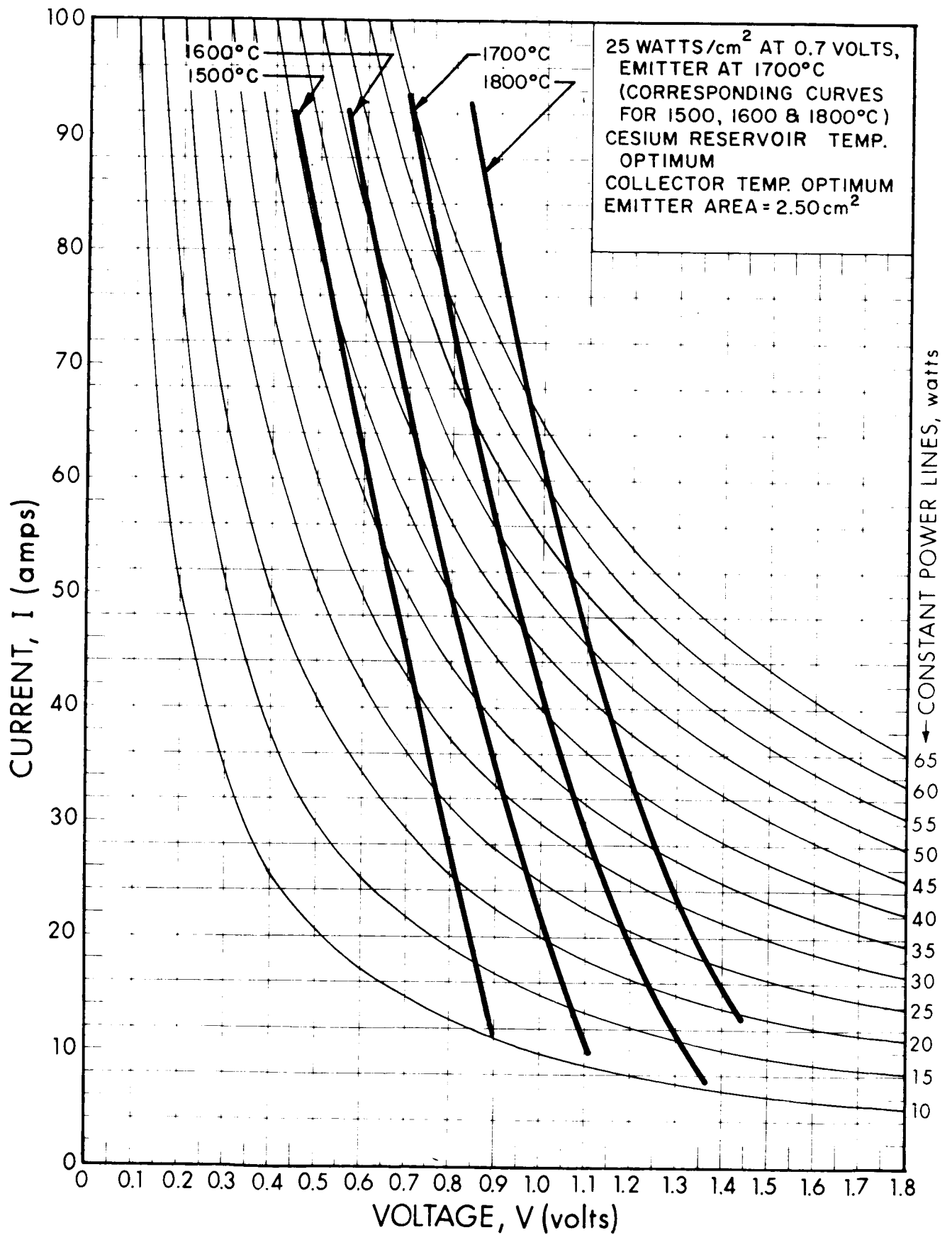


FIG. 5-13 I-V CURVE - 25 w/cm<sup>2</sup> CONVERTER

4-12-1961

5-19

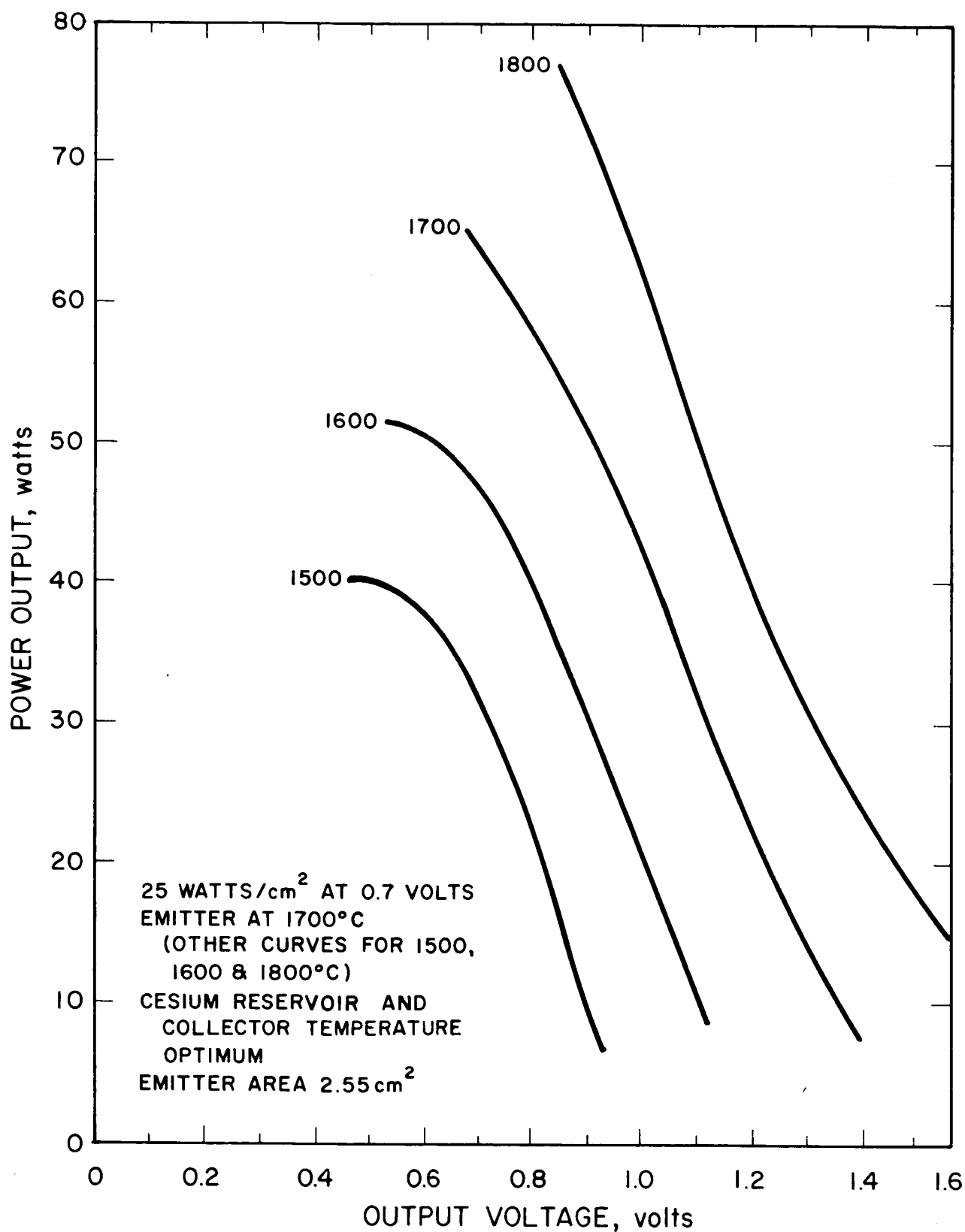


FIG. 5-14 P-V CURVE - 25 w/cm<sup>2</sup> CONVERTER

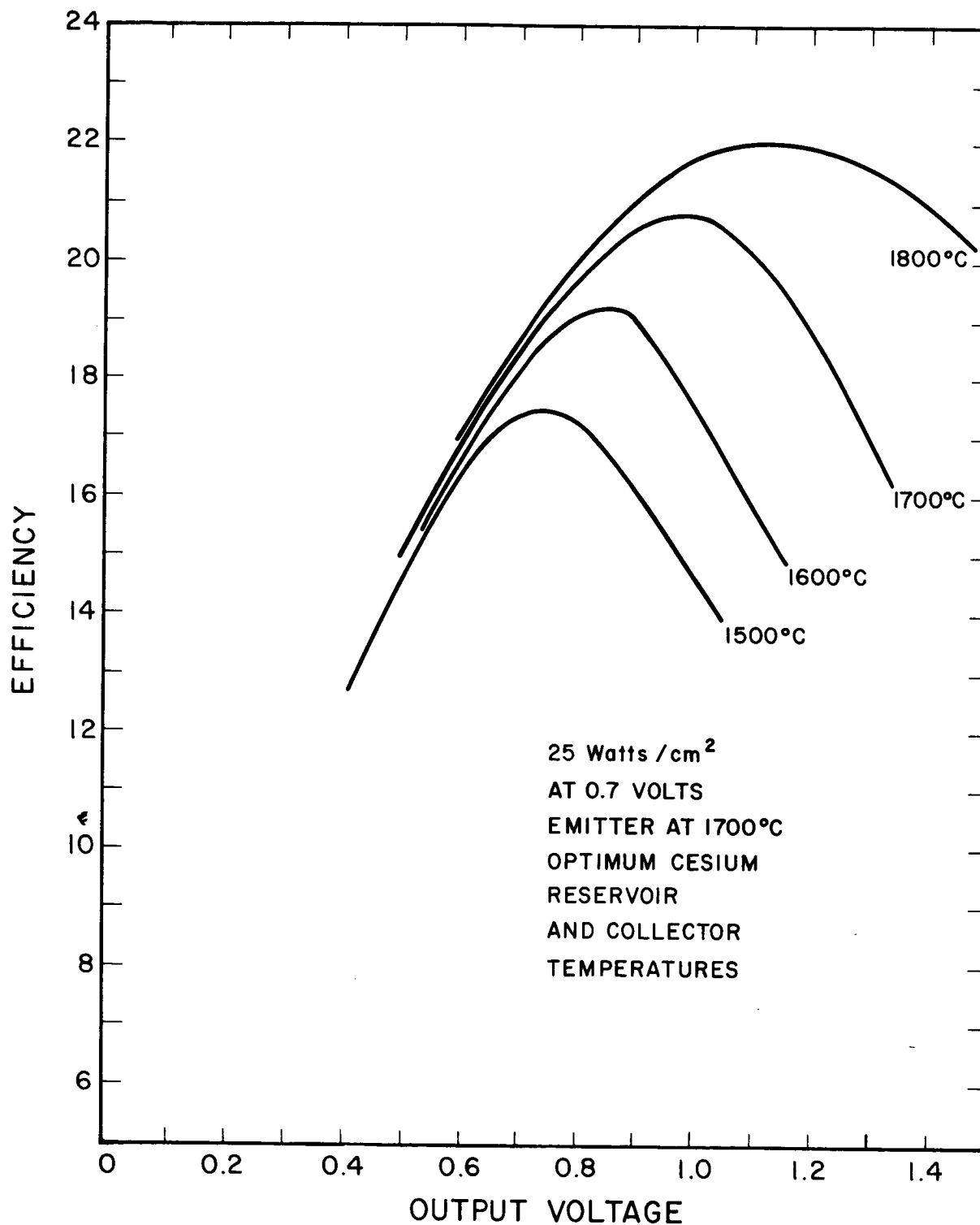


FIG. 5-15 EFFICIENCY CURVE - 25 w/cm<sup>2</sup> CONVERTER

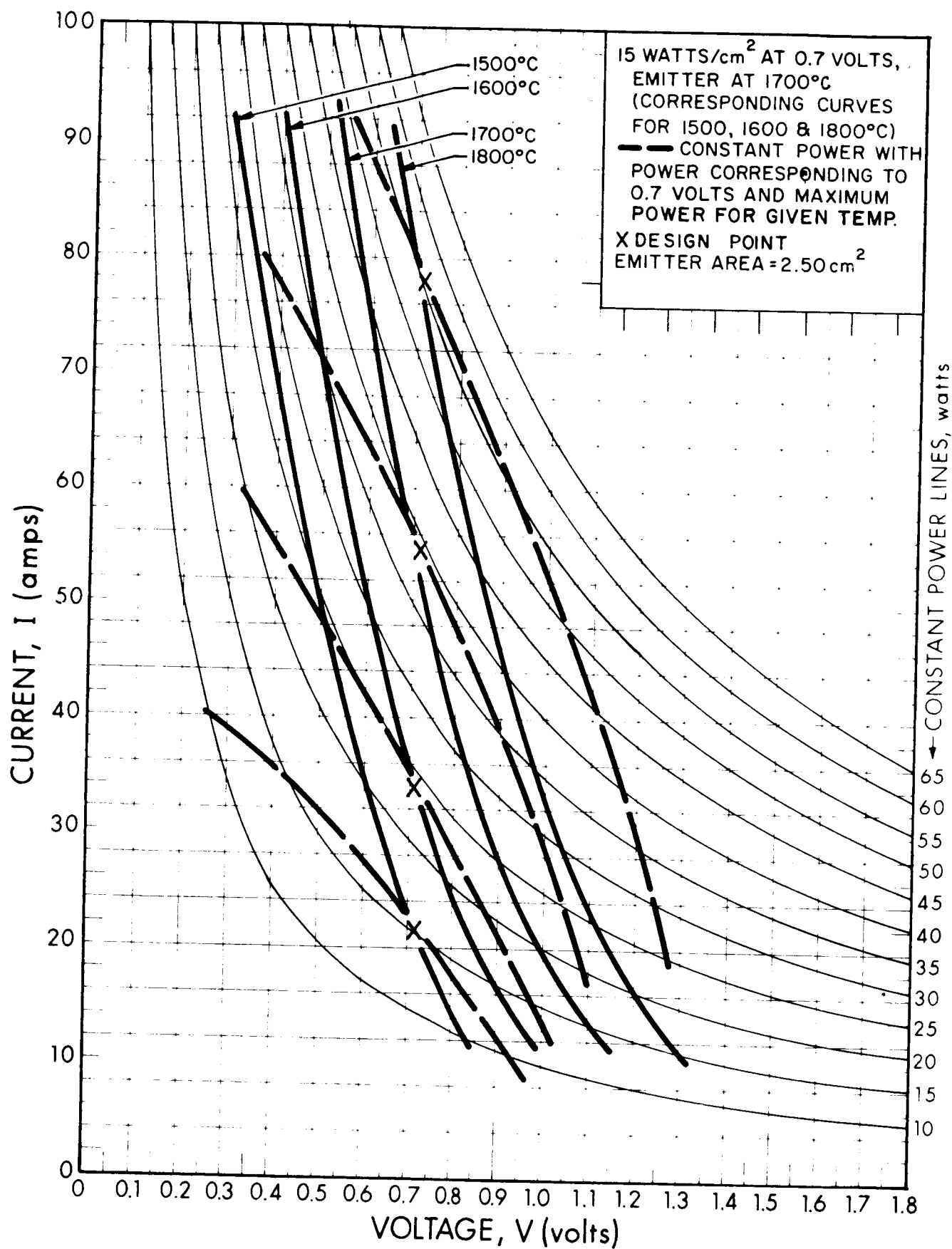


FIG. 5-16 I-V CURVES FOR CONSTANT POWER INPUT - 15 W/cm<sup>2</sup> CONVERTER

4320-Final

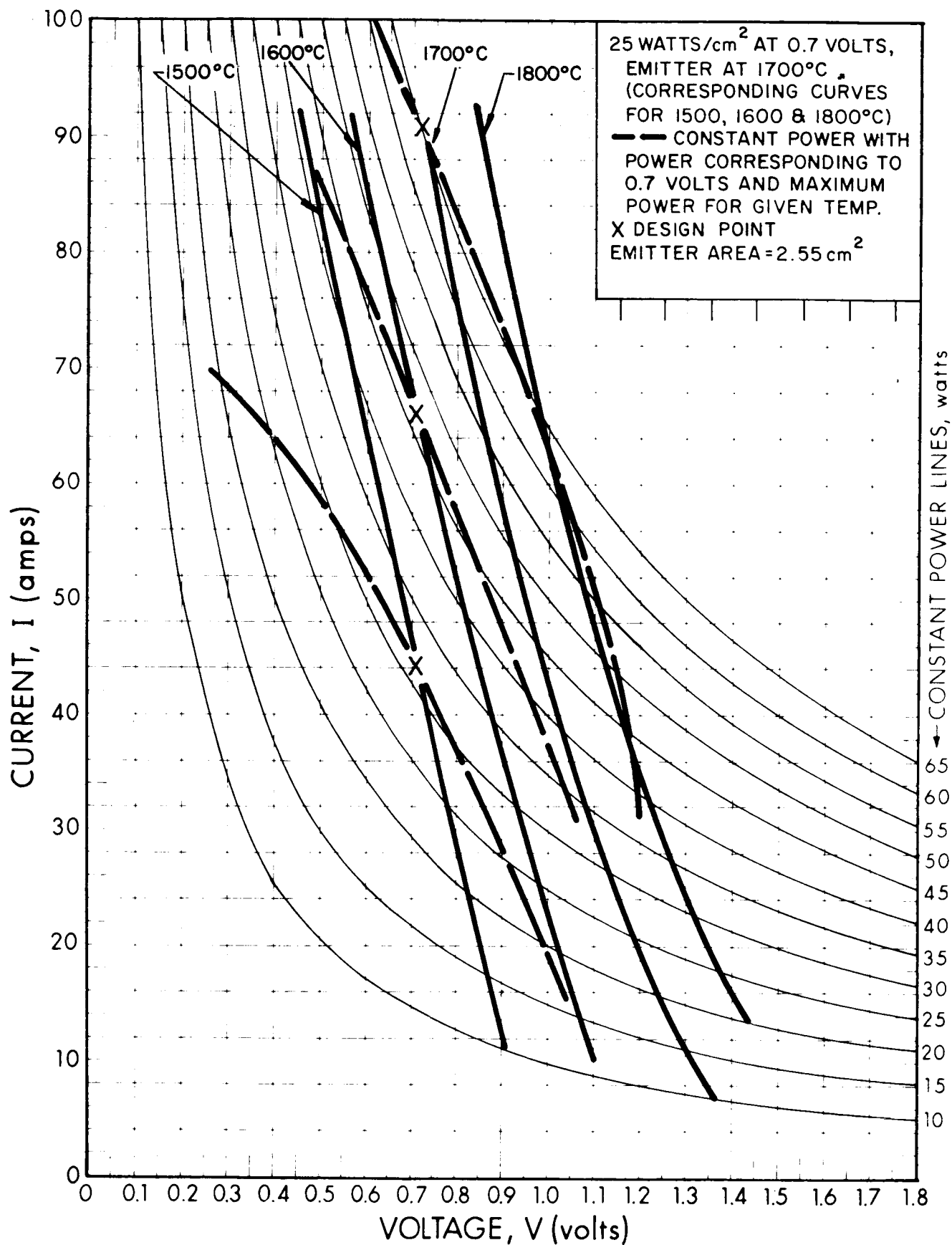


FIG. 5-18 I-V CURVES FOR CONSTANT POWER INPUT - 25 w/cm<sup>2</sup> CONVERTER

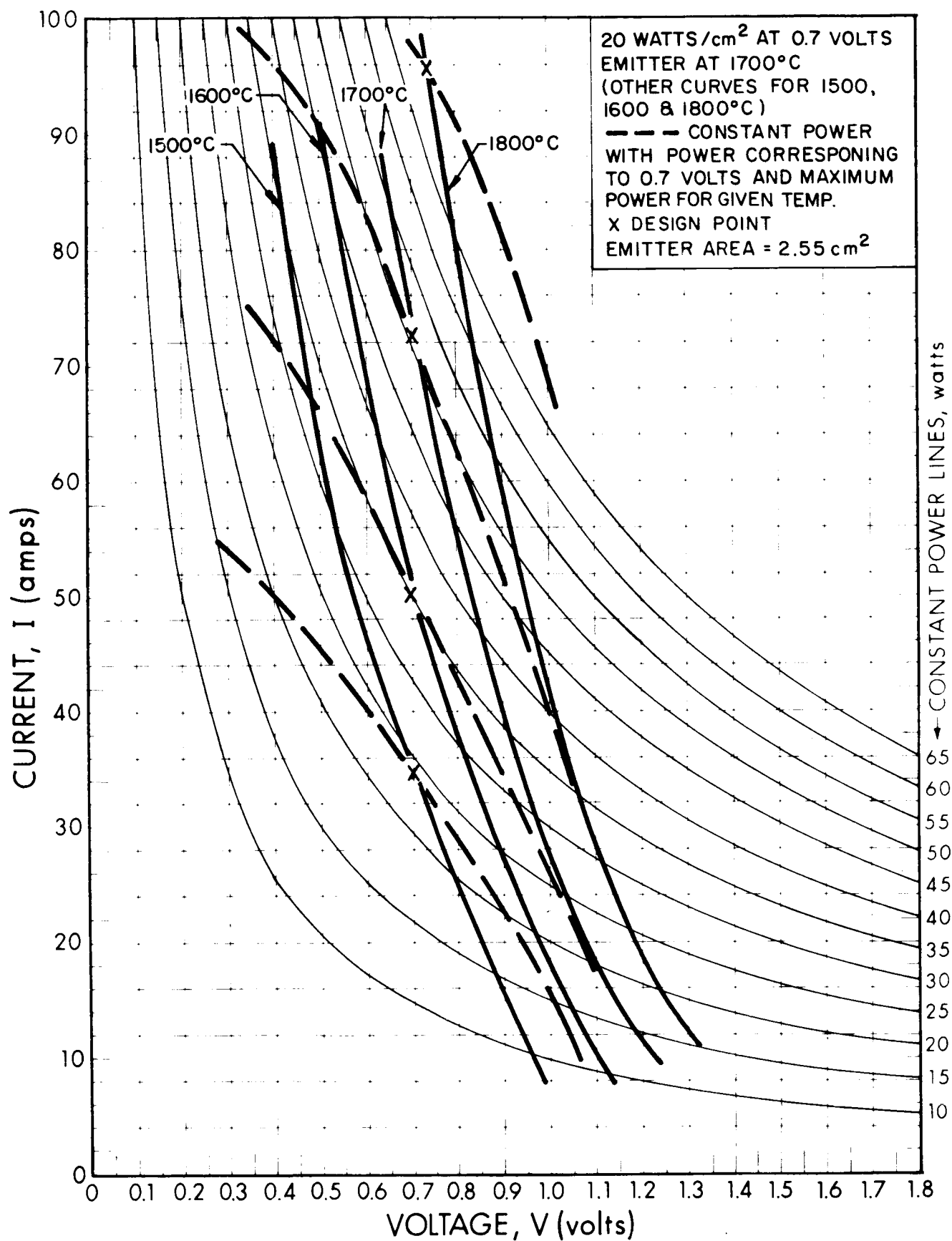


FIG. 5-17 I-V CURVES FOR CONSTANT POWER INPUT - 20 W/cm<sup>2</sup> CONVERTER



### 5.3 Life and Reliability

Failure of a thermionic converter can be characterized in three ways:

1. Gradual performance degradation
2. Catastrophic failure resulting in an open condition
3. Catastrophic failure resulting in a shorted condition

Life and reliability data on converter operation is limited. Approximately 13 diodes have been operated as long as 500 hours at high emitter temperatures. Four converters were operated for a lifetime of greater than 3000 hours steady-state at emitter temperatures and power outputs which were relatively low compared to those which will be used in a high performance generator.

Life tests simulating the 300 nautical mile orbit around the earth (55 minutes light, 35 minutes dark) have been made on thermionic converters. So far one converter has withstood greater than 2000 cycles. To qualify for a 1-year operation in a 300 n. mi. orbit requires that converters be capable of withstanding 5844 cycles. The cyclic data to date seems to indicate no fundamental reasons why converters cannot be made to operate in a cyclic condition reliably. However, converter tests under simulated space conditions rather than laboratory conditions may indicate needed design changes.

Figure 5-19 shows the emitter temperature and power output at operating time for the four converters that were tested for 3000 hours.

Performance degradation mechanisms have been identified to some extent. However, insufficient information is available to identify all degradation mechanisms or to identify such statistical data as mean time to failure, corrosion rate, etc. Important performance degradation mechanisms are:

1. Evaporation of the emitter
2. Seal corrosion
3. Slow leakage of the cesium

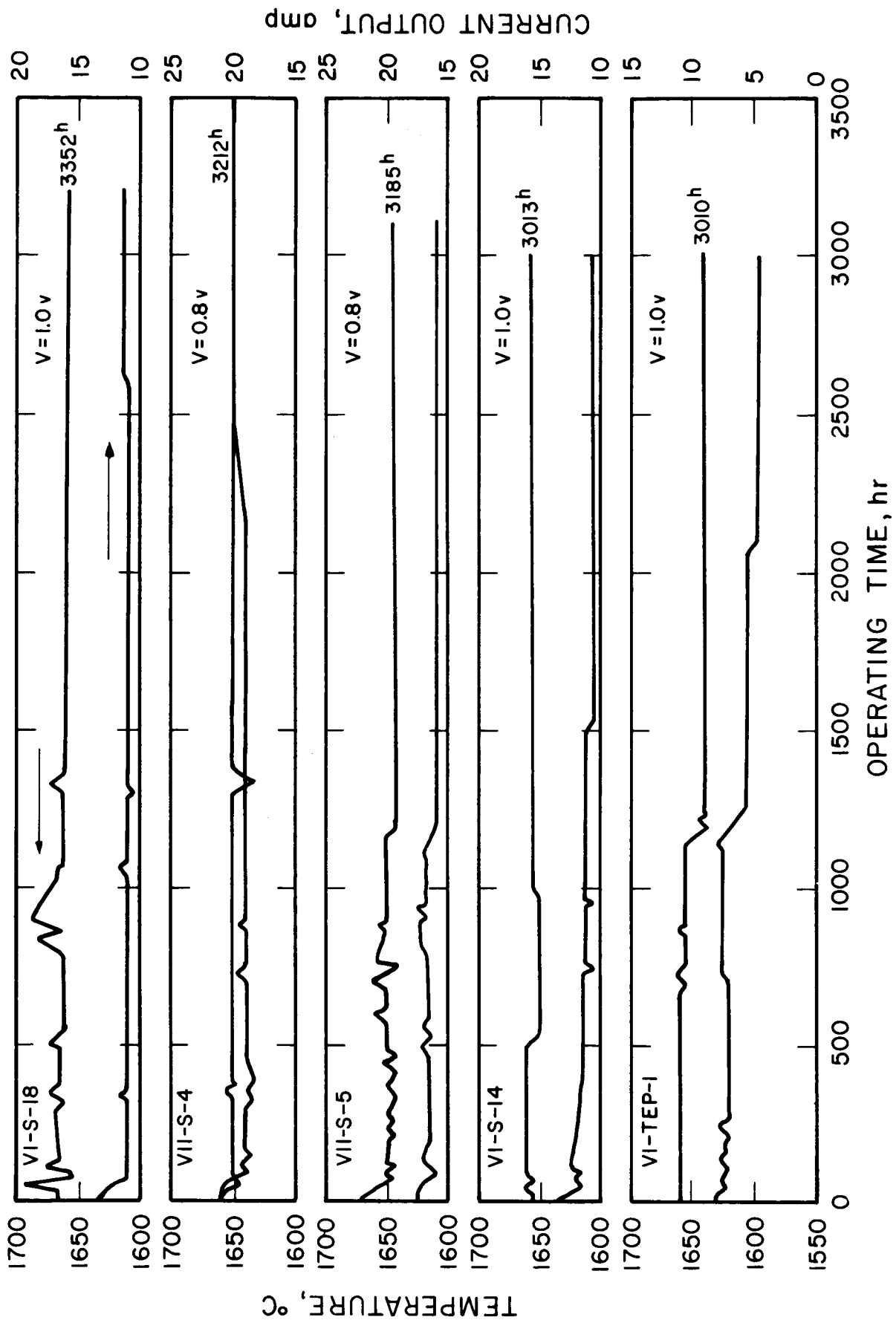


FIG. 5-19 EMITTER TEMPERATURE AND POWER OUTPUT VS OPERATING TIME FOR TYPICAL CONVERTER.  
(OUTPUT VOLTAGE CONSTANT)

4. Diffusion or surface migration of materials to affect the collector and/or emitter work functions

Figure 6-20 is a plot of the evaporation rates of various candidate thermionic converter emitter materials. Shown also in this figure is a shaded band which represents what is approximately the maximum evaporation rate which can be tolerated in an emitter material in order to keep heavy deposits from forming on the collector surface in a period of approximately 1000 hours. The formation of collector coatings can drastically increase the radiation heat transfer between emitter and collector, change the collector work function, and may give rise to thick collector coatings which, in flaking off, may cause emitter to collector shorts in a thermionic converter. The essential feature of this figure is that an approximate upper temperature limit is placed on all the materials for long term operation in a thermionic converter. It appears that the upper operational temperature limit for tantalum and rhenium is approximately  $1800^{\circ}\text{C}$  if operational times on the order of 1000 hours are desired. For operational times approaching 10,000 hours, the upper temperature limit would be closer to  $1675^{\circ}\text{C}$ . Tungsten, on the other hand, could be operated for approximately 10,000 hours at a temperature of approximately  $1800^{\circ}\text{C}$ .

High quality seals have now been perfected which have demonstrated no significant cesium corrosion after 1000 hours of converter operation. Temperature limits on seal operation are not known but it is estimated that  $700^{\circ}\text{C}$  would be an upper limit. No data is now available on lifetime of the seals although seal corrosion is amenable to accelerated life testing.

The most prevalent mechanism for catastrophic failure of the converter is leakage of the cesium through cracks created by metal fatigue, corrosion, recrystallization, and related phenomena. All the mechanisms of cesium leakage are not yet known and will depend to a great extent on long life testing.

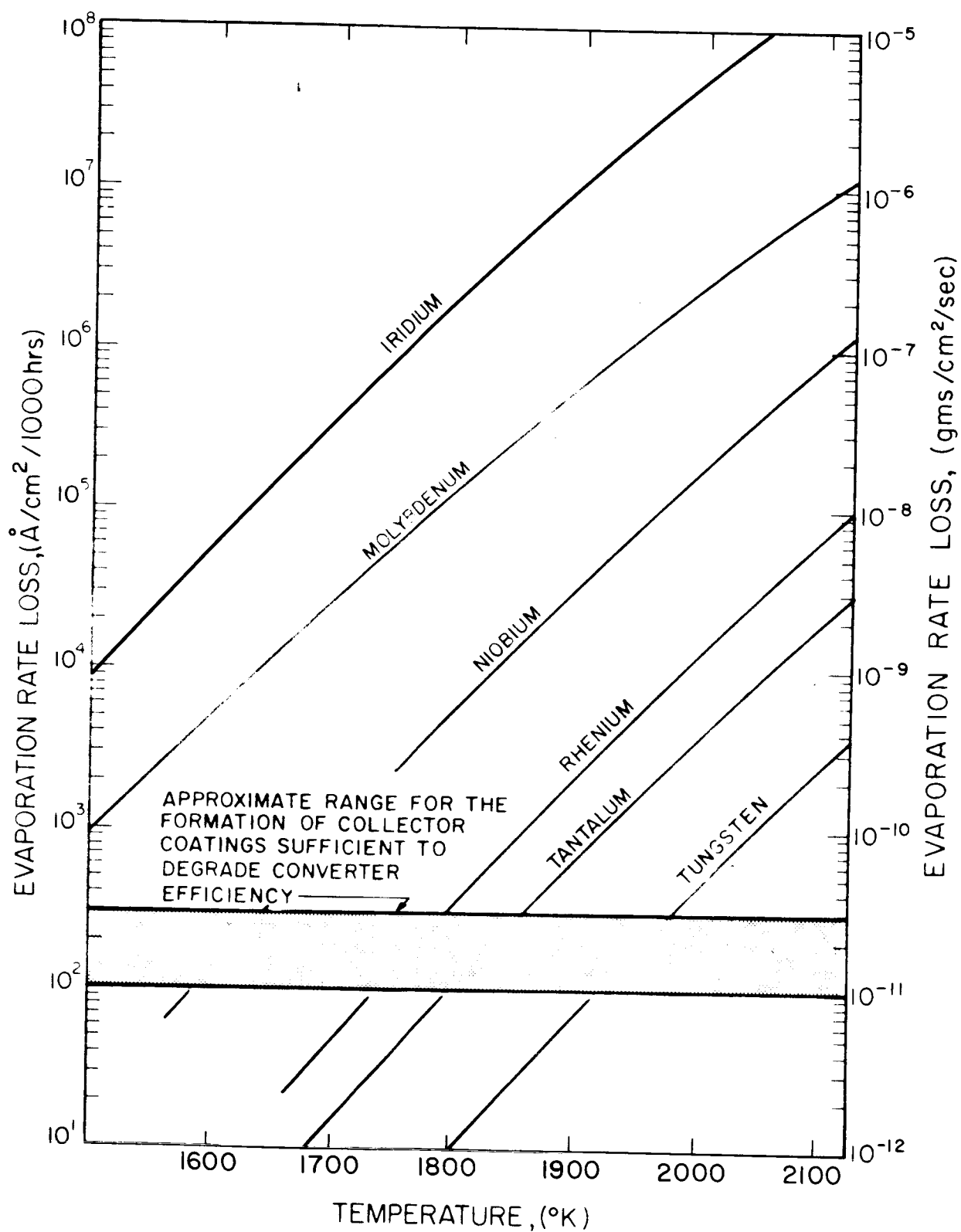


FIG. 5-20 EVAPORATION RATES FOR TYPICAL EMITTER MATERIALS

It is felt that shorting of a converter is less likely than the open condition. Shorting can be caused by the meeting of the emitter and collector through flaking of chips, loosening of bonds to create unstable conditions, metal fatigue and expansion, and other phenomena. As soon as the emitter and collector touch at operating temperatures, the emitter will rapidly cool and the collector will grow hot. This process will tend to shrink the emitter spacing and maintain a shorted condition.

#### 5.4 Future Performance

Figure 5-21 shows bandwidths of performance characteristics obtained by converters in 1962 and 1964. As shown, converter performance increased dramatically during the 2-year interval. The bandwidth consists of a composition of numerous I-V curves obtained on various kinds of converters as reported in the literature. Laboratory converters at several organizations have exhibited much higher power outputs than the converters on prototype flight hardware. These laboratory converters consist of variable spacing test devices specifically intended to allow extremely close spacings to occur. The bandwidth in Fig. 5-21 labeled 1968 is a judgment regarding what can be obtained in practical hardware by decreasing spacing, optimizing materials and optimizing the heat transfer of the converter. The two major problems in converter design consist of the heat transfer necessary to operate at high current and obtain low collector work functions. It is felt that both of these problems will be adequately solved by 1968 to provide perhaps a 50 watt/cm<sup>2</sup> diode, characteristic of prototype laboratory hardware, in 1970.

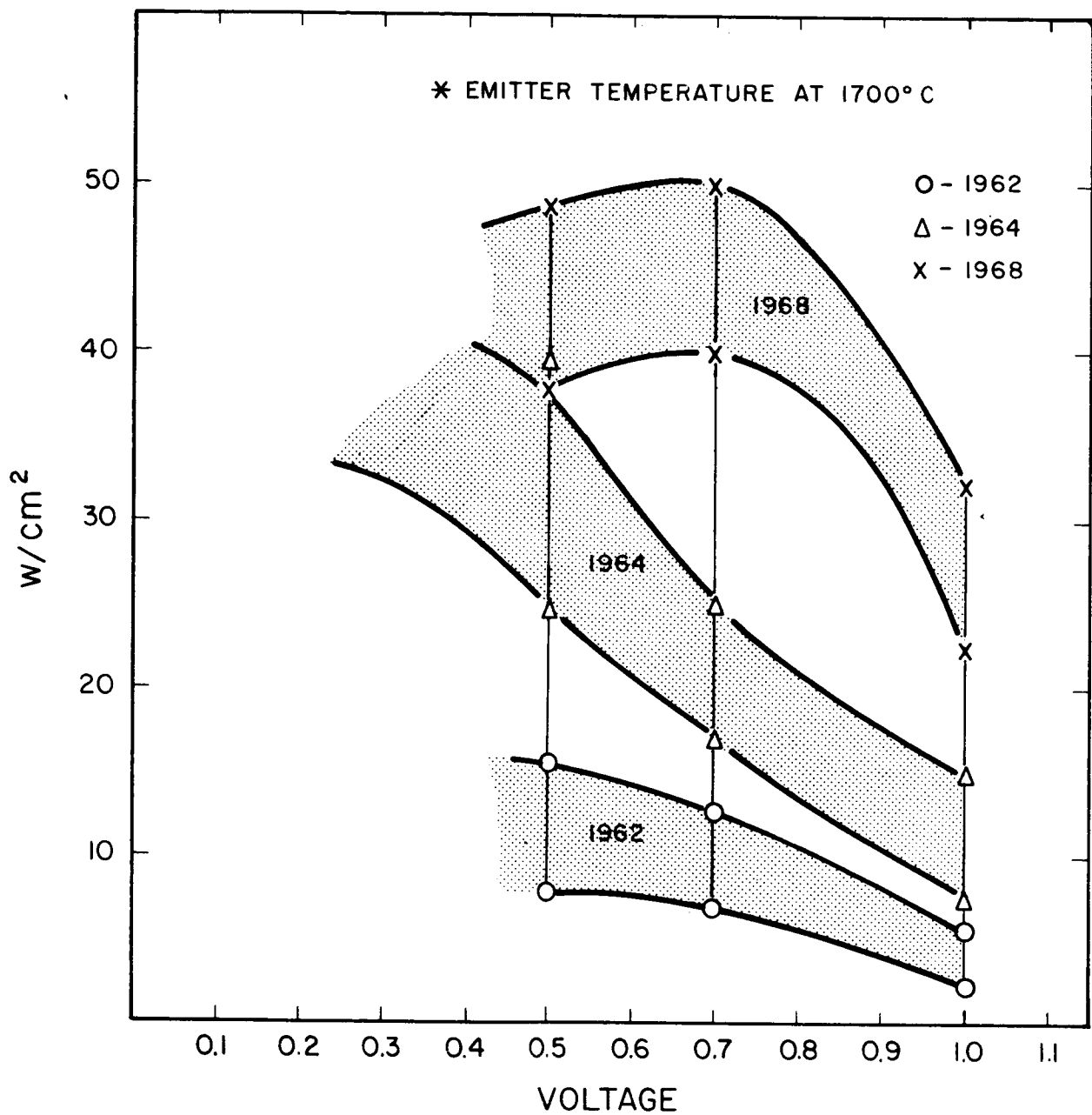


FIG. 5-21 CONVERTER PERFORMANCE PREDICTIONS

## 6. THERMIONIC GENERATOR

### 6.1 Description

The thermionic generator consists of the thermionic converters, structure for holding the converters, cavity, power leads, front cone, and shielding, instrumentation, attachments to the generator support, and related items. Also, additional control units such as solar flux control, cesium reservoir control, and other items may be held onto the generator structure.

Figure 6-1 shows a cross section of a five-converter generator which uses a cubical cavity. The outline of the converters shown corresponds to converters manufactured in 1962 and 1963. A photograph of generator, JG-1, assembled in 1962, is shown in Fig. 6-2. The five converters were mounted by spot-welded tabs into a cubical molybdenum structure. For this early generator, no special precautions were taken to shield the structure and minimize heat losses.

A second generator, JG-2, is shown assembled and mounted on a supporting ring prior to test in a vacuum system in Fig. 6-3.

Figure 6-4 shows a layout of a four-converter generator, designed in 1964, utilizing a cubical cavity and converters with straight fins as radiators rather than cups. Figure 6-5 shows a photograph of a model of the four-converter generator outlined in Fig. 6-4.

As discussed in other sections of this report, many variations in the number of converters per generator, the shape of the cavity, and other details of the structure and supporting items are possible. To date, however, only three cubical cavities with five converters and a cylindrical cavity with three converters have been assembled using high temperature cesium vapor converters.

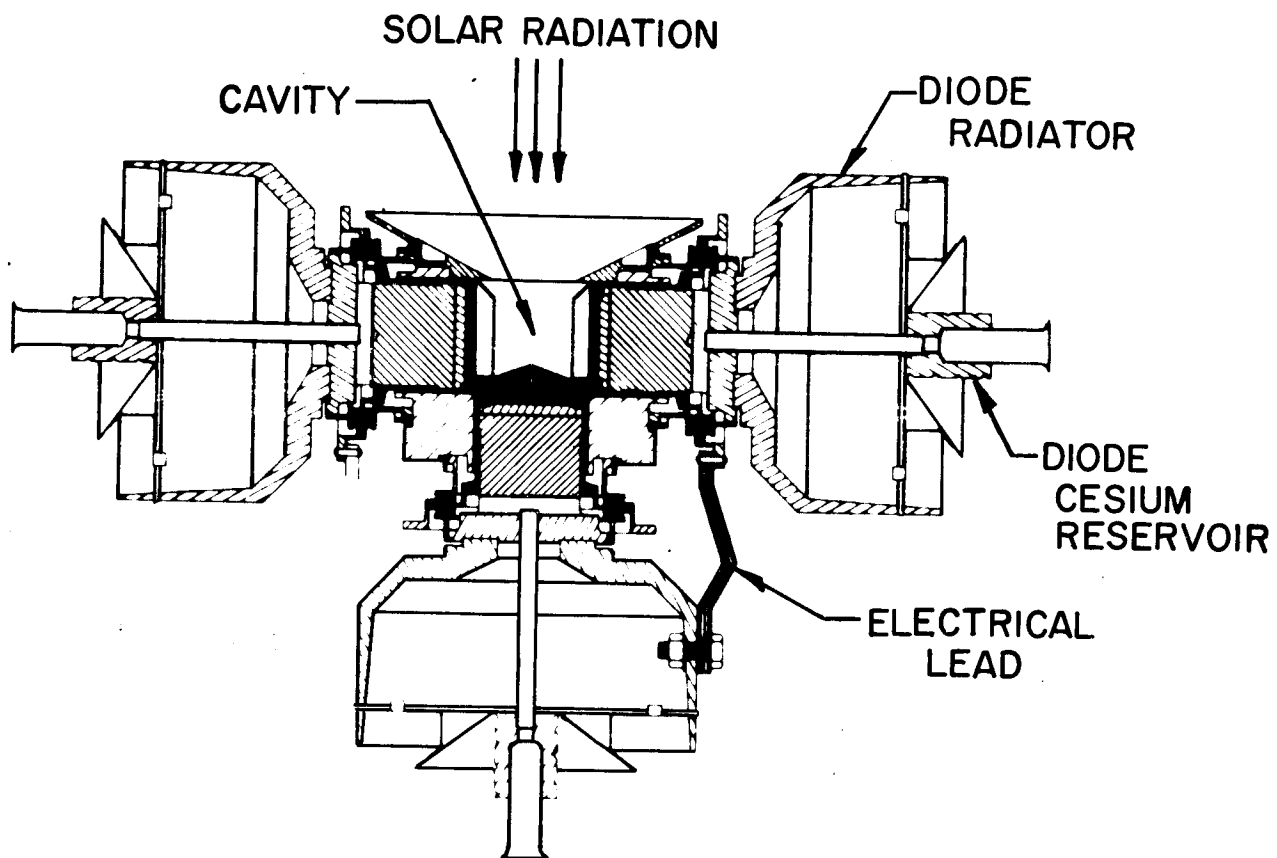


FIG. 6-1 CROSS SECTION OF FIVE-CONVERTER GENERATOR



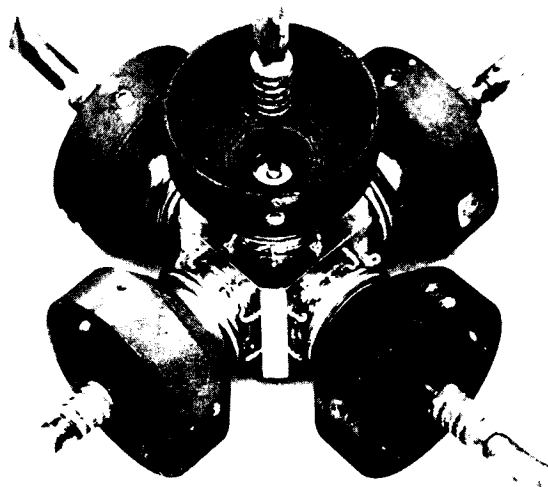


FIG. 6-2 FIVE-CONVERTER SET GENERATOR (SET 1)

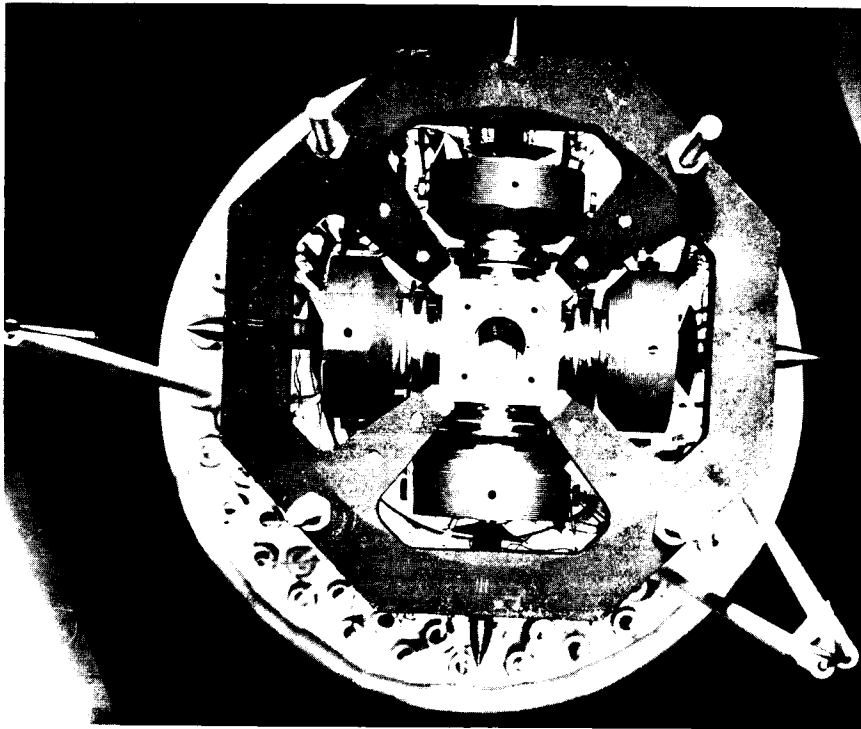


FIG.6-3 GENERATOR JG-2 (assembled 1962)

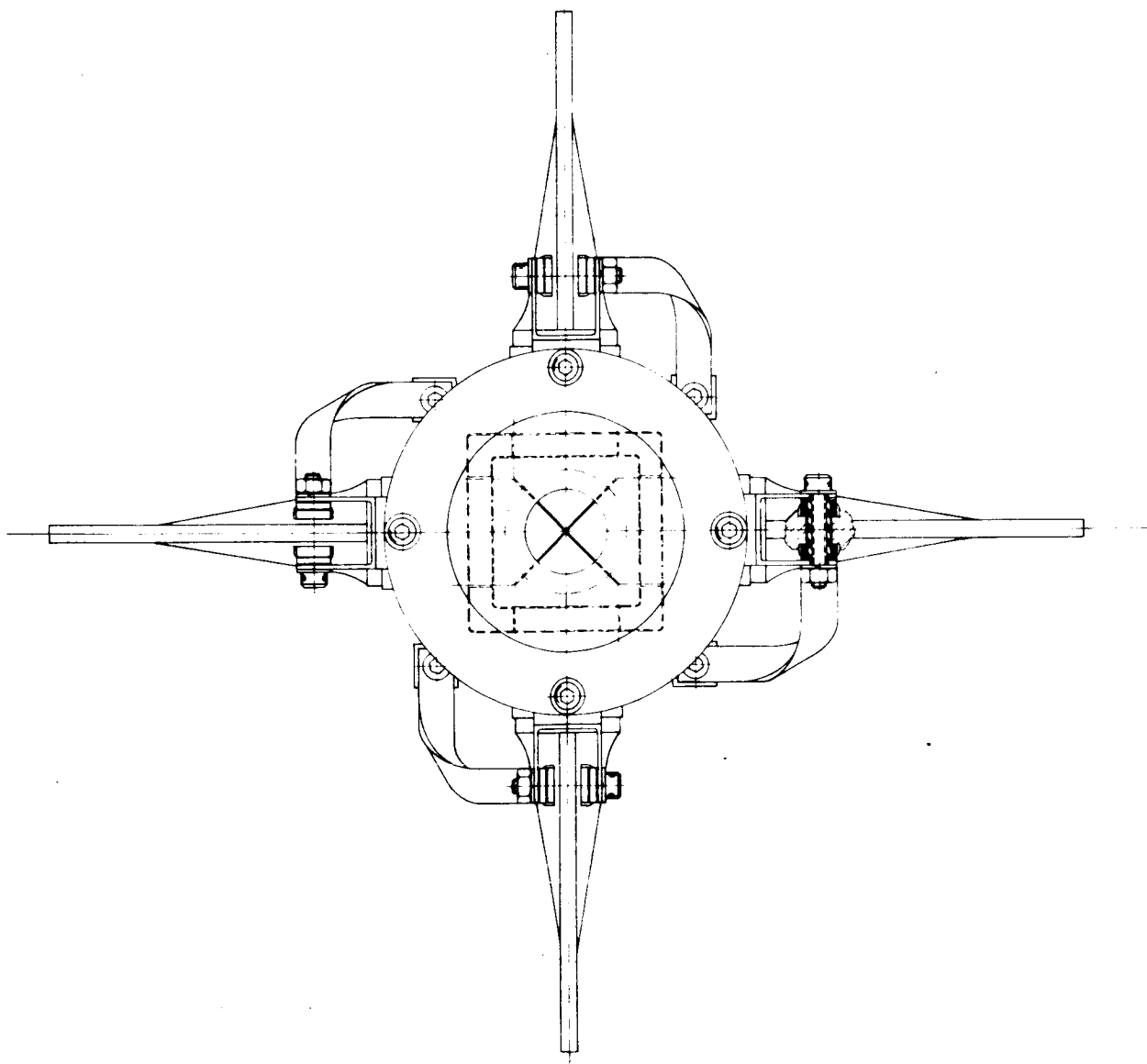


FIG. 6-4 LAYOUT OF FOUR-CONVERTER GENERATOR

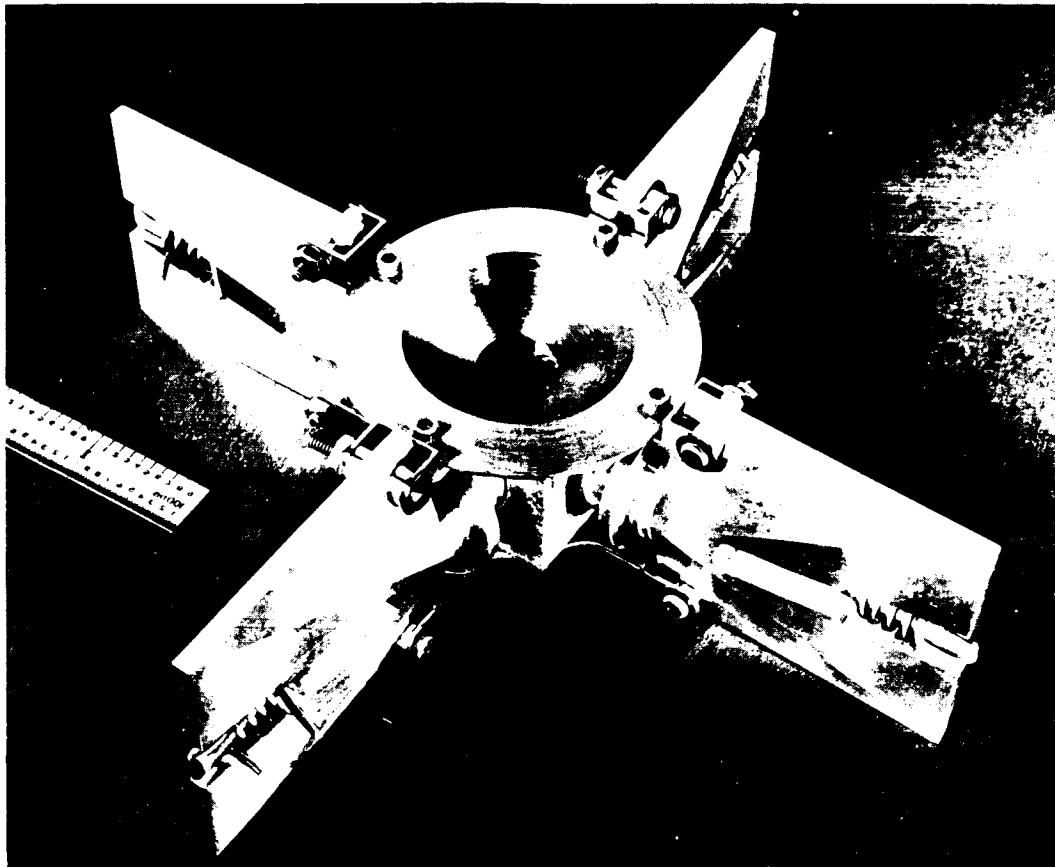


FIG. 6-5 FOUR CONVERTER GENERATOR MOCK-UP (ASSEMBLED 1.64)

## 6.2 Performance Characteristics

Figure 6-6 shows I-V curves obtained during laboratory tests of a five-converter generator in late 1964.

For the laboratory tests, an electric heater with appropriate shielding is placed inside the cavity to simulate the input of solar radiation. The watt number in Fig. 6-6 includes the filament heating power as well as the electron bombardment power. The flux distribution and reradiation losses are different than would be obtained in the solar testing of the generator as illustrated in the curves of Fig. 6-7.

Figure 6-7 compares solar and laboratory test data obtained on a five-converter generator in late 1964. Power output and efficiency is shown as a function of solar power input to the cavity. Efficiency calculations in Fig. 6-7 are based on electrical power from the generator divided by total solar or electric power into the cavity; therefore, in the case of the solar tests, reradiation and reflection losses are included in the curves of Fig. 6-7.

Figures 6-6 and 6-7 illustrate the state of the art in generator performance to date. An 8 percent efficient generator was demonstrated using solar radiation and 10 percent was demonstrated in a laboratory environment.

The I-V curves of Fig. 6-6 show the "flat" type of curve characteristic of converters which are tested with constant power input (see discussion in Section 5).

Figure 6-8 shows further curves of the power output and efficiency obtained during laboratory tests in late 1964 for a five-converter generator.

Figure 6-9 illustrates the number of converters required in a generator as a function of the power required from the generator. Parameters which are varied include the emitter area of each converter and the watts/cm<sup>2</sup> from each converter. As shown, the number of converters required can vary considerably. For example, for 1,000 watts output, the required number of converters can vary from 16 to 46 in the range of 1.5 to 2.5 cm<sup>2</sup> emitter area and 15 to 25 w/cm<sup>2</sup>.

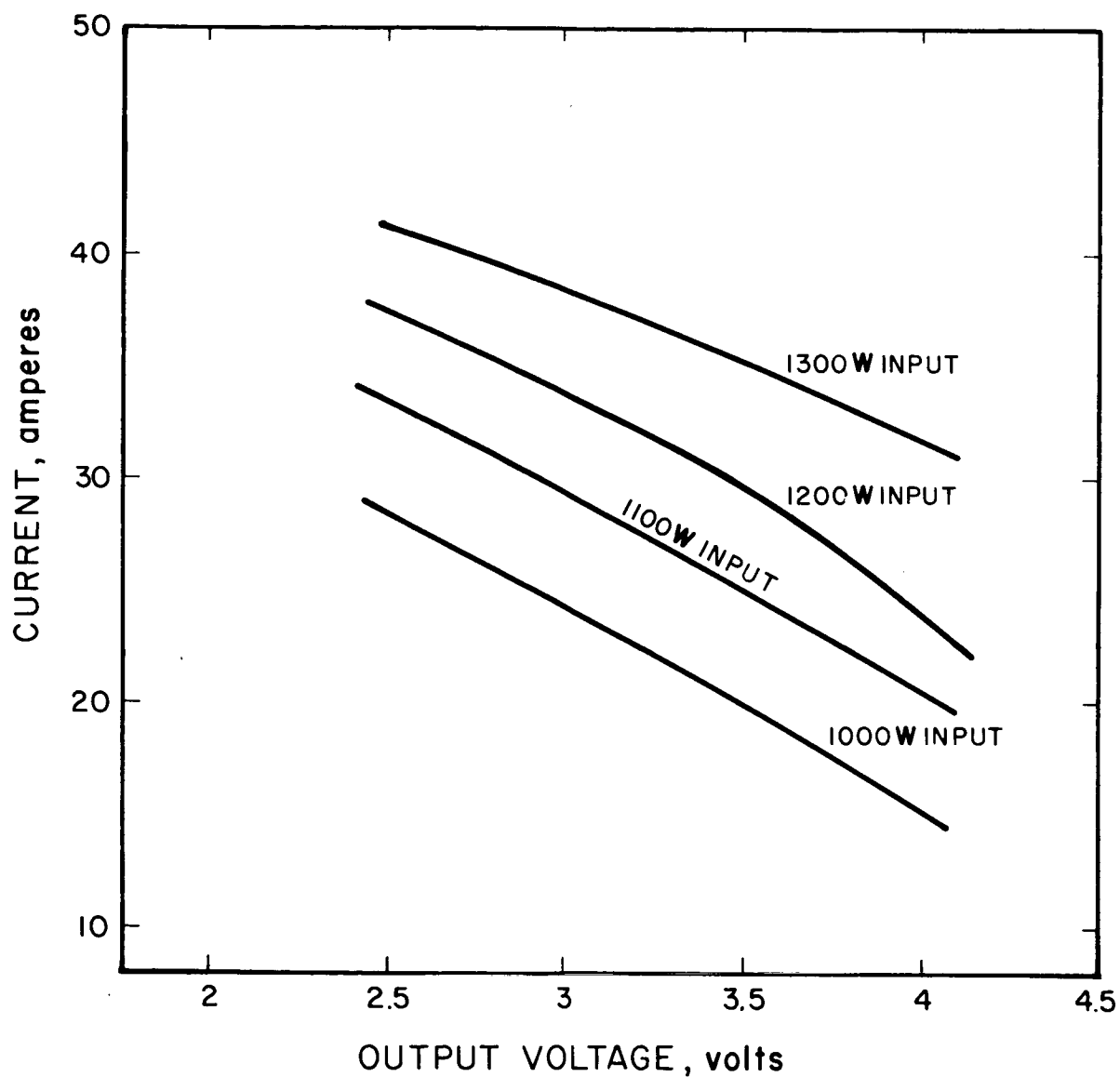


FIG. 6-6 I-V CURVES - LABORATORY TEST DATA. FIVE-CONVERTER GENERATOR (late 1964) JG-2b

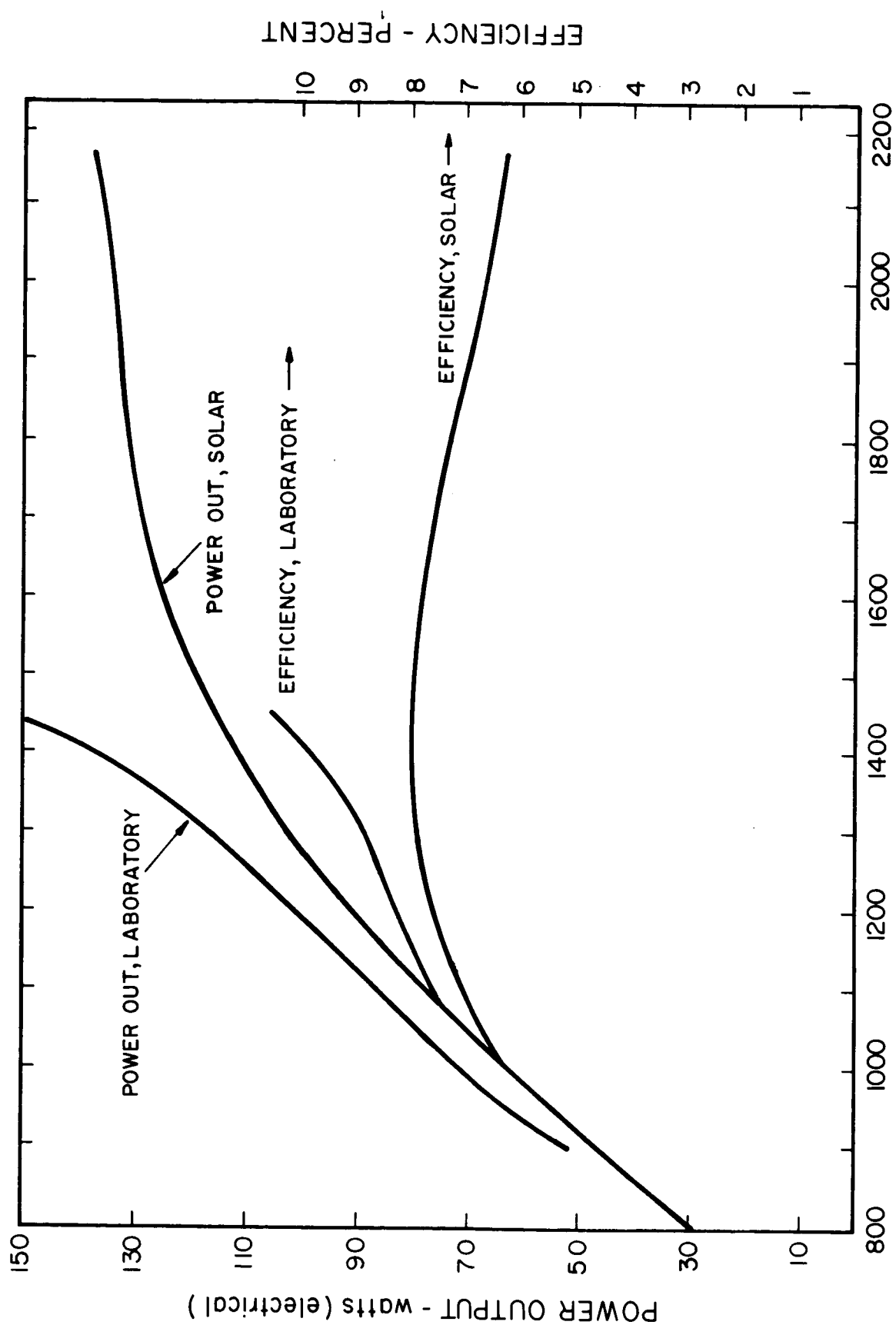


FIG. 6-7 SOLAR AND LABORATORY TEST DATA ON FIVE-CONVERTER GENERATOR (Late 1964)

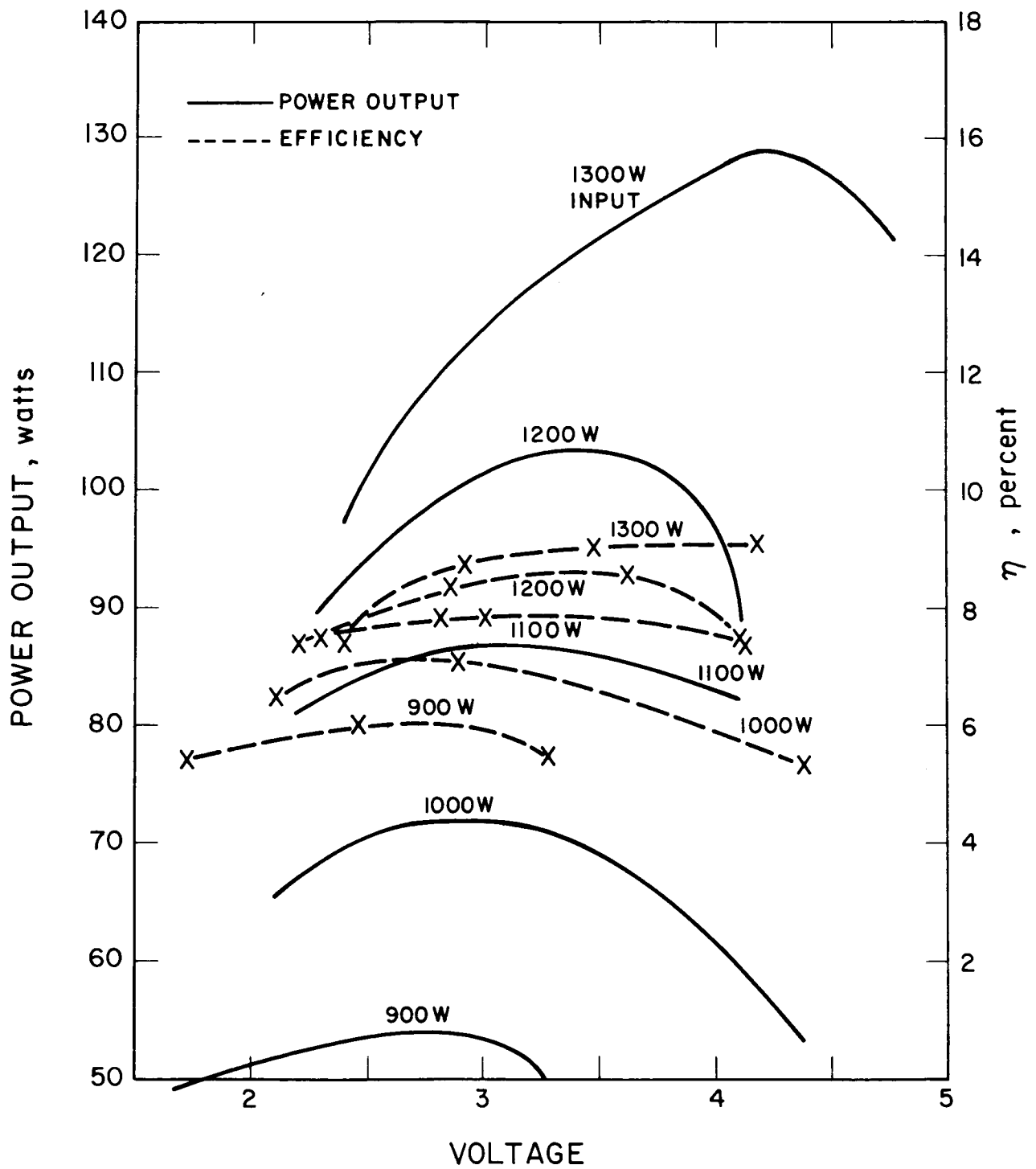


FIG. 6-5 LABORATORY TEST DATA ON FIVE-CONVERTER GENERATOR  
(late 1940) JG-25

73616027



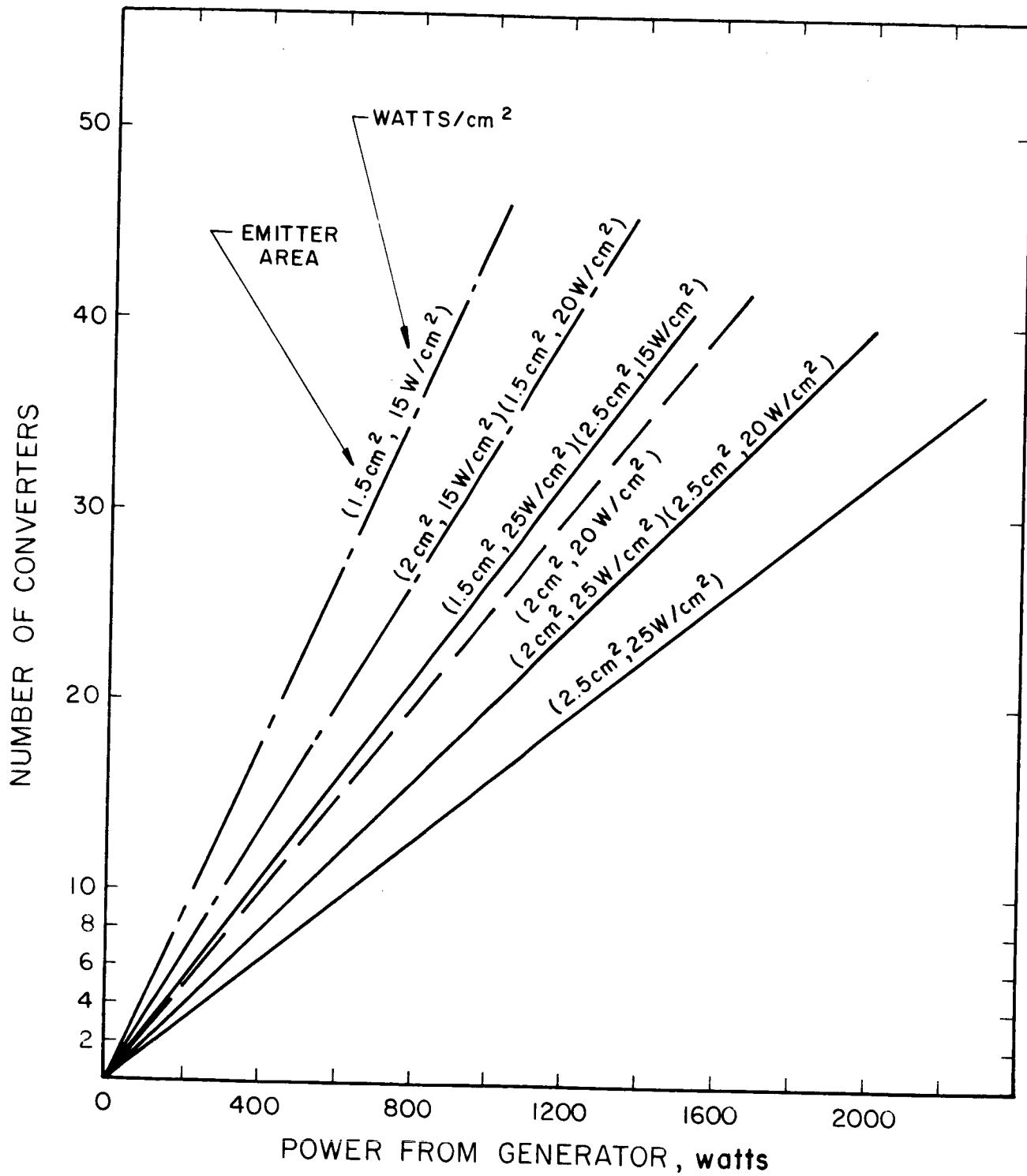


FIG. 6- NUMBER OF CONVERTERS REQUIRED VS POWER FROM GENERATOR

Figure 6-10 shows typical generator output characteristics which might be obtained in an advanced design. Characteristics were drawn for a five-diode generator but can be extrapolated to any other number of converters. The power and current curves are similar to those demonstrated by existing generators. The power curve will not peak but will exhibit fairly flat characteristics over a voltage range of one volt. The emitter temperature with constant power into the generator will vary depending on the load point.

### 6.3 Thermal Response

An important consideration in use of the thermionic generator in an orbital application is the amount of energy and time required to warm or cool the generator. Thermal response of the generator will vary considerably depending on generator design, converter design, flux distribution, and other factors.

A typical thermal response curve is shown in Fig. 6-11 for generator JG-1 tested in late 1962. Other generators, with other designs, would exhibit similar thermal response characteristics although the rise and fall times and rates of decay may vary.

As shown, the output from the generator will shut down rather quickly when the solar energy no longer enters the cavity. This is due to the rapid cool-down of the converter emitters.

The seals, radiator, and cesium reservoir of the converters will gradually decay; eventual temperature levels will depend on the time length of darkness, background radiation, etc.

When the solar flux reenters the cavity, the emitter will be rapidly heated and the space between the emitter and collector will open. It is expected that this opening would be signaled by a large open circuit voltage in the converter. This voltage would vary according to the spacing and may oscillate somewhat as variations in emitter-collector spacing occur.

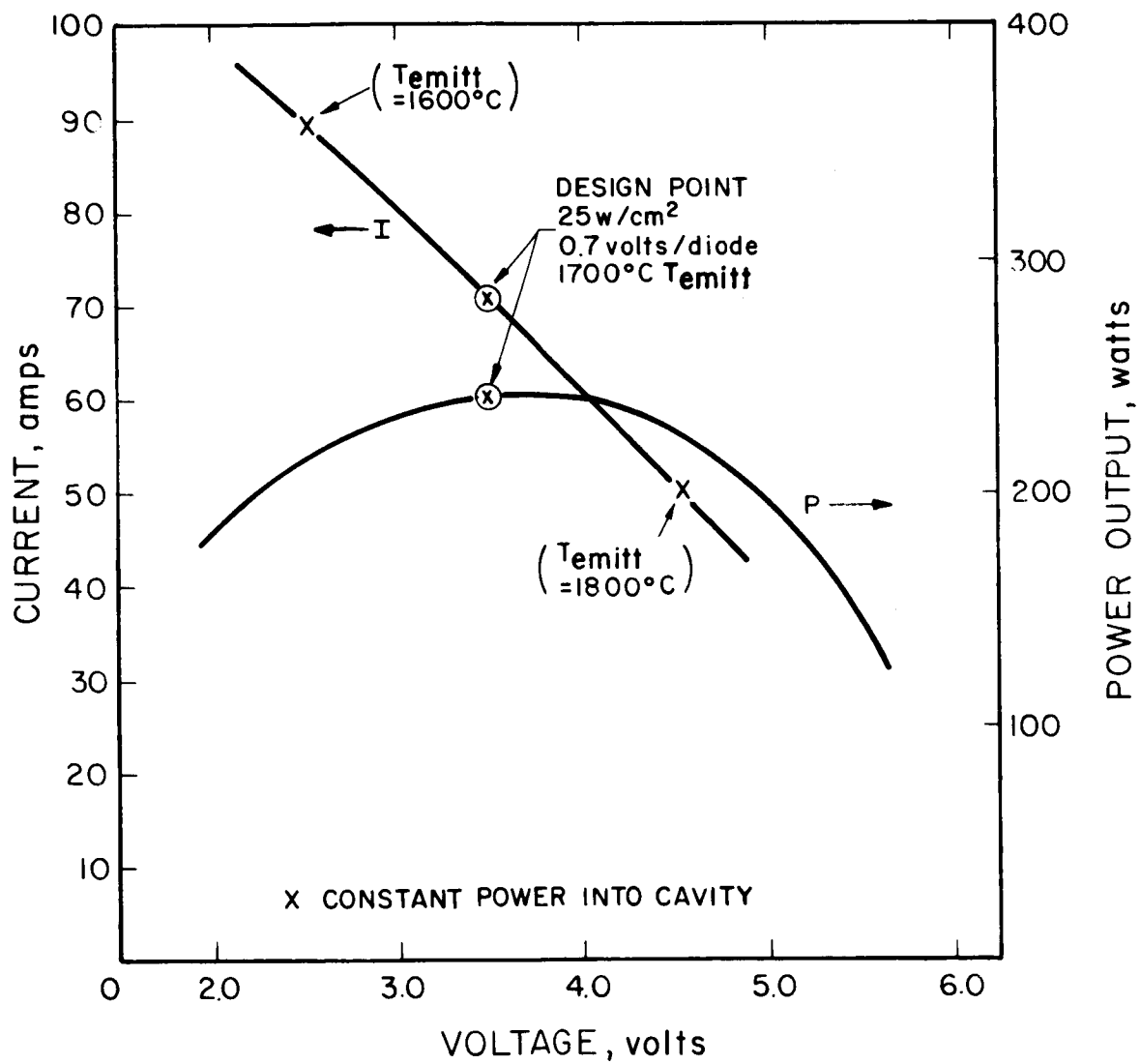


FIG. 7-10 TYPICAL FIVE-DIODE GENERATOR OUTPUT CHARACTERISTICS - ADVANCED DESIGN

NOTE: 1.) NO AUXILIARY HEATERS WERE USED  
 2.) TEMPERATURE OF CHAMBER WALL = 40°F  
 CONVERTERS VI-1, 2, 4 AND 5 IN SERIES

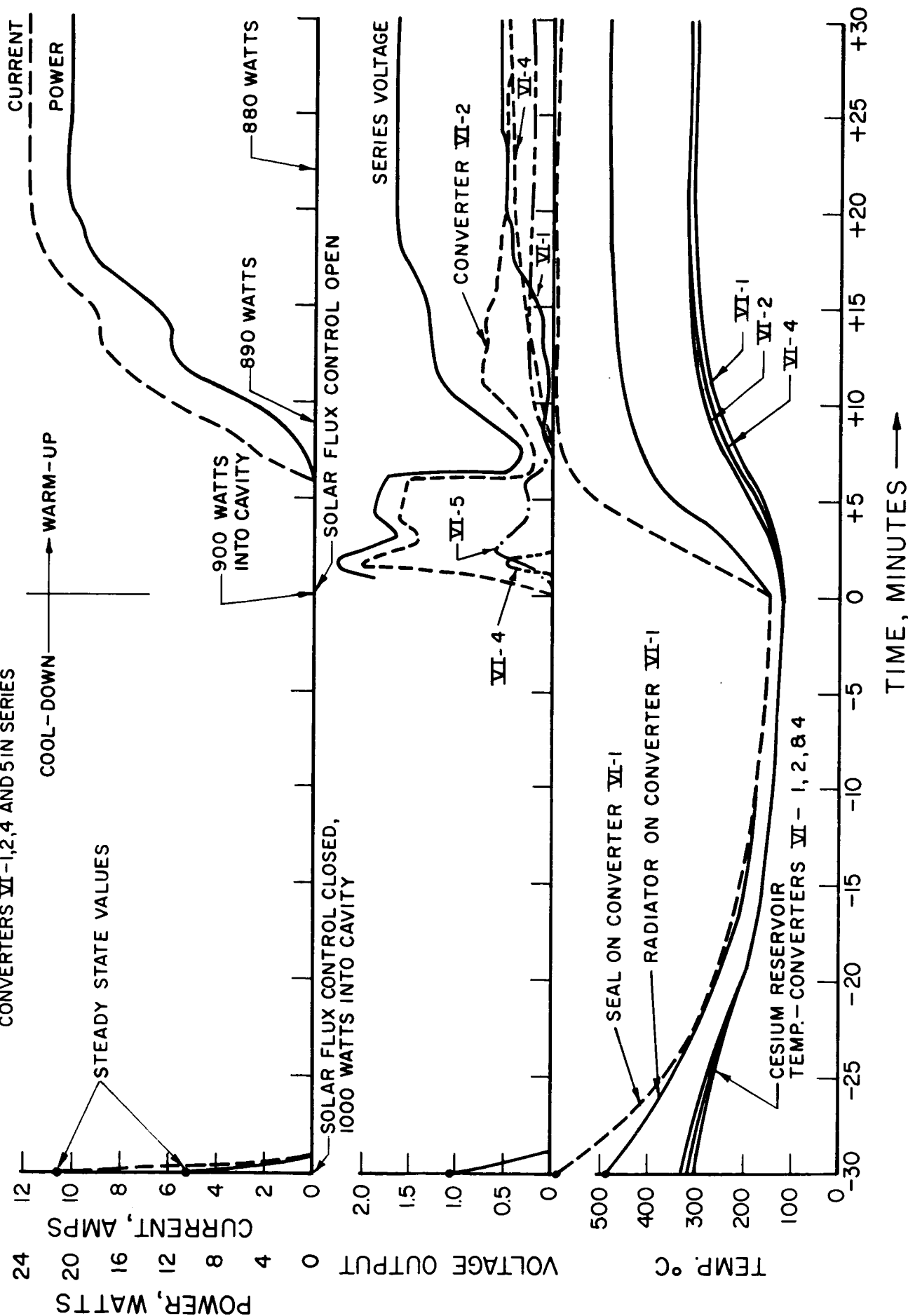


FIG. 6-11 TYPICAL THERMAL RESPONSE OF GENERATOR VI-1

Eventually, converter temperatures will be reached which allow current output to occur. At this point the voltage from the converter will drop and power will begin to be drawn from the converter. As the reservoir, radiator, and other parts of the converter gradually warm up, each converter will reach operating conditions in a time which is determined by the thermal response of the generator/converter structure.

#### 6.4 Misorientation Losses

Misorientation of the solar-thermionic system will cause a power loss from the generator due to three phenomena.

1. Less solar radiation entering the cavity
2. A decrease in cavity temperature
3. Redistribution of flux in the cavity which creates mismatch of converters and results in cooling of several converters

The third source of loss is by far the most important to thermionic generator operation and is illustrated in Fig. 6-12. Shown is the typical power loss and voltage loss due to misalignment demonstrated with four converters in a solar test with generator JG-1 in late 1962. The converters were "side" converters in a cubical cavity. Relative power loss is shown for four cases; cases 1 and 3 correspond to the case where the misalignment is such that the focal image moves along a diagonal of the cube. Cases 2 and 4 correspond to the case where the focal image moves across the converters.

As shown, a misalignment of 5 minutes of arc resulted in a 2 to 5 percent loss of power. A misalignment of 10 minutes of arc resulted in a power loss of 10 to 20 percent.

Power loss as a function of misorientation depends on cavity emissivity, cavity shape, arrangement of converters within the cavity, and other phenomena. The results of Fig. 6-12 are considered to be typically illustrative of the ball-park numbers which can be expected.

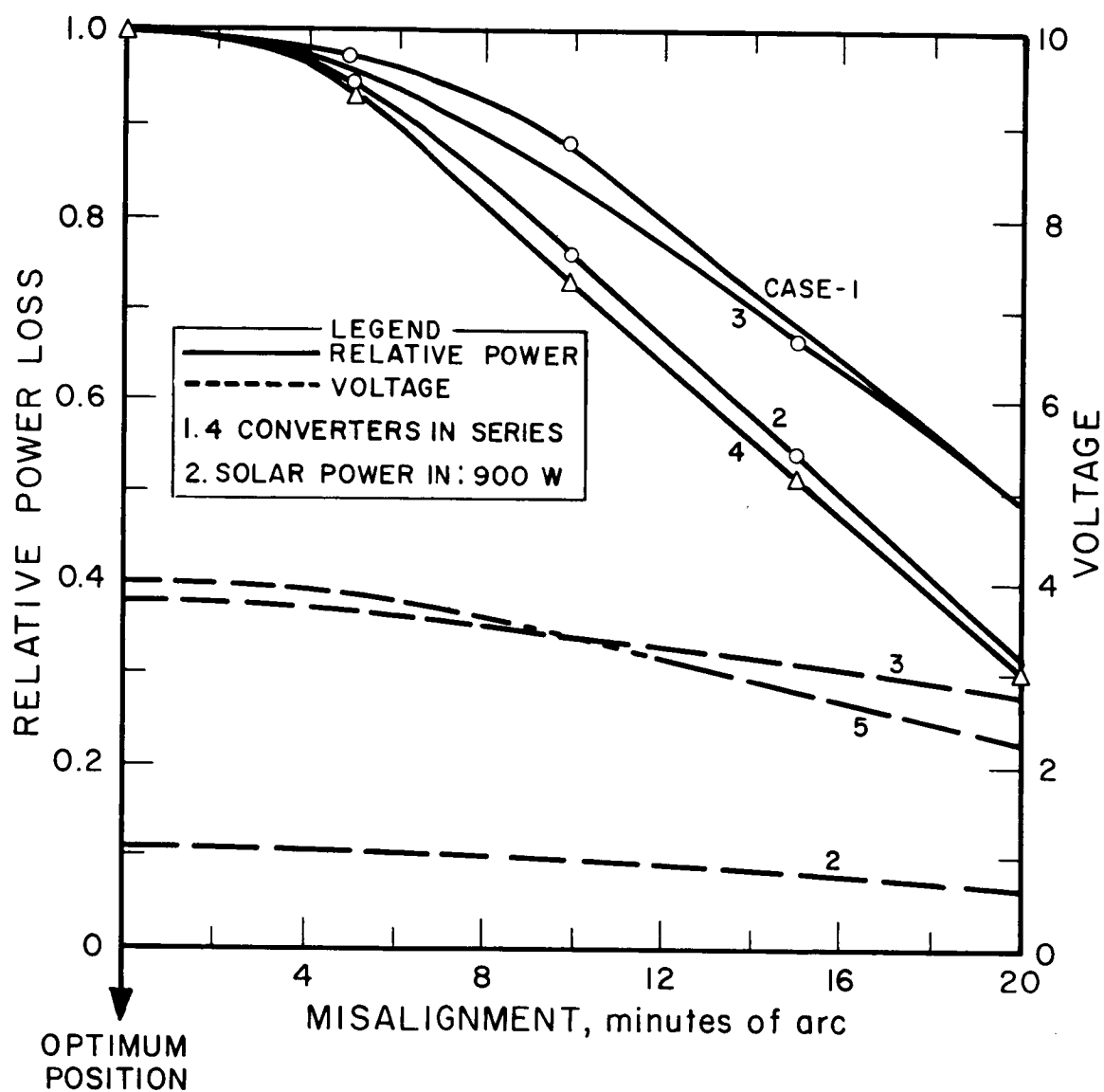


FIG. 6-12 TYPICAL POWER LOSS AND VOLTAGE LOSS DUE TO MISALIGNMENT - FOUR-CONVERTER ARRANGEMENT ON SIDES OF CUBICAL CAVITY

## 6.5 Generator Losses

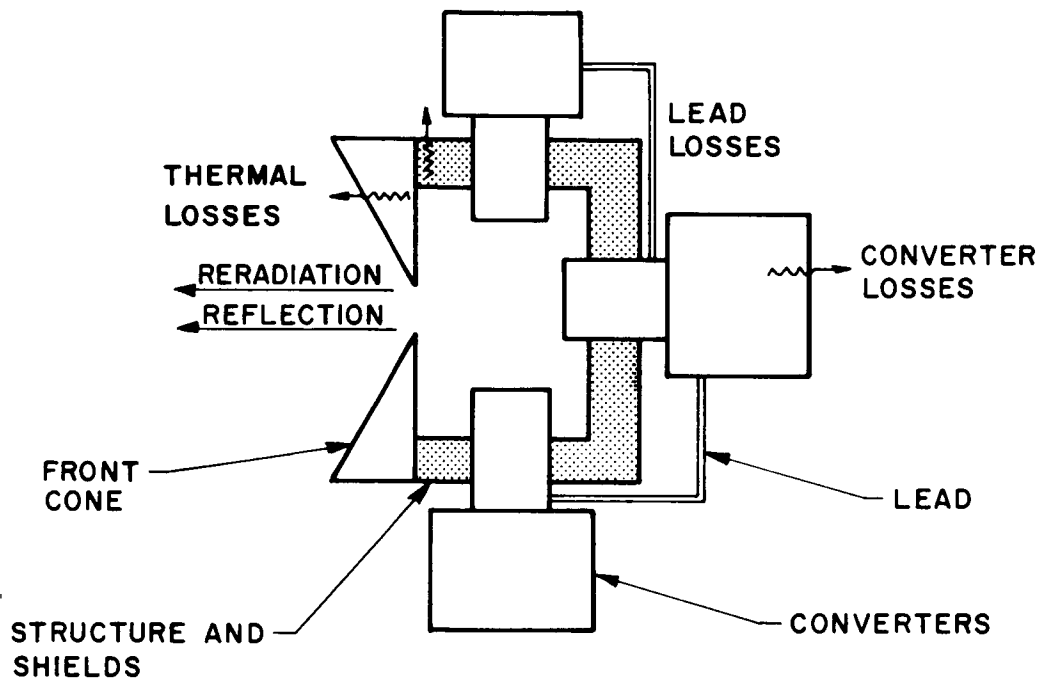
Figure 6-13 illustrates the main sources of generator loss that can be expected in a practical converter. All of these losses contribute to inefficiency of the system.

The effect of generator losses on generator efficiency is shown in Fig. 6-14. The converter efficiency corresponds to the converter efficiency curves derived in Section 5. Further losses in the system will occur due to lead losses and structural thermal losses. As shown in Fig. 6-14 the generator losses will generally increase with cavity temperature. Also shown are anticipated mismatch losses in a typical system configuration.

### 6.5.1 Heat Loss Through Insulation Gap

Due to the fact that converters are generally connected in series, the separate converter bodies cannot be allowed to come into electrical contact with each other, the generator structure, or with the shielding assembly, since this would short circuit the generator output. The electrical insulation is generally accomplished by using a vacuum gap between the generator structure and the converters. With this scheme, radiant energy will be lost from the cavity through these openings. The design problem is one of minimizing this radiation loss from the cavity within practical limits of having a reasonable gap width that allows for assembly tolerances. Both blackbody and reradiation losses from the insulation gap will occur. The blackbody loss case has been studied in the most detail since a generator design concept using radiating devices incorporated on the converter envelope would require a basic converter design modification.

In calculating the loss of blackbody radiation from the insulation gap, it is assumed that the losses occur from a cavity of emissivity equal to 1 and that the radiation occurs to a free space environment. The radiation loss is approximately



### GENERATOR LOSSES

1. LEAD LOSSES
2. CONVERTER LOSSES
3. RERADIATION FROM CAVITY
4. REFLECTION FROM CAVITY
5. STRUCTURAL THERMAL LOSSES
  - a. RADIATION LOSSES THROUGH "HOLES" IN STRUCTURE
  - b. CONDUCTION LOSSES FROM CAVITY TO GENERATOR, FRONT CONE AND STRUCTURE
  - c. RADIATION LOSSES THROUGH SHIELDING

FIG. 6-13 GENERATOR LOSSES



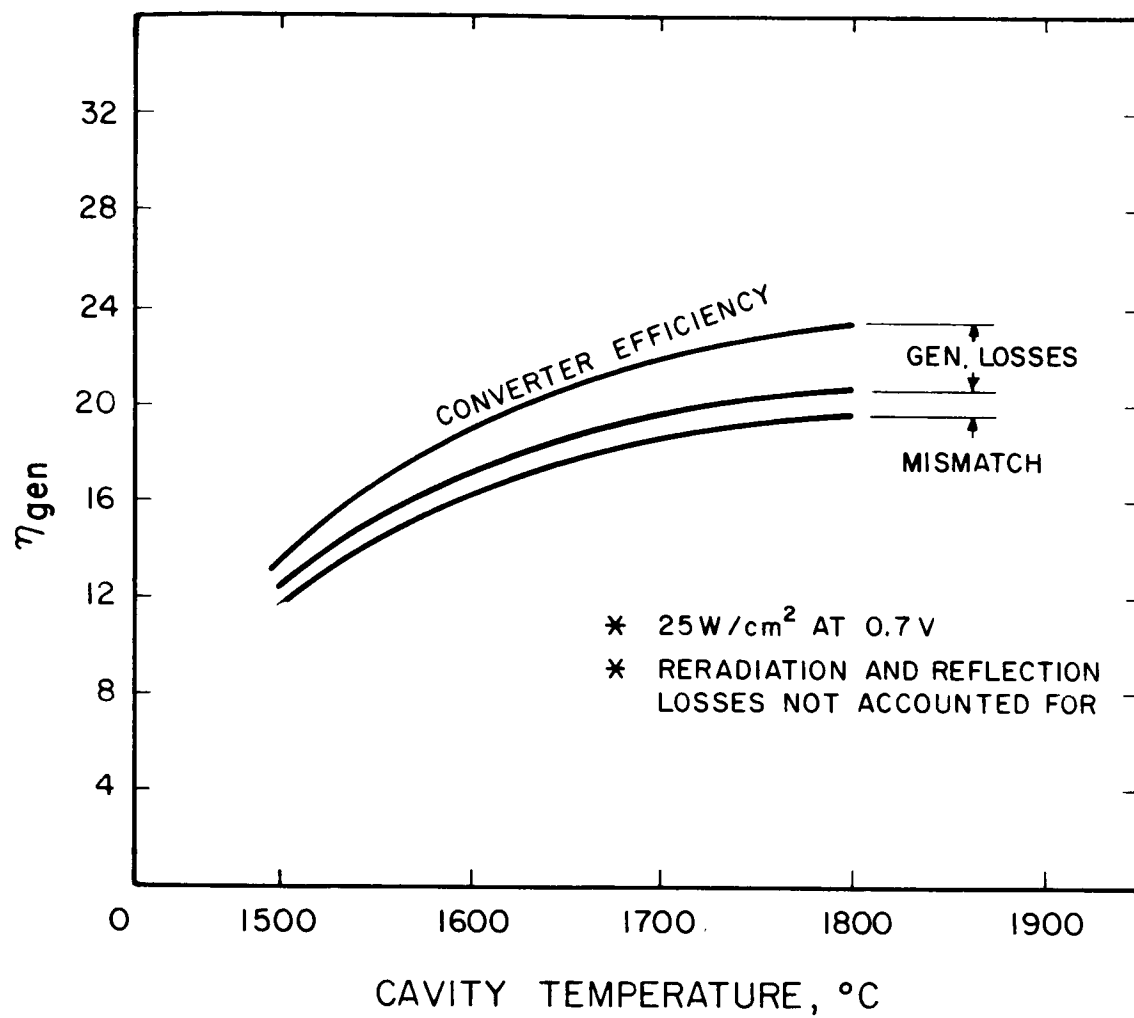


FIG. 6-14 POSSIBLE GENERATOR EFFICIENCY

$$P_{\text{gap}} = \epsilon_o A \sigma T_o^4$$

where

A = cross sectional area of insulation gap

T<sub>o</sub> = cavity temperature

$\epsilon_o \approx 1$

$\sigma$  = Stefan-Boltzmann constant

Figure 6-15 is a plot of heat loss for a 16-converter generator configuration. The heat loss is given for insulation gaps from 8 to 14 mils in steps of 2 mils. The graph shows that the anticipated loss for a 16-converter generator configuration with a 10 mil insulation gap is about 226 watts at a cavity temperature of 2,000°K. The calculations assumed a converter diameter of 1.5 inches. The radiation loss shown in Fig. 6-15 will depend linearly on the number of converters and the diameter of the converter.

It appears possible to prevent a significant amount of thermal energy from escaping through the insulation gap by the use of a reradiating wall similar to the configuration shown below. The energy loss through the gap is:

$$P_{\text{gap rad}} = \frac{A\sigma}{\left(\frac{1}{\epsilon_r} + \frac{1}{\epsilon_o} - 1\right)} (T_o^4 - T_r^4) = A\epsilon_r\sigma (T_o^4 - T_r^4)$$

where

A = cross sectional area of gap

$\epsilon_r$  = emissivity of the reradiating wall (for tantalum at 800°K,  
 $\epsilon_r = 0.16$ )

$\epsilon_o = 1$  is the effective cavity (blackbody) emissivity

T<sub>r</sub> = 800°K is the temperature of the reradiating surface

T<sub>o</sub> = cavity temperature

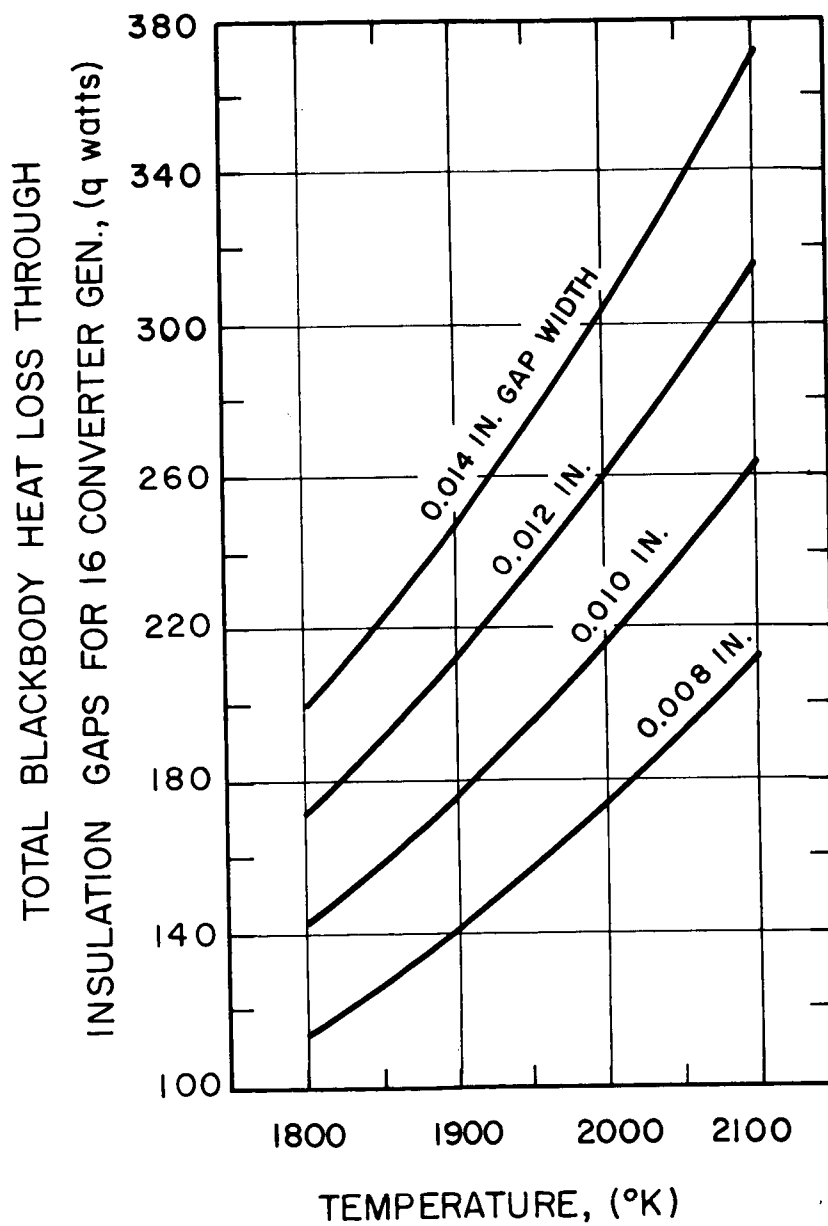


FIG. 6-15 TOTAL HEAT LOSS (blackbody) THROUGH INSULATION GAPS FOR 16-CONVERTER SET GENERATOR VS CAVITY TEMPERATURE (gap width as parameter)

Thus,

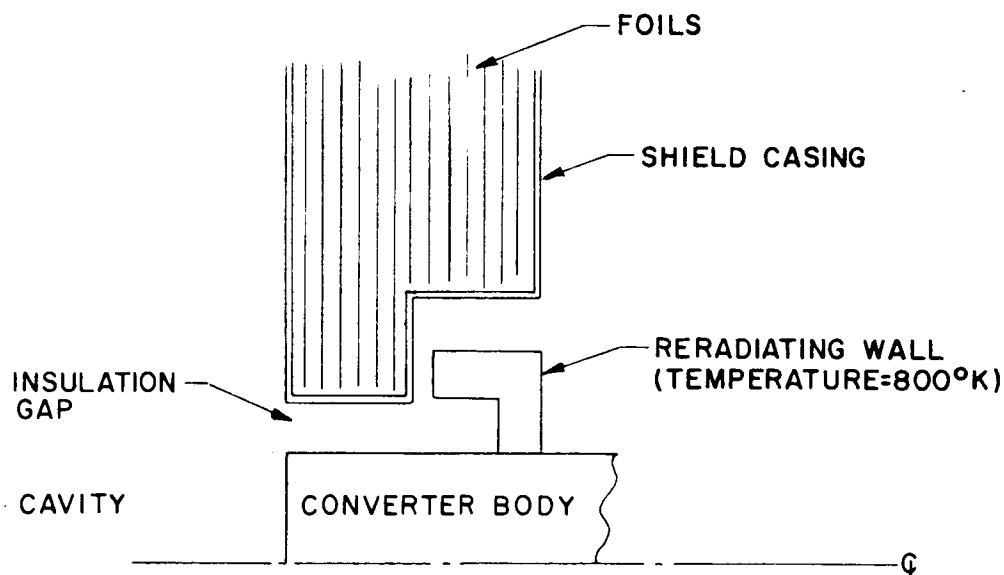
$$P_{\text{gap rad}} = 0.16A [E(T_o) - E(800)], \text{ watts}$$

or

$$P_{\text{gap rad}} = 0.16A [E(T_o) - 2.3], \text{ watts}$$

where

$E(T_o)$  = blackbody emissive power at  $T_o^{\circ}\text{K}$



A DESIGN OF RERADIATING WALL FOR INSULATION GAP

The above equation presupposes that the reradiating surface is maintained at a constant temperature of  $800^{\circ}\text{K}$ . This condition is necessary to insure that the converter operation (particularly the seals) is not disturbed by the presence of the reradiating surface. The  $800^{\circ}\text{K}$

reradiating surface temperature is maintained by the proper combination of surface-area and emissivity. In general, the reradiating surface must be of such a geometry that it "sees" little else besides the cavity and the cavity must be able to see only the reradiating surface. When this is the case, the model for heat transfer can be assumed to be heat transfer between two infinite walls. In this case, the cavity is one wall and since it is a blackbody (the emissivity is one). The other wall has the emissivity that corresponds to the tantalum metal at  $800^{\circ}\text{K}$  (this value is 0.16).

Figure 6-16 is a plot for the 16-converter generator configurations. The total radiant energy loss is plotted versus cavity temperature for converter-shielding gaps varying from 0.008 to 0.014 inch. A comparison of the blackbody loss case with that occurring after incorporation of reradiating walls, shows that substantial energy economy may be effected by incorporating the reradiating walls in future converter designs. For a  $2,000^{\circ}\text{K}$  cavity temperature, the radiation loss through the converter-shielding gap with a reradiating wall is reduced to 16 percent of the blackbody loss present when no reradiating wall is used. The gap loss could be reduced to approximately 9 watts for a four-converter generator by using reradiating walls in the insulation gap. For a four-converter design using 20 to 30 foils for shielding and operating at  $2,000^{\circ}\text{K}$ , overall losses could be decreased to less than one half of the value obtained with no reradiating walls present. The motivation to reduce the insulation gap loss is due to the realization that of the overall generator structure thermal losses (neglecting converter heat rejection) the gap losses are second in magnitude to the cavity opening reradiation losses.

#### 6.5.2 Conduction Loss

This loss is due to continuous metal sections leading from inside the cavity to the exterior. Energy is conducted from the cavity and radiated to the low temperature environment on the outside.

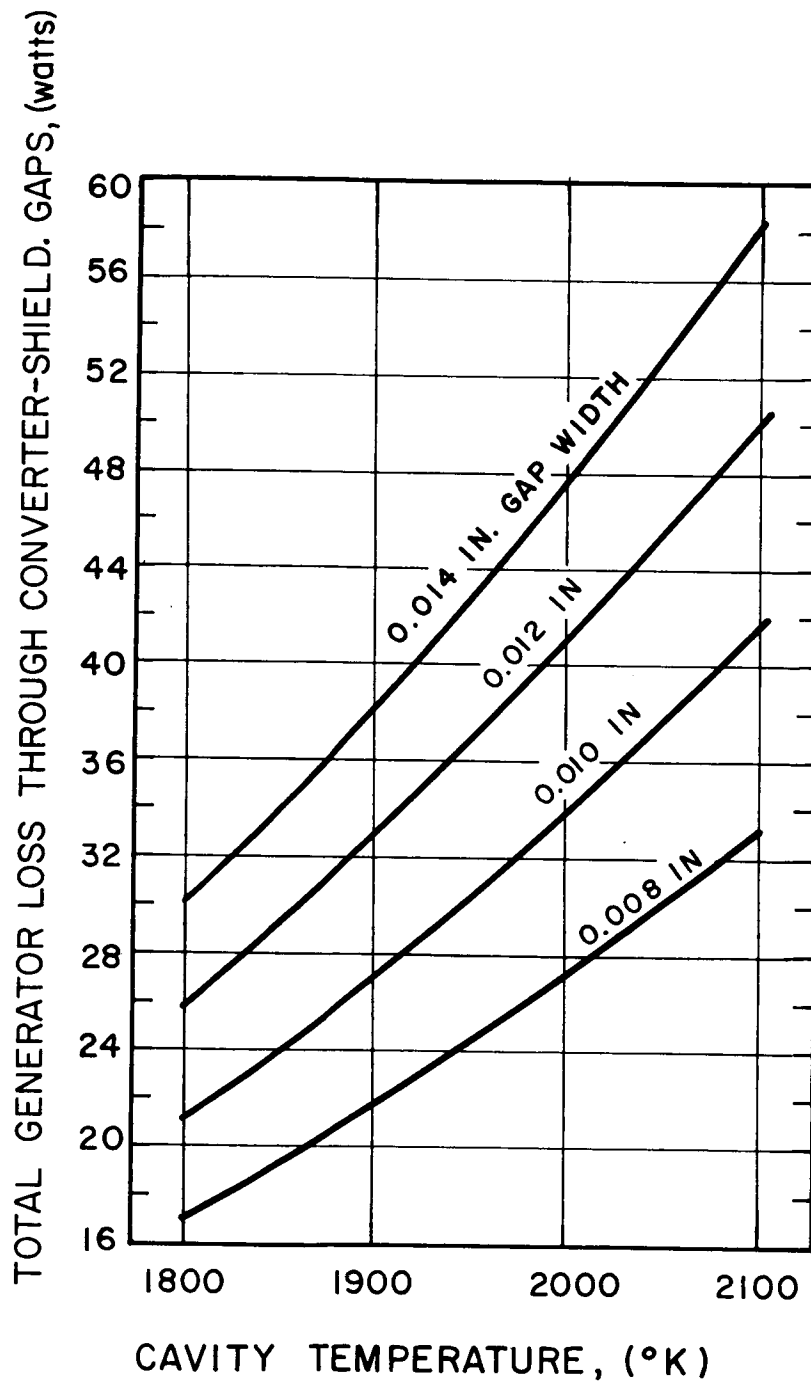


FIG. 6-16 RADIANT ENERGY LOSS THROUGH INSULATION GAPS (with reradiating wall) FOR 16-CONVERTER SET GENERATOR VS CAVITY TEMPERATURE (gap width as parameter)

In the design concept under consideration, the conduction loss occurs to a significant extent at two places:

1. At the lip of the flux trap cone bordering on the cavity entrance
2. At the shielding retaining sleeves surrounding the converter openings in the radiation shielding

The most significant of these two losses occurs at the lip of the flux trap cone due to the much larger area involved.

The heat loss from the cavity due to conduction at the flux trap cone is

$$q = \epsilon \sigma A (T_o^4 - T_{\text{cone}}^4) \text{ watts}$$

where

$T_{\text{cone}}$  = cone temperature

$T_o$  = cavity temperature

$\epsilon$  = effective emissivity of the cone and cavity combination

$A$  = interior surface area of the cone flux trap which faces the cavity

It is evident that once the interior cone surface temperature  $T_{\text{cone}}$  is known,  $q$  can be readily found. In practice it has been found that the flux trap cone can be made to run at a temperature of approximately 800°K. Assuming this approximate temperature and an emissivity of approximately 0.1 for the cone area facing the cavity, the cavity loss due to this mechanism can be computed. For example, assume a generator suitable for use with a 5-foot concentrator with a 0.75-inch entrance. The area of the cone which is exposed to the cavity interior corresponds to a ring 0.750 inch in average diameter and having a width of perhaps 0.140 inch. The net area of this annular ring is approximately 2.1 cm<sup>2</sup>. The cavity loss to this annular ring is approximately 18 watts for an effective emissivity of 0.1. Table 6-I summarizes the calculated  $q$  for the 1,900 to 2,100°K temperature range.

TABLE 6-I  
SUMMARY OF CONDUCTION LOSSES AT FLUX TRAP CONE  
AND RETAINING SLEEVES

| <u>Cavity<br/>Temperature<br/>(°K)</u> | <u>q<sub>cone</sub><br/>(watts)</u> | <u>q<sub>sleeves</sub><br/>(one converter)<br/>(watts)</u> |
|--|-------------------------------------|--|
| 1,900                                  | 15.1                                | 3.4  |
| 2,000                                  | 18.3                                | 3.4  |
| 2,100                                  | 22.5                                | 3.4  |

This estimate is felt to be conservative as long as the interior of the cavity does not see the crack between the converters and the front flux trap cone. In an actual generator a shield should be placed so that the edge of the flux trap cone does not look directly at the interior of the cavity but faces a low emissivity emitter surface which reduces the effective emissivity of the cavity-cone combination to approximately 0.08 instead of 0.1.

The conduction loss at the converter shielding retaining sleeve is a complex function of:

1. Temperature variation in the shielding
2. Temperature distribution along the converter envelope
3. Emissivity and geometry of the gap between converter and sleeve
4. Thermal conductivity and geometry of the sleeve

To a first approximation it can be assumed that the average temperature of this retaining sleeve is approximately 1,200°K. Assuming a tantalum sleeve thickness of 0.002 inch, a sleeve length of 0.200 inch and a temperature drop of 500°C, the conduction loss per converter is:

$$q_c = -kA \frac{dT}{dx} \approx (0.71)(4.83 \times 10^{-3})(985) \approx 3.4 \text{ watts}$$



Since the average temperature of the retaining sleeve will not change much for cavity temperature between 1,900 and 2,100°K, the conduction loss through the sleeve has been assumed constant at 3.4 watts per converter over the entire cavity temperature range. These losses together with the flux trap losses are shown in Table 6-I.

#### 6.5.3 Heat Loss Through Radiation Shielding of the Generator Structure

##### Radiation Shielding Losses Assuming Constant Shield Emissivity Over Entire Temperature Range

The assumption of constant shield emissivity, though not usually found in practice, simplifies the shielding equations, and yields solutions that lead to a better understanding of shield behavior when emissivity changes are taken into account. In this analysis, steady state heat flow through multiple layers of shielding is considered. The shields may be disks or cylinders but are assumed to be thin in comparison to their curvature that they may be regarded as a flat parallel geometry as far as the analysis is concerned. It is assumed that a vacuum exists in the cavity, as well as between the individual layers of the shield, and in the space adjacent to the exterior shield. It is further assumed that all heat flow is a result of radiation heat transfer between shields and that no thermal conduction occurs between the individual shield layers. This last assumption is acceptable, if the areas of contact between adjacent layers are small and the bond is poor so that the overall thermal resistance of these contacts is large. The shield layers will contact each other only at dimples in the foil. This method of shield assembly has been found to be satisfactory in the past.

It can be shown that for two very large surfaces (i and j) of area A, which are close together, the net radiation interchange from surface i to surface j is approximately:

$$q_{i,j} = A\sigma(T_i^4 - T_j^4) \frac{1}{\left(\frac{1}{\epsilon_i} + \frac{1}{\epsilon_j} - 1\right)}$$

where

$q_{i,j}$  = net heat transfer from layer i to j

$T_i$  = temperature of shielding layer i

$T_j$  = temperature of shield layer j

$\sigma$  = Stephan-Boltzmann constant

$A$  = shielding area

$\epsilon_i, \epsilon_j$  = emissivity of layer i and j respectively

The heat transfer between surface 0 and layer 1 is thus

$$\frac{q_{0,1}}{A} = \frac{1}{\frac{1}{\epsilon_0} + \frac{1}{\epsilon_1} - 1} \sigma(T_0^4 - T_1^4)$$

where

$T_0$  = cavity temperature

and between the two layers 1 and 2 with an emissivity  $\epsilon$ ,

$$\frac{q_{1,2}}{A} = \frac{1}{\left(\frac{1}{\epsilon} + \frac{1}{\epsilon} - 1\right)} \sigma(T_1^4 - T_2^4) = \frac{\epsilon}{2-\epsilon} \sigma(T_1^4 - T_2^4)$$

In general, the specific heat transfer can be written

$$\frac{q_{k, k+1}}{A} = \frac{\epsilon}{2-\epsilon} \sigma(T_k^4 - T_{k+1}^4)$$

if both layers have the same emissivity  $\epsilon$ . For the nth layer radiating into space with emissivity  $\epsilon_n$  we have

$$\frac{q_n}{A} = \epsilon_n \sigma T_n^4$$

For steady state heat flow the heat flux is the same for each shield, hence,

$$q_{0,1} = q_{1,2} = \dots = q_{n-1,n} = q_n$$

When the emissivity values are assumed to be the same for successive layers, then

$$(T_1^4 - T_2^4) = (T_k^4 - T_{r+1}^4)$$

This shows that for two adjacent layers the difference between the fourth powers of the temperature is a constant, hence, for n layers (i.e., n-1 sets of adjacent layers) we have

$$T_1^4 - T_n^4 = (T_{n-1}^4 - T_n^4) (n-1)$$

Equating the heat flow between the cavity and the first layer with the heat flow between the (n-1) th and nth layer we obtain

$$T_o^4 = T_1^4 + \frac{\epsilon + \epsilon_o - \epsilon_o \epsilon}{\epsilon_o (2-\epsilon)} (T_{n-1}^4 - T_n^4)$$

Also equating the heat flow between the nth layer and space with the flow between the n-1 and nth layer we obtain

$$T_{n-1}^4 - T_n^4 = \frac{\epsilon_n (2-\epsilon)}{\epsilon} T_n^4$$

Solving simultaneously we obtain

$$T_n^4 = T_o^4 / (C_1 C_2 + 1)$$

$$C_1 = \frac{\epsilon_n (2-\epsilon)}{\epsilon}$$

$$C_2 = \frac{\epsilon + \epsilon_o - \epsilon_o \epsilon}{\epsilon_o (2-\epsilon)} + n-1$$

and the heat loss per unit area is

$$\frac{q_n}{A} = \epsilon_n \sigma \frac{T_o^4}{\left[ \frac{\epsilon_n (2-\epsilon)}{\epsilon} \right] \left[ \frac{\epsilon + \epsilon_o - \epsilon_o \epsilon}{\epsilon_o (2-\epsilon)} + n-1 \right] + 1}$$

we can thus write

$$\frac{q_n}{A} = C_{\epsilon, \epsilon_o, \epsilon_n} \sigma T_o^4$$

where

$$C_{\epsilon, \epsilon_o, \epsilon_n} = \frac{\epsilon_n}{\left[ \frac{\epsilon_n (2-\epsilon)}{\epsilon} \right] \left[ \frac{\epsilon + \epsilon_o - \epsilon_o \epsilon}{\epsilon_o (2-\epsilon)} + n-1 \right] + 1}$$

$C_{\epsilon, \epsilon_o, \epsilon_n}$  is actually the effective emissivity in that it represents the ratio of heat lost to heat that would be lost by a blackbody at the cavity temperature,  $T_o$ .

This equation indicates the effectiveness of the shielding in reducing the blackbody radiation from the cavity. It can be shown that for any given set of parameters  $\epsilon$ ,  $\epsilon_o$ , the effect of varying  $\epsilon_n$  is less for large values of  $n$ . If we consider the fact that throughout the shielding the lowest possible emissivity values will be used, then it is evident that unless  $\epsilon_n$  is much smaller than

$\epsilon$ , the reduction in  $q/A$  will not be substantial. As a general rule though, it is desirable to reduce all losses to the absolute minimum, hence, if possible, the outer shield should have the lowest possible emissivity, even if one has to go to special coatings\*.

$C_{\epsilon, \epsilon_0, \epsilon_n}$  is quite insensitive to changes in  $\epsilon_0$ , hence, this value need be known only approximately in calculations. As a general rule  $\epsilon_0$  should be made as small as possible.

We will now consider the case where the emissivities of all the shields are the same, i.e.,

$$\epsilon_1 = \epsilon_2 = \epsilon_3 = \dots = \epsilon_{n-1} = \epsilon_n$$

then

$$C_{\epsilon, \epsilon_0, \epsilon_n} \equiv C_{\epsilon, \epsilon_0} = \frac{\epsilon \epsilon_0}{\epsilon + \epsilon_0 n (2 - \epsilon)}$$

and

$$C_{\epsilon, \epsilon_0} \cong C_{\epsilon} = \frac{\epsilon}{n (2 - \epsilon)} \quad \text{for } n > 10$$

At 2000°K tantalum has a total normal emissivity of 0.24. This is the value to be used for  $\epsilon_0$ . Thus,

$$C_{\epsilon, \epsilon_0} = \frac{0.24\epsilon}{\epsilon + 0.24n (2 - \epsilon)}$$

To find the heat radiated per unit area, i.e.,  $q/A$  we use the equation

$$\frac{q}{A} = C_{\epsilon, \epsilon_0} \sigma T_o^4$$

---

\*The long term stability of any proposed coating should be carefully checked before such a scheme is adopted.

Figure 6-17 shows the variation of heat loss per unit area with the number of radiation shields. The emissivity values used as parameters are  $\epsilon = 0.05, 0.1, 0.15$  and the values of  $C_{\epsilon, \epsilon_0}$  are calculated from the equations above. The plots show that the dependence of  $q/A$  on  $\epsilon$  is very pronounced for any number of shields used and that in order to obtain very good insulation without using an unreasonable number of shields, shields with very low emissivity must be used throughout, or if this cannot be done due to the necessity of using shield material of high emissivity adjacent to the cavity wall, then a sufficient number of low emissivity outer shields must be used in order to have a low, effective emissivity for the entire shielding structure. The required number of shields to achieve a given heat loss is very sensitive to the value of the emissivity of the shields.

In practice, the emissivity cannot be assumed to be constant throughout the temperature range usually involved. In such cases, a continuum approximation should be developed for a discrete set of shields. The continuum case will be considered in the next section.

#### Radiation Shielding with Emissivity a Function of Temperature - One Set of Shields

The calculation methods developed above may be used to estimate the approximate number of shields required for a given heat loss when the shield materials show only a slight variation of emissivity with temperature over the range of application. In such cases, either an average emissivity may be used to obtain upper and lower limits of the required number of shields or an average value of these limits is used as a most probable value.

When the shield emissivity variation with temperature is large over the temperature range of interest the methods described above will give only a rough estimate. Thus, an approximation adaptable to shields having a variable emissivity is desirable.

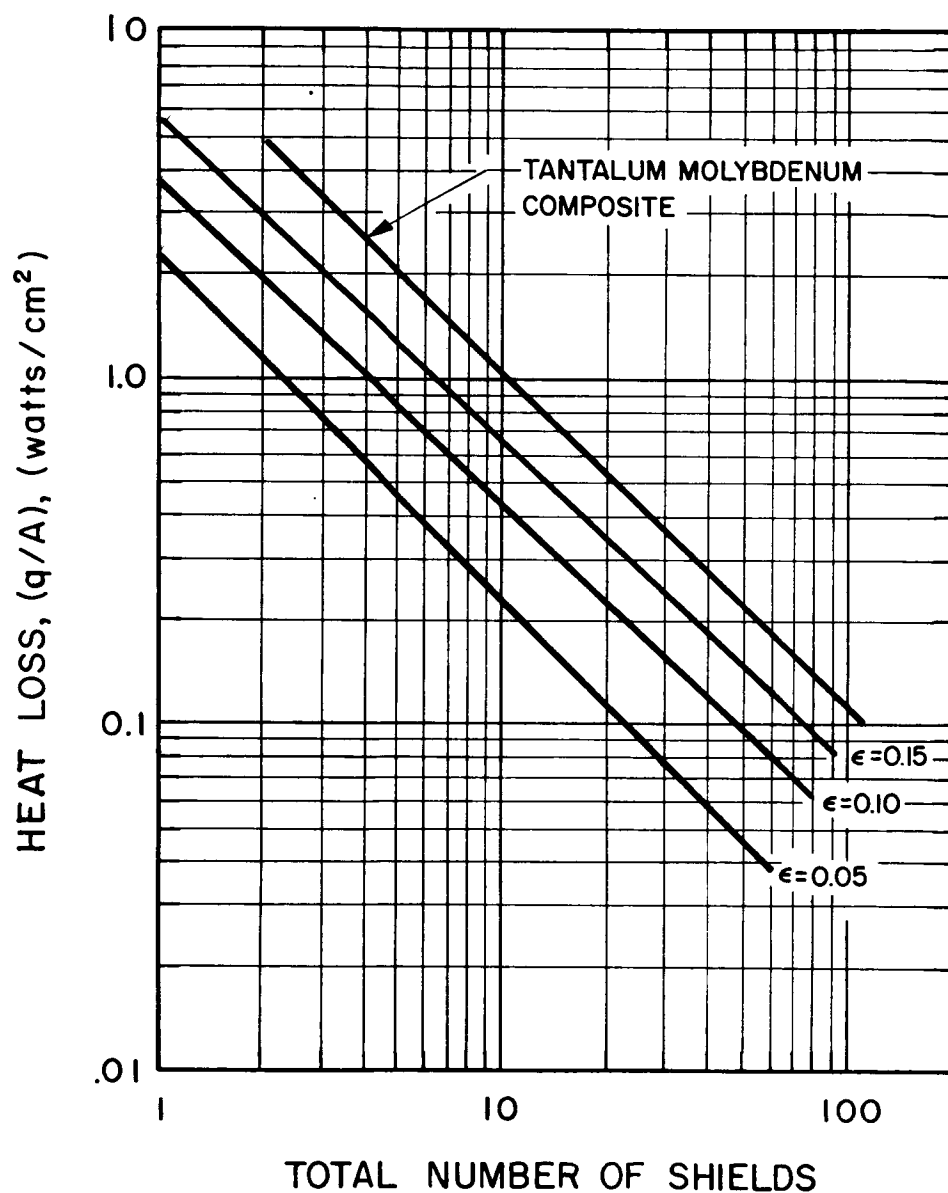


FIG. 6-17 COMPARISON OF HEAT LOSS VS NUMBER OF SHIELDS FOR CONSTANT EMISSIVITY AND FOR AN ACTUAL TANTALUM-MOLYBDENUM COMPOSITE SHIELD (cavity temperature =  $2000^\circ\text{K}$ )

An approach to the problem of shields with variable emissivity is to regard  $n$  (the number of shields) as a continuous variable, i.e., values of  $n$  will be considered that are not integers. In this manner, the difference in temperature between any two foils is now the variation of temperature with respect to  $n$  within the shield system. The number of shields required to produce any desired loss can be closely estimated to any degree of accuracy from results obtained after certain mathematical manipulations have been performed. The procedure is illustrated below.

Assume that between any two successive shields ( $k, k + 1$ ) the temperature difference  $\Delta T$  is sufficiently small so that an average value of  $\epsilon_k$  may be assumed to be valid for both shields, then the heat transfer relation for two successive shields can be derived,

$$\begin{aligned}\frac{q_{k, k+1}}{A} &= \frac{\epsilon \sigma}{2-\epsilon} (T_k^4 - T_{k+1}^4) = \frac{\epsilon \sigma}{2-\epsilon} [(T_{k+1} + \Delta T)^4 - T_{k+1}^4] \\ &= \frac{\epsilon \sigma}{2-\epsilon} T_{k+1}^4 \left[ \left(1 + \frac{\Delta T}{T_{k+1}}\right)^4 - 1 \right]\end{aligned}$$

Using the first two terms of the binomial expansion of  $(1 + \Delta T/T_{k+1})^4$  we obtain

$$\left(1 + \frac{\Delta T}{T_{k+1}}\right)^4 \approx 1 + 4 \frac{\Delta T}{T_{k+1}}$$

hence,

$$\frac{\Delta T}{T_{k+1}} = \frac{1}{(4 T_{k+1}^4)} \left[ \frac{(2-\epsilon) q}{\epsilon \sigma A} \right]$$

For well-shielded cavities,  $q/A$  is very small, hence,  $\Delta T/T_{k+1}$  is small and the second order term of  $O[(\Delta T/T)^2]$  may be neglected. The temperature difference between any two shields is thus:



where  $\epsilon$  is now the average value of the emissivity for both shields. The value of  $\Delta T$  given above is actually the value that results per unit change in the number of shields, hence,

$$(dT/dn) = - (1/4)(q/A) \left( \frac{2-\epsilon}{\epsilon} \right) (1/T^3)$$

In this equation,  $n$  is being treated as continuous rather than being restricted to integers. The minus sign is introduced because an increase in  $n$  results in a decrease in  $T$ , hence, for increasing  $n$ ,  $dT/dn$  is negative. Then,

$$dn = - \frac{4\sigma}{(q/A)} \frac{\epsilon}{2-\epsilon} T^3 dT$$

$$\int_0^n dn = n = - \frac{4\sigma}{(q/A)} \int_{T_0}^{T_n} \frac{\epsilon}{2-\epsilon} T^3 dT$$

$$n = \frac{4\sigma}{(q/A)} \int_{T_n}^{T_0} \frac{\epsilon}{2-\epsilon} T^3 dT = \frac{22.7 \times 10^{-12}}{(q/A)} I(T_0, T_n)$$

$$I(T_0, T_n) \equiv \int_{T_n}^{T_0} \frac{\epsilon}{2-\epsilon} T^3 dT$$

$T_0$  = cavity wall temperature

$T_n$  = temperature of outermost shield

If  $q/A$  is specified, then  $T_n$  may be conveniently found from a plot of  $q/A$  versus  $T$  for the material under consideration.

Note that when  $T_n = T_0$  then  $n = 0$ , therefore,  $n$  is the number of shields outside the first, since the first shield is assumed to be at the cavity temperature  $T_0$ . For the case where  $\epsilon$  is constant, the equation above reduces to the simple case treated earlier:

$$n = \frac{\sigma}{(q/A)} \frac{\epsilon}{2-\epsilon} [T_0^4 - T_n^4]$$

For the case of  $\epsilon = 0.1$ , we have for  $q/A = 9.2 \times 10^{-2}$  the value of  $T_n = 638^\circ\text{K}$  hence,  $n = 51.3$ . The value calculated previously is 50 shields, hence, both methods are in reasonable agreement. The error here is approximately 2 percent. If higher powers of  $\Delta T/T$  are retained in the binomial expansion it can be shown that the error in the number of shields calculated by the method derived is always a positive one, hence, the method gives slightly conservative estimates.

#### Radiation Shielding with Emissivity a Function of Temperature - Two Sets of Shields

The only shield materials acceptable for use above approximately  $1600^\circ\text{K}$  are tantalum and tungsten. Unfortunately, these materials have relatively high values of emissivity at the lower temperatures ( $1000^\circ\text{K}$ ), hence, at lower temperatures it is desirable to use shields having a low emissivity. Below  $1600^\circ\text{K}$ , molybdenum shields may be used, below  $1000^\circ\text{K}$  nickel is satisfactory and at  $800^\circ\text{K}$  copper could be used. In studying composite shields, we find that the equations above may be used with modifications. The details of this modification will be discussed later in this section.

Examination of the total normal emissivities of tantalum and tungsten over the temperature range of 1600 to  $2100^\circ\text{K}$ , shows that throughout this temperature range tantalum has a slightly lower emissivity. In conjunction with its workability it would appear that tantalum is the most desirable shield material at the high temperatures. Over the 1600 to  $800^\circ\text{K}$  temperature range molybdenum has the lowest emissivity when compared with tungsten and tantalum. Below  $800^\circ\text{K}$  copper shields would give a slight improvement over molybdenum but the extra fabrication effort does not make the use of copper worth while.

Before proceeding with this analysis, it should be pointed out that the maximum shielding thickness allowable by generator structure considerations is approximately 0.150 inch. This

rough upper limit on the shielding thickness results from the necessity of preventing the shielding from disturbing the desirable temperature distribution in the converter. With 1 mil shield foil and a 4 mil separation between shields, approximately 30 shields can be accommodated in the 0.150 inch space allowed for shielding.

In analyzing the composite shield heat transfer, the continuum approach breaks down for cases where two adjacent shields have grossly dissimilar emissivities. If the emissivity difference between adjacent foils is small (as in the practical case) then the total number of shields may be found by using for  $\epsilon(T)$  the emissivity variation with temperature of the specific metals chosen for the shielding. If, on the other hand, the emissivities are very different, then at each dissimilar junction the temperature drop must be found by the equations;

$$\frac{q}{A} = \frac{\sigma}{\frac{1}{\epsilon_k} + \frac{1}{\epsilon_{k+1}} - 1} (T_k^4 - T_{k+1}^4)$$

If a composite shield of tantalum and molybdenum foils is used, then,

$$n_{Ta} = \frac{22.7 \times 10^{-12}}{(q/A)} \int_{1600}^{T_o} \epsilon/(2-\epsilon) \cdot T^3 dT = \text{number of tantalum foils}$$

and

$$n_{Mo} = \frac{22.7 \times 10^{-12}}{(q/A)} \int_{800}^{1600 - \Delta T_{Ta,Mo}} \epsilon/(2-\epsilon) \cdot T^3 dT$$

= number of molybdenum foils

where

$\Delta T_{Ta,Mo}$  = temperature drop at the tantalum molybdenum junction.

For large junction temperatures and small heat losses,  $\Delta T_{Ta,Mo}$  is small and may be neglected in most instances. For example,

$$\Delta T_{Ta-Mo} = 107.5 (q/A)$$

If instead of assuming shields of two different materials, the shields were assumed to be all molybdenum, then

$$\Delta T_{Ta,Ta} = (q/A) \frac{11}{0.0933} = 118 (q/A)$$

so that the error in  $\Delta T$  is

$$\delta(\Delta T) = (118 - 107.5) q/A = 10.5 (q/A)$$

Since  $(q/A)$  is of the order of  $10^{-1} - 1$ , then the error is of the order of  $+1$  to  $10^{\circ}C$  and, hence, is negligible. The continuum approach to the composite shield thus appears to give a very close approximation to reality.

Some calculations have been made for a three-section shield using tantalum, molybdenum, and copper in the appropriate temperature ranges. The preliminary results indicate that it will be very difficult to keep the copper in a proper operating temperature range (lower than  $800^{\circ}K$ ) and the added complexity of the shields does not appear to make the three-section shield worthwhile at this time. For the remainder of this section, the composite tantalum-molybdenum shield will be stressed.

#### Tantalum-Molybdenum Composite Shield

Assume a shield consisting of tantalum foils adjacent to the cavity and extending into the shielding to the point at which the temperature is approximately  $1600^{\circ}K$ . From this point onward the foils are molybdenum. The materials for the composite shield design

were selected on the basis of the lowest practical emissivity values available for a given temperature range consistent with the material exhibiting physical and chemical characteristics that are satisfactory from the viewpoint of overall system performance. In this section, the equations are developed for calculating the specific number of shields required for specific heat loads. Plots are presented of the heat loss versus the total number of shields, and the number of molybdenum and tantalum shields with cavity temperature as a parameter.

The equation for the total number of shields for the tantalum-molybdenum composite reduces to

$$N = n_{\text{Mo}} + n_{\text{Ta}} = \frac{22.7 \times 10^{-12}}{(q/A)} \left[ \int_{T_n}^{1600} \epsilon/(2-\epsilon) \cdot T^3 dt + \int_{1600}^{T_o} \epsilon/(2-\epsilon) \cdot T^3 dT \right]$$

The first term on the right is the number of tantalum shields (excluding the cavity wall) and the second term is the number of molybdenum shields. The equation takes this simplified form because the emissivities of tantalum and molybdenum are approximately equal at 1600°K. The integral can thus be used to calculate the number of shields required for a given heat load. Shielding requirements have been investigated for 1800, 1900, 2000, and 2100°K cavity temperatures and for heat losses ranging from 0.1 to 1 watt per cm<sup>2</sup>. Some results are plotted in Fig. -18. The integrals were evaluated numerically by Simpson's one third rule and by the trapezoidal rule, as appropriate. The results show that for 30 foils the heat loss at a 2000°K cavity temperature is 0.33 watt per cm<sup>2</sup>. At 1900°K the loss is reduced to 79 percent of the value at 2000°K. This reduction in loss at 2000°K cavity temperature could be achieved with the addition of 8 shields. Most of the foils will be molybdenum.

#### Temperature Variation in the Tantalum-Molybdenum Composite Shield

The temperature distribution in a shield system is often required. This information is of particular interest if there is a desire to insert a temperature-sensitive material between certain

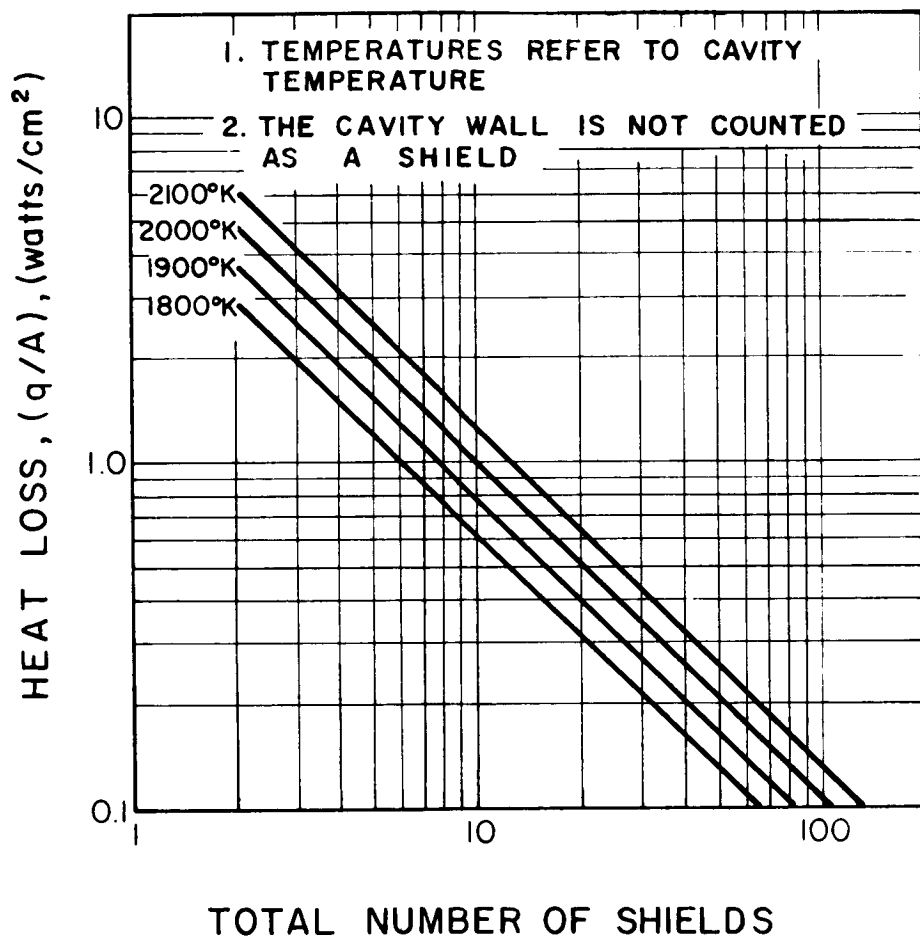


FIG. 6-18 TOTAL SHIELD REQUIREMENTS VS HEAT LOSS FOR A TANTALUM-MOLYBDENUM COMPOSITE SHIELD AT SELECTED CAVITY TEMPERATURES (tantalum above 1600°K, molybdenum below 1600°K)

layers. In this section, a general method for finding the temperature distribution  $T(n)$  is outlined and  $T(n)$  is evaluated and plotted for the tantalum-molybdenum composite shield.

For the equation for the number of shields, it is clear that the number of shields required to cause a temperature drop  $T_1 - T_2$  (for  $T_1 > T_2$ ) is

$$n = \frac{4\sigma}{(q/A)} \int_{T_2}^{T_1} \frac{\epsilon}{2-\epsilon} T^3 dT$$

hence,

$$n = \frac{4\sigma}{(q/A)} \int_T^{T_0} \frac{\epsilon}{2-\epsilon} T^3 dT$$

where  $T$  is the temperature  $n$  shields away from the cavity wall. Values of  $n$  and  $T$  for a cavity temperature of  $2000^\circ\text{K}$  is shown in Fig. 6-19. The plots give the foil temperature as a function of the number of foils  $n$  away from the cavity wall. The heat loss rate is the parameter for these curves. The curves end on a line that is the envelope of the outer shield temperature versus the total number of shields. Each graph is for a different cavity temperature.

#### Generator-Structure and Overall Efficiencies

The generator-structure efficiency is a measure of how well the generator performs its function of transferring heat to the diodes. It is the fraction of the energy arriving at the cavity that is available to the converters. Figure 6-20 gives values of the losses typically encountered in the generator-structure of the four-converter generator. It is felt that the scale of losses will generally hold true for most generator structures. The gap losses are by far the most serious for a well-designed converter. However, reradiation and reflection losses from the cavity (not shown in Fig. 6-20) are far more serious.

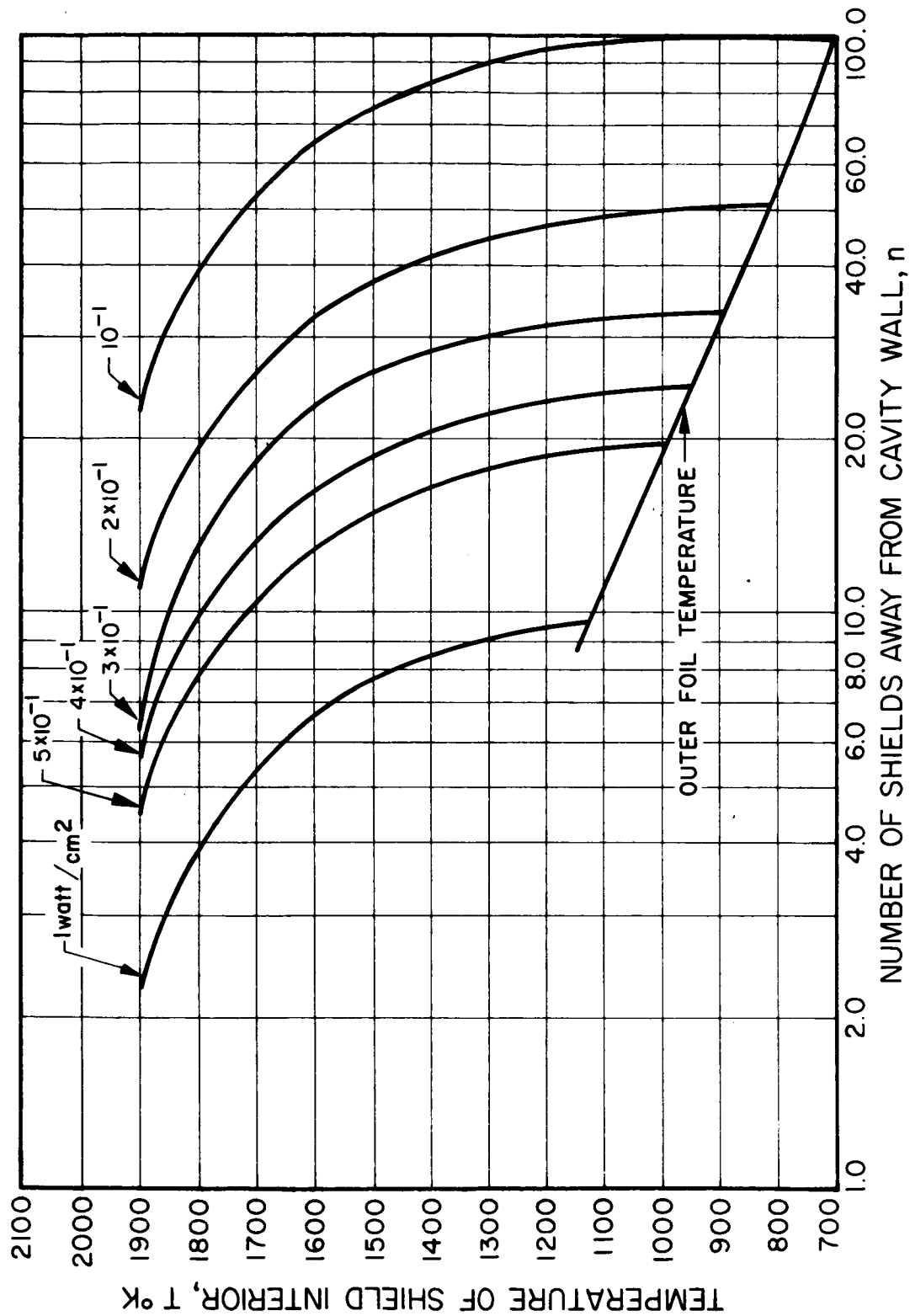


FIG. 6-19 VARIATION IN THE TEMPERATURE OF THERMAL RADIATION SHIELDS VS. NUMBER OF SHIELDS AWAY FROM CAVITY WALL FOR SELECTED HEAT-LOSS RATES (shielding material: tantalum above 1600°K, molybdenum below 1600°K, cavity temperature = 2000°K)



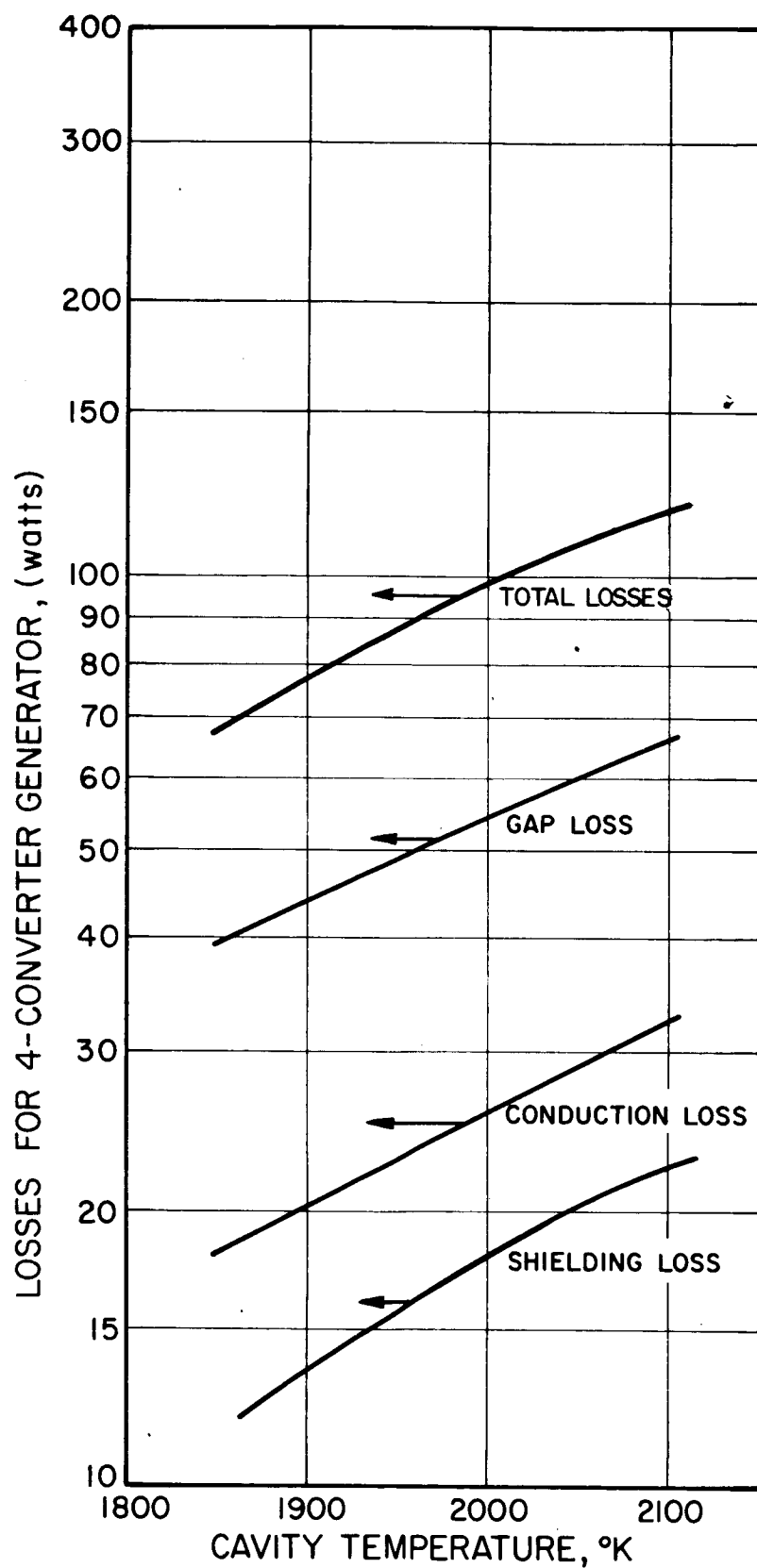


FIG. 6-20 TYPICAL LOSSES FOR 4-CONVERTER GENERATOR AS A FUNCTION OF CAVITY TEMPERATURE.